NEUTRONS FOR SOCIETY

Université Grenoble Alpes

THÈSE

Pour obtenir le grade de

DOCTEUR DE L'UNIVERSITE GRENOBLE ALPES

Spécialité : Physique pour les Sciences du Vivant

Arrêté ministériel : 25 mai 2016

Présentée par

Loreto MISURACA

Thèse dirigée par Prof. **Judith PETERS**, Université Grenoble Alpes
et codirigée par Dr. **Bruno DEMÉ**, ILL
et Dr. **Philippe OGER**, CNRS

préparée au sein du **Laboratoire Institut Laue-Langevin** dans **l'École Doctorale Physique**

Les protomembranes à l'origine de la vie

Protomembranes at the origin of life

Thèse soutenue publiquement le **22 mars 2021**,
devant le jury composé de :

Madame Judith PETERS
Professeure, Université Grenoble Alpes, Directrice de thèse

Monsieur Jean-Paul DOULIEZ
Directeur de Recherche, Institut National de Recherche pour l'Agriculture, l'Alimentation et l'Environnement (INRAE), Rapporteur

Madame Daniela UHRÍKOVÁ
Professeure, Comenius University in Bratislava, Rapportrice

Monsieur Roland WINTER
Professeur, Technische Universitat Dortmund, Examinateur

Madame Giovanna FRAGNETO
Professeure, Institut Laue Langevin (ILL), Examinatrice

Madame Juliette JOUHET
Directrice de Recherche, Centre Nationale de la Recherche Scientifique (CNRS), Examinatrice

Monsieur Hans GEISELMANN
Professeur, Université Grenoble Alpes, Président

CONTENTS

ACRONYMS

FOREWORD

The aim of this thesis is to validate and investigate the properties of a new membrane model for the first living systems at the origin of life.

The thesis is presented as a compendium of four scientific articles, each of them involving the study of the model systems from a specific point of view and by means of different experimental techniques. Two of the articles have been published in scientific journals and the remaining ones are currently under submission.

Chapter 1 introduces the context of the scientific project, namely the current knowledge about the expected conditions and timescale for the origin of life on planet Earth. It presents the current state of the art of lipid science, with special focus on the studies that provide information about possible proto-membranes that could have been formed in prebiotic environmental conditions. Finally, it introduces all the different models that were employed in this study building from the current scientific knowledge.

Chapter 2 describes all the experimental techniques that were used in order to carry out the study. In particular, the basic science behind the scattering techniques is briefly detailed, together with information about what can be probed depending on the selected experimental conditions. For each technique, a short summary is presented to highlight the main properties, length- and time-scale that can be investigated. Furthermore, the chapter describes the protocols used for sample preparation and the corresponding final sample state.

Chapter 3 contains the experimental results, divided into two sections and presented in form of scientific articles. The first section explores the role of the fatty alcohol in the properties and stability of the protomembrane model, the results of which are object of one scientific article. The second section explores the effects of alkane incorporation and the positioning within the membranes, with results being divided into the three remaining scientific articles. Before each article, a foreword introduces the subject related to the specific study, summarizes the main findings and details my personal contributions. When appropriate, additional notes at the end of each article discuss some of its results in the context of the thesis, comparing and linking the findings of the different papers with each other.

Chapter 4 draws the general conclusions of the Ph.D. project. The implications of the observed phenomena at high temperature are discussed particular, as well

as the positioning of alkanes inside the model protomembranes. In both cases, suggestions for further work are given in order to complement the results obtained in this work. Final perspectives are summarized with focus on the protomembrane biological functioning (e.g. membrane fluidity and permeability) to enrich the extensive physical and chemical characterization here presented.

Chapter 5, finally, contains a short summary of all the previous thesis chapters translated in french language.

1 ORIGIN OF LIFE

1.1 TIMELINE

1.1.1 From Earth's first steps to the oldest evidence of life

Planet Earth is about 4.5 billion years old. For a period of time after its formation, about 0.3 billion years, the planet was heavily bombarded by large objects which caused a molten, sterile surface (*1*) and the Moon formation (*2*). However, mineralogical evidences suggest that liquid water and an atmosphere, different from the modern one (a very recent paper suggests it was Venus-like (*3*)), were already present around 4.4 billion years ago (*4*).

It is difficult to estimate a time where the first living *protocellular* entities could have appeared, because (among the many unknowns) this would require defining what kind of energy source was used by these systems, i.e. whether they were auto-trophic (photo-synthetic, chemio-synthetic) or hetero-trophic and whether they were also thermo-philic and (/or) piezo-philic. Therefore, we will consider as upper limit for life appearance (*abiogenesis*) the time at which liquid water and an atmosphere were present, i.e. $\approx$ 4.4 billion years.

On the other hand, undisputed proof of photo-trophic life has been found as early as 3.5 billion years in microfossils (*5*), which could be pushed to 3.8 billion years by indirect analysis with Carbon isotopes (*6*) (or recently even more, yet debated: 4.1 billion years (*7*)). From what discussed, we can set the safest time window for life appearance to [4.4 - 3.5] billion years.

1.1.2 LUCA

As discussed in the literature (*6*), the 3.5 billion years microfossil data found by Schopf (*5*) make a conservative estimation for life appearance, because these organisms already had a quite high degree of complexity (oxygen-producing photoautotrophy). Instead, comparative genomics suggests the existence of a non-photosynthetic Last Universal Common Ancestor (LUCA) (*8*).

The existence of LUCA has been deducted from the similarities in the genetic code between the three domains of life on Earth: Archaea, Bacteria and Eukarya. Also, from this common pool of genes it is possible to conclude that LUCA (*8*):

1. was a cellular organism, hence it possessed a cytoplasmic membrane;

2. possessed a protein synthesis mechanism, in analogy with the today's living forms;

3. it was likely a piezophile, as piezophily (optimal growth under High Hydrostatic Pressure (HHP)) is evenly distributed between the domains of life.

1.1.3 What before LUCA?

In my work, subject of this thesis, I focus on what happened well before the existence of LUCA, i.e. when the first forms of proto-living entities assembled from a pool of simple molecules available on the prebiotic Earth. To answer this question is extremely challenging *a priori*, simply because there cannot be direct evidences (no fossils) about what happened. What can be done experimentally, instead, is to start from a few assumptions about the environment and the molecule abundance on the early Earth, and then test *in vitro* specific molecular species to see whether this path could eventually lead to living forms.

It is yet under debate whether life originated on Earth (*9*), or if some already assembled living systems were brought to our planet from the outer space (the so-called *Panspermia*) (*10*, *11*). To date, there is no evidence of extraterrestrial life, therefore most of the research in the field has been devoted to explore possible paths that could have led to life's origin on the early planet Earth.

In this work, I will assume that, even though the constituent organic material may have been brought by meteoritic impacts, terrestrial life began on planet Earth. Nevertheless, the results and conclusions presented here are general and could be easily extended to an *exo-planetarian* origin of life.

1.2 ENVIRONMENT - STATE OF THE EARTH

1.2.1 Early Earth molecular abundance

The synthesis of all necessary life "building blocks" depends heavily on the conditions of the early Earth environment in the time window that has been previously defined. However, the three most popular scenarios to date are (*9*):

- **Miller-Urey hypothesis -** Miller and coworkers (*12*–*14*) were able to synthesize several of the naturally available amino acids in a lab experiment where a highly reducing atmosphere was subject to electrical discharges.

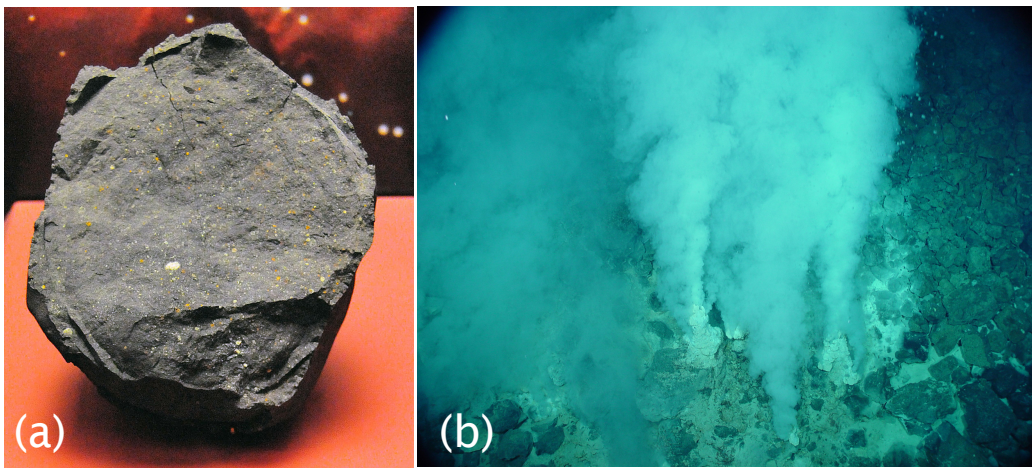

Figure 1: (a) A fragment of the *Murchison meteorite*, a carbonaceous chondrite rich in organic compounds, and one of the most studied meteorites. Image taken from (23).(b) An example of white smoker hydrothermal vent, the *Champagne vent* (Marianas Trench). Image taken from (24).

On the same track, it was shown (15, 16) that also other molecules such as adenine, cytosine and uracil could have been formed through similar experimental conditions. Nevertheless, these findings rely on strongly reducing atmosphere conditions, while all currently accepted scenarios for the Earth atmosphere do not meet this requirement (17).

- **Meteorites -** Studies of a common class of meteorites, known as carbonaceous chondrites (panel (a) of Figure 1), have shown the presence of several amino acids, hydrocarbons (18) and, of highest importance to this work, carboxylic acids that can form boundary structures (19, 20). Thus, these compounds could have been brought on Earth by meteoritic impacts.

- **Hydrothermal vents -** These are crust fractures present in the deep sea even nowadays (panel (b) of Figure 1), where hot water comes out and quickly mixes with the oceanic cold water. These systems have been studied as prebiotic source of chemical energy and as suitable locations for the formation of molecules such as short hydrocarbons (21), carboxylic acids and n-alkanols (22).

Of course, the above mentioned hypotheses are not mutually exclusive, hence it can be that more than one (or all together) contributed as sources for the early planet molecular abundance. All of the above scenarios give us an idea of some of the constituents likely present in life's *primordial soup*:

1. numerous amino acids, e.g. aspartic acid, glycine, alanine, homoalanine (12), leucine, valine, isoleucine, proline, serine, threonine (13) (from both electrical discharge synthesis and Murchison meteorite analysis (14));

2. nucleobases, both purines (*15*, *25*) and pyrimidines (*16*);
3. monocarboxylic (fatty) acids, up to at least 12 carbon chains (C = 2 - 12 from discharge synthesis (*26*), C = 2 - 8 from Murchison meteorite (*27*));
4. linear alkanes, on a wide length distribution centered at C = 18 (*18*), and in some cases Polycyclic Aromatic Hydrocarbons (PAH) (*28*).

1.2.2 Hydrothermal vents

As stated in the previous paragraph, hydrothermal vents may have had an additional role in the abiogenesis, namely as source of sustained chemical energy that would have been useful to fuel proto-metabolic processes (*21*). This makes the deep-sea vents one of the most popular environmental scenarios where life itself could have developed. A first reason is that harvesting chemical energy would have been a much simpler mechanism than the photosynthesis for the first living systems (*8*). Second, the conditions in the deep-sea biosphere were likely much more stable for long periods of time compared to Earth's surface, profiting additionally from the screen, offered by the ocean, against radiations and meteoric impacts.

1.2.3 Hot springs

A recent alternative environmental scenario was proposed to take into account polymer synthesis reactions and address some weak point of the hydrothermal vents hypothesis (*29*, *30*). For example, it has been shown that high ionic salt concentration inhibits self-assembly of membranes (*31*, *32*), although specialized lipid mixtures can still form stable membranes (*33*). The alternative scenario involves terrestrial hot springs (Figure 2) that would contain fresh water provided by the atmospheric precipitations. These ponds, by undergoing multiple wet-dry cycles of evaporation and re-hydration, could have provided the chemical potential and the activation energy (high temperature) needed to drive the condensation of monomers (*29*).

1.2.4 Matter at extremes

Although there is currently no agreement between the most suitable environment, all scenarios share a general common feature, namely the high temperature conditions. This goes in line with previous studies that formulated theories about the mean early Earth temperature (proposed to be in the range $85 < T < 110\ ^{\circ}C$

Figure 2: Example of today's hot springs on Mount Lassen (California). Image taken from (*34*).

(*35*) although probably referring to the vicinity of hydrothermal systems). Besides, the high temperature is a plausible requirement because all reactions that lead to polymerization (of amino acids or nucleic acid chains) would need to cross an activation energy barrier (*36*, *37*), therefore the thermal energy is seen as a likely energy source. Following this line of reasoning, it is crucial to gain knowledge on how a self-assembled compartment (membrane compartment) would have maintained the capability to entrap monomers on their way to polymerization, without undergoing disruption due to high temperature.

In the case of the hydrothermal vent scenario, another physical parameter is expected to have played a role, and hence its effects need to be equally taken into account: the HHP, which in today's oceans can reach values of $p \approx 1000\,\mathrm{bar}$.

In the case of membranes, the high temperature is known to fluidify the acyl chains to the point where the membrane loses its capability to retain the encapsulated molecules and solutes, which is the reason why today's hyperthermophilic microorganisms have developed more complex membranes (*38*).

The situation is further complicated when accounting for the early planet molecular limitations, where only short single chain amphiphiles were present and they must have acted as membrane-forming agents instead of the modern phospholipids. The fatty acids are known to have much higher Critical Vesicle Concentration (CVC) (*39*), defined as the minimum concentration needed to form vesicles, and the high temperature likely increases the percentage of solubilized monomers.

Other studies have been performed to explore the role of HHP in lipid membranes, which are the most pressure sensitive cellular components (*40*, *41*). Sev-

eral response mechanisms toward HHP have been found and studied, e.g. increase in bilayer thickness, changes in the packing parameter and hence the lipid intrinsic curvature curvature (defined and detailed in the next section), phase transition shifts, interdigitation (*42*, *43*). It is of crucial importance to investigate the effects of pressure and temperature on any model proto-cellular systems and to determine what suitable strategies can play a role in withstanding such harsh environments.

1.2.5 A common or a rare event?

As a concluding remark for this section, there is a fundamental question in the Origin of Life (OOL) field that needs to be addressed: is life appearance a rare phenomenon or rather a common one in the universe? It is no doubt that the answer to this question has great implications on the feasibility of all laboratory experiments devoted to finding and testing model prebiotic phenomena. Moreover, it could provide us with estimations on what our chances of finding extraterrestrial life are. A very recent study has tackled the issue by attempting an objective Bayesian analysis of life appearance and the development of intelligent life (*44*).

Bayesian inference is a statistical method used to calculate the probability of a hypothesis from the knowledge of some outcome. In this case, the (only) outcome available is the appearance of life on Earth (and the estimation of the time window since the planet became habitable). Kipping (*44*) found that, assuming to rerun Earth's clock, the probability of life forming vs. the one of life not forming is $\approx 3:1$ for the most conservative estimate (if life appeared 3.5 billion years ago (*5*)) and it rises up to $\approx 9:1$ when considering the more disputed estimate (if life appeared 4.1 billion years ago (*7*)).

Although the above-mentioned study only refers to the Earth (the probabilities found are related to our planet, assuming to rerun Earth's clock multiple times), these results give support to the idea that life may be a common phenomenon in Earth-like planets, and therefore a not-so-rare feature in the universe. It is equally important, therefore, to extend our knowledge about all possible processes that can lead to the origin and the development of life 1) by geological-mineralogical studies, 2) by performing laboratory experiments with controlled conditions (as it has been done in this thesis work) and 3) by searching for possible bio-signatures in other planets.

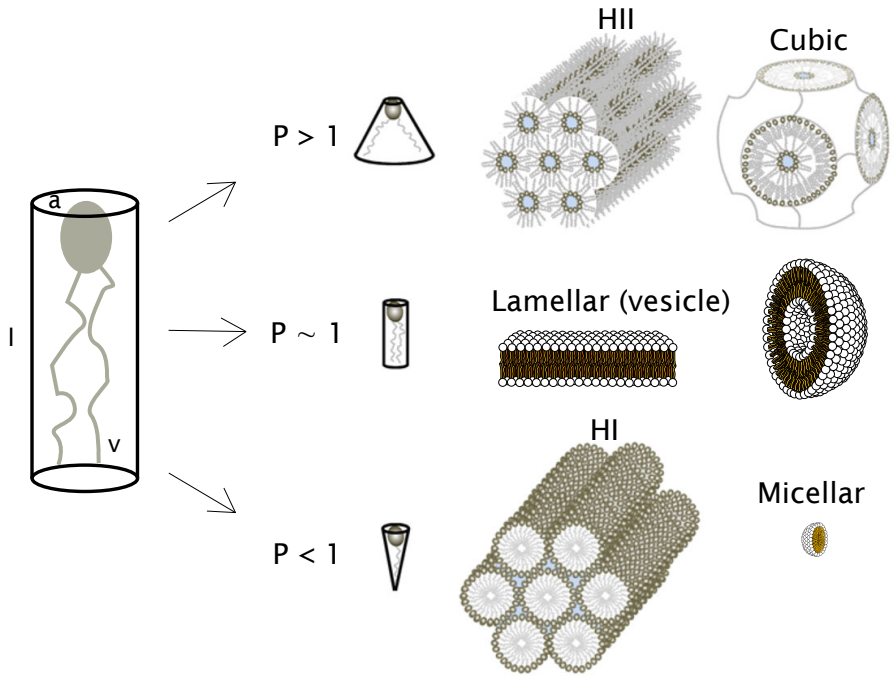

Figure 3: Left: sketch of the intrinsic lipid geometry and the quantities a (headgroup area, l (lipid length) and v (lipid volume) that allow to calculate the packing parameter P. Right: some of the different phases that can be obtained, depending on the lipid packing parameter. Image adapted from (*49*).

1.3 LIPID WORLD

The lipid membrane is among the most important structures possessed by every living organism. It also plays a central role in the OOL studies and is the focus of this thesis. For its importance, the term *Lipid world* has been adopted (*45*), in some cases as an alternative to the *RNA world* (*46*, *47*). A number of studies can be found where a *lipid world* scenario for the origin of life, the motivations behind and the implications are discussed in detail (*34*, *45*, *48*).

Generally speaking, lipids are hydrophobic or amphiphilic (with both a hydrophilic and a hydrophobic moieties) macrobiomolecules that are used in living organisms for many purposes, e.g. energy storage, signaling, and as structural membrane components.

The amphiphilic character is the one that allows the self-assembly in solution into a variety of macromolecular structures driven by the hydrophobic effect (*50*). The main ones that are found and discussed in this work are the *micelles*, the *vesicles* and the *droplets* (Figure 3).

Micelles are tiny spherical shaped objects formed by a layer of lipids, whose head groups (hydrophilic) are arranged at the edge of the supramolecular aggregate, while the acyl chains are placed towards the center, to avoid contact with the aqueous solvent and minimize the free energy of the aggregate (the surface

tension). The formation of this (and/or the others) kind of structures and their curvature depends on the intrinsic geometry of the given lipid type, described by the so-called *packing parameter* (*50*, *51*) (graphical representation in Figure 3).

The packing parameter P is a dimensionless quantity that is defined as (*40*):

$$P = \frac{v}{al} \tag{1}$$

where v is the molecular volume, l the lipid length, a the area of the head group at the interface with water. If $P < 1$ (positive curvature), the lipids have a conical geometry (with the base in the head group) and they will form high curvature assemblies such as micelles. This is frequently the case if, for example, the lipid head groups are charged (so that they will repel each other) and/or for lipids with single and/or short tails (e.g. short-chain fatty acids).

The vesicles are hollow structures where the lipids arrange into bilayers to form one or more concentric shells. A vesicle with a single bilayer shell is named Uni-Lamellar Vesicle (ULV), otherwise it will be referred as Multi-Lamellar Vesicle (MLV). These structures form when the lipids have a packing parameter $P \sim 1$ (zero curvature). This packing is typical of lipids having a cylindrical intrinsic geometry, therefore they are able to arrange in a lamellar, flat surface (with respect to the lipid length scale, see Figure 3). Because of the hydrophobic effect and since the head groups are hydrophilic, the most favoured arrangement will be as a bilayer with the acyl chains in the middle and the head groups exposed at the interface with water.

For the sake of completeness, there are a number of other non-lamellar phases that form when $P < 1$ e.g. the hexagonal phase HI, or *inverted* phases that form when $P > 1$ (negative curvature), e.g. the so-called hexagonal II (HII) or the cubic phases (depicted in Figure 3). Although these are believed to play important roles in biology (*49*), they were not observed in any experimental condition employed in the present work thus they will be neglected here.

Finally, lipids can form droplets, oily aggregates suspended in the aqueous solvent. They form typically when the lipid head groups are weakly hydrophilic, therefore the hydrophobic effect is the dominating factor and will cause the lipids to phase separate in small spherical aggregates, in order to minimize the contact surface with water.

What has been discussed above concerns any kind of amphiphilic molecules. However, lipids include a high variety of types, depending on the characteristics and type of their moieties: the type/size/charge of the head groups and the number/length/saturation of the acyl chains. In particular, two big classes must be differentiated for what follows in this work: *fatty acids* and *phospholipids* (Figure 4).

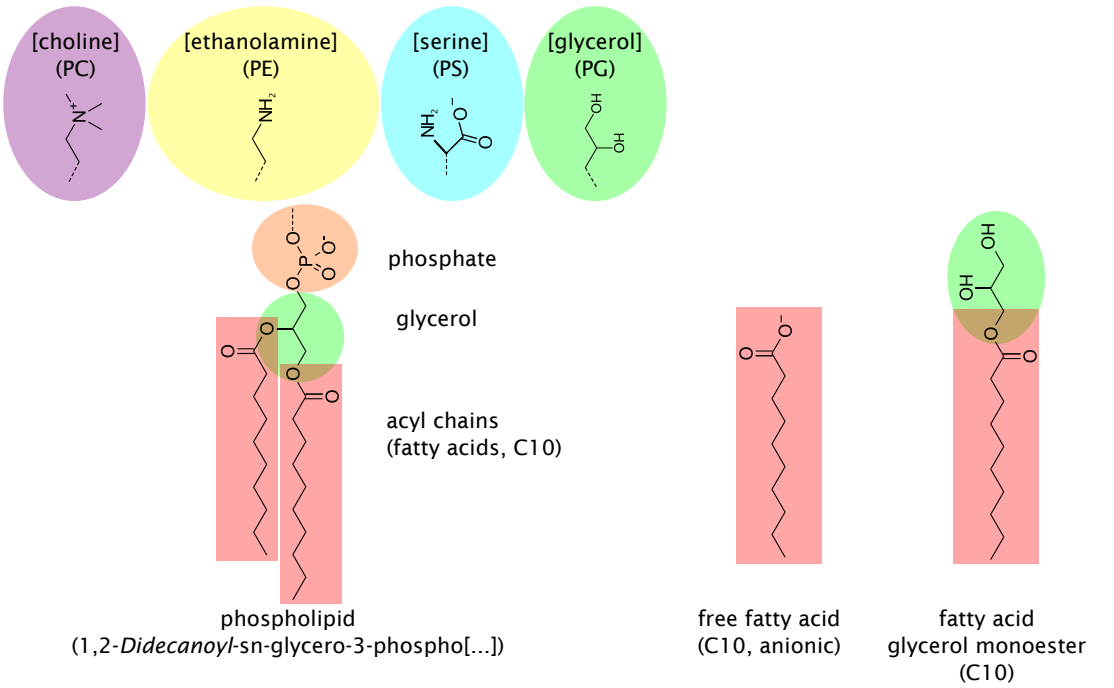

Figure 4: Left: Example of phospholipid: two acyl chains (in this case, C10 chains) are linked via ester bonds to a glycerol molecule, which in turn has an ester bond with a phosphate group; on top, four among the most common headgroup types are shown, which bind to the phosphate to give the corresponding phospholipid type (PC, PE, PS, PG). Right: the molecule of free fatty acid that will be studied throughout this work (decanoic acid, C10), in its anionic form, and also its glycerol monoester (monocaprin) that has been mixed with the decanoic acid in some former studies (*36*, *52*, *53*).

Fatty acids are carboxylic acids with an aliphatic chain (which can vary in size and/or degree of insaturation) (example in Figure 4). Here, it is the carboxylic acid that will be considered as the lipid head group. In the text, they will be referred sometimes as *single chain amphiphiles* to include also same length alcohol molecules.

Phospholipids are more sophisticated molecules constituting the main components of all cellular membranes in today's living cells. They typically have two acyl chains attached by ester bonds to a glycerol molecule. The glycerol has a third ester bond to a phosphate, to which is linked a hydrophilic group that differs depending on the phospholipid type (see Figure 4).

As it is made clear by the molecule structure observation in Figure 4, it is somewhat improper to see the phospholipids and the fatty acids as alternative amphiphilic systems. The definition of a *headgroup* itself, for the fatty acids, sounds as a stretch. However, the carboxylic acid still allows for hydrogen bonding with water, therefore it can play the role of a weakly hydrophilic group. A consequence of such "hydrophilic weakness" is the possibility to form the previously introduced lipid droplets with these systems (a phase that is not usually observed with phospholipids).

In both systems (phospholipids and single chain amphiphiles), the length of the acyl chains has a significant impact on the packing and structuring of the membrane (because longer chain will increase the contribution of the hydrophobic effect).

1.4 PROTOMEMBRANES - STATE OF THE ART

Although phospholipids are most probably better at securing membrane functions (as suggested by the ubiquitous presence in all modern cells), their presence in the prebiotic environment is questioned because their synthesis would have required a number of complex pathways (*54*). This is the reason why the simpler, single chain amphiphiles are considered the most probable agents for the membrane self-assembly in a prebiotic environment. As discussed in the previous sections, it has been shown that monocarboxylic acids could have been provided by meteorites (*19*, *20*) or synthesized in the proximity of hydrothermal vents in solution (*22*). All OOL studies must take into account such considerations when considering suitable model of protomembranes.

Because of the very special properties of single-chain amphiphilic molecules and the important role they play in biophysics and soft matter, research on fatty acids is a vast scientific field. Without attempting a full and exhaustive coverage, the reader can refer to dedicated reviews (*55*, *56*) or textbooks (*57*, *58*). Here, I will focus on the advances that have been made in the fatty acid field with specific relevance to the OOL investigation.

Hargreaves and Deamer (*39*) were among the firsts to explore the possibility for single chain amphiphiles to self-assemble into vesicles ((*59*)) as well as into micelles. In particular, the vesicles were found to form at specific concentration and pH conditions depending on the lipid chain length. Vesicles of pure fatty acids were observed to appear within a narrow range in the surrounding of the pK_a, the acid dissociation constant of the corresponding fatty acid. Otherwise, lower pH values ($pH < pK_a$) lead to phase separation and assembly into droplets, while higher pH ($pH > pK_a$) favour self-assembly into micelles. The authors pointed out the potential role of these vesicles as bio-membrane models in an OOL scenario.

Later on, Apel et al. (*60*) explored in detail the properties of fatty acid vesicles with chain length ranging from 8 to 12 carbons, defining the CVC and pH range for vesicle existence in each case. Moreover, the addition of even small percentages of same chain alcohols (10:1 fatty acid : alcohol ratio) was found to decrease significantly the CVC, which the author interpreted in terms of *hydrogen bond* strength

that would favour fatty acid : alcohol self-assemblies rather than the fatty acid *hydrogen bond* with water molecules. The fatty acid : alcohol membranes proved to be able to encapsulate a model enzyme and to protect it from degradation by a protease in solution.

The vesicles made from mixtures of short, saturated chain fatty acids (C < 12), being the most abundant species that can be synthesized by Fischer-Tropsch reactions (*22*, *61*) and also the ones most found in the carbonaceous chondrites (meteorites) (*27*, *62*), are indeed the ones which are considered as the most prebiotically relevant (*63*).

The above mentioned characterization studies on the fatty acid vesicles were all performed at ambient temperature. However, as discussed in the previous sections, it is important to explore the capability of these model membranes to be stable at high temperature conditions. Mansy and Szostak (*36*) addressed the issue and performed studies of oligonucleotide retention at temperatures up to T = 100 °C. Although they focused mostly on longer, unsaturated aliphatic chains (palmitoleic/ oleic/ linoleic acids, C = 16 and 18), they also explored the behaviour of the more prebiotically plausible decanoic acid : decanol mixture (C10, 2:1 ratio). They found the latter model to have surprisingly thermostable properties, as the vesicles were able to retain oligonucleotides up to T ≈ 60 °C (further increased to T ≈ 70 °C when adding a fraction of the decanoic acid glycerol monoester, or monocaprin, to the mixture).

Another study was performed by Kapoor et al. (*53*) to further explore the behaviour of a suitable model protocell. Here, a 1:1 mixture of decanoic acid and decanol was studied by varying not only temperature, but also HHP. The authors followed the pressure-temperature dependence on the chain packing and fluidity of these vesicular systems. They found that this model membrane could maintain its physiological state profiting from the synergistic effect of the two thermodynamic variables, up to values of T = 50 °C and p = 1400 bar.

In many cases, the vesicle suspensions have been prepared in a buffered solution, typically bicine (*36*, *53*, *64*–*66*), to provide a stable pH at all temperatures. Bicine is a zwitterionic buffering agent derived from glycine, with pK_a 8.3 (Figure 5). A buffered solution is certainly not plausible as an early Earth environment, however other studies (*60*, *67*) have shown that the same kind of fatty acid vesicles can form in water (most efficiently if starting from a completely deprotonated acid solution (*67*)).

However, as discussed earlier, high ionic salt concentration inhibits the vesicle self-assembly instead (*31*, *32*), and specialized lipid mixtures are needed in order to obtain stable vesicles. Many successful strategies have been proposed: addition of the fatty acid glycerol monoester (*52*), addition of small amounts of prebiotically available amino acids (which would also act as precursors of mem-

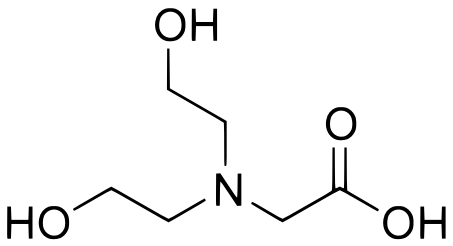

Figure 5: Molecular structure of bicine, the buffer used for all experiments in this work.

brane proteins) (*68*), the use of a wide mixture of C10-C15 fatty acids and alcohols in alkaline conditions (*33*) and addition of C10 isoprenoids (*33*, *69*).

Furthermore, the intercalation of some apolar hydrocarbons such as PAH derivatives (also prebiotically available (*28*)), inside model proto-membranes was also explored. The PAH derivatives were found to act as stabilizing agents with significant effects in lowering the CVC, against pH variations, decreasing membrane permeability (*70*) and as first pigments for a primitive version of photosynthesis (*71*, *72*).

As a concluding remark, although the vesicle membrane structures are the main focus of this thesis, there is also another kind of lipid self-assembly whose role has been investigated in the framework of the OOL studies: the lipid droplets.

These systems, originally studied as more general aggregates rich in polymers, proteins or nucleic acids by Oparin (*73*, *74*) and named *coacervates*, were suggested as alternative candidates of membrane-free protocells that could counteract the low molecular concentrations in solution, grow by sequestering new molecules, divide (*75*) and be even capable of self-propelled directional motion (*76*). Although the coacervates have received less attention in the OOL as compared to membrane forming compartments (the vesicles), recent studies have shown the possibility of a complex interplay between coacervates and vesicles in creating multi-compartmentalized cell-like systems that could potentially model the proto-organelles behaviour (*77*), or as a hybrid protocell model with a self assembled fatty acid membrane at the surface of a coacervate (*78*).

1.5 PROJECT AND OBJECTIVES

The project of this thesis is built on the current state of the art, summarized in the previous section, in order to find the most suitable early life membrane models.

Since the prebiotic synthesis of amphiphilic molecules is favoured for the shortest chain lengths (*61*–*63*), this work focuses on fatty acids, fatty alcohols and phos-

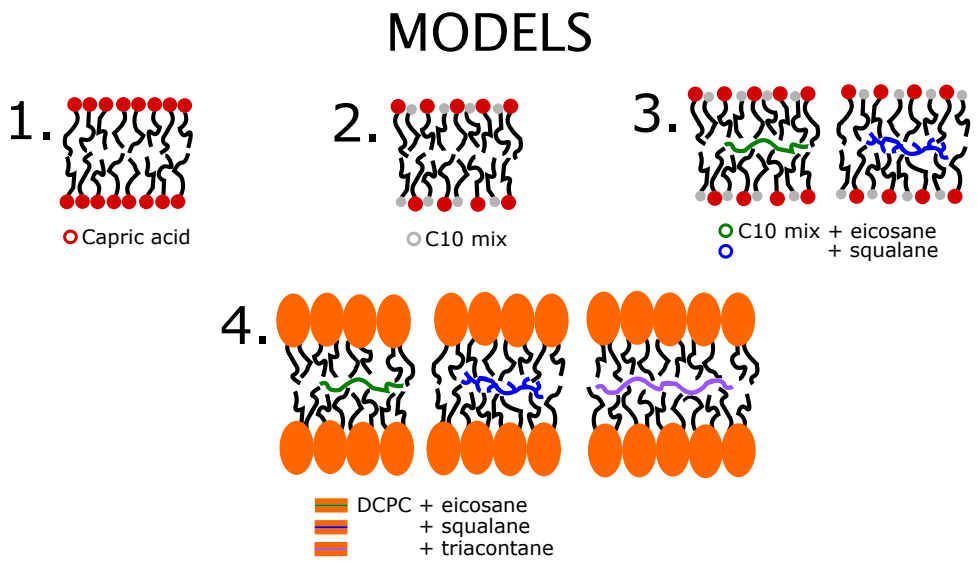

Figure 6: Sketch the membrane models investigated in this work.

pholipids having saturated chains of 10 carbon length, among the shortest that are able to self-assemble into bilayers (*34*, *60*).

Four main models, all in close relationship to each other, were employed and studied as proto-membrane systems (Figure 6):

- **The first model** is a membrane made by a bilayer of decanoic (common name: "capric") acid, which is the C10 fatty acid known to form vesicles above a CVC of approximately 40 mM (*60*). Studies at ambient temperature have shown that this system is stable in a narrow range of pH, precisely around the pK_a of the decanoic acid ~ 7.1 (*53*, *60*, *72*).

- **The second model** is a 1:1 mixture of decanoic acid with a fatty alcohol having the same chain length, the 1-decanol. Many previous studies have worked on mixtures with the same (*53*) or similar ratios (for example 9:1 (*60*) or 2:1 (*36*)), making it one of the most widely studied proto-membrane models. The addition of even small quantities of the fatty alcohol has been found to lower dramatically the CVC and to stabilize vesicles at higher pH values than the fatty acid pK_a (*39*, *53*, *60*). Furthermore, the membrane permeability to oligonucleotides as a function of temperature (*36*) and the membrane fluidity as a function of HHP and temperature (*53*) were studied for this system.

An extensive and detailed study of the structural and dynamical properties of these first two models was performed in order to gain deeper knowledge on the response of both systems to high temperatures. Indeed, significant differences were found at high temperatures from an onset at $T \approx 60\,^{\circ}C$. This has great implications on the membrane thermostability at the highest temperatures, the ones

of interest for the OOL scenarios. The details of this research will be found in the "Article 1" of the **RESULTS** chapter.

- **The third model** is proposed in analogy with recent findings in the field of extremophiles (*38*, *79*). Cario et al. observed an impact in the unsaturation level of long chain isoprenoid alkanes (referred as "apolar lipid") in a hyperthermophilic piezophile archaeon upon variation of pressure and temperature conditions (*38*). The authors hypothesized a structural role of these branched hydrocarbons in the membrane to tune its properties, as needed for functionality, in response to variations of pressure-temperature. Such stabilizing role was further confirmed by studies on model archaeal membranes (*80*). Using the same line of reasoning, the 1:1 decanoic acid and decanol mixture (hereafter C10 mix) is here enriched with small percentages of one of the following alkanes: *squalane*, a 30-carbon (C30) branched alkane that has been shown to affect in multiple ways the membrane organization in model archaea membranes (*79*, *80*); *eicosane*, a linear C20 alkane as a more prebiotically available alternative. The C10 mix containing eicosane can be considered as the *master model* of the project, that sums up the requested features of prebiotic molecular abundance and need for a strategy against high temperature and HHP.

The possibility that such alkane molecules could have acted as membrane stabilizers at extreme conditions of temperature and HHP was investigated in two parallel works. In the first, MLV systems including or missing the alkanes were studied, in both structure and dynamics, as a function of temperature and HHP simultaneously. This study is detailed in the "Article 2" of the **RESULTS** chapter.

The second work is focussed on the behaviour of ULV instead. In particular, the nature of the conformational changes observed at $T > 60\,^{\circ}C$ is explored and interpreted from a structural and dynamical (single molecule as well as collective) perspective. More details will be found in the "Article 3" of the **RESULTS** chapter.

- **The fourth model** is a bilayer made of 1,2-didecanoyl-sn-glycero-3-phosphocholine (hereafter DCPC), a phospholipid consisting of a choline headgroup and two C10 acyl chains (Figure 4), with addition of alkanes (either eicosane, squalane or the C30 linear *triacontane*). This system was employed as a mimic protomembrane model that could be prepared in flat multilayer stacks (due to the much more hydrophilic headgroup), still possessing equal chain length in the hydrocarbon region as the decanoic acid and decanol molecules.

The last model was used to localize the positioning of the alkane molecules, when successfully included in the membrane, with near-atomic resolution. The study is detailed in the "Article 4" of the **RESULTS** chapter.

Figure 7 summarizes all molecular species and the sub-projects (each resulting in a separate Article) that are described in this thesis.

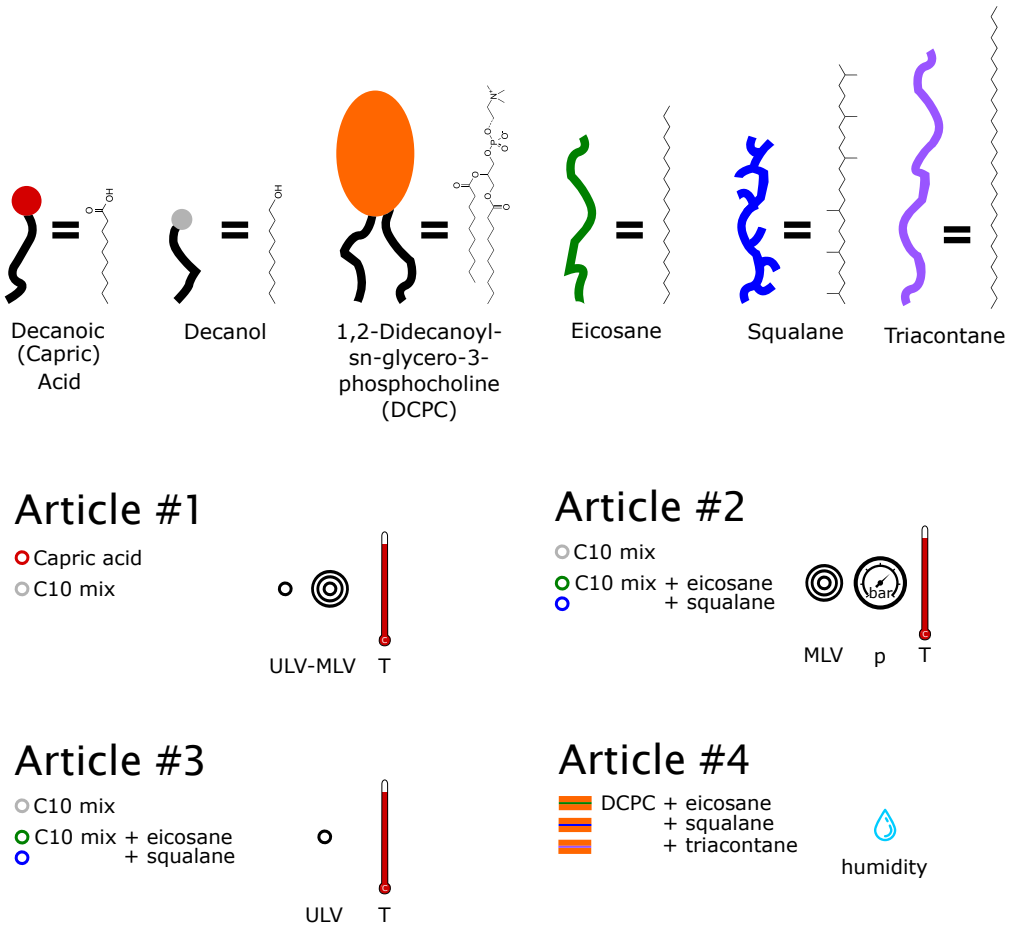

Figure 7: Top: Chemical formula and sketch of all molecules employed in the project. Bottom: graphical summary of all works performed with the membrane models, listing in particular which systems were used in each work and the environmental variables tuned (temperature, HHP, humidity).

2 METHODS

2.1 SCATTERING TECHNIQUES

Scattering can be generally defined as the process in which some kind of wave-particle changes its direction of propagation because of inhomogeneities in the target. The new trajectory and energy of the scattered beam contains information about the characteristics of the scattering medium (particle sizes and shapes, correlations, molecule dynamics, molecular weights etc). This motivates the development of scattering techniques as valuable scientific tools to access such information, focusing on the specific features of interest by choosing appropriate incident beam, angle configurations etc. as it will be discussed in the following.

In general, every scattering experiment can be schematised in the same general form (regardless of the incident beam type). As depicted in Figure 8, a beam of flux Φ is sent towards a target and a fraction of the particles will be scattered to a specific direction in 2ϑ-φ covered by the solid angle $d\Omega$, where it will be collected by a position sensitive detector. The formalism that follows is the one typically used for neutron scattering (*81*), although it can be applied to any kind of incident beam with small variations.

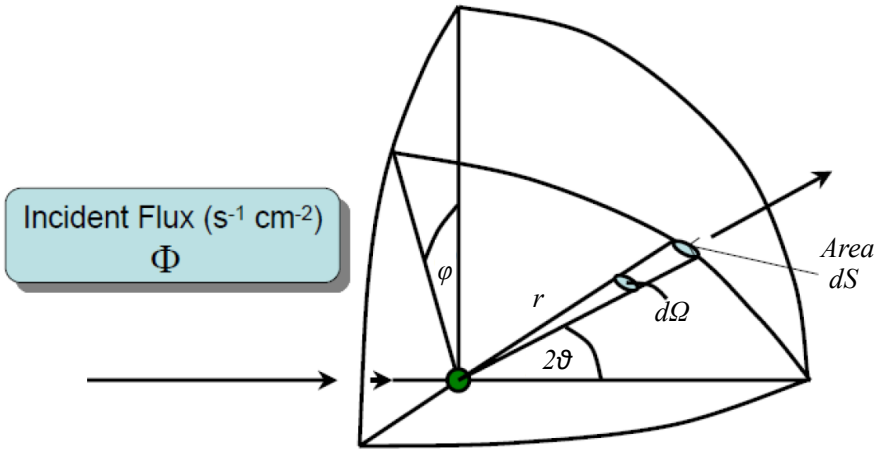

Figure 8: Sketch of the scattering geometry. An incident beam of flux Φ hits a target and is scattered in the direction 2ϑ-φ, where it is collected by a detector of area dS.

The outcome of a scattering experiment gives an experimental quantity known as the *Scattering Cross-section*, which can be operatively defined as follows (*82*):

$$\text{Double Differential Scattering Cross-section} := \frac{d^2\sigma}{d\Omega dE'} \tag{2}$$

where σ is the so-called *Total Scattering Cross-Section* (or simply *Scattering Cross-Section*), i.e. the number of wave-particles scattered per second divided by the incident flux. The *double differential* in the definition allows to focus only on the fraction of beam scattered into a small solid angle $d\Omega$ in the direction ϑ, φ and with final energy between E' and $E' + dE'$.

The double differential scattering cross-section (ddscs) can be linked to another quantity termed *Scattering Function*, purely dependent on the sample (i.e. the target in a scattering experiment) characteristics, via the so-called *Master equation*:

$$\begin{aligned}\left(\frac{d^2\sigma}{d\Omega dE}\right)_{\underline{k}_0 \to \underline{k}_1} &= \frac{1}{N}\frac{k_1}{k_0}\frac{1}{2\pi\hbar}\int_{-\infty}^{\infty}\sum_{ij}\left\langle b_i^* b_j\right\rangle\left\langle e^{-i\underline{q}\cdot\underline{R}_i(0)} e^{i\underline{q}\cdot\underline{R}_j(t)}\right\rangle e^{-\frac{i}{\hbar}Et} dt = \\ &= \frac{k_1}{k_0}\frac{\sigma}{4\pi} S(\underline{q}, E)\end{aligned} \tag{3}$$

where $\left(\frac{d^2\sigma}{d\Omega dE}\right)_{\underline{k}_0 \to \underline{k}_1}$ is the ddscs leading to the transition $\underline{k}_0 \to \underline{k}_1$, with $\underline{k}_0$ and $\underline{k}_1$ the wavevectors of the incident and scattered wave-particle of the beam; $\hbar$ is the reduced Plank constant, N the number of incident wave-particles hitting the target. The quantities b_i and b_j are the *Scattering Lengths* of the scatterers i and j, defined from the respective *Scattering Cross sections*:

$$\sigma = 4\pi b^2. \tag{4}$$

One important remark is in order here: as neutrons and atomic nuclei are microscopic particles, they obey to quantum-mechanical laws. In Equation 3, $\underline{R}_i$ and $\underline{R}_j$ are the position operators of the ith and the jth nucleus, which are generally not commuting. Neutron scattering should be treated within the framework of quantum mechanics, but since the 50ties of the last century, when L. Van Hove introduced an approach which gives a classical interpretation of the scattering formalism (*83*), most neutron users are following this approach and I will do the same here. The operators $\underline{R}_i$ and $\underline{R}_j$ commute in the two following cases only (*84*):

- when $t = 0$ or
- if the energy transfer $E = \hbar\omega$ between the neutron and the nucleus can be supposed as very small compared to the average energy of the neutrons

$E_n = \frac{1}{2}k_B T$. In the latter case, the operators $\underline{R}_i$ and $\underline{R}_j$ become position vectors and the thermal average $\langle ... \rangle$ becomes a classical average $\langle ... \rangle_{cl}$.

From now on, I will adopt this classical approach.

Although the energy variable E is explicit in the right hand side of the Master equation, the variable denoting the scattering direction (Ω) has been translated with another variable, $\underline{q}$. This quantity is the so-called *Scattering vector*, and it is defined as:

$$\underline{q} = \underline{k}_0 - \underline{k}_i \tag{5}$$

so that $\underline{q}$ contains the information of the scattered beam direction with respect to the incident beam.

The detailed procedure to derive the above mentioned Master equation, by using 1-st order perturbation theory and a proper approximated expression for the potential (known as *Fermi's pseudo-potential*), can be found elsewhere (*81*, *82*) and will not be developed here.

The Scattering Function $S(\underline{q}, E)$ contains all the information about the sample under study, hence it is the final purpose of any scattering experiment. A physical interpretation can be obtained using Van Hove's *Correlation Function* $G(\underline{r}, t)$ (*83*):

$$S(q, \omega) = \frac{1}{2\pi} \int_{-\infty}^{\infty} dt e^{-i\omega t} \int_{-\infty}^{\infty} dr e^{-iQ \cdot r} G(\underline{r}, t). \tag{6}$$

The *Correlation Function* $G(\underline{r}, t)$ is a quantity that describes the correlation between two scatterers in the sample, as a function of both their relative positions and time. From Equation 6, one can see that the $S(\underline{q}, E)$ is nothing less than the double Fourier Transform, in space and time, of Van Hove's $G(\underline{r}, t)$.

Thus, finding the complete expression of the Scattering Function would allow to learn about the evolution of the relative position of every scatterer in the sample, at all times.

As underlined by the above mentioned Equation 6, the output of a scattering experiment (via Equation 3) requires to perform a double Fourier transform in order to obtain information about the physical, real space. In fact, the scattering vector $\underline{q}$ plays the role of the displacement vector $\underline{r}$ in the so-called Fourier, or reciprocal space. As it will be shown later in the text, this *real space - reciprocal space* relationship will require to focus on specific length-scales in the sample by studying the $\underline{q}$ range of interest accordingly. The same reasoning applies between the sample time-scale and the corresponding experimental energy range.

Furthermore, the definition of the Fourier transform itself (with the extremes of integration being $\pm\infty$) sets limitations *a priori* about the experimental accessibility of $S(\underline{q}, E)$, and hence $G(\underline{r}, t)$ and our knowledge of the system.

A due comment about the nature of the atomic scattering length b will be useful in the later sections. As mentioned, Equation 3 is derived by assuming an approximated form of the neutron-atom interaction potential, the *Fermi pseudo-potential*. In simple terms, this potential assumes that the incident neutron *sees* the atom in the target as a point. This assumption is well justified because the neutrons used for scattering have wavelengths of $\approx 10^{-10}$m, while the atomic nucleus size is $\approx 10^{-15}$m. This translates into writing the potential in the form of *Dirac's delta* distribution (a pseudo-function $\delta(x)$ for which $\delta(0) = +\infty$, $\delta(x \neq 0) = 0$ and $\int_{-\infty}^{+\infty} \delta(x) = 1$). Therefore, the Fourier transform will give a constant function in q: $b(q) = b$, i.e. the neutron atomic form factor is a constant in q. This statement is not true in other cases, with two noteworthy examples: x-ray scattering, because x-rays interact with the electron cloud of the atoms (hence both have comparable wavelength/size); Small-Angle Scattering (SAS), where the size of the probed scatterers (in our case, from membranes to entire vesicles) is of the order (or bigger) than the incident neutron/x-ray wavelengths.

2.1.1 Neutron Scattering

Within the framework of all scattering techniques, a peculiar case is given by the use of free neutrons as incident beam. This constitutes the field of Neutron Scattering, the main experimental approach that has been employed in this work, for both structural and dynamical investigation purposes.

Neutrons are subatomic particles that, in the bound state and together with protons, constitute the nuclei of all ordinary matter in the universe. They are made of two down-quarks and one up-quark, but can be considered as elementary particles for our purposes. Neutrons are unstable in the free state and undergo β decay within a lifetime of $\tau = (886 \pm 1)$s:

$$n \rightarrow p + e + \overline{\nu} \qquad\qquad N(t) = N(0)e^{-t/\tau} \tag{7}$$

where n, p, e, $\overline{\nu}$ are the neutron, proton, electron and electron anti-neutrino respectively; N(t) is the number of neutrons existing at time t. Given the free neutron lifetime, the fraction of decaying neutrons during a scattering experiment can be safely neglected.

Free neutrons can be produced by either nuclear fission or spallation. An example of nuclear fission reactor for neutron production is the large scale facility

Institut Laue Langevin (ILL) located in Grenoble (France), where all the neutron scattering experiments presented in this thesis were performed.

ILL has a High Flux Fission reactor which produces a flux of $1.5 * 10^{15} \frac{neutrons}{cm^2 s}$ with a nominal thermal power around 58.3 MW (*85*), making it the most powerful continuous neutron source for scientific research in the world to present date. After moderation, the neutrons with desired energy are sent to about 40 state-of-art instruments, each of them designed to meet specific diffraction, spectroscopy or nuclear physics needs.

What makes neutron scattering worth the neutron production efforts, in terms of cost and manpower, is a number of very special properties that come from the intrinsic nature of the neutron itself. Some of its main characteristics are summarised in Table 1. The most remarkable consequences of such properties are:

- the relatively big mass makes it easy to discriminate the neutron energy by simply measuring the Time of Flight (ToF); for instance, neutrons moderated at T = 300 K (known as *Thermal Neutrons*) will have a velocity of $\approx 2200\,m\,s^{-1}$, while *Cold Neutrons* (T = 25 K) will travel at $\approx 640\,m\,s^{-1}$;

- *Thermal* and *Cold* neutrons have wavelengths of the order of single atoms size ($\lambda = 1.8\,Å$ and $6.2\,Å$, respectively), allowing the same resolution as with x-rays;

- at the same time, *Thermal* and *Cold* neutrons possess very low energy ($E = 25\,meV$ and $2\,meV$, respectively) while x-rays at the same resolution have energies of the order of $\approx keV$; this means, from one hand, that neutrons are a much softer probe where radiation damage is negligible (unlike x-rays); on the other hand, they are much more sensitive to small energy excitation (e.g. thermal excitations, $1K_BT = 25.7\,meV$) of the sample;

- the null electric charge makes neutrons only sensitive to the atomic nuclei and not to their electronic cloud, allowing a deeper penetration in the sample and making it sensitive to small atoms and their isotopic substitution;

- the magnetic dipole moment can be used to probe magnetic structures and excitations (e.g. *magnons*), although this will not be of specific interest in the present study;

- the half-integer spin can be used to polarize the beam (a property that is used for the Neutron Spin-Echo (NSE) spectroscopy technique, later described) and it also plays a major role in the definition of coherent and incoherent neutron scattering.

Table 1: Basic properties of the neutron.

mass	$1.675 * 10^{-27}$kg
charge	0
magnetic dipole moment μ_n	$-1.913\mu_N$
spin	$\frac{1}{2}$

The last listed consequence has extremely important implications on the way neutrons are used to probe either structure or dynamics when needed. We recall the definition of the Scattering Function $S(\underline{q}, E)$ as it has been found in Equation 3:

$$\frac{\sigma}{4\pi}S(\underline{q},E) = \frac{1}{N}\frac{1}{2\pi\hbar}\int_{-\infty}^{\infty}\sum_{ij}\left\langle b_i^* b_j\right\rangle\left\langle e^{-i\underline{q}\cdot\underline{R}_i(0)}e^{i\underline{q}\cdot\underline{R}_j(t)}\right\rangle e^{-\frac{i}{\hbar}Et}dt. \tag{8}$$

An underlying statement in this definition is that all nuclear spins in the sample are randomly distributed. Nevertheless, because even same atom species (and isotopes) with different spin orientation lead to different scattering lengths b as *seen* by the neutrons and because b can be either positive or negative, we have:

$$\langle b\rangle^2 \neq \left\langle b^2\right\rangle \tag{9}$$

and this inequality can be used to re-write the $S(\underline{q}, E)$ formula:

$$\begin{aligned}\frac{\sigma}{4\pi}S(\underline{q},E) =& \frac{1}{N}\frac{1}{2\pi\hbar}\int_{-\infty}^{\infty}\sum_{ij}\sum_{i\neq j}\langle b\rangle^2\left\langle e^{-i\underline{q}\cdot\underline{R}_i(0)}e^{i\underline{q}\cdot\underline{R}_j(t)}\right\rangle e^{-\frac{i}{\hbar}Et}dt+\\ &+\frac{1}{N}\frac{1}{2\pi\hbar}\int_{-\infty}^{\infty}\sum_{i}\left\langle b^2\right\rangle\left\langle e^{-i\underline{q}\cdot\underline{R}_i(0)}e^{i\underline{q}\cdot\underline{R}_i(t)}\right\rangle e^{-\frac{i}{\hbar}Et}dt =\\ =&\frac{1}{N}\frac{1}{2\pi\hbar}\int_{-\infty}^{\infty}\sum_{ij}\langle b\rangle^2\left\langle e^{-i\underline{q}\cdot\underline{R}_i(0)}e^{i\underline{q}\cdot\underline{R}_j(t)}\right\rangle e^{-\frac{i}{\hbar}Et}dt+\\ &+\frac{1}{N}\frac{1}{2\pi\hbar}\int_{-\infty}^{\infty}\sum_{i}\left[\left\langle b^2\right\rangle-\langle b\rangle^2\right]\left\langle e^{-i\underline{q}\cdot\underline{R}_i(0)}e^{i\underline{q}\cdot\underline{R}_i(t)}\right\rangle e^{-\frac{i}{\hbar}Et}dt.\end{aligned} \tag{10}$$

This can be simplified as follows:

$$\frac{\sigma}{4\pi}S(\underline{q},E) = \frac{\sigma_c}{4\pi}S_{coh}(\underline{q},E) + \frac{\sigma_i}{4\pi}S_{inc}(\underline{q},E) \tag{11}$$

The Scattering function is now divided in two terms:

- the first, named *Coherent Scattering function*, contains information about the position of *different* atoms at *different* times, leading to interference effects; therefore, it is suitable for structural studies;
- on the other hand, the *Incoherent Scattering function* contains information about the position of the *same* atom at *different* times, which means that it can be used for dynamical studies; the incoherent signal does not give interference and it is a flat function in q.

It is now clear why and how the neutrons constitute a special probe to study matter at both structural and dynamical level. In the following paragraphs there will be a short focus about the basics for each of the techniques used during the thesis work, linking the general aspects of neutron scattering to the specific cases of application. For the details about the actual experimental conditions of each experiment, the reader can refer to the Articles where the corresponding results are presented (or, in some cases, the Articles' Supplementary Information).

2.1.1.1 *Small Angle (Neutron/X-ray) Scattering & Static Light Scattering*

Figure 9 shows a simplified scattering geometry, were a beam of wavelength λ is scattered elastically from an ordered 2D-array of point scatterers. Using the definition of the scattering vector q (as in Equation 5) and the wavevector k ($k_0 = k_i \equiv k$ for elastic scattering), one obtains:

$$q = 2k \sin(\vartheta/2) = \frac{4\pi}{\lambda} \sin(\vartheta/2) \tag{12}$$

which means that, for a given λ, one can scan q by simply varying the scattering angle ϑ. Besides, Figure 9 allows an easy derivation of the *Bragg law*, stating that constructive interference in the scattered signal will occur when the path length difference between two scattered waves will be a multiple of λ:

$$2d \sin(\vartheta/2) = n\lambda. \tag{13}$$

Merging Equations 12 and 13 (setting n = 1 for first order diffraction) we get:

$$qd = 2\pi, \tag{14}$$

an extremely useful relationship between a quantity in the reciprocal space q, whose value can be chosen during the experiment by changing the scattering angle ϑ, and a corresponding quantity in the real space d that infers about the

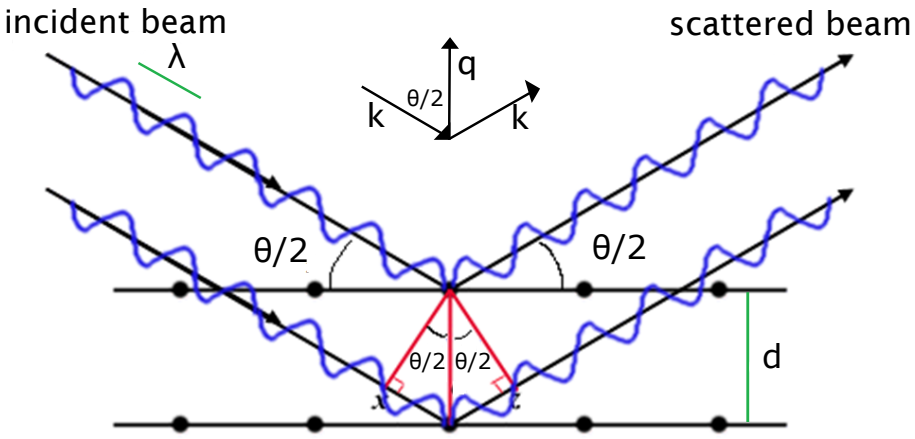

Figure 9: Sketch of scattering geometry in two dimensions, underlying the direction of the vectors $\underline{k}$ and $\underline{q}$, the scattering angle ϑ and the derivation of Bragg's law.

length of some repeat distance in the sample. This link leads us to a very useful implication that is thoroughly used in every scattering experiment: the higher the scattering angle, the smaller the repeat distances that can be probed in the sample; conversely, by studying the signal arising from neutrons scattered at very low angles, one can probe larger length-scales (20 - 1000 Å). This is the concept at the basis of the widespread techniques of SAS, in particular used with x-rays (Small Angle X-ray Scattering (SAXS)) or neutrons (Small Angle Neutron Scattering (SANS)) (*86*).

The output of a SAS experiment will have the following general form:

$$I(q) = |F(q)^2 * S(q)| \tag{15}$$

where $I(q)$ is the scattered intensity as collected by the detectors; $F(q)$ is the average *Form factor* of the scatterers, the equivalent of the scattering length b (Equation 4) but now with a q dependence due to the large dimension of the scattering objects; $S(q)$ is the *Structure factor*. All quantities can be intended as consisting of purely coherent scattering, as the incoherent scattering will contribute as a flat background in q that can be easily subtracted during the analysis. Because the measured quantity is an intensity, we have only access to the square of the Form factor leading to a sign indetermination (an issue more generally known as the *Phase problem* of diffraction, the solving of which will require additional strategies and will be discussed in the next subsection).

For the particular case of the systems studied in the present work, the theoretical forms of the Form and the Structure factors will resemble the ones that are depicted in Figure 10:

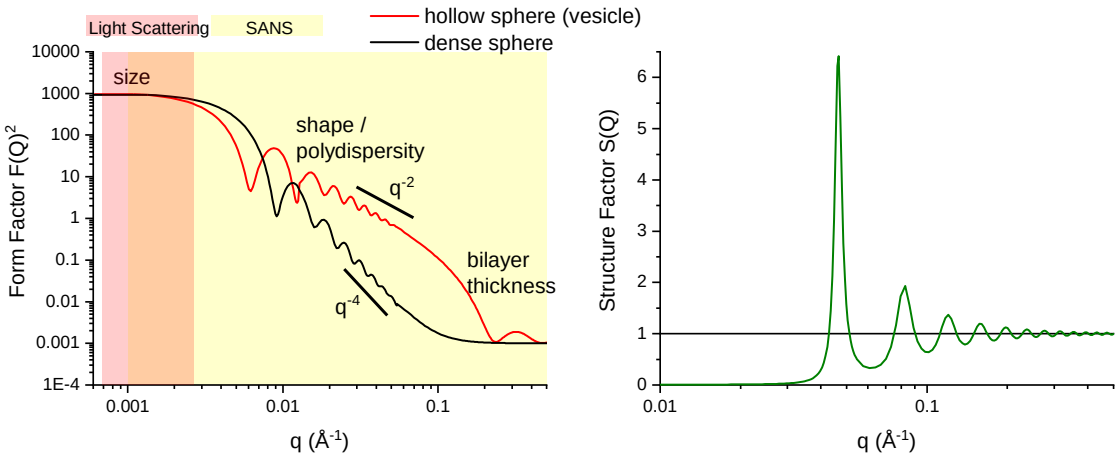

Figure 10: Example of theoretical Form and Structure factors. Left: Form factors of dense spheres as compared with hollow spheres. The latter will be the model used to fit the vesicles form factor. Highlighted are the q ranges which are typically covered by either Light Scattering or SAS.Right: plot of the theoretical structure factor of a lamellar membrane phase.

- $F(q)$ contains averaged information about each single scatterer that, in the case of this work, is the vesicle (either MLV or ULV). Depending on the q range observed, one can investigate the overall vesicle size and shape distribution (lowest q), the size polydispersity and lamellarity (mid q range), the membrane thickness and thickness polydispersity (high q). The presence of smaller objects, e.g. micelles, would appear as an additional signal in the middle/high q range depending on their size;

- $S(q)$, on the other hand, contains information about the correlation between different particles/structures; for instance, one could see the correlation between vesicles interacting with each other in a concentrated solution (low q) or the interaction between subsequent membranes in MLVs (mid q range). In the latter case, the relative position of the higher orders of correlation will tell about the membrane phase (e.g. lamellar, hexagonal, cubic etc.) and the repeated distance between membranes (d-spacing).

As a short mention, a straightforward consequence of Equation 12 is the fact that one can go for another beam type with a much bigger wavelength to access a very small q range. This is what happens with the Static Light Scattering (SLS) technique, where a laser of visible wavelength is used as incoming beam (in our case $\lambda = 632\,nm$). This complementary technique can therefore be used to supplement SAS at the smallest q range (as shown in Figure 10) and have information about vesicle size and possible aggregation.

SANS - SAXS - SLS *at a glance*

- Smallest angle (/smallest q) = big objects overall shape (e.g. vesicle size, shape).
- Increasing angle = zooming in ((e.g. lamellarity, membrane thickness).
- Neutrons (SANS) allow quantitative data analysis (absolute units) and contrast variation (D_2O labelling).

The SAS data acquired during this thesis work were analysed in different ways depending on the experimental conditions and needs:

- The SANS ULV and MLV data were analysed by fitting them with a simple vesicle (or lamellar for the MLV) form factor, with the addition of bilamellar vesicles or dense spheres (for the micelles) form factors when needed; the fits were performed using the software SASView (*87*), where all the needed model functions for $F(q)$ are available (for the matematical definitions of all form factors used in the analysis, refer to the Supplementary Information of Articles 1 and 3);
- The SAXS MLV data, that did not allow to be fully fitted with suitable models because of the much lower contrast, were analysed by fitting the first membrane correlation within MLVs with Gaussian functions on top of a power law of the form q^{-c};
- The SLS data were fitted by verifying that the $I(q)$ could be approximated with a function of the form $I(q) \propto e^{-\frac{q^2 R_g^2}{3}}$ (*Guinier approximation*), with R_g the vesicle *gyration radius* (*86*).

2.1.1.2 *Small-Angle Neutron Diffraction*

In theory, the full knowledge of the form factor in the range $[0-\infty]$ would allow a complete understanding of the scattering objects average properties at all length scales, from the overall macromolecular structure (e.g. the entire vesicle) to the position and arrangement of every single atom. The Fourier transform of the form factor, assuming its phase is known, would give the so-called *neutron Scattering Length Density (SLD)* (in the case of x-rays, the *electron density*) profile that tells about the position of each atom species (with the corresponding scattering length) in the real space. In practice:

1. every instrument can cover a limited portion of the scattering vector q with a certain q resolution, therefore we can only have a partial knowledge of the form factor. The Fourier transform, defined in theory as ranging from $]-\infty,+\infty[$, will therefore be an approximation as well;

2. there is an indetermination of the phase of the form factor (the *Phase problem*);

3. experimentally, the form factor decays quickly with q (in the range of our interest, like q^{-4} for hard spheres with sharp interfaces (*88*), q^{-2} for random bilayers (*89*)); therefore, the form factor signal is only visible in a narrow q range, above which it is covered by instrumental background.

A clever solution for the last-mentioned limitation, namely the low (and quickly decaying) signal of the form factor, was pioneered in the 70s (*90*–*93*). Starting from Equation 15, the idea is to use the structure factor for sampling specific positions in q of the form factor. In a multilayer membrane stack, the $S(q)$ will give well defined and intense Bragg peaks at q positions which correspond to the membrane repeat distance (or d-spacing, through Equation 14). Because the collected signal I(q) is always consisting of the product of both form and structure factors, the measured intensity of the Bragg peaks (the $S(q)$) will be modulated by the intensity of $F(q)$ even though the latter is not visible (because covered by the incoherent background). One can then use this property to approximate the continuous Fourier transform (which would require an integral in $]-\infty,+\infty[$) with a discrete *Fourier series* of the detected *Structure factor terms*. In this way, an approximation of the SLD can be calculated, giving valuable insights about the membrane properties at almost atomic level: bilayer thickness, water thickness between membranes, lipid head-group size, hydrocarbon region size etc. This technique will be referred in this thesis as Small Angle Neutron Diffraction (SAND).

SAND *at a glance*

- SLD can give information of the membrane at atomic scale.
- At high resolution (high q), the $F(q)$ is covered by the background.
- Study $S(q)$ intensity modulation to sample $F(q)$.

In a typical SAND experiment, the neutron beam is sent towards multilayer lipid films on a perfectly flat solid support (silicon wafers). The signal, collected by scanning the sample orientation, will give a series of 2ϑ vs Ω images (2ϑ is the

scattering angle between incident and scattered beam, Ω the angle of the sample with respect to the incident beam direction, $\Omega = 0$ when the flat film is parallel to the incident beam). The resulting images show the position, intensity and shape of the Bragg reflections. Some example of SAND 2D maps will be shown in the Foreword and main text of Article 4. The reflections are then integrated over a small Ω range, leading to a series of I_h values (h indicating the reflection order). The formula to determine the SLD from the I_h terms is the following:

$$\rho(z) = a * \sum_h \left(\pm |F_h| \cos\left(\frac{2\pi h z}{d}\right)\right) + b \tag{16}$$

where:

- $\rho(z)$ is the neutron SLD along the vertical direction z of the multilayer;
- the sum is performed over all Bragg reflections that are visible from the data, denoted with h;
- d is the membrane d-spacing;
- $F_h = (h * I_h)^{1/2}$ are the structure factor terms for each Bragg order h, found as the square roots of the intensity of each peak I_h, with an additional correction factor h (the inverse of the *Lorentz factor* (*90*)).
- a and b are scaling and offset parameters to account for experimental differences (e.g. differences in sample quantity, background etc).

The "$\pm$" sign appearing in Equation 16 is expression of the above mentioned *Phase problem* for the case of SAND on lipid multilayers. In fact, since membranes are centrosymmetric, the problem of the phase assignment reduces to a sign assignment.

To overcome it, one way is to perform contrast variation measurements at different $H_2O - D_2O$ ratios. The reason for it is that the structure factor term dependence with the D_2O percentage is expected to vary linearly (*91*). Therefore, one can use the linearity requirement to spot the occurrence of phase changes.

Another possibility is to perform the so-called membrane *swelling experiments* where, assuming that the form factor does not change with the hydration level, one can use the shift of the Bragg peaks in q (that occurs when the water layer between the membranes increases) to sample the underlying form factor shape (and therefore spotting the minima, after which phase change will occurr).

All these strategies will be described and discussed in more detail in the related work in Article 4.

2.1.1.3 *Elastic Incoherent Neutron Scattering*

The incoherent neutron scattering signal, which is considered as a flat *noise* to be subtracted from coherent scattering data (SANS, SAND), can reveal many insights about the molecular dynamics of the scatterers, as it was mentioned earlier in the section. In particular, the $S_{inc}(q, E)$ contains information that is stored in its energy dependence. Because of the high mass of the neutrons, the energy of the incident and scattered beams can be easily discriminated by measuring the corresponding ToF, so that they constitute a useful spectroscopic probe. In full analogy with the relation shown in Equation 6, we can relate $S_{inc}(q, E)$ to an *auto-correlation function* that describes the correlation between the position of the same scatterer at different times.

Depending on the nature of the energy exchange between neutrons and sample, one can distinguish between Elastic, Quasi-Elastic and Inelastic scattering. The latter technique will be neglected as it is not relevant in this study. In general, a $S_{inc}(q, E)$ function for a defined q contains several distinct features:

- An elastic peak. In theory, this should have the form of a *Dirac's delta*. In practice, it will have a form defined by the instrumental resolution (usually resembling a Gaussian function). This peak contains the signal from neutrons that did not exchange energy with the sample. To simplify, these neutrons have *seen* the corresponding scatterers as immobile (or in a motion too slow for the instrumental resolution).

- A broadening of the elastic peak (quasi-elastic) at its base. This contains the signal from neutrons which probe the scatterers while these are moving in a timescale that can be detected by the instrument used. This broadening is usually modeled as one or more Lorentzian functions (summed if the motions are uncorrelated, convoluted if the motions are correlated). The reason for such a shape comes from the proportionality between $S_{inc}(q, E)$ and the imaginary part of the sample generalised susceptibility (which has a Lorentzian form), the derivation of which is beyond the scope of this thesis and can be found dedicated textbooks (*81*).

- A background, containing all motions that are too fast to be probed because of the instrumental resolution (it can be thought like an extremely large Lorentzian broadening).

Elastic Incoherent Neutron Scattering (EINS) is a technique that focuses on the elastic peak intensity (thus its integral) as a function of q, as well as other variables related to the sample environment such as temperature, pressure etc. As a second level of analysis, the EINS intensity curves $I(q, E = 0)$ can be analyzed

in the framework of the widely used Gaussian approximation (*94*). The latter assumes $I(q, E = 0)$ to have a Gaussian form at low q arising from harmonic motions of the scatterers around their equilibrium positions:

$$I(q, E = 0) \propto e^{-\frac{q^2 \langle \Delta u^2 \rangle}{3}} \tag{17}$$

where $\langle \Delta u^2 \rangle$ is the so-called Mean Square Displacement (MSD), a measure of the average dynamics probed at the timescale (= energy resolution) accessible by the spectrometer. Such approximation is considered valid for low enough values of q, usually $q^2 \langle \Delta u^2 \rangle \leqslant 1$ (but not strictly, depending on the scatterer shape (*95*)). Additionally, more sophisticated models (*96*, *97*) can also be used to perform EINS data analysis, but because these were not useful for the present work they will not be further discussed.

EINS *at a glance*

- Study of dynamics from loss of elastic signal → MSD.

2.1.1.4 *Neutron Spin Echo Spectroscopy & Dynamic Light Scattering*

There are two other methods that can be used to obtain valuable information on the sample dynamics using light and neutron scattering used in additional, alternative ways. Despite these being two different techniques, they have many common points which justify a common description.

The first one, Dynamic Light Scattering (DLS), exploits the nature of the photons emitted by a LASER: in fact, by definition the LASER produces a coherent beam of photons that is of perfectly equal wavelength and phase. Because of that, it becomes possible to measure extremely small fluctuations δI in the scattered beam, after interaction with a sample of slowly moving scatterers. In this sense, DLS can be considered as another quasi-elastic technique that can be used as complementary to Quasi-Elastic Neutron Scattering (QENS) (with different length-scales, because of its q range and q resolution, and timescales).

It is possible to demonstrate (*98*) that:

1. the autocorrelation function of a property (e.g. the scatterer position $r(t)$) is proportional to the autocorrelation function of the fluctuations (e.g. $\delta r(t)$):

$$G(r, \tau) = \langle r(t) r(t + \tau) \rangle = \langle \delta r(t) \delta r(t + \tau) \rangle + \langle r \rangle^2 \tag{18}$$

2. the correlation time can be calculated from the fluctuations through:

$$\tau = \int_0^\infty d\tau \frac{\langle \delta r(t) \delta r(t+\tau) \rangle}{\langle \delta r^2 \rangle} \tag{19}$$

3. the *electric field* autocorrelation function $g_1(q,\tau)$ is linked to the *intensity* autocorrelation function $g_2(q,\tau)$ (the one experimentally measured) by the Siegert relation (*99*):

$$g_2(q,\tau) = 1 + \beta |g_1(q,\tau)|^2 \tag{20}$$

Thus, one can use the intensity fluctuations to calculate the field autocorrelation function and trace back the average dynamics of the scatterers.

The experimentally obtained DLS autocorrelation functions g_2 were analysed following the method of the moments (a re-visit of the method of cumulants) developed in (*100*). The first two moments μ_1 ($\mu_1 = 2\Gamma$, with Γ the decay rate and 2 a factor coming from the Siegert relation) and μ_2, left as free parameters in the fit, were then used to obtain the scatterer (vesicle) mean diffusion coefficients and the corresponding polydispersity (Figure 11).

For particles moving by Brownian diffusion, the decay rate is linked to the diffusion coefficient D by the relation $\Gamma = Dq^2$. In some cases, a sum of two populations, each one having its own μ_1 and μ_2, was necessary for successful fits (indicating the existence of different families of scatterers of different sizes).

The Brownian diffusion coefficient D experimentally determined is then used to estimate the hydrodynamic radius R_h using the Stokes-Einstein equation:

$$D = \frac{k_B T}{6\pi R_h \mu} \tag{21}$$

with k_B the Boltzmann constant, T the temperature, μ the solvent viscosity (solvent viscosity and refraction index η were assumed as the ones of H_2O).

DLS *at a glance*

- Autocorrelation function from light intensity fluctuations
- Diffusion coefficient from $\Gamma = Dq^2 \rightarrow$ hydrodynamic radius R_h.

The second technique is named NSE. It was developed by Mezei (*101*) and it can be used as a clever strategy to obtain an extremely fine energy resolution without worrying about the beam monochromaticity (thus profiting from higher flux).

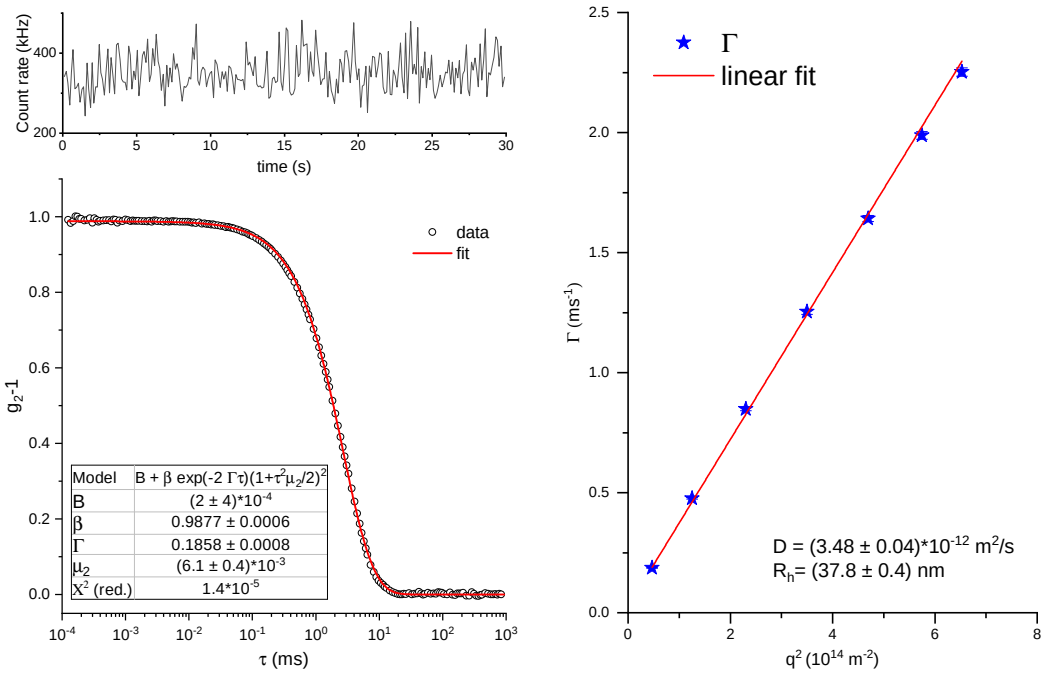

Figure 11: Example of DLS data for C10 mix vesicles extruded through a 200 nm pore membrane, T = 25 °C and 30° angle. Top left: signal at the detector. After translating vertically to zero average, the correlator calculates the absolute integral of the product of the signal and a copy of itself translated horizontally of a t = τ. The result is a point, function of the correlation time τ, constituting the auto-correlation function (bottom left). The auto-correlation function, calculated for all possible τ values, is then fitted using the model from (*100*). Right: Γ parameters found from the fits at all measured scattering angles, plotted as a function of q^2 to highlight the $\Gamma = Dq^2$ dependence. This ensures that the scatterers are moving of Brownian motion, and the slope allows calculating the diffusion coefficient D (and, consequently, the hydrodynamic radius R_h).

The central property used here is the neutron *spin*. Basically, a beam of neutrons of relatively broad wavelength (= velocity) distribution is first polarised to a certain direction at the base of a coil. Then, the neutrons enter the coil, where a magnetic field is applied to cause a precession of the neutron spins (*Larmor precession*). The time required for each neutron to travel through the entire coil (since every one has a different velocity) will in general be different, therefore the spin orientation of each neutron will be different as well at the end of the coil.

After that, the neutrons enter into a second coil which has the exact length and magnetic field intensity as the first coil, but a magnetic field that can be thought as directed in the opposite direction (in reality, the field is not reversed, but there is a 180° spin flip device that has an equivalent effect). The neutrons will start preceding *backwards*. One can think about this second coil as if the neutrons were bounced back to the first coil, moving towards their starting point. Also in this

case the neutrons will spend different times in the second coil depending on the energy, but the important outcome is that they will arrive to the end of it having all the exact same polarization as the one that was selected at the beginning, leading to an *Echo* signal measured at the detector.

Now one can think about placing a sample between the first and second coil. The interaction of the neutrons with the sample, if the scattering is not completely elastic, will cause small loss (or gain) of neutron energy (and this difference will be the same no matter the incoming neutron energy, because it is a property of the sample), therefore they will have slightly different energies and arrive with slightly different polarization at the detector. These are the main basic concepts about the NSE technique: using neutron precession to make them act as *microscopic clocks* allows to discriminate the smallest possible energy exchanges with the sample. Because the second coil can usually be moved, one has access to different q values so that the slowest dynamics at different length scales can be studied.

It can be demonstrated (*101*) that the polarization of the scattered beam P_x is linked to the $S(q,\omega)$ as it follows:

$$P_x = \int_{-\infty}^{+\infty} S(q,\omega) e^{-i\omega t} dt = F(q,t) \tag{22}$$

Therefore, NSE gives access to the Fourier transform in time of the scattering function (a quantity usually known as *Intermediate Scattering function* $F(q,t)$).

NSE *at a glance*

- No matter the neutron incoming energy, the energy loss/gain due to interaction will depend on the sample dynamics.
- Uses neutron spin precession and time of flight to discriminate very small energy exchanges.
- P_x gives direct access to the intermediate scattering function $F(q,t)$.
- Dynamics probed $\approx$ sub-microsecond (e.g. membrane undulation and compression).

The NSE data acquired here were analysed in the framework of the Zilman-Granek theory (*102*) to model the relaxation due to the membrane fluctuations

(undulation, compression). For that, each intermediate scattering function $F(q,t)$ obtained from the experiments, was fitted with a function of the form:

$$F_{theory}(q,t) = e^{-Dq^2\tau} e^{-(\Gamma_{ZG} q^3 \tau)^{2/3}} \tag{23}$$

where the first exponential models the diffusion of the entire particles (in our case the vesicles) by Brownian motion, with diffusion coefficient D. This coefficient was found, during the experiment, using an online DLS available at the NSE instrument used and fixed as a parameter for the NSE analysis. The second term is a stretched exponential coming from the Zilman-Granek theory, with the parameter Γ_{ZG} defined as:

$$\Gamma_{ZG} = 0.025\gamma \sqrt{\frac{K_B T}{\tilde{\kappa}}} \frac{K_B T}{\eta} \tag{24}$$

(K_B the Boltzmann constant, η the solvent viscosity, $\gamma \approx 1$ for $\tilde{\kappa} \ll K_B T$). The expression for $\tilde{\kappa}$ is found using a correction that considers density fluctuations in addition to bending fluctuations in the membrane (*103*–*105*):

$$\tilde{\kappa} = \kappa \left(1 + 24 \frac{2d^2}{d^2_{bilayer}} \right) \tag{25}$$

where κ is the membrane bending rigidity, d the height of the monolayer neutral surface, $d_{bilayer}$ the bilayer thickness.

2.2 OTHER TECHNIQUES

2.2.1 Fourier Transform InfraRed Spectroscopy

As mentioned in the Neutron Scattering section, one of the properties that make neutrons an useful probe to study the dynamics of biological samples is the energy: $E \cong 25\, meV$ for thermal neutrons, $E \cong 2\, meV$ for cold neutrons. These energies are of the same order of the thermal energy of matter ($1 K_B T = 25.7\, meV$). To obtain photons of comparable energy:

$$\lambda = \frac{hc}{E = 25.7\, meV} \approx 10^4 nm \tag{26}$$

or, translated into the more commonly used wavenumber: $k = \frac{2\pi}{\lambda} \approx 10^3 cm^{-1}$. This portion of the electromagnetic spectrum is known as *Infrared* region. Fourier Transform Infrared Spectroscopy (FTIR) is an absorption spectroscopic technique

where the incoming light beam is infrared, thus one can get information about the thermal vibrations active in the sample. In the specific case of interest, some of the motions related to the acyl chains that constitute the membranes are in a region that is easily accessible by FTIR spectrometers and is far away (well resolved) from other contributions. These are:

- CH_3 asymmetric stretching - $\approx 2950\,cm^{-1}$
- CH_2 asymmetric stretching - $\approx 2920\,cm^{-1}$
- CH_3 symmetric stretching - $\approx 2870\,cm^{-1}$
- CH_2 symmetric stretching - $\approx 2850\,cm^{-1}$

During the experiments of this work, the CH_2 symmetric stretching peak was followed as a function of temperature variation, to explore changes in the molecule dynamics.

2.2.2 Solid State Nuclear Magnetic Resonance

Nuclear Magnetic Resonance (NMR) spectroscopy is used in diverse fields for both structural and dynamic studies of both liquid and solid systems (or liquid suspensions, as in the case of lipid membranes). Here we will briefly consider static measurements done with ^2H solid state Nuclear Magnetic Resonance (ssNMR) to study structure and dynamics of MLV suspensions.

NMR spectroscopy is based on magnetic properties of nuclei. From an experimental point of view it requires the use of two magnetic fields. The first intense, static magnetic field H_0 (for the case of the spectrometer used, H_0 = 12 T) in which the sample is placed, orients the nuclear magnetic moments leading to the creation of a macroscopic magnetization. The second, oscillating and weak field, switches the macroscopic magnetization from its position and records the return of the latter to its initial position. The Free Induction Decay (FID) signal recorded is the NMR signal. A suitable pulse sequence of the second weak field can be used in order to record an *echo* signal, in a similar fashion as what has been described in the previous NSE subsection. This cancels the dead time between pulse-sending and signal-recording of the coil devoted to the two purposes.

In our study, we recorded ^2H NMR spectra (frequency 76.77 MHz), by means of the so-called quadrupolar (or solid) echoes sequence. Samples were partially enriched with perdeuterated acyl chains (*106*, *107*) to probe the membrane behavior.

The Fourier transform applied on the measured quadrupolar echo will give a spectrum (frequency domain) made by a superposition of signals coming from

each ^{2}H site (*108*). Because each ^{2}H atom *senses* a different electronic environment depending on its position, it will exhibit its own resonance. This, in the Fourier transformed spectrum, will be seen by a peak doublet separated by a *quadrupolar splitting* $\Delta\nu_Q$ (*106*).

This quantity will be used, for the sake of our study, to calculate the *order parameter* of each methyl-methylene group in the acyl chains as a function of sample composition and temperature, through the relation given by Davis (*106*). In addition, using the relation developed by Douliez et al. (*109*), the thickness of the bilayer hydrocarbon region was calculated and compared to the SANS data results.

FTIR, ssNMR *at a glance*

- FTIR: thermal vibrations of (CH_2)-(CH_3).
- ssNMR: (CH_2)-(CH_3) order parameters, hydrocarbon region thickness.

Figure 12 summarizes the experimental techniques used in this work, as a function of the respective observable length- and time-scales.

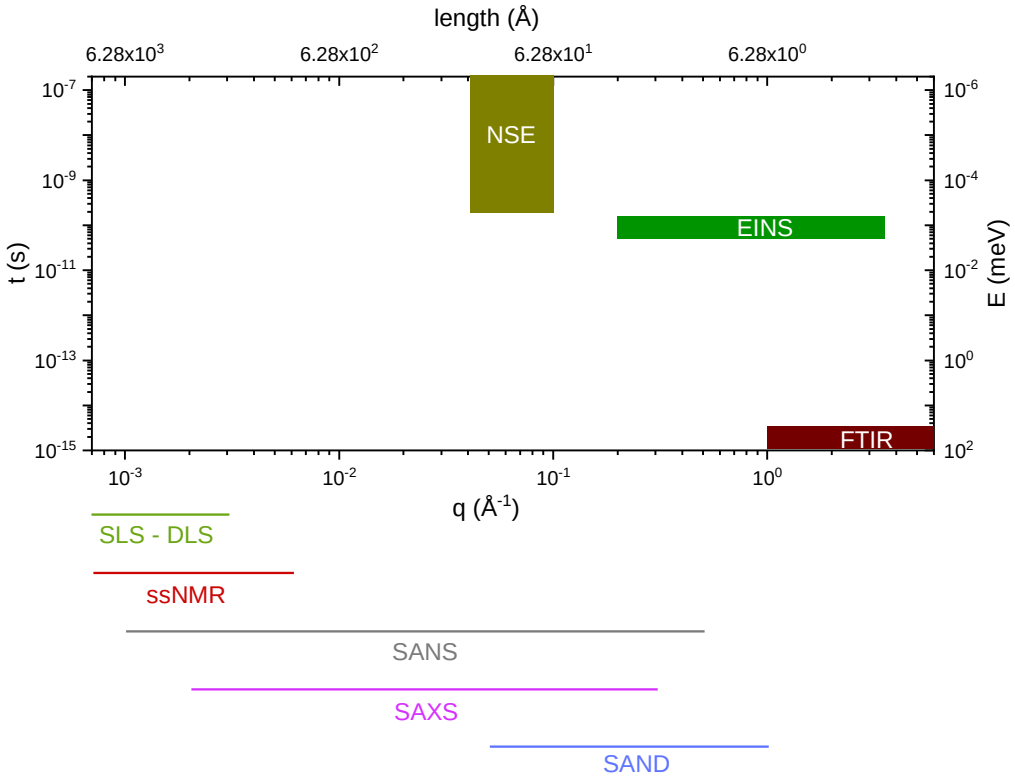

Figure 12: Summary of all experimental techniques that have been used in this project, located at the specific q (length) and time (energy) scales at which they have been employed. The techniques devoted to the structural studies do not discriminate between different energies, therefore they have been indicated as horizontal segments. N.B.: These ranges do not reflect the maximum values reachable by each technique, but only the ones that have been used in this work.

2.3 SAMPLE PREPARATION

2.3.1 Vesicles

Decanoic acid, sodium decanoate, 1-decanol, eicosane, squalane, triacontane (and all the corresponding deuterated forms), bicine buffer and D_2O were purchased from Sigma Aldrich (Merck). The samples were prepared by dissolving the decanoic acid (and the decanol, when needed) in a $CHCl_3$ solution, followed by drying with a flush of nitrogen (the decanoic acid + 1-decanol mixture is liquid at ambient temperature). When the sodium decanoate was used, instead of the acidic form, a mixture of 1:1 $CHCl_3$:CH_3OH was needed for solubilization.

The samples were then placed in a desiccator and left under vacuum overnight. The sample weights were checked at each step, to make sure that all the organic solvent was evaporated. At the final stage, a sample loss of $\approx 5\%$ was measured for the samples including the decanol. This was imputed to its partial evaporation because the loss was not observed in the pure decanoic acid samples. For the samples consisting of decanoic acid : 1-decanol (C10 mix) the final ratio was 1:1.

The bicine buffer was prepared at a concentration of 0.2M in H_2O, following previous protocols (*36*, *53*, *64*, *65*). For the ssNMR experiments, the buffer was solubilized in ^2H depleted water. In the case of SANS and FTIR experiments, the buffer solution was prepared by dissolving hydrogenated bicine in D_2O. In all cases, the buffer was filtered with a 0.2 µm millipore membrane before use.

The dried organic solutions were then suspended in buffer, titrated to desired pH/pD with aliquots of NaOH/NaOD, and vigorously vortexed for $\approx$ 1min, leading to final milky-foamy solutions characteristic of the presence of large MLVs.

Different sample concentrations were employed depending on the experiment to be performed and the corresponding instrumental sensitivity. For some of the experiments (e.g. ssNMR, SANS, SAXS) the samples were measured as they were at this stage, and these samples will be referred as MLVs in the text.

For other experiments (e.g. SLS, DLS, FTIR, Fluorescence), it was important to obtain a well monodisperse suspension of ULVs. For this reason, samples were extruded using the equipment provided by Avanti Polar Lipids (Alabaster, AL), with the heating block regulated at 40 °C and using 100 nm polycarbonate membranes (Figure 13). The extrusion was always performed less than 24h before the corresponding experiments. Light Scattering pre-characterization measurement ensured that the extruded vesicles were stable at ambient temperature for several days (data not shown).

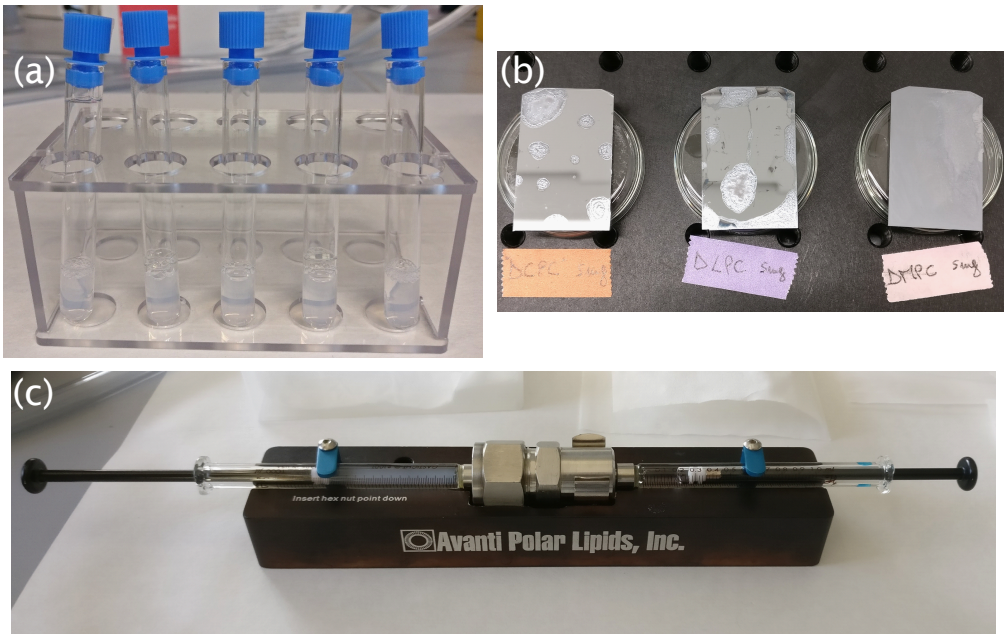

Figure 13: (a) Example of sample appearance after extrusion through a 100 nm membrane. The ones shown are five copies of C10 mix 80 mM in bicine 0.2M at T = 25 °C. (b) Example of flat multilayers prepared by spreading organic solutions on silicon flat wafers, before annealing. From left to right: DCPC (C10), DLPC (C12), DMPC (C14). (c) Equipment used for the extrusion, provided from Avanti Polar Lipids (Alabaster, AL).

2.3.2 Flat multilayers

A phospholipid short chain analogue of the C10 mixtures, the 1,2-Didecanoyl-sn-glycero-3-phosphocholine (DCPC) (Sigma Aldrich (Merck)), was used to prepare oriented multilayers on silicon substrates. First, flat silicon wafers (Si-Mat, Kaufering, Germany) (thickness $(275 \pm 25)\mu m$) were cut to a rectangle shape of $\approx 3 \times 4\,cm^2$. Wafers were cleaned with successive rinsing of H_2O, ethanol, acetone, ethanol followed by drying with a nitrogen flush and placed on a flat surface.

Organic solutions of 5 mg DCPC (and the desired amount of alkanes, when needed) in chloroform:methanol (2:1) were prepared. For consistency with the most used alkane percentage in the single-amphiphile mixtures (C10 mix samples), i.e. 2% alkane:amphiphile molar ratio, the DCPC samples including alkanes were prepared at 4% alkane:phospholipid molar ratio to account for the double tail of the latter compound.

The organic solutions were spread uniformly onto the wafers and let drying under fume hood (Figure 13). The wafers were slightly tilted to all directions when needed, in order to ensure that the film deposition was occurring as uniformly as possible on the wafer while the chloroform evaporated. The wafers were placed

singularly inside falcon tubes and left dry overnight inside a desiccator with vacuum pumping. After drying, few drops of H_2O were added inside each Falcon tube, the containers were closed and placed in an oven for annealing at 40 °C, 100% Relative Humidity (RH) for 24 hours. The samples were stored as they were at this stage, and then inserted inside the Humidity Chamber at least 4 hours before the measurements for equilibration.

3 RESULTS

3.1 THE ROLE OF FATTY ALCOHOL

3.1.1 Article 1: High-Temperature Behavior of Early Life Membrane Models

3.1.1.1 *Foreword*

The first series of experiments were aimed at exploring the effect of the fatty alcohol (decanol) mixing with the same chain fatty acid (decanoic acid). For that, such mixture was studied and compared at all steps with another sample that was made uniquely by decanoic acid.

Although the above-mentioned systems, or similar types, have been used in previous works (*36*, *53*, *60*), this is the first systematic study on both models simultaneously, aimed at quantifying features like the quantity, type, characteristics of the macro-structures formed at room temperature and their response to the temperature increase up to T = 80 °C.

In particular, a very pronounced effect has been observed in the vesicle thermal behaviour that is purely due to the presence of the alcohol. Perhaps surprisingly, considering the wide use of the C10 mix model (at various acid:alcohol ratios), this clear onset in the vesicle structuring was not identified before, even though it is possible that some of the previous studies have indirectly observed the consequences of this phenomenon. We interpreted some of the previous findings in view of our results in the "Discussion" section of the paper.

For this work, I designed all the experiments and wrote the proposals to obtain neutron beamtime on D33 (SANS). I prepared the samples for Differential Scanning Calorimetry (DSC), ssNMR, SANS and performed the experiments on D33, D16 (SANS) and the DSC platform. I participated to the ssNMR experiments which were performed at the “Institut Europeen de Chimie et Biologie ”(IECB, Bordeaux, FR) and discussed the data analysis with the collaborators. I analyzed the D33 and D16 (SANS) data, supervised the analysis of DLS data performed by my M.Sc. trainee Antonio Caliò and wrote the paper.

The paper has been published in *Langmuir (ACS)* (*110*).

LANGMUIR

pubs.acs.org/Langmuir Article

High-Temperature Behavior of Early Life Membrane Models

Loreto Misuraca, Antonino Caliò, Isabelle Grillo, Axelle Grélard, Philippe Marie Oger, Judith Peters, and Bruno Demé*

Cite This: *Langmuir* 2020, 36, 13516–13526 Read Online

ACCESS | Metrics & More | Article Recommendations | Supporting Information

ABSTRACT: Origin of life scenarios generally assume an onset of cell formation in terrestrial hot springs or in the deep oceans close to hot vents, where energy was available for non-enzymatic reactions. Membranes of the protocells had therefore to withstand extreme conditions different from what is found on the Earth surface today. We present here an exhaustive study of temperature stability up to 80 °C of vesicles formed by a mixture of short-chain fatty acids and alcohols, which are plausible candidates for membranes permitting the compartmentalization of protocells. We confirm that the presence of alcohol has a strong structuring and stabilizing impact on the lamellar structures. Moreover and most importantly, at a high temperature (> 60 °C), we observe a conformational transition in the vesicles, which results from vesicular fusion. Because all the most likely environments for the origin of life involve high temperatures, our results imply the need to take into account such a transition and its effect when studying the behavior of a protomembrane model.

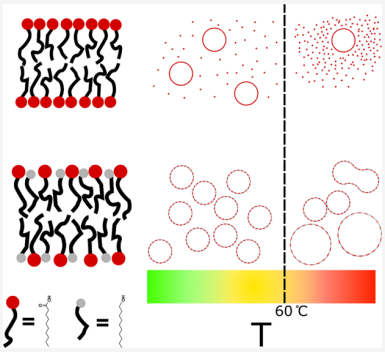

Downloaded via Loreto Misuraca on November 17, 2020 at 08:23:58 (UTC).
See https://pubs.acs.org/sharingguidelines for options on how to legitimately share published articles.

INTRODUCTION

Compartmentalization of the protocell and thus the formation of the lipid boundary between the cell and its environment are central to the emergence of early life and to assure the required conditions for energy-dependent life processes. Indeed, uni- or multi-lamellar vesicles (ULVs–MLVs) are believed to be the ancestors of cell membranes[1,2] and to have provided a privileged environment to early biopolymers, enabling the formation of the earliest protomembranes and cells. To create such barriers, membranes were composed of self-assembling amphiphilic molecules. Contemporary membranes are all based on phospholipids, a group of highly functionalized, diverse, and adaptable molecules, whose presence at the early stages of life is not probable. Another aspect that suggests the progressive transition between early amphiphiles and modern phospholipids is that the latter require a complex synthesis pathway and are unlikely to have been produced spontaneously but rather elaborated in successive selective steps.[3]

In contrast, simple amphiphilic substrates were likely formed in the relatively harsh but potentially wet conditions of the early Earth by Fischer–Tropsch processes.[4,5] Photo-oxidation likely valorized alkanes by transforming them into oxygenated amphiphilic materials such as fatty acids and fatty alcohols. This synthesis would have led to a high abundance of short-chain fatty acids (FAs) (C < 12), the abundance of which falls exponentially with the tail length.[1,6] FAs have been proven to form vesicles when the chain length is eight or more carbons.[7]

A pioneering work has documented the ability of these amphiphiles to form membrane structures in solution, the stability of which is strongly dependent on environmental conditions.[8] The first requirement for vesicle formation is a solution pH equivalent to the FA dissociation constant (pK_a) so that approximately half of the protonated molecules act as hydrogen bond donor to the adjacent ionized ones.[9,10] The second requirement is to reach the critical vesicle concentration (CVC),[9] below which these single-chain amphiphiles exist only as monomers in solution or aggregated in micellar structures. The CVC of pure FA vesicles has been measured quantitatively as a function of the chain length.[7] A decrease in the CVC was observed with increasing chain length, as expected, because longer apolar hydrocarbon tails favor the more packed bilayered structures. Furthermore, the addition of small amounts of fatty alcohols (with same length as the FA in a 10:1 FA: alcohol molar ratio) was found to dramatically lower the CVC and also to allow vesicle formation at pH values higher than the pK_a of the acid. This can be explained because the alcohol ability to form hydrogen bonds with the anionic FA balances the lack, at high pH, of hydrogenated FAs that would serve the same purpose (as it happens in the pure FA samples around its pK_a). However, FA vesicles do not withstand high salinity, especially when divalent cations such as Mg^{2+} or Ca^{2+} are involved.[7,11,12]

All these major limitations have led to a paradoxical situation where the molecules that can self-assemble into vesicles and were probably the most abundant in an origin of life scenario,

Received: July 31, 2020
Revised: October 15, 2020
Published: November 4, 2020

ACS Publications © 2020 American Chemical Society

https://dx.doi.org/10.1021/acs.langmuir.0c02258
Langmuir 2020, 36, 13516–13526

namely, the FA with C < 12, are also seen as the least promising ones because of their observed sensitivity to the environment.

Some of these apparent issues have been potentially solved by considering a mixture of the same chain alcohol and FA, as mentioned above, for its effect on the CVC and the pH of vesicle formation. On the other hand, the sensitivity towards salt concentration has also been shown to be lowered either by alcohol addition,[13] by using mixtures of different lengths of FA,[14] or by prebiotic amino acids binding the FA membrane.[15] These studies prove that ways to overcome the sensitivity toward high salinity exist while still considering plausible prebiotic systems and environmental conditions. Yet, previous studies on the thermal behavior and stability of protomembranes have been focusing on longer aliphatic chains[16,17] driven by the observed environmental sensitivity at ambient temperature. Nevertheless, some surprisingly thermostable properties have been observed even for vesicles made with short-chain amphiphiles. In particular, vesicles made with mixtures of decanoic "capric" acid−decanol or "capric" acid−decanol−monocaprin (2:1 and 4:1:1 molar ratio, respectively) were shown to retain encapsulated oligonucleotides up to 70 °C for more than 1 h or 100 °C for more than 1 min.[16] These findings suggest that the observed sensitivity of the membranes made by short aliphatic chains toward changes in pH, amphiphile, and salt concentrations does not necessarily imply a lack of stability towards temperature variations.

A first temperature−pressure study of the C10 mixture (capric acid + decanol 1:1 ratio) in buffered solution (bicine, 0.2 M, pH 8.5) has been performed by Kapoor et al.[18] They observed and assigned two phase transitions experienced by the system: the first, at 10 °C, was identified as "the appearance of disordered fluid-like chains"; the second, at ≈ 60 °C, was explained as "morphological changes of lipid entities with overall fluid-like chains" (e.g., a shift in the micelle−vesicle equilibrium). Interestingly, they also observed an increase in the vesicle size beyond 50 °C (diameter increasing from 120 nm at 45 °C to 160 nm at 55 °C), although the temperature range investigated (5−55 °C) did not allow them to study in more detail the phenomenon at higher temperatures.

In this article, we extend the studies up to 80 °C and present a deeper and quantitative characterization of the membrane model composed of a capric acid/decanol 1:1 mixture (hereafter called C10 mix, Figure 1a) by following the properties and the evolution of the corresponding vesicles (partitioning, size distribution, lamellarity, membrane thickness, and signs of micelle presence) as a promising model of protocellular compartmentalization. We compare its characteristics with a similar model made of pure capric acid (Figure 1b). The stability with temperature is investigated for both systems to understand the capability of the vesicles to withstand the high temperatures expected at hydrothermal vents/hot springs. It is of great interest to investigate the thermal stability of the protomembranes as the high temperature would have allowed a number of important non-enzymatic reactions to take place (e.g., DNA strand separation and reannealing).[16]

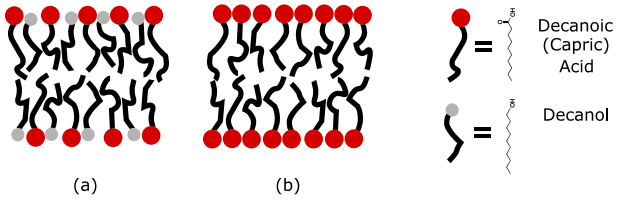

Figure 1. Protomembrane models: (a) bilayer made from a mixture of capric acid and decanol; (b) bilayer made of capric acid.

We find that the alcohol insertion leads to a number of substantial differences in the vesicle behavior:

- It leads to a much larger proportion of vesicles at the expense of other aggregates (micelles) or monomers in solution.
- It protects vesicles from low-temperature vesicle disruption, maintaining the multilamellar structures when present.
- It triggers an abrupt conformational change above 60 °C. This leads to a transition from multilamellar vesicles to large unilamellar structures.

Such findings, in turn, could set a high T limit for the stability of vesicle systems to 60 °C at ambient pressure but could also open new alternative perspectives related to the observed changes in the amphiphiles' self-assembly. Our results point toward an alcohol-induced, T-triggered, and slowly reversible vesicular fusion process.

EXPERIMENTAL SECTION

Sample Preparation. Decanoic acid, 1-decanol, bicine buffer, and D_2O were purchased from Sigma Aldrich (Merck). The samples were prepared by dissolving the decanoic acid (and the decanol, when needed) in a $CHCl_3$ solution followed by drying with a flush of nitrogen (the decanoic acid +1-decanol mixture is liquid at ambient temperature). The samples were then placed in a desiccator and left under vacuum overnight. The sample weights were checked at each step to make sure that all the chloroform was evaporated. At the final stage, a sample loss of ∼5% was measured for the C10 mix samples probably due to a partial evaporation of the decanol. The final decanoic acid/1-decanol in the C10 mix samples was 1:1.

The bicine buffer was prepared at a concentration of 0.2 M in H_2O. For the NMR experiments, the buffer was solubilized in ^2H-depleted water. In the case of SANS experiments, the buffer solution was prepared by dissolving hydrogenated bicine in D_2O. In all cases, the buffer was filtered with a 0.2 μm Millipore membrane before use.

The dried organic solutions were then suspended in buffer, titrated to desired pH/pD with aliquots of NaOH/NaOD, and vigorously vortexed, leading to final milky-foamy solutions.

For the solid-state NMR and SANS on D16 experiments, the total amphiphile concentration was set to 350 mM, and the samples were measured as they were at this stage.

For DSC, SLS-DLS, and SANS on D33, the total amphiphile concentration was 80 mM. Samples were extruded using the equipment provided by Avanti Polar Lipids, with the heating block regulated at 40 °C and using 100 nm polycarbonate membranes. The extrusion was always performed with 11 passes per sample and less than 24 h before the corresponding experiments. Light scattering pre-characterization measurement ensured that the extruded vesicles were stable at ambient temperature for several days (data not shown).

Static−Dynamic Light Scattering. The multi-angle static light scattering measurements in the angular range 25−150° and the dynamic light scattering measurements at 150° (giving the results of Figure 2 in the text) were performed on an ALV CGS-3 instrument (ALV GmbH, Langen, Germany) at the Institut Laue Langevin (ILL) Grenoble with an incoming laser light of λ = 633 nm wavelength. Then, 1 mL of each sample was loaded on round-bottom borosilicate cuvettes after filtration through 0.45 μm Millipore filters (0.2 μm for the buffer) and left for 10 min in the toluene bath for thermalization before starting the measurements. A buffer measurement at the same conditions was performed to subtract its contribution, as well as toluene as a standard with known Rayleigh ratio (R_{tol} = 1.35 × 10^{-5} cm^{-1}):

https://dx.doi.org/10.1021/acs.langmuir.0c02258
Langmuir 2020, 36, 13516−13526

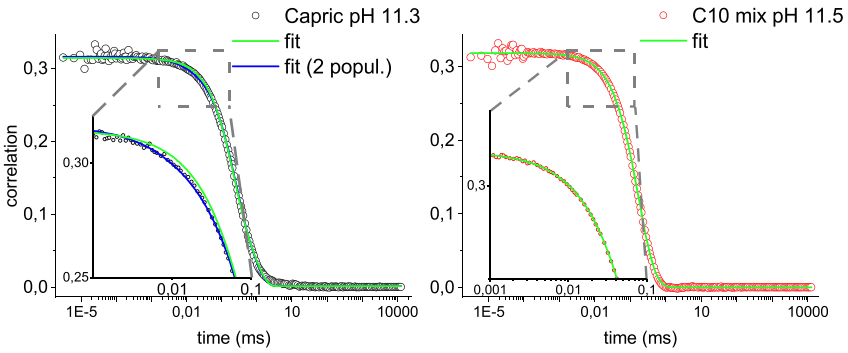

Figure 2. Dynamic light scattering auto-correlation curves at high pH 11.4 and corresponding zooms on the short correlation times (insets) at 25 °C. Left: capric acid, 80 mM; right: C10 mix, 80 mM. The solid lines are fits to the data as described in the "Experimental Section".

$$R_{sample} = R_{tol} \times (I_{sample} - I_{solvent})/I_{toluene} \quad (1)$$

where R, the Rayleigh ratio, is defined as the scattered intensity per unit of the solid angle, scattering volume, and incident intensity; I is the scattered intensity. The scattered intensity is corrected for the scattering volume (the sample volume visible for the detector) using $I_{sample/solv/tol} = I_{exp} \times \sin(\theta)/I_0$, where θ is the scattering angle and I_0 the incoming intensity.

For the DLS measurements at the 90° fixed angle, as a function of temperature, the instrument used was a Malvern Zetasizer Nano ZS90. For the latter, 200 μL quartz cells were used.

For the SLS measurements (ALV), the scattered intensity was collected for 10 s per angle. For DLS (ALV and Malvern), three runs of 30 s each were collected per angle for an error estimation of the diffusion coefficients.

The SLS scattering data were treated using the Guinier approximation,[19] whose validity was verified for the 100 nm extruded vesicles. In fact, for the cases where $q \times R_g \leq 1$ (q being the scattering vector, $q = 4\pi n \sin(\theta/2)$; R_g is the gyration radius), one can approximate the scattering intensity (the Rayleigh ratio) as

$$\ln(R_{sample}) \approx \ln(I_0) - q^2 R_g{}^2/3 \quad (2)$$

so that in a log-linear plot, the slope of the fitted line gives an estimation of R_g.

The dynamic light scattering correlation functions were analyzed following the method of the moments (a re-visitation of the method of cumulants) developed in ref 20. The first two moments μ_1 (corresponding to the decay rate Γ) and μ_2 were left as free parameters in the fit. For particles moving by Brownian diffusion, the decay rate is linked to the diffusion coefficient D by the relation $\Gamma = Dq^2$. In some cases, a sum of two populations, each one having its own μ_1 and μ_2, was necessary for successful fits (indicating the existence of different families of scatterers of different sizes).

The experimentally determined Brownian diffusion coefficients D were then used to estimate the hydrodynamic radius R_h using the Stokes−Einstein equation:

$$D = k_B T/(6\pi R_h \mu) \quad (3)$$

with D as the diffusion coefficient, k_B as the Boltzmann constant, T as the temperature, and μ as the solvent viscosity (solvent viscosity and refraction index n were assumed the same as for H_2O).

Fits of the DLS autocorrelation functions were performed using the Origin software (OriginLab Corp., Northampton, MA).

Differential Scanning Calorimetry. For the DSC experiments, a microDSCIII calorimeter (Setaram, France) was used. Two Hastelloy C cells of 0.5 mL sample volume were used for both the samples and the buffer. The samples were measured against the buffer as a reference. The explored temperature range was $-4 < T < 85$ °C with a scanning rate of 0.5 °C /min. Three heating cycles were collected (the first for annealing, the last two to verify the reproducibility). No corrections or baseline subtractions were applied, the scans being used for qualitative comparison.

Solid-State NMR. The capric acid sample was prepared by hydrating 6 mg of perdeuterated ($^2H_{19}$) capric acid with 100 μL of 0.2 M bicine buffer prepared in deuterium-depleted water (hydration of 94%). The C10 mix sample was prepared by mixing 3 mg of perdeuterated capric acid with decanol (1:1 molar ratio) and hydrated with 100 μL of the same buffer (hydration of 97%). Samples were transferred into 100 μL 4 mm zirconia rotors for NMR analyses. ^{2}H-ssNMR experiments were performed at 76.77 MHz with a phase-cycled quadrupolar echo pulse sequence (90°x-t-90°y-t-acq)[21] and using a Bruker Avance III 500 MHz WB (11.75 T) spectrometer equipped with a solid-state CPMAS 4 mm H/X probe (IECB structural biophysics platform, Bordeaux, France). Acquisition parameters were as follows: a spectral window of 500 kHz, $\pi/2$ pulse width of 3.9 μs, interpulse delays of 40 μs, and recycling delay of 1.3 s; the number of scans ranged from 500 to 3000. Samples were equilibrated for 30 min at each temperature before the acquisition. The acquisition time for capric acid and C10 mix spectra was 10 and 65 min, respectively. Spectra were processed using a Lorentzian line broadening of 400 Hz before Fourier transformation from the top of the echo. Samples were equilibrated for 30 min at a given temperature before data acquisition. All spectra were processed and analyzed using Bruker Topspin 4.0.6 software.

Small-Angle Neutron Scattering. SANS measurements were performed on two instruments, available at the ILL (Grenoble, France):

- D33 (https://www.ill.eu/users/instruments/instruments-list/d33/),[22] with two neutron wavelength configurations (λ = 5 Å and λ = 14.5 Å) and three sample-detector distances (2, 10, and 12 m) to cover the widest range of scattering vector ($1.3 \times 10^{-2} < q < 5.6$) nm^{-1}.
- D16 (https://www.ill.eu/users/instruments/instruments-list/d16/), with neutron wavelength λ = 4.5 Å and a sample-detector distance of 0.95 m, leading to the scattering vector range ($2.6 \times 10^{-1} < q < 5.3$) nm^{-1}.

The sample suspensions, of 200 μL each, were loaded in 1 mm quartz cells (Hellma, Germany) on a sample holder with thermal regulation. For the start at a low temperature during the temperature scans, samples were equilibrated for at least 20 min. Then, for every T jump, the minimum equilibration time before starting the data acquisition of the first sample in the sample changer was 10 min; this time increased as samples were sequentially measured. We did not notice any inconsistencies due to the sample positions in the sample changer. All data were corrected for the scattering of the sample container and the instrumental background. H_2O was measured for detector efficiency calculation and scaling to absolute units (cm^{-1}). A flat background was subtracted to account for the q-independent incoherent neutron scattering signal.

The outcome from a SANS experiment is a series of curves of I versus q, where

$$I(q) = |F(q)^2 \times S(q)| = |P(q) \times S(q)| \quad (4)$$

$P(q) = F(q)^2$ being the particle form factor and $S(q)$ being the structure factor. The form factor contains information about the shape of the

https://dx.doi.org/10.1021/acs.langmuir.0c02258
Langmuir 2020, 36, 13516−13526

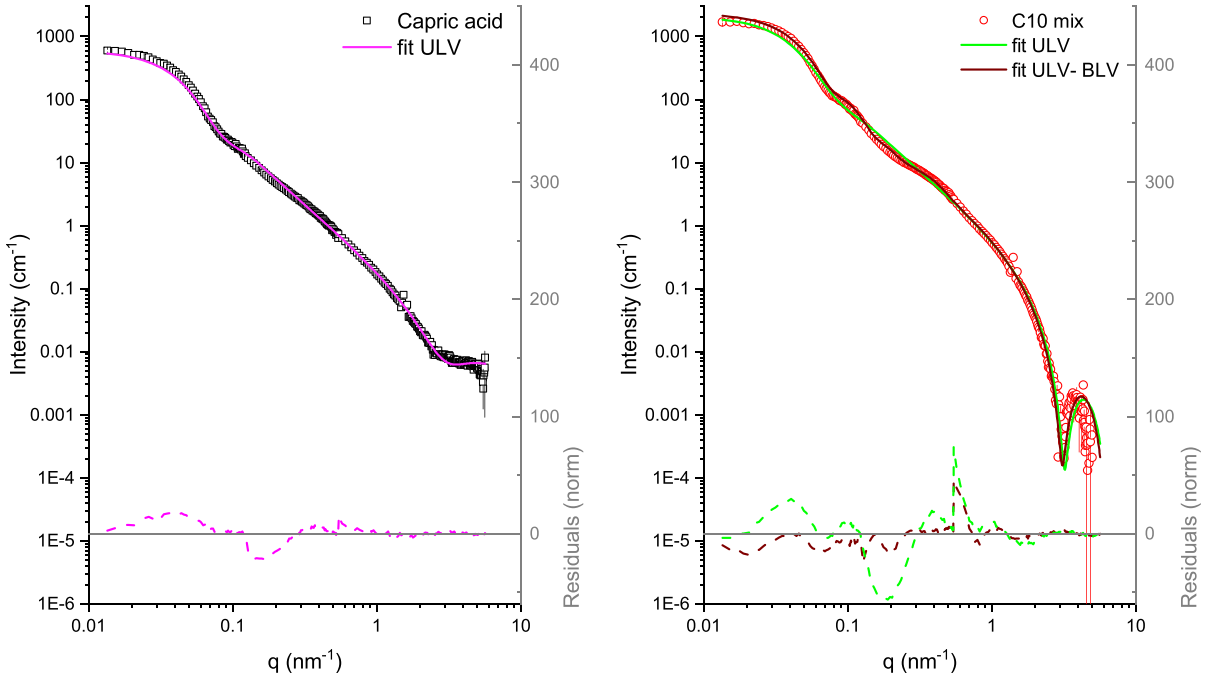

Figure 3. SANS curves collected on D33 for the capric acid sample: 80 mM (left) and C10 mix 80 mM (right) at 25 °C and corresponding fits. Sample pH: 7.3 (capric acid) and 8.5 (C10 mix). For the C10 mix, two models are compared and show that the pure unilamellar vesicle (ULV) model fails to describe correctly the features in the data; therefore, a fraction of 40% of bilamellar vesicles (BLVs) has to be added. The dotted lines are the normalized residuals in a linear scale (right hand axis). The error bars are displayed only every five data points for clarity.

scatterers at different length scales (the q range) covered: in the case of vesicles, this will be the vesicle size, shape, size polydispersity, lamellarity, bilayer thickness, and polydispersity. The structure factor contains information about possible interaction between neighbor vesicles and, most importantly, the interaction between subsequent membranes forming the MLVs. The position of the first maximum of the correlation, due to the membrane $S(q)$ in a SANS curve, can give a direct estimation of the membrane d-spacing through the relation $d = 2\pi/q$ (with d: d-spacing; q: scattering vector).

The fitting of the SANS curves were performed using the SASView public software (http://www.sasview.org/). The equations for all the model form factors employed can be found in the "Material and methods" section (Supporting Information).

RESULTS AND DISCUSSION

Vesicle Stability at Ambient Temperature. First, we studied the two model systems, capric acid and C10 mix, at room temperature T = 25 °C. Because only the general features (vesicle presence and amount, bilayer thickness, and micelle presence and amount) were investigated at this stage, the samples were extruded through a 100 nm polycarbonate membrane in order to obtain a suspension of monodisperse vesicles. We verified that the use of bicine as buffer, commonly used in previous works with similar systems,[16,18,23,24] did not affect vesicle stability and properties at ambient temperature. This was done by screening a number of concentrations and pH conditions of the samples in buffered solution with static light scattering (SLS) (Figure S1, Supporting Information). Our results show a well-defined vesicle population only at the lowest measured pH (7.8) and the highest concentration (80 mM) data for the capric acid sample, while in the C10 mix, the same is found also at higher pH (up to 11.5) and lower concentration (down to 40 mM). These are qualitatively consistent with what was previously found for the pK_a and the CVC of similar samples (pure capric acid and C10 mix, 10:1 acid/alcohol ratio) that were suspended and titrated in water.[5,7] The bicine buffer did not lead to any significant variation in the behavior of the model vesicles.

Dynamic light scattering (DLS) was then used as a tool to disentangle populations of very different sizes (from tens of nanometers to micrometers), allowing for the detection of the presence of micelles and vesicles. By fitting the autocorrelation curves considering one (or two) population of scatterers, we can show that under very alkaline conditions (pH ≫ pK_a), micelles are detected in pure capric acid samples, while for the C10 mix, only vesicles are visible at every measured condition (pH and T) (Figure 2; data at pH 7.8 and 8.1 are shown in Figure S2, Supporting Information). We found, for the micelles, a mean diameter of 1−2 nm, consistent with the expected size of capric acid micelles.

We thus kept a constant pH of 7.3 for the capric acid (to keep it nearby its pK_a[25]) and 8.5 for the C10 mix for the following small-angle neutron scattering (SANS) measurements. The vesicles made of pure capric acid present common features with those formed with the C10 mix, as found from our SANS results and fits to the data (Figure 3 and Table 1; see the "Materials and methods" section for the fitting model formulas and Table S1 for all used parameters, Supporting Information):

Table 1. Main Parameters Extracted from the SANS Data Fitting at Ambient Temperature[a]

parameter	capric acid	C10 mix	
scale (total)	0.34	1	
population fraction	1	0.6 (ULV)	0.4 (BLV)
core radius (nm)	28.0	38.3 (ULV)	9.2 (BLV)
shell thickness (nm)	1.8	2.0 (ULV)	2.0 (BLV)
solvent thickness (nm)			11.8 (BLV)

https://dx.doi.org/10.1021/acs.langmuir.0c02258
Langmuir 2020, 36, 13516−13526

- Both have vesicles with much smaller sizes than the extrusion pore diameter of 100 nm (59.6 and 80.6 nm diameter composed of 2 × (core radius + shell thickness)), although the C10 mix vesicles have a larger mean radius.
- A membrane thickness of about 2 nm, as expected for a bilayer of amphiphiles with 1 nm chain length.

[a]Sample pH: 7.3 (capric acid) and 8.5 (C10 mix). Note, in particular, the scale factor of 0.34 calculated for the capric acid, a sign that only a fraction of capric acid contributes to the vesicle form factor. Full parameter list can be found in Table S1 (Supporting Information).

The following major differences are visible and inform about the substantial impact of the alcohol insertion. First, because the SANS data are very sensitive to the vesicle lamellarity, it is observed that, while the capric acid vesicles are always unilamellar, the C10 mix presents a fraction of bilamellar vesicles (BLVs). Although the extrusion performed in this experiment could have interfered with the capability to form multilamellar structures in both samples, the data suggest a higher propensity of the latter (C10 mix) to form membrane stacks. This will be further confirmed also on non-extruded samples, as discussed in the next section.

The observed bilamellar vesicles differ substantially from ordinary phosphatidylcholine (PC) MLVs for what concerns the water layer thickness (11.8 nm for the C10 mix, Table 1) between the lamellae, and their characteristics resemble more the typical values found at maximum swelling for charged lipids in pure water,[29] while for PC lipids, the water layer thickness is usually within 2−3 nm (DMPC, DPPC, DOPC, and POPC).[26−28]

As another main difference in the pure capric acid solution, according to the fit to the data in an absolute scale, we find that only ∼30% of the FA contributes to the vesicle form factor, even close to its pK_a. This gives a second piece of indirect evidence about the fraction of the FA (∼65−70%) that remains in solution as monomers or self-assembled into micelles. For the C10 mix sample, we observe that the totality of the lipids (i.e., both the capric acid and the decanol) assemble into vesicles.

We conclude that the addition of alcohol brings many consequences on the vesicle self-assembly other than what has been found previously (namely, the decrease in the FA CVC and the broadening of the pH range of vesicle existence as observed in refs 7 and 18). The totality of the FA/alcohol mixture assembles into vesicles and leads to bigger, and in some cases multilayered, structures. No sign of micelles or monomers in solution (FA nor alcohol) is detected in the C10 mix as opposed to the pure capric acid sample where only a small sample fraction aggregated into vesicles.

Thermal Stability. The vesicle thermal behavior was explored by means of differential scanning calorimetry (DSC, solid lines in Figure 4) and DLS (symbols in Figure 4) to explore membrane phase transitions (DSC) and follow vesicle dimension evolution (DLS). For all the experiments in this section, the pH levels of capric acid and C10 mix were set to 7.7 and 8.5, respectively. Because the focus here was to screen the mean vesicle size with temperature and to detect the gel−fluid membrane phase transition, the samples were extruded prior to the experiments.

The DSC thermogram of C10 mix vesicles shows a first sharp transition at 10.3 °C assigned to the gel−fluid membrane phase transition and a second, much broader one, detected above 60 °C. This result is consistent with what was observed previously.[18] The latter transition, for $T \geq 60$ °C, was interpreted by ref 18 as a conformational micelle−vesicle equilibrium change. Here, we additionally investigated pure capric acid vesicles and observed a single sharp transition at 13.9 °C but no sign of a second broad one.

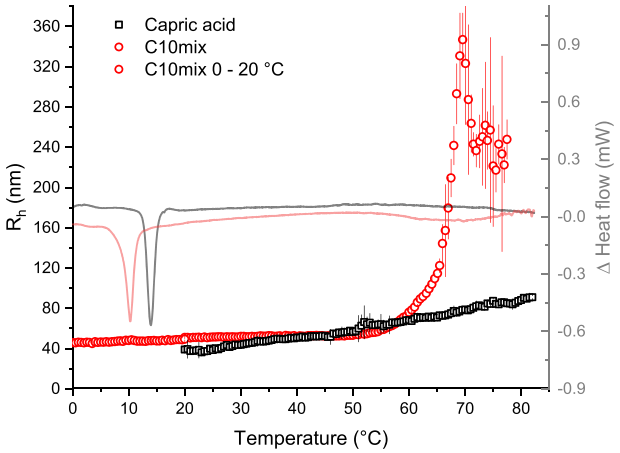

Figure 4. Left axis: resulting R_h found from fitting the DLS autocorrelation functions at a fixed angle (90°) as a function of the temperature for the pure capric acid at 80 mM (black squares) and C10 mix at 80 mM (red circles). The additional dataset collected for the C10 mix in the range 0−20 °C proves that there is no effect of the gel−fluid phase transition in the vesicle size, as expected. Right axis: DSC thermograms of the same samples (red and black lines).

For this reason, the high-temperature broad transition does not seem linked to a vesicle−micelle equilibrium shift as previously proposed.

The capric acid sample is in fact the only one giving evidence for the presence of micelles (observed directly in our DLS data and indirectly in our SANS data as a lack of the expected vesicle signal, Figure 2 and Table 1). Furthermore, our DLS data versus T (Figure 4, symbols) show a corresponding, steep increase in the mean vesicle radius occurring at the same temperature and only for the C10 mix. This, together with the marked difference with the pure capric acid vesicles, suggests that the observed high-temperature effect is an alcohol-triggered phase transition toward bigger macrostructures.

The thermal behavior of the samples was also addressed by performing solid-state (ss) ^{2}H NMR and SANS as a function of temperature for capric acid and C10 mix water dispersions. In this case, the samples were not extruded to avoid interferences in the sample lamellarity. ssNMR was used to bring quantitative structural and dynamic information about the dispersions, as has been accomplished long ago on liquid-crystal-like assemblies such as biological membranes, lipids, colloids, and surfactants dispersed in water.[30−32] In our case, perdeuterated capric acid was used in order to probe the membrane dynamics (experimental details and ssNMR data analysis can be found in the Supporting Information, Figure S3 and Table S2). Figure 5 shows some wide-line spectra recorded for a few temperatures for capric acid and C10 mix water dispersions.

In the capric acid data (left of Figure 5), an isotropic, very intense Lorentzian line dominates most spectra from 0 to 80 °C indicative of small-sized objects (1−100 nm) tumbling very fast compared to the ssNMR time scale.[33] Close attention to the spectrum at 0 °C allows detection of a so-called "powder" (non-oriented) pattern indicating that slowly tumbling much larger

https://dx.doi.org/10.1021/acs.langmuir.0c02258
Langmuir 2020, 36, 13516−13526

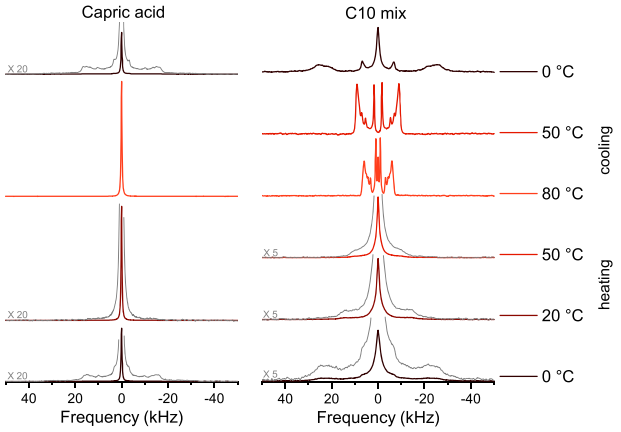

Figure 5. $^2H_{19}$-ssNMR spectra of $^2H_{19}$-capric acid 350 mM (left) and $^2H_{19}$-capric acid/decanol 350 mM (right) water dispersions (94 and 95% hydration, respectively) as a function of temperature, from bottom to top, on increasing the temperature from 0 to 80 °C and cooling back to 50 and 0 °C. Gray solid lines show details of the baseline by multiplying the vertical scale by 20 (left) and 5 (right).

objects (microns to submicron size) are also identified. At the other temperatures, there is no sign of large objects in the capric acid sample.

Conversely, in the case of the C10 mix (right set of curves in Figure 5), the coexistence of broad powder patterns and isotropic lines is observed at all temperatures, and the latter are much less abundant as was the case in the former sample. This points again toward a higher propensity of the alcohol-enriched vesicles to maintain the big multilayer structures. The hydrophobic bilayer thickness (b_H) at T = 20 °C, calculated from the NMR spectral simulations assuming no chain interdigitation, was $b_H = 2 \times L_{chain} = (1.66 \pm 0.08)$ nm (Table S3, Supporting Information). This value is slightly lower than the one found from SANS fitting, $b = (2.0 \pm 0.1)$ nm (Table 1 and Table S1, Supporting Information), and the discrepancy may reflect twice the size of the small FA headgroup, $(b - b_H)/2 = (2.0-1.66)$ nm$/2 \approx 0.17$ nm.

Finally, the spectrum of the C10 mix at 80 °C (hence above the conformational transition seen at $T \geq 60$ °C, Figure 4) shows an oriented-like pattern (bilayer normal perpendicular to the magnetic field of the spectrometer). Returning to 50 °C shows the same but a wider oriented-like pattern, which differs considerably (the isotropic line is absent) from that observed on increasing temperature. Returning further to 0 °C shows a superimposition of the powder pattern and isotropic lines with, however, a lower proportion (Figure S5, Supporting Information). This clearly indicates a hysteresis related to the thermal history of the sample, suggesting intense thermally induced sample reorganization.

We questioned whether the addition of decanol triggered a transition from a lamellar to a non-lamellar phase, e.g., hexagonal or cubic, as this can grow with a preferential direction and lead to NMR spectra such as the one observed for the C10 mix at 80 °C (inverted phases being improbable because of the low amphiphile concentration used). For that, we performed SANS experiments on the same samples.

At high (D_2O) contrast, SANS is extremely sensitive to the presence and dimensions of MLVs and ULVs (LUVs and SUVs) and to small spherical or elongated micelles as their dimensions are within the q range of interest in this study (1.5×10^{-3} to 0.6

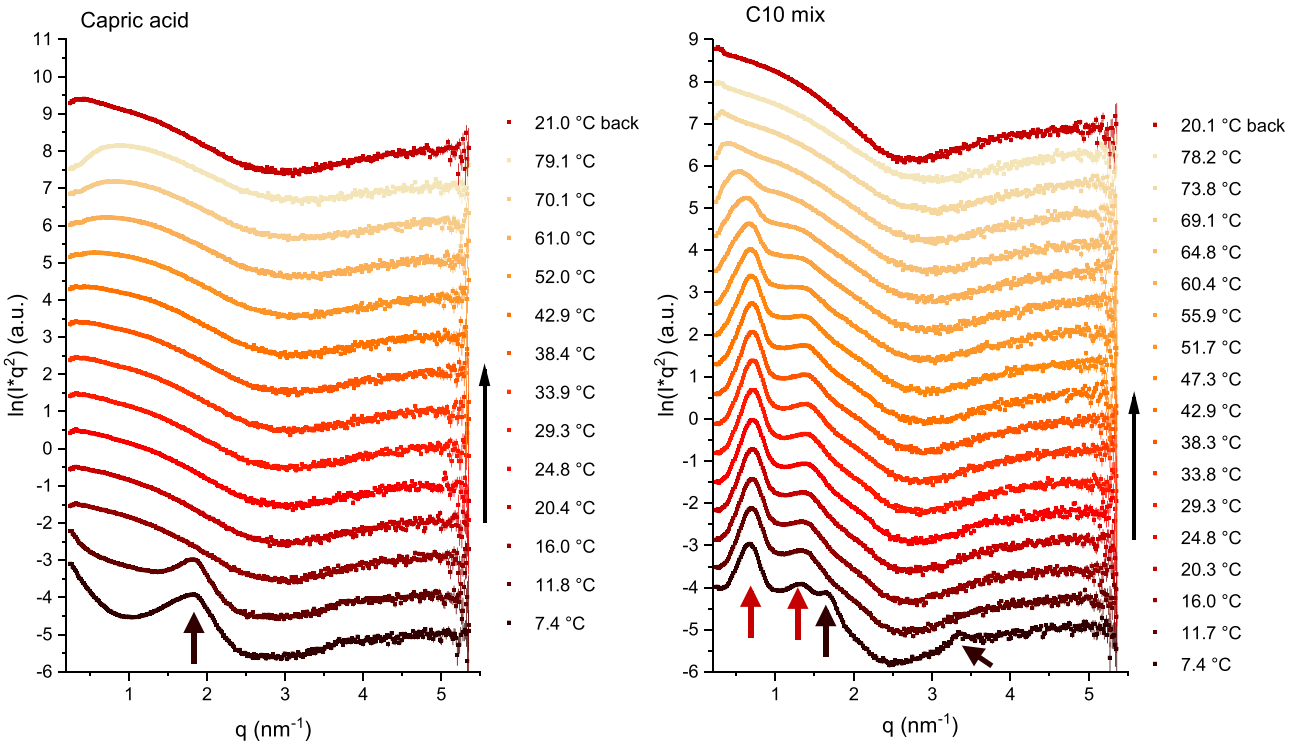

Figure 6. SANS curves collected on D16 at different temperatures, shown in the representation $\ln(I \times q^2)$ vs q, to highlight the presence of membrane correlations. Left: capric acid sample at 350 mM. Right: C10 mix sample at 350 mM. Arrows show the first two orders of the observed lamellar phase structure factor $S(q)$.

https://dx.doi.org/10.1021/acs.langmuir.0c02258
Langmuir 2020, 36, 13516−13526

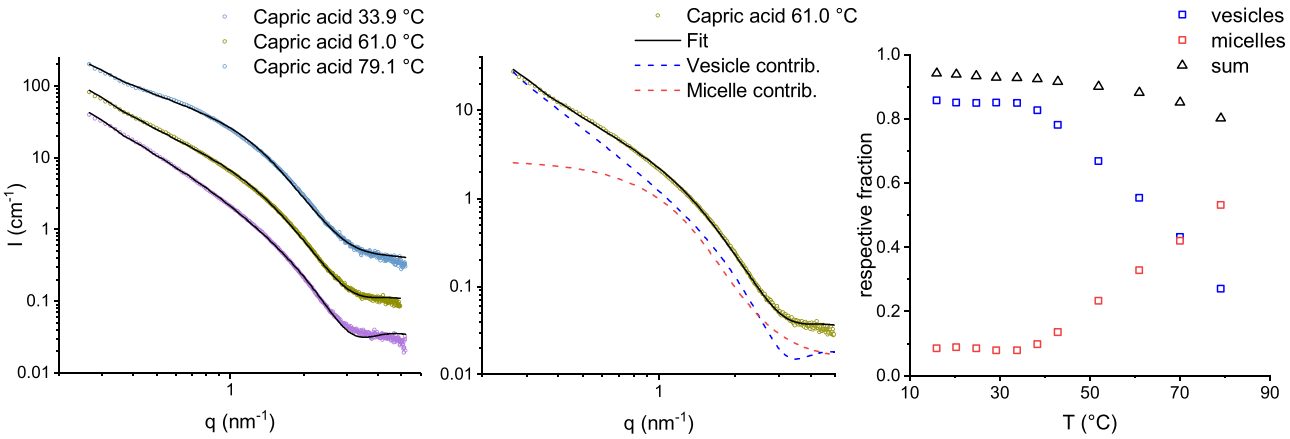

Figure 7. Left: examples of fits performed on the capric acid SANS data from D16. The error bars are displayed every five data points. Middle: plot of the vesicle and micelle contributions and their sum for T = 61 °C. Right: respective fraction of vesicles and micelles.

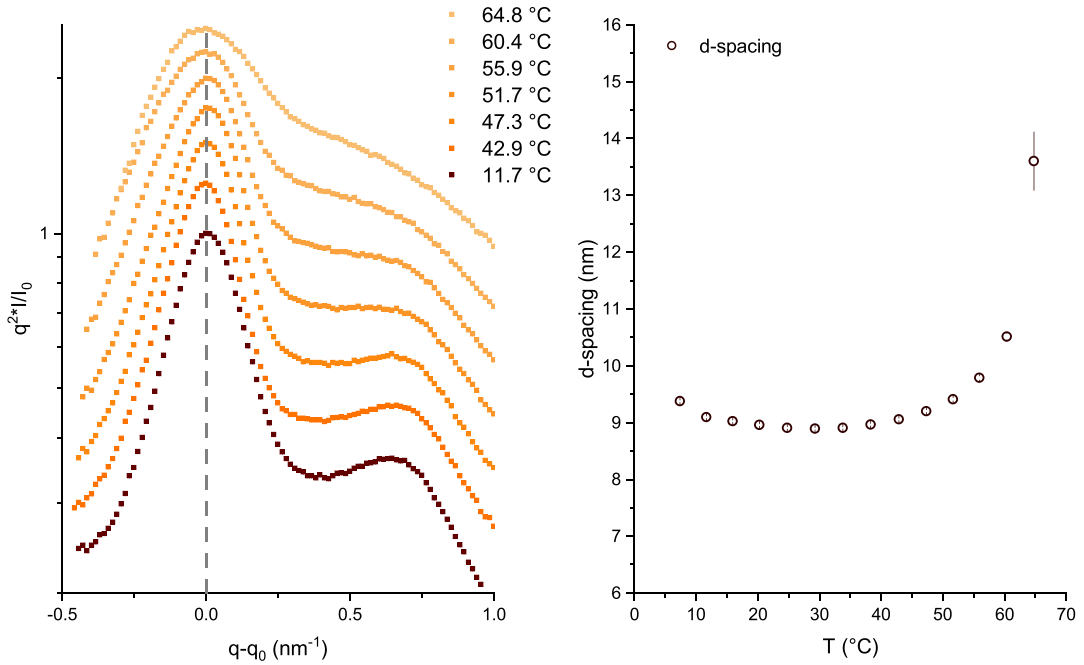

Figure 8. Left: C10 mix SANS curves collected on D16, zoomed around the first lamellar correlation peak, in the representation $q^2 \times I/I_0$ vs $q - q_0$ to highlight the first- and second-order lamellar peak broadenings upon heating. Some of the curves at low temperature were skipped for clarity. Right: *corresponding* d-spacing of the swollen C10 mix phase as a function of T.

Å^{-1}, which corresponds in real space to dimensions of 420 to 1 nm). The multilamellar structures can be studied following the correlation between the adjacent membranes (given by the static structure factor $S(q)$).[34] For instance, the relative position between the oscillation's maxima, observed as broadened peaks in the SANS curves, will differ for lamellar (positions n, $2n$, $3n$..., n being the order) or hexagonal (n, $\sqrt{3}n$, $2n$...) phases.[35] Thus, this represents a convenient way to distinguish between lamellar and non-lamellar phases.

Additionally, even in the cases where there is no phase ordering and the correlations are absent (so that $S(q) = 1$ over the entire q range and no structure peak is observed), it is still possible to distinguish, from the decay of the curves (representing the form factor $P(q)$), between planar lamellae and solid cylinders, characteristic of elongated micelles (the hexagonal phase "building blocks", diluted and free to move in solution).[36] The planar lamellae would decay with a $\sim q^{-2}$ power decay, while for cylinders, the decay would follow a $\sim q^{-1}$ decay.

The SANS curves were collected for both the capric acid and C10 mix samples as a function of temperature in the range 7−80 °C (Figure 6). All the curves show a decay close to a q^{-2} power decay, indicating the presence of vesicles. The capric acid vesicles (left plot of Figure 6) possess a correlation peak at q = (1.8 ± 0.1) nm^{-1} that corresponds to a d-spacing of (3.4 ± 0.1) nm. This correlation disappears at 16 °C, and no other correlation is visible at higher temperatures. From 16 to 43 °C, the curves are identical. From 52 °C onward, a change is observed in the low q region. Remarkably, the fits performed on the capric acid curves for $T \geq 16$ °C show the need to consider a model of vesicles coexisting with micelles to properly reproduce the experimental data (Table S4, Supporting Information). In Figure 7, some of the fits are shown, as well as the normalized

https://dx.doi.org/10.1021/acs.langmuir.0c02258
Langmuir 2020, 36, 13516−13526

respective fraction corresponding to each species (Figure 7, right panel). At $T \leq 35$ °C, ~85% of capric acid contributes to the vesicle signal while ~10% goes into micelles. When $T \geq 35$ °C, a steep decrease in vesicle amount is observed followed by a concomitant increase in the micelle signal. The sum of the two components also goes slightly down with the temperature increase, probably due to FA solubilization.

Upon cooling back to 20 °C, the proportion of micelles and vesicles is recovered (micelle/vesicle ratio: 10% before heating, 12% after cooling back), but the total amount of self-assembled material is diminished, which may be a sign of the occurrence of some phase separation. Finally, cooling down to 8 °C causes the complete recovery of the correlation peak (data not shown).

On the other hand, the correlation peaks observed in the C10 mix (right plot of Figure 6) show that the sample is biphasic at a low temperature (7 °C): the first phase has a correlation at $q = (0.7 \pm 0.1)$ nm^{-1} (d-spacing of (9.4 ± 0.1) nm), the second at $q = (1.70 \pm 0.1)$ nm^{-1} (d-spacing = (3.7 ± 0.1) nm). Since the second-order peaks are visible for both correlations at $2 \times q_i$, we are in the presence of two coexisting lamellar phases. Above 10 °C, only the swollen phase is visible, at $q = (0.7 \pm 0.1)$ nm^{-1} (d-spacing = (9.4 ± 0.1) nm). The gel−fluid phase transition of the C10 mix, occurring at $T = 10$ °C (DSC thermogram of Figure 4), can explain the slight decrease (~0.5 nm) in the d-spacing of the swollen phase from 7 to 30 °C as a thinning of the bilayer upon melting (Figure 8, right). Remarkably, the d-spacing decrease in $\Delta d = (0.42 \pm 0.03)$ nm from 7 to 20 °C is in extremely good agreement with the decrease in hydrophobic bilayer thickness (Δb_H) as calculated from the NMR spectral simulations, $\Delta b_H = (0.44 \pm 0.11)$ (Supporting Information). Approaching the second phase change (above 50−60 °C), the membrane phase undergoes a fast swelling (now due to the water layer thickening between membranes) seen as a shift of the correlation toward lower q until disappearance. This effect was observed in the literature and referred to as an unbinding transition.[29,37] Both the C10 mix curves at the highest temperature $T = 78$ °C and after cooling back to $T = 20$ °C fit extremely well with a bilayer form factor, with an ~q^{-2} decay (Figure 9 and Table S5, Supporting Information). This decay is much different from the one that would be observed in the case of elongated cylindrical micelles, with an ~1 nm radius (plotted as a gray dashed line in Figure 9). These results indicate that the high-temperature structure of the C10 mix samples is still a unilamellar membrane. Interestingly, the two fitting results differ slightly in the bilayer thicknesses (1.8 nm at 85 °C and 2.1 nm at 20 °C, uncertainty 0.1 nm) and their polydispersity (0.27 at 85 °C and 0.15 at 20 °C).

These are in line with the consideration that the molten amphiphiles' chains allow a wider range of bent/kinked configurations at higher temperatures. Most importantly, no scaling factor is required to fit the two curves, which means that no amphiphile solubilization or disaggregation happens while the temperature is increased unlike with the pure capric acid where progressive solubilization takes place (Figure 7).

The experimental results lead toward a high-temperature, alcohol-triggered phase transition occurring above $T = 60$ °C that leads to bigger structures still possessing a bilayer (Figure 9), which are oriented upon application of a magnetic field (Figure 5). Furthermore, the alcohol addition stabilizes the membrane by preventing a temperature-induced vesicle dissolution into micelles.

Our data confirm that the decanol addition has a marked stabilizing effect on the membrane at ambient temperature. In addition, we found additional measurable differences in the amphiphile behavior that complement the previous findings,[7,18] such as

- a marked increase in the vesicle amount at the expense of micelles (Figures 2 and 3 and Table 1) and
- a higher propensity to form bigger and multilamellar vesicles (Figure 3).

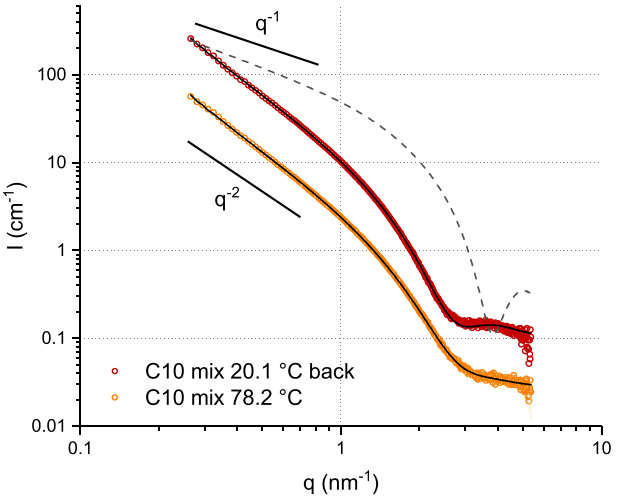

Figure 9. Fitting to the SANS curves obtained on D16 for the C10 mix at 78.2 °C and cooled back to 20.1 °C, each with a bilayer model. The error bars are displayed every five data points for clarity. The black dashed line shows the model of a system of elongated micelles with a 1.0 nm radius and 100 nm length. The black straight lines show the q^{-1} and q^{-2} decay behaviors. Models considering vesicles or hollow cylinders, with core radius $R > 20$ nm, could fit equally well the data in this q region.

Apel and co-workers[7] interpreted the stabilizing effect of the alcohol, for the vesicle self-aggregation at ambient temperature, in terms of hydrogen bonding. In particular, they measured quantitatively that the aggregates of ionic FAs−alcohols (giving vesicles) are thermodynamically more favorable than the FA hydrogen bonds with water that induce micelle formation or favor monomers in solution. This interpretation can explain our observed increase in the vesicle population at the expense of the micelles. However, this does not explain the higher propensity to form bigger and even multilamellar structures. Our data imply that the alcohol must also affect considerably the amphiphile-packing parameter.[38] Supposing the intrinsic geometry of the ionic FA as conic (because of the electrostatic repulsion of the anionic headgroups), the hydrogen bond with a neutral FA molecule leads to a geometry that is approaching the cylindrical one and therefore can allow for the formation of flat or low curvature aggregates like vesicles. Nevertheless, it is the ionic FA−alcohol aggregates that lead most effectively to a cylindrical intrinsic geometry so that planar structures are more easily formed and much bigger multilamellar vesicles can be produced.

It is in the thermal behavior that the two systems, differing by the presence of the alcohol, show the most remarkable distinctions, and some of them are found in the low temperature region. As shown in Figure 6, we observe for the capric acid at $T < 16$ °C a single lamellar phase with a d-spacing = (3.4 ± 0.1) nm at a much lower value than that expected for the membrane correlation in an MLV. On the other hand, at $T < 11$ °C, the C10 mix shows a coexistence of such a collapsed phase (with slightly different d-spacing = (3.7 ± 0.1) nm) with the expected MLV

https://dx.doi.org/10.1021/acs.langmuir.0c02258
Langmuir 2020, 36, 13516−13526

swollen phase (d-spacing = (9.4 ± 0.1) nm). We interpret the occurrence of the collapsed phase as the probable crossing of the corresponding FA Krafft temperature (Figure S6, Supporting Information), known as the temperature below which the surfactant solubility is below its critical micelle concentration (CMC), causing flocculation. Therefore, the observed transition at a low temperature of the capric acid (with its effect visible in the data in Figures 4−6) is due to the flocculation/solubilization (as monomers or assembled into small vesicles/micelles) rather than to a gel−fluid membrane transition. The coexistence observed in Figure 6 (right) indicates that the decanol has the effect of partially preventing flocculation so that an MLV phase is still present with the amphiphiles in the gel phase so to give a thicker membrane (lowest temperatures in Figure 8 right). Upon chain melting at $T \geq 10$ °C, the d-spacing decreases slightly (≤0.5 nm) due to a decrease in the bilayer thickness when crossing the gel−fluid transition, as also observed in ref 17. From $T = 30$ °C, the solvent-induced swelling becomes more important, and d-spacing starts to increase.

Most importantly in this study, the mixture containing decanol undergoes a high-temperature phase transition, not observed in the pure FA system, which leads to much bigger (Figure 4), orientable (Figure 5), yet still bilayer (Figure 9) structures. High temperatures also have the effect of causing an unbinding transition of the MLV swollen phase ($T \approx 65-70$ °C) that leads to unilamellar membranes (Figures 6 and 9) only observed in the case of the C10 mix.

The peculiar oriented-like spectral shapes observed with NMR at 80 and 50 °C (Figure 5) have already been observed for bilayer micelles (bicelles) when the system is under the form of small lipidic discs that align as a nematic phase in the magnetic field.[39−41] It has been also observed for the model and natural membranes (MLVs) that are deformed by magnetic fields.[42,43] This happens when the elastic energy maintaining the vesicles with an average spherical shape is lower than the magnetic energy.[43] In such a situation, the vesicle is deformed as a prolate ellipsoid along the magnetic field direction, the elastic modulus of the membrane being orders of magnitude lower than that of classical plasma membranes, which are not affected by magnetic fields. Because vesicles are being detected with neutrons, we favor the latter explanation. As pointed out by the work of Dazzoni et al.,[43] the extent of the huge deformation observed here (long axis/short axis ratio ≈ 8−10, see Supporting Information) is directly proportional to the vesicle size. Therefore, the observed high-temperature transition that leads to bigger structures has likely favored the occurrence of such deformation. Nevertheless, the membrane packing of the C10 mix vesicles is also stable at the highest measured temperature (Figure S4, Supporting Information).

Taken together, these results point toward the appearance of large, unilamellar vesicles at $T \geq 60$ °C formed by fusion of the vesicles existing at a low temperature. This interpretation is supported by the observed vesicle mean size increase (Figure 4), the MLV unbinding to give unilamellar vesicles (Figure 6, right), and the decrease in the small (< 100 nm) vesicle fraction until complete disappearance (Figure 5, right and Figure S5, Supp. Info). The second high-temperature broad transition observed in the DSC thermogram of the C10 mix (Figure 4) is therefore a result of such a fusion process rather than a shift of the equilibrium between vesicles and micelles as previously reported.[18]

We note that the occurrence of this high-temperature conformational transition has probably been observed with its effect in previous studies, although not directly identified: (i) Jordan and co-workers,[14] by studying a different system made with mixtures of C10−C15 FA/alcohols at strongly alkaline pH, high salt concentrations (NaCl, $MgCl_2$, $CaCl_2$), and high temperature $T = 70$ °C with confocal microscopy, observed in several cases the occurrence of big elongated structures, where "the filaments appeared to be composed of chains of individual vesicles". Although on different systems and in non-equilibrium conditions (the sample stage was not heated during measurements), their observation could be the effect of the high-temperature transition described here. Although we observed oriented structures with ssNMR at a high temperature, which could be because of an elongated shape of the bilayer structures, we could not conclude whether the orientation or also the deformation itself was triggered by the static magnetic field of the spectrometer. For this reason, we refer to the high-temperature products as large unilamellar vesicles with a not necessarily spherical mean shape that is not the focus of the present study. (ii) Mansy and Szostak[16] examined a mixture of capric acid/decanol in a 2:1 ratio by measuring the vesicle capability to retain encapsulated oligonucleotides as a function of temperature. They observed the occurrence of material leakage above 50−60 °C. In view of our results, we can argue that the observed leakage may not be due simply to a sudden increase in the protomembrane permeability but a consequence of the morphological changes happening above that temperature threshold: the conformational transition and, perhaps more importantly in this case, the unbinding transition of the bilamellar vesicle fraction (probably present as the experimental buffer/pH/extrusion size conditions were the same as in our study). From this perspective, the actual permeability of the model protomembrane may still be sufficiently low even at higher temperatures, thus additional studies are required to address this point taking into account the MLV unbinding transition and the vesicle fusion processes that we identified.

The occurrence of this transition at $T \geq 60$ °C could appear as unfavorable in terms of the C10 mix stability at the highest temperatures, the focus of our study given the implications for the origin of life. The pure FA vesicles, although less stable at room temperature, would not undergo the high-T transition and hence appear more thermostable after all. Nevertheless, our results (Figure 7) show that the temperature increase induces a partial vesicle disassembling in the pure capric acid that leads to a higher amount of micelles. Conversely, in the C10 mix, no vesicle-to-micelle transition is observed, and the bilayer structuring (probed by SANS) and packing (probed by NMR) are preserved at the highest temperatures. Therefore, rather than protomembrane disruption, solubilization, or micellar aggregation, the high temperature triggers the fusion of the small vesicles assembling in favor of large unilamellar bilayered structures.

■ CONCLUSIONS

In summary, we found that the addition of same-length fatty alcohol to a short-chain C10 fatty acid suspension in an equimolar ratio leads to several substantial effects. It improves the vesicles' stability at room temperature at the expense of the other amphiphile states (micelles and free monomers). It partially prevents the vesicles from undergoing flocculation at temperatures lower than the expected Krafft point of the fatty acid. Most importantly, it triggers a high-temperature conformational change at $T \geq 60$ °C that leads to vesicle fusion with stable membranes at temperatures as high as 80 °C, the highest

https://dx.doi.org/10.1021/acs.langmuir.0c02258
Langmuir 2020, 36, 13516−13526

investigated in this study. On one hand, this sets a warning on the interpretation of the results from all experiments of this kind (i.e., whether what is observed correlates with the occurrence of such phase transition at high temperature). In addition, as a perspective relevant to the origin of life, it sets the basis for further studies: namely, whether such a transition could serve as a prebiotic mean of solute exchange between different vesicles. This would set a milestone in our understanding of processes related to the origin of life.

■ ASSOCIATED CONTENT

Supporting Information

The Supporting Information is available free of charge at https://pubs.acs.org/doi/10.1021/acs.langmuir.0c02258.

Equations for the SANS model form factors, preliminary sample screening data, full list of parameters used for fits/simulations, and annexes (PDF)

■ AUTHOR INFORMATION

Corresponding Author

Bruno Demé − *Institut Laue - Langevin, 38042 Grenoble, France;* orcid.org/0000-0002-9523-7662; Email: deme@ill.fr

Authors

Loreto Misuraca − *Univ. Grenoble Alpes, CNRS, LIPhy, 38000 Grenoble, France; Institut Laue - Langevin, 38042 Grenoble, France;* orcid.org/0000-0002-2259-7050

Antonino Caliò − *Institut Laue - Langevin, 38042 Grenoble, France; INSA Lyon, Université de Lyon, CNRS, UMR5240 Villeurbanne, France*

Isabelle Grillo − *Institut Laue - Langevin, 38042 Grenoble, France*

Axelle Grélard − *Univ. Bordeaux, CNRS, IECB, 33607 Pessac, France*

Philippe Marie Oger − *INSA Lyon, Université de Lyon, CNRS, UMR5240 Villeurbanne, France;* orcid.org/0000-0001-6298-6870

Judith Peters − *Univ. Grenoble Alpes, CNRS, LIPhy, 38000 Grenoble, France; Institut Laue - Langevin, 38042 Grenoble, France;* orcid.org/0000-0001-5151-7710

Complete contact information is available at: https://pubs.acs.org/10.1021/acs.langmuir.0c02258

Notes

The authors declare no competing financial interest.

■ ACKNOWLEDGMENTS

This work was funded by the French National Research Agency program ANR 17-CE11-0012-01 to P.O. and J.P. We benefited from the facilities and expertise of the Biophysical and Structural Chemistry platform (BPCS) at "Institut Européen de Chimie et Biologie" (IECB), CNRS UMS3033, Inserm US001, Bordeaux University (http://www.iecb.ubordeaux.fr/index.php/fr/plateformestechnologiques). L.M. is supported by a scholarship from the Institut Laue-Langevin (ILL) PhD program. The authors thank ILL for neutron beamtime on D33 (DOI: 10.5291/ILL-DATA.9-13-788) and D16 (DOI: 10.5291/ILL-DATA.TEST-3108). The ILL Partnership for Soft Condensed Matter (PSCM) is acknowledged for the access to the DSC and DLS platforms and for lab infrastructures. This work benefited from the SasView software, originally developed by the DANSE project under NSF award DMR-0520547 (http://www.sasview.org/). L.M. is grateful to Jean Paul Douliez and Sylvain Prevost for fruitful discussions and Erick Dufourc for valuable feedbacks.

■ DEDICATION

This article is dedicated to the memory of our colleague at the Institut Laue-Langevin, Dr Isabelle Grillo (1973−2019).

■ REFERENCES

(1) Joyce, G. F.; Szostak, J. W. Protocells and RNA Self-Replication. *Cold Spring Harbor Perspect. Biol.* **2018**, *10*, a034801.

(2) Segré, D.; Ben-Eli, D.; Deamer, D. W.; Lancet, D. The Lipid World. *Orig. Life Evol. Biosphys.* **2001**, *31*, 119−145.

(3) Fiore, M.; Strazewski, P. Prebiotic Lipidic Amphiphiles and Condensing Agents on the Early Earth. *Life* **2016**, *6*, 17.

(4) McCollom, T. M.; Ritter, G.; Simoneit, B. R. T. Lipid Synthesis under Hydrothermal Conditions by Fischer-Tropsch-Type Reactions. *Orig. Life Evol. Biosphys.* **1999**, *29*, 153−166.

(5) Monnard, P.-A.; Deamer, D. W. Preparation of Vesicles from Nonphospholipid Amphiphiles. In *Methods in enzymology*; Elsevier: 2003, Vol. *372*, pp. 133−151.

(6) Budin, I.; Prywes, N.; Zhang, N.; Szostak, J. W. Chain-Length Heterogeneity Allows for the Assembly of Fatty Acid Vesicles in Dilute Solutions. *Biophys. J.* **2014**, *107*, 1582−1590.

(7) Apel, C. L.; Deamer, D. W.; Mautner, M. N. Self-Assembled Vesicles of Monocarboxylic Acids and Alcohols: Conditions for Stability and for the Encapsulation of Biopolymers. *Biochim. Biophys. Acta* **2002**, *1559*, 1−9.

(8) Morigaki, K.; Walde, P. Fatty Acid Vesicles. *Curr. Opin. Colloid Interface Sci.* **2007**, *12*, 75−80.

(9) Hargreaves, W. R.; Deamer, D. W. Liposomes from Ionic, Single-Chain Amphiphiles. *Biochemistry* **1978**, *17*, 3759−3768.

(10) Haines, T. H. Anionic Lipid Headgroups as a Proton-Conducting Pathway along the Surface of Membranes: A Hypothesis. *Proc. Natl. Acad. Sci.* **1983**, *80*, 160−164.

(11) Maurer, S. E.; Tølbøl Sørensen, K.; Iqbal, Z.; Nicholas, J.; Quirion, K.; Gioia, M.; Monnard, P.-A.; Hanczyc, M. M. Vesicle Self-Assembly of Monoalkyl Amphiphiles under the Effects of High Ionic Strength, Extreme PH, and High Temperature Environments. *Langmuir* **2018**, *34*, 15560−15568.

(12) Deamer, D. The Role of Lipid Membranes in Life's Origin. *Life* **2017**, *7*, 5.

(13) Chen, I. A.; Salehi-Ashtiani, K.; Szostak, J. W. RNA Catalysis in Model Protocell Vesicles. *J. Am. Chem. Soc.* **2005**, *127*, 13213−13219.

(14) Jordan, S. F.; Rammu, H.; Zheludev, I. N.; Hartley, A. M.; Maréchal, A.; Lane, N. Promotion of Protocell Self-Assembly from Mixed Amphiphiles at the Origin of Life. *Nat. Ecol. Evol.* **2019**, *3*, 1705−1714.

(15) Cornell, C. E.; Black, R. A.; Xue, M.; Litz, H. E.; Ramsay, A.; Gordon, M.; Mileant, A.; Cohen, Z. R.; Williams, J. A.; Lee, K. K.; Drobny, G. P.; Keller, S. L. Prebiotic Amino Acids Bind to and Stabilize Prebiotic Fatty Acid Membranes. *Proc. Natl. Acad. Sci.* **2019**, *116*, 17239−17244.

(16) Mansy, S. S.; Szostak, J. W. Thermostability of Model Protocell Membranes. *Proc. Natl. Acad. Sci.* **2008**, *105*, 13351−13355.

(17) Douliez, J.-P.; Houssou, B. H.; Fameau, A.-L.; Navailles, L.; Nallet, F.; Grélard, A.; Dufourc, E. J.; Gaillard, C. Self-Assembly of Bilayer Vesicles Made of Saturated Long Chain Fatty Acids. *Langmuir* **2016**, *32*, 401−410.

(18) Kapoor, S.; Berghaus, M.; Suladze, S.; Prumbaum, D.; Grobelny, S.; Degen, P.; Raunser, S.; Winter, R. Prebiotic Cell Membranes That Survive Extreme Environmental Pressure Conditions. *Angew. Chemie* **2014**, *126*, 8537−8541.

(19) Guinier, A.; Fournet, G.; Yudowitch, K. L. *Small-Angle Scattering of X-Rays*; 1955.

(20) Frisken, B. J. Revisiting the Method of Cumulants for the Analysis of Dynamic Light-Scattering Data. *Appl. Opt.* **2001**, *40*, 4087−4091.

https://dx.doi.org/10.1021/acs.langmuir.0c02258
Langmuir 2020, 36, 13516−13526

(21) Davis, J. H.; Jeffrey, K. R.; Bloom, M.; Valic, M. I.; Higgs, T. P. Quadrupolar Echo Deuteron Magnetic Resonance Spectroscopy in Ordered Hydrocarbon Chains. *ACS Symposium Series* **1976**, *34*, 70−77.
(22) Dewhurst, C. D.; Grillo, I.; Honecker, D.; Bonnaud, M.; Jacques, M.; Amrouni, C.; Perillo-Marcone, A.; Manzin, G.; Cubitt, R. The Small-Angle Neutron Scattering Instrument D33 at the Institut Laue−Langevin. *J. Appl. Crystallogr.* **2016**, *49*, 1−14.
(23) Hanczyc, M. M.; Fujikawa, S. M.; Szostak, J. W. Experimental Models of Primitive Cellular Compartments: Encapsulation, Growth, and Division. *Science* **2003**, *302*, 618−622.
(24) Chen, I. A.; Szostak, J. W. A Kinetic Study of the Growth of Fatty Acid Vesicles. *Biophys. J.* **2004**, *87*, 988−998.
(25) Cape, J. L.; Monnard, P.-A.; Boncella, J. M. Prebiotically Relevant Mixed Fatty Acid Vesicles Support Anionic Solute Encapsulation and Photochemically Catalyzed Trans-Membrane Charge Transport. *Chem. Sci.* **2011**, *2*, 661−671.
(26) Janiak, M. J.; Small, D. M.; Shipley, G. G. Nature of the Thermal Pretransition of Synthetic Phospholipids: Dimyristoyl-and Dipalmitoyllecithin. *Biochemistry* **1976**, *15*, 4575−4580.
(27) Nagle, J. F.; Tristram-Nagle, S. Structure of Lipid Bilayers. *Biochim. Biophys. Acta* **2000**, *1469*, 159−195.
(28) Pabst, G.; Rappolt, M.; Amenitsch, H.; Laggner, P. Structural Information from Multilamellar Liposomes at Full Hydration: Full q-Range Fitting with High Quality x-Ray Data. *Phys. Rev. E* **2000**, *62*, 4000.
(29) Demé, B.; Dubois, M.; Gulik-Krzywicki, T.; Zemb, T. Giant Collective Fluctuations of Charged Membranes at the Lamellar-to-Vesicle Unbinding Transition. 1. Characterization of a New Lipid Morphology by SANS, SAXS, and Electron Microscopy. *Langmuir* **2002**, *18*, 997−1004.
(30) Seelig, J. Deuterium Magnetic Resonance: Theory and Application to Lipid Membranes. *Q. Rev. Biophys.* **1977**, *10*, 353−418.
(31) Davis, J. H. The Description of Membrane Lipid Conformation, Order and Dynamics by 2H-NMR. *Biochim. Biophys. Acta* **1983**, *737*, 117−171.
(32) Dufourc, E. J.; Mayer, C.; Stohrer, J.; Althoff, G.; Kothe, G. Dynamics of Phosphate Head Groups in Biomembranes. Comprehensive Analysis Using Phosphorus-31 Nuclear Magnetic Resonance Lineshape and Relaxation Time Measurements. *Biophys. J.* **1992**, *61*, 42−57.
(33) Douliez, J. P.; Bellocq, A. M.; Dufourc, E. J. Effect of Vesicle Size, Polydispersity and Multilayering on Solid State ^{31}P-and ^{2}H-NMR Spectra. *J. Chim. Phys.* **1994**, *91*, 874−880.
(34) Nallet, F.; Laversanne, R.; Roux, D. Modelling X-Ray or Neutron Scattering Spectra of Lyotropic Lamellar Phases: Interplay between Form and Structure Factors. *J. Phys. II* **1993**, *3*, 487−502.
(35) Tyler, A. I. I.; Law, R. V.; Seddon, J. M. *Methods in Membrane Lipids*; Owen, D. M., Ed.; Springer: 2015.
(36) Pedersen, J. S. Analysis of Small-Angle Scattering Data from Colloids and Polymer Solutions: Modeling and Least-Squares Fitting. *Adv. Colloid Interface Sci.* **1997**, *70*, 171−210.
(37) Mutz, M.; Helfrich, W. Unbinding Transition of a Biological Model Membrane. *Phys. Rev. Lett.* **1989**, *62*, 2881.
(38) Israelachvili, J. N.; Mitchell, D. J.; Ninham, B. W. Theory of Self-Assembly of Hydrocarbon Amphiphiles into Micelles and Bilayers. *J. Chem. Soc. Faraday Trans. 2 Mol. Chem. Phys.* **1976**, *72*, 1525−1568.
(39) Raffard, G.; Steinbruckner, S.; Arnold, A.; Davis, J. H.; Dufourc, E. J. Temperature− Composition Diagram of Dimyristoylphosphatidylcholine− Dicaproylphosphatidylcholine "Bicelles" Self-Orienting in the Magnetic Field. A Solid State ^{2}H and ^{31}P NMR Study. *Langmuir* **2000**, *16*, 7655−7662.
(40) Aussenac, F.; Laguerre, M.; Schmitter, J.-M.; Dufourc, E. J. Detailed Structure and Dynamics of Bicelle Phospholipids Using Selectively Deuterated and Perdeuterated Labels. ^{2}H NMR and Molecular Mechanics Study. *Langmuir* **2003**, *19*, 10468−10479.
(41) Loudet-Courreges, C.; Nallet, F.; Dufourc, E. J.; Oda, R. Unprecedented Observation of Days-Long Remnant Orientation of Phospholipid Bicelles: A Small-Angle X-Ray Scattering and Theoretical Study. *Langmuir* **2011**, *27*, 9122−9130.
(42) Pott, T.; Dufourc, E. J. Action of Melittin on the DPPC-Cholesterol Liquid-Ordered Phase: A Solid State ^{2}H-and ^{31}P-NMR Study. *Biophys. J.* **1995**, *68*, 965−977.
(43) Dazzoni, R.; Grélard, A.; Morvan, E.; Bouter, A.; Applebee, C. J.; Loquet, A.; Larijani, B.; Dufourc, E. J. The Unprecedented Membrane Deformation of the Human Nuclear Envelope, in a Magnetic Field, Indicates Formation of Nuclear Membrane Invaginations. *Sci. Rep.* **2020**, *10*, 5147.

https://dx.doi.org/10.1021/acs.langmuir.0c02258
Langmuir 2020, 36, 13516−13526

High Temperature Behaviour of Early Life Membrane Models

Loreto Misuraca[a,b], Antonino Caliò[b,c], Isabelle Grillo[b], Axelle Grélard[d], Philippe Marie Oger[c], Judith Peters[a,b], Bruno Demé[b,*]

[a] Univ. Grenoble Alpes, CNRS, LIPhy, 38000 Grenoble, France

[b] Institut Laue - Langevin, F-38042 Grenoble Cedex 9, France

[c] INSA Lyon, Université de Lyon, CNRS, UMR5240, Villeurbanne, France

[d] Univ. Bordeaux, CNRS, IECB, 33607 Pessac, France

Supplementary Information

Materials and methods

Form factor models used for SANS data analysis

The following form factors models were used for the fittings (and summed with each other when needed):

1. Unilamellar vesicle [1]

$$P(q) = scale\frac{\Phi}{V_{shell}}\left[\frac{3V_{core}(\rho_{solvent}-\rho_{shell})j_1(qR_{core})}{qR_{core}} + \frac{3V_{tot}(\rho_{shell}-\rho_{solvent})j_1(qR_{tot})}{qR_{tot}}\right]^2 + C \quad (5)$$

with Φ the shell volume fraction, V the volumes of the core of shell or the overall vesicle (V_{tot}), R the radii, ρ the neutron scattering length densities of solvent and shell, $j_1(x) = (sinx - cosx)/x^2$ the spherical Bessel function, C the flat background level.

The fitting parameters are therefore the following:
- Φ: determined from the sample preparation and always fixed;
- scale: as the curves are in absolute scale, if all sample having volume fraction Φ contributes to the vesicle form factor, then scale = 1;
- background;
- $\rho_{solvent}$: calculated from $\rho = \frac{\Sigma_{i=1}^{N} b_i}{V}$ and using tabulated values for the neutron coherent scattering lengths b_i of the atoms in the solvent (buffer and D_2O), always fixed for the fittings;
- ρ_{shell}: same as for $\rho_{solvent}$, calculated from the sample molecules and always fixed;

- R_{core};
- bilayer thickness = $R_{tot} - R_{core}$;
- radius polidispersity, assuming a Shultz distribution;
- thickness polidispersity, assuming a Gaussian distribution.

2. Multilayer vesicle (used for bilamellar vesicle populations)

$$P(q) = scale\frac{\Phi(\rho_{shell} - \rho_{solvent})}{V_{shell}}\sum_{i=1}^{N}\left[\frac{3V(r_i)\sin(qr_i) - qr_i\cos(qr_i)}{(qr_i)^3} - \frac{3V(R_i)\sin(qR_i) - qR_i\cos(qR_i)}{(qR_i)^3}\right]^2 + C \quad (6)$$

with r_i the solvent radius before shell I, R_i the shell radius for shell i. The fitting parameters are analogous as in the unilamellar vesicle model, except that it is normalised for the vesicle volume fraction (core + shell) and for the additional parameters:
- solvent thickness = r_i - R_{i-1};
- N: number of shells, fixed to 2 for the bilamellar vesicles.

3. Sphere [1] (used for micelle populations)

$$P(q) = \frac{scale}{V}\left[\frac{3V(\rho_{solvent} - \rho_{sphere})(sin(qr) - qrcos(qr))}{(qr)^3}\right]^2 + C \quad (7)$$

used to model spheres with uniform neutron scattering length density ρ_{sphere}, radius r and volume V. Free fitting parameters:
- scale: sphere (micelle) volume fraction;
- r : sphere radius.

Vesicle stability at ambient temperature

Figure S1 shows the SLS data obtained for the Capric acid and C10 mix samples, respectively, presented as Guinier plots log(I) vs. q^2. The expected linear behaviour according to Eq. (2), assuming monodisperse scatterers, is observed for the Capric Acid only at the highest measured concentration and pH 7.8; conversely, the C10 mix curves are well described by the Guinier approximation over the whole measured q range, with the only exception of the lowest concentration 20 mM. This is an indication that the alcohol addition broadens extensively the vesicle domain (in pH and amphiphile concentration), in agreement with the previous observations [2,3].

For the cases where the Guinier approximation was satisfied, we found for the gyration radii the values R_g = (45.1 ± 0.6) nm for the Capric acid 80 mM and R_g = (46.7 ± 0.9) nm for the C10 mix 80 mM.

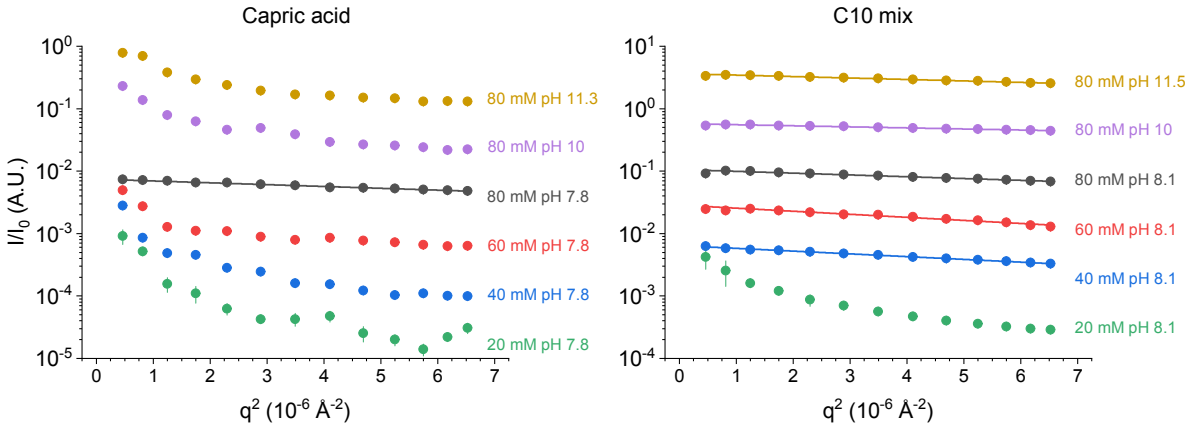

Figure S1. Static light scattering intensities, at different concentrations and pH. Left: Capric acid. Right: C10 mix. The y scales refer to the curves at 80 mM and pH 7.8 and 8.1, respectively, while all the other curves are shifted for clarity. The solid lines are linear fits performed in all the cases where the Guinier approximation was satisfied.

We verified whether there was an effect of the concentration and pH in the C10 mix R_g values. We found the following values:

- 80 mM: (46.7 ± 0.9) nm,

- 60 mM: (58.9 ± 0.8) nm,

- 40 mM: (55.2 ± 1.0) nm,

- pH 10 80 mM: (34.6 ± 0.4) nm,

- pH 11.5 80 mM: (41.0 ± 0.4) nm.

Although small, these results show possible dependencies of the C10 mix R_g with the sample concentration and pH. Nevertheless, the concentration of 80 mM was the only one where a satisfactory Guinier regime could be detected with the Capric acid (as pointed out in Figure S1, see also how the Capric acid data at 80 mM have a factor 10 less intensity). This motivated our use of the concentration 80 mM for full consistency between the two samples.

Additional detail about the vesicle stability at 25 °C is provided by the DLS measurements. DLS at the highest measurable angle 150° permits to see a possible indication of micelle presence as traces in the case of the pure Capric acid samples at high pH or low concentrations. In fact, assuming two populations of different sizes moving by Brownian diffusion, each decay constant $\Gamma_{vesicle}$ and $\Gamma_{micelle}$ (one per population) will follow the law $\Gamma = D\,q^2$. For this reason, going to the highest possible q value will allow $\Gamma_{vesicle}$ and $\Gamma_{micelle}$ to be most different as possible, hence easier to be disentangled.

As presented in the main article, the Capric acid data at high pH requires the use of a two-population fitting function, while this is not the case for the C10 mix, where a single population is always sufficient. Figure S2 shows the correlation functions and relative fits for pH 8, where the large majority of vesicles allows both samples to be fitted with a single population.

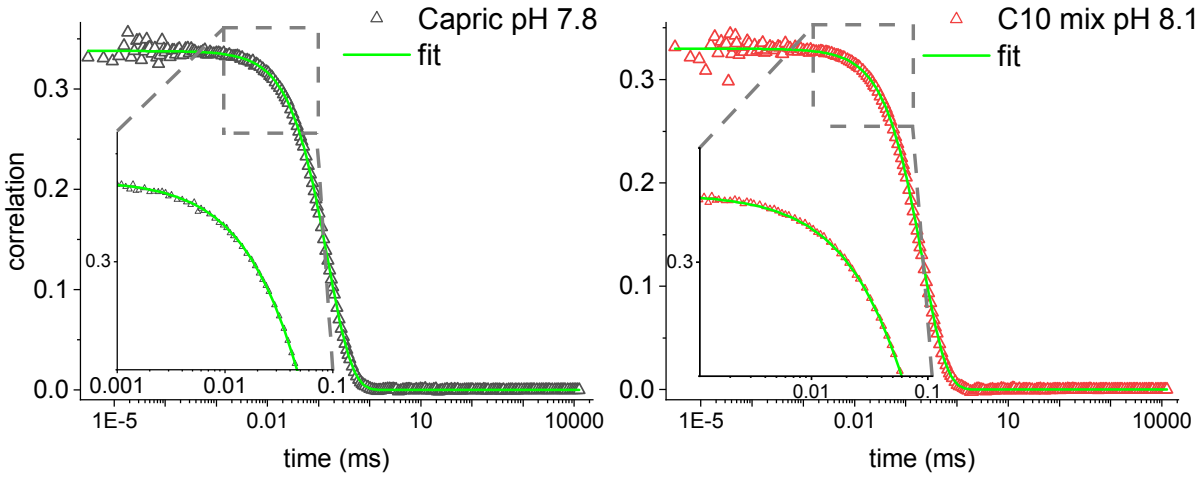

Figure S2. Dynamic light scattering correlation curves taken at the highest scattering angle 150°, at high pH 7.8 and 8.1 respectively, and corresponding zooms on the short correlation times. Left: Capric acid; right: C10 mix. The solid lines are fits to the data as described in the "Experimental" section.

By using the Stokes-Einstein relation (Eq. 3) to determine the corresponding hydrodynamic radii R_h, we find the following values: (43.4 ± 0.4) nm for the Capric acid and (60.7 ± 0.6) nm for the C10 mix.

SANS experiments at 25 °C (Figure 3 in the main text) allowed ensuring that the observed "particles" observed with SLS-DLS were actually bilayered vesicles (hollow spheres). The curve of Capric acid sample was fitted with a Unilamellar Vesicle model. Conversely, the C10 mix sample was fitted with a Unilamellar vesicle model and a fraction of bilamellar vesicles. The full set of parameters (fixed and free) are shown Table S1. As the extremely low errors for the parameters did not take into account parameter correlations, an uncertainty of 0.1 nm = 1 Å was considered everywhere in the text. For the same reasons, the computed X^2 should be considered as relative estimation of the fit quality.

Table S1: Parameters from fitting of the SANS curves at ambient temperature.

	Capric acid	**C10 mix**	
q range (Å^{-1})	0.0013 – 0.56	0.0013 – 0.56	
scale	0.34 ± 0.01	1 (fixed)	
	ULV	ULV	BLV
population fraction	1 (fixed)	0.60 ± 0.01	0.40 (bound to ULV fraction: 1-0.60)
*sample scattering length density (SLD) (*10^{-6} Å^{-2})*	0.22 (fixed)	-0.04 (fixed)	-0.04 (fixed)
*solvent SLD (*10^{-6} Å^{-2})*	6.24 (fixed)	6.24 (fixed)	6.24 (fixed)
shell volume fraction	0.0158 (fixed)	0.0155 (fixed)	
vesicle volume fraction			0.0599 (fixed)
core radius (Å)	280 ± 1	383 ± 1	92 ± 1
shell thickness (Å)	18 ± 1	20 ± 1	20 (bound to ULV thickness)
solvent thickness (Å)			118 ± 0.2
radius polidispersity (PD)	0.35 ± 0.01	0.18 ± 0.01	0.62 ± 0.02
solvent thickness PD			0.29 ± 0.01
X^2/Npts	38.5	50.1	

Thermal stability

NMR Spectral simulations and order parameters

Wide-line solid-state NMR spectra were simulated by calculation in the time domain (as free induction decays) and then Fourier transformed. Individual components are built from experimental estimates of quadrupolar splittings ($\Delta\nu_Q^k$) and individual line-widths (line-width is considered constant throughout the pattern). Small variations are allowed to match with sharp experimental features on spectra. An example of simulation performed is shown in Figure S3 and Table S2. For Capric acid containing a perdeuterated chain, weights for individual C-$^2H_2$ or C-$^2H_3$ depend on the number of deuterons per

labelled carbon position; the individual time dependent signals are then added accordingly leading after Fourier transformation to the multicomponent powder pattern spectrum. Such a simulation leads to individual quadrupolar splittings, $\Delta\nu_Q^k$, for labelled carbon positions, k, and subsequently to S_{CD} order parameters in bilayer membranes [4]: $S_{CD}^k = 4\Delta\nu_Q^k/3A_Q$, where A_Q is the static coupling constant of 167 kHz [5]. Order Parameters can be used to calculate the average length of a hydrocarbon chain [6] (Table S3).

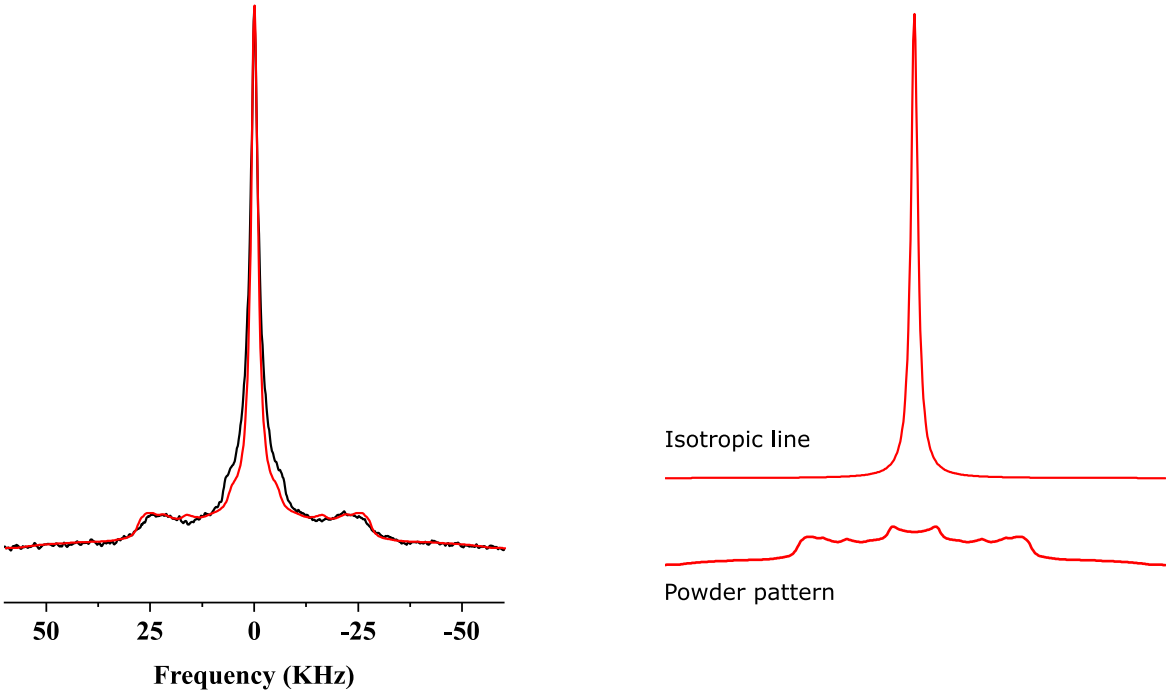

Figure S3. Left: Experimental ^{2}H-NMR spectrum of the $^2H_{19}$-Capric acid:decanol (1:1) dispersion at 0°C (black solid line) and its simulated counterpart (red solid line). Right: simulated isotropic and powder pattern contributions with corresponding proportions.

Liposome deformation leading to non-spherical distributions of bilayer normals with respect to the magnetic field was taken into account by introducing in the simulation the ellipsoidal orientation dependence, $p(\theta) \sim \frac{sin^2\theta}{sin^2\theta + \frac{c}{a}cos^2\theta}$, where θ is the orientation of bilayer normal with respect to the magnetic field direction and c and a the ellipsoid axes [7,8].

Table S2. Parameters necessary for the simulation as in Figure S3.

Powder pattern					Isotropic line		
Labelled Carbon Position	**Quadrupolar Splitting (KHz)**	**Lorentzian Line width (Hz)**	**Number of deuteron**	**Proportion (%)**	**Quadrupolar Splitting (KHz)**	**Lorentzian Line width (Hz)**	**Proportion (%)**
2	55.5	2000	2	60 ± 5	0	2000	40 ± 5
3	55.5	2000	2				
4	55.5	2000	2				

5	52.5	2000	2				
6	52.5	2000	2				
7	49	2000	2				
8	44.5	2000	2				
9	33.5	2000	2				
10	11.5	2000	3				
c/a	1						

The isotropic line is simulated with the same program with no quadrupolar splitting. The total spectrum is obtained by adding isotropic line and powder pattern in appropriate proportions in order to match the experimental spectrum. The simulation program for wide line spectra has been developed in FORTRAN code by E. Dufourc and implemented in a user-friendly graphical interface (Microsoft .NET) for Windows platforms by A. Grélard. This procedure has been applied to the acquired data and results are summarized in Table S3.

Table S3. Order parameters, $^{2}H_{19}$-capric acid average chain length and prolate ellipsoid long-to-short axes ratio.

System	**$^{2}H_{19}$-Capric acid**	**$^{2}H_{19}$-Capric acid:Decanol (1:1 molar)**			
Temperature	0°C	0°C	20°C	80°C	50°C return
Labelled Carbon Position, k	**$^{a}S_{CD}$**				
2	-0.27	-0.44	-0.26	-0.098	-0.148
3	-0.27	-0.44	-0.26	-0.098	-0.148
4	-0.27	-0.43	-0.23	-0.098	-0.148
5	-0.26	-0.42	-0.23	-0.095	-0.142
6	-0.26	-0.40	-0.17	-0.093	-0.140
7	-0.25	-0.37	-0.11	-0.082	-0.132
8	-0.22	-0.25*	-0.08	-0.070	-0.114
9	-0.17	-0.19*	-0.05	-0.053	-0.088
10	-0.06	-0.09	-0.02	-0.016	-0.028
$^{b}S_{mol}$	1.0	1.0	0.7	0.7	0.7
$^{c}L_{chain}$ (nm)	0.93	1.05	0.83	0.70	0.72

[d]c/a	1.0	1.0	1.0	10.0	8.0

[a]Obtained from spectral simulations as described above and calculated from splittings for orientations of bilayer normals at 90° to the magnetic field, using the equation $S_{CD}^{k} = 4\Delta\nu_{Q}^{k}/3A_{Q}$. Assignment was performed by assuming a monotonous distribution of ordering along the chain for fatty acid dispersions [9,10]. Some positions could not be separated. Accuracy varies from 0.5% to 5 % for patterns of very low intensity observed at 0°C and 20°C. *Simulation very difficult for positions 7-10 due to the presence of a huge isotropic line, accuracy estimated to 50%.

[b]The molecular order parameter, S_{mol}, was taken = 1.0 for low temperatures and = 0.7 for ambient and high temperatures [6,11]

[c]L_{chain} was calculated from [6,11], accuracy ± 0.04 nm.

[d]Ellipsoid long-to-short axes ratio from [7].

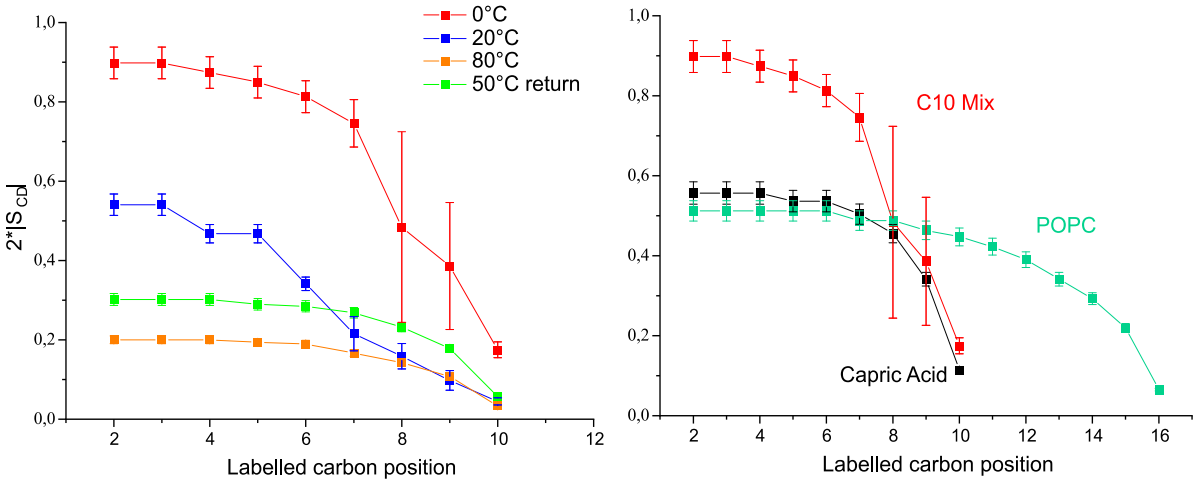

Figure S4. S_{CD} order parameter profiles for various systems. A) $^{2}H_{19}$-Capric acid:decanol (C10 mix with perdeuterated Capric acid) dispersion as a function of labelled carbon positions and temperature. $2|S_{CD}|$ is plotted to express ordering along the axis of motional averaging of the membrane, the bilayer normal. $2|S_{CD}| = 1$ means complete ordering (i.e. no time and space fluctuations of C-D bond) whereas $2|S_{CD}| = 0$ indicates complete disordering, as in liquids. B) Comparison of profiles near 0 °C (0 °C for Capric acid and C10 Mix and POPC membranes at 2 °C) [12]. Lines serve as eye guides only.

Figure S4 (right plot) demonstrates that the order parameter profiles are very similar for Capric acid, C10mix and POPC (a model phospholipid membrane), near 0°C, *i.e.*, a plateau of order parameters near the interface and a stepped decrease on going towards the bilayer center, characteristic of chain packing observed in biomembranes [6,11,13].

The fraction of isotropic signal has a very different behaviour for the Capric acid and the C10 mix systems (Figure S5). In the former, there is ≈ 70% of isotropic line at 0 °C, which increases to 100% at 20 and 80 °C. The ≈ 70% percentage is recovered when the sample is cooled down to 0 °C, indicating complete reversibility of the process.

The C10 mix shows instead an increase of the isotropic line until a maximum of 60% at 50 °C and is almost absent for 80 °C where the oriented-like pattern (bilayer normal perpendicular to the magnetic field) appears. Returning to 50 °C shows the same but wider oriented-like pattern, and the isotropic line is still absent. Returning further to 0 °C shows a superimposition of powder pattern and isotropic lines

with, however, a lower proportion. These data clearly indicate a hysteresis related to the thermal history of the sample suggesting intense thermally induced sample reorganization.

Perhaps more interestingly, the C10 mix data show that the conformational transition occurring at T ≥ 60 °C as shown in the main text, leads to a complete disappearance of all the species contributing to the isotropic line (monomers, micelles, small vesicles of size ≤ 100 nm). All the small structures fused together to form the observed large ellipsoidal vesicles.

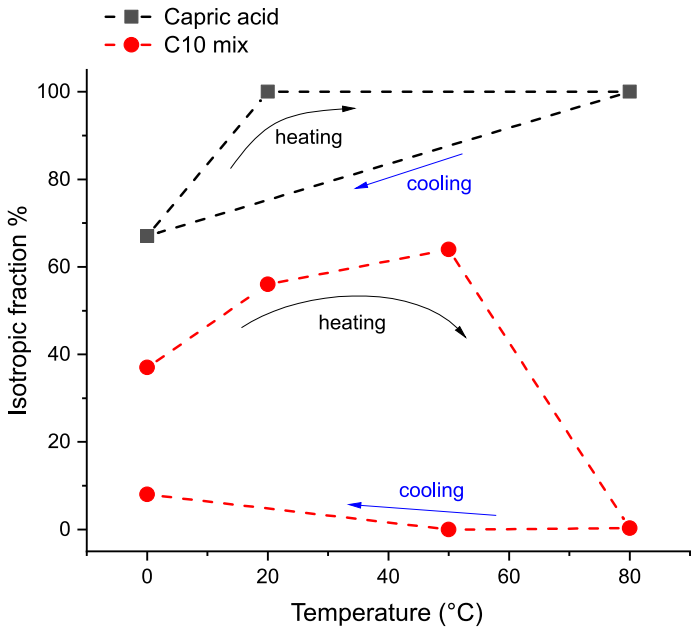

Figure S5. Isotropic fraction of the two samples as a function of the temperature, accuracy ± 5%.

Fitting of SANS data

Regarding the SANS experiments as function of temperature, the MLV d-spacing was calculated by fitting a Gaussian function with a linear background in the surrounding of the 1st correlation. We note that the resulting C10 mix MLV d-spacing = (9.4 ± 0.1) nm is significantly lower then what is found by fitting the data of the bilamellar vesicles (11.8 nm solvent thickness + 2.0 nm bilayer thickness = 13.8 nm, Table 1 in the main text). This is likely due to the much higher concentration used in the thermal stability measurements (350 mM instead of 80 mM, SANS and ssNMR vs temperature). Nevertheless, the comparison is possible with the DLS and DSC data (Figure 4) and it is visible how the main features of the thermal behaviour are reproduced in both concentrations: the first transition at 10 °C and the second one above 60 °C. For the Capric acid curves at T ≥ 16 °C (where no correlations were observed) the data were fitted with a sum of Unilamellar vesicle and a Sphere form factors (the latter accounting for micelle presence). The full list of fitting parameters is shown in Table S4.

On the other hand, the C10 mix curves at 85 °C and 20 °C, both taken after the unbinding transition occurred, were fitted with a Unilamellar vesicle form factor. We note that, considering the accessible q range of the instrument used in this experiment ($2.6 * 10^{-1} < q < 5.3$ nm^{-1}), no information can be obtained about the size and shape of the vesicles, but only about the lamellar phase and partitioning (i.e. the fraction of sample contributing to the lamellar phase). Table S5 shows the results.

Table S4. a) Fitted parameters for capric acid at 350 mM SANS data as function of temperature, acquired in the range ($2.6 * 10^{-1} < q < 5.3$) nm^{-1}; b) Parameters fixed during the fits.

a)

Fitted parameters

Sample	Micelle fraction	Vesicle fraction	Micelle radius	X^2/Npt
15 °C	0.09	0.86	13	22.7
20 °C	0.09	0.85	13	18.9
25 °C	0.09	0.85	13	19.0
30 °C	0.08	0.85	13	20.0
35 °C	0.08	0.85	12	22.4
40 °C	0.10	0.83	10	23.8
45 °C	0.14	0.78	9	26.1
55 °C	0.25	0.67	8	27.5
65 °C	0.35	0.55	8	25.4
75 °C	0.45	0.43	7	21.9
85 °C	0.57	0.27	7	31.2
20 °C (back)	0.10	0.76	13	27.7

b)

Fixed parameters

total scale	1
solvent SLD (*10^{-6} Å^{-2})	6.24
sample SLD (*10^{-6} Å^{-2})	0.22
vesicle shell thickness (Å)	18

vesicle core radius (Å)	250
vesicle shell volume fraction	0.069
micelle radius polidispersity	1

Table S5. SANS fitting parameters of C10 mix sample at 85 °C and after cooling back to 20 °C, respectively.

	C10 mix 85 °C	**C10 mix 20 °C back**
scale	1.03 ± 0.01	1.05 ± 0.01
sample SLD (× 10^{-6} Å-2)	-0.04 (fixed)	-0.04 (fixed)
solvent SLD (× 10^{-6} $Å^{-2}$)	6.24 (fixed)	6.24 (fixed)
shell volume fraction	0.068 (fixed)	0.068 (fixed)
core radius (Å)	227 ± 1	231 ± 1
shell thickness (Å)	18 ± 1	21 ± 1
thickness PD	0.27 ± 0.01	0.15 ± 0.01

Figure S6 plots the known Krafft temperatures of FAs with chain lengths from 12 to 18 carbons in presence of Na^+ as counterion, as found from the literature [14,15], and the possible extrapolation to the chain length C = 10 assuming a linearity. The Krafft temperature of the Capric acid would be 5 °C < T < 15 °C, consistently with the appearance of the collapsed phase in the SANS data at 7 and 11 °C (Figure 6 in the text).

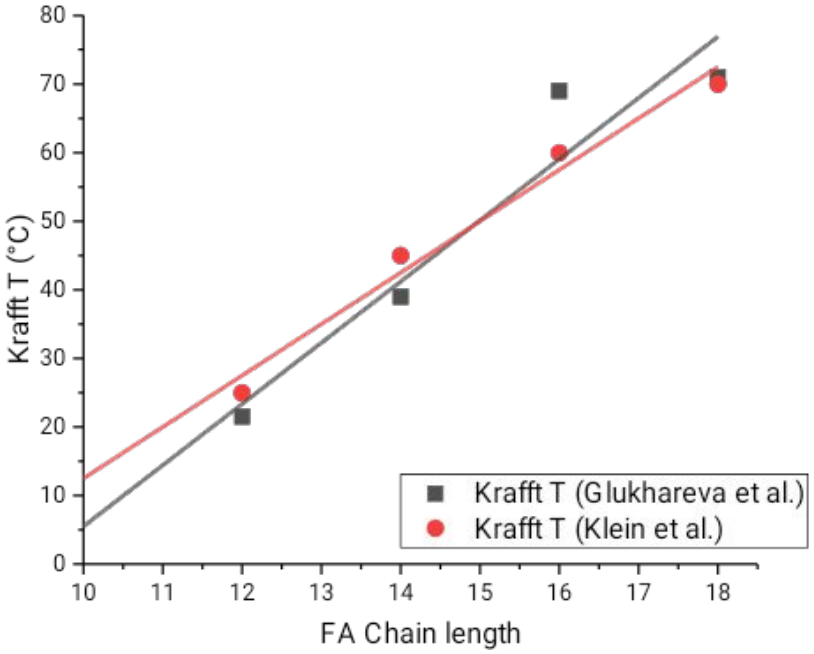

Figure S6. Krafft temperatures according to Klein et al. [14] and Glukhareva et al.[15] for FA chain lengths from 12 to 18 Carbons. The lines are linear fits to each dataset, showing the extrapolated values for the 10 Carbon length (the Capric Acid).

Supp. Info. References

(1) Guinier, A.; Fournet, G.; Yudowitch, K. L. Small-Angle Scattering of X-Rays. **1955**.

(2) Apel, C. L.; Deamer, D. W.; Mautner, M. N. Self-Assembled Vesicles of Monocarboxylic Acids and Alcohols: Conditions for Stability and for the Encapsulation of Biopolymers. *Biochim. Biophys. Acta (BBA)-Biomembranes* **2002**, *1559* (1), 1–9.

(3) Kapoor, S.; Berghaus, M.; Suladze, S.; Prumbaum, D.; Grobelny, S.; Degen, P.; Raunser, S.; Winter, R. Prebiotic Cell Membranes That Survive Extreme Environmental Pressure Conditions. *Angew. Chemie* **2014**, *126* (32), 8537–8541.

(4) Davis, J. H. The Description of Membrane Lipid Conformation, Order and Dynamics by 2H-NMR. *Biochim. Biophys. Acta (BBA)-Reviews Biomembr.* **1983**, *737* (1), 117–171.

(5) Burnett, L. J.; Muller, B. H. Deuteron Quadrupole Coupling Constants in Three Solid Deuterated Paraffin Hydrocarbons: C2D6, C4D10, C6D14. *J. Chem. Phys.* **1971**, *55* (12), 5829–5831.

(6) Douliez, J.-P.; Léonard, A.; Dufourc, E. J. Conformational Order of DMPC Sn-1 versus Sn-2 Chains and Membrane Thickness: An Approach to Molecular Protrusion by Solid State 2H-NMR and Neutron Diffraction. *J. Phys. Chem.* **1996**, *100* (47), 18450–18457. https://doi.org/10.1021/jp961220v.

(7) Pott, T.; Dufourc, E. J. Action of Melittin on the DPPC-Cholesterol Liquid-Ordered Phase: A Solid State 2H-and 31P-NMR Study. *Biophys. J.* **1995**, *68* (3), 965–977. https://doi.org/10.1016/S0006-3495(95)80272-9.

(8) Helfrich, W. Lipid Bilayer Spheres: Deformation and Birefringence in Magnetic Fields. *Phys. Lett. A* **1973**, *43* (5), 409–410. https://doi.org/https://doi.org/10.1016/0375-9601(73)90396-4.

(9) Davis, J. H.; Jeffrey, K. R. The Temperature Dependence of Chain Disorder in Potassium Palmitate-Water. A Deuterium NMR Study. *Chem. Phys. Lipids* **1977**, *20* (2), 87–104. https://doi.org/https://doi.org/10.1016/0009-3084(77)90083-4.

(10) Otten, D.; Beyer, K. Chain Length Mismatch and Packing Constraints of Free Fatty Acids in a Hexagonal Detergent Host Phase. A Wide Line Deuterium NMR Study. *Chem. Phys. Lipids* **1995**, *77* (2), 203–215. https://doi.org/https://doi.org/10.1016/0009-3084(95)02472-U.

(11) Douliez, J. P.; Léonard, A.; Dufourc, E. J. Restatement of Order Parameters in Biomembranes: Calculation of C-C Bond Order Parameters from C-D Quadrupolar Splittings. *Biophys. J.* **1995**, *68* (5), 1727–1739. https://doi.org/10.1016/S0006-3495(95)80350-4.

(12) Herrera, F. E.; Sevrain, C. M.; Jaffrès, P.-A.; Couthon, H.; Grélard, A.; Dufourc, E. J.; Chantôme, A.; Potier-Cartereau, M.; Vandier, C.; Bouchet, A. M. Singular Interaction between an Antimetastatic Agent and the Lipid Bilayer: The Ohmline Case. *ACS omega* **2017**, *2* (10), 6361–6370. https://doi.org/10.1021/acsomega.7b00936.

(13) Douliez, J.-P.; Ferrarini, A.; Dufourc, E.-J. On the Relationship between C-C and C-D Order Parameters and Its Use for Studying the Conformation of Lipid Acyl Chains in Biomembranes. *J. Chem. Phys.* **1998**, *109* (6), 2513–2518. https://doi.org/10.1063/1.476823.

(14) Klein Regina A4 - Touraud, Didier A4 - Kunz, Werner, R. A.-K. Choline Carboxylate Surfactants: Biocompatible and Highly Soluble in Water. *Green Chem.* **2008**, *v. 10* (4), 433-435–2008 v.10 no.4. https://doi.org/10.1039/b718466b.

(15) Glukhareva, N. A.; Pletnev, M. Y. SOLUBILITY AND KRAFFT POINTS OF BINARY-MIXTURES OF INDIVIDUAL SOAPS WITH SODIUM ACYLYSE ETHIONATES. *Colloid J. Russ. Acad. Sci.* **1993**, *55* (4), 530–534.

3.2 ALKANE EFFECTS AND POSITIONING

3.2.1 Article 2: Alkanes increase the stability of early life membrane models under extreme pressure and temperature conditions

3.2.1.1 *Foreword*

Having defined the important role and consequences of the presence of decanol in mixture with decanoic acid, the next studies were devoted to explore the effects of the alkanes in the model membrane. The first of the three works, that were realized on this effect, explored the combined effect of temperature and hydrostatic pressure in the lamellar arrangement and amphiphile chain dynamics of MLV systems.

The alkanes are found to decrease significantly the mean repeat distance (d-spacing) of the MLV assemblies at all temperatures, perhaps because they affect the collective dynamics of each shell (that is influenced by the thermal energy) so that the membrane repulsion is lowered. Squalane showed the largest effect. The d-spacing of the alkane-lacking sample is also significantly affected by the pressure, which is not found in the samples containing the alkanes.

The internal membrane chain dynamics (probed in sub-nanosecond scale and expressed in terms of hydrogen MSD) is also modified by the alkane (eicosane) presence. This is especially visible at the highest measured temperature (T = 85 °C), where the average hydrogen dynamics is kept at significantly lower values by the eicosane. Furthermore, the pressure dependence of the model lacking the alkanes (already observed in the structural data) is also observed in the dynamics, as well as the absence of pressure dependence in the sample with eicosane.

In this work, I designed the experiments and wrote the proposals to obtain neutron beamtime on IN13 and syncrothron beamtime on I22 (Diamond Light Source, UK). I prepared the samples, performed the experiments on IN13 and I22, analyzed the results and wrote the paper.

The paper has been published in *Communications Chemistry (Nature)* (*111*).

communications chemistry

ARTICLE

https://doi.org/10.1038/s42004-021-00467-5 OPEN

Alkanes increase the stability of early life membrane models under extreme pressure and temperature conditions

Loreto Misuraca [1,2], Bruno Demé[2], Philippe Oger[3] & Judith Peters [1,2]✉

Terrestrial life appeared on our planet within a time window of [4.4–3.5] billion years ago. During that time, it is suggested that the first proto-cellular forms developed in the surrounding of deep-sea hydrothermal vents, oceanic crust fractures that are still present nowadays. However, these environments are characterized by extreme temperature and pressure conditions that question the early membrane compartment's capability to endure a stable structural state. Recent studies proposed an adaptive strategy employed by present-day extremophiles: the use of apolar molecules as structural membrane components in order to tune the bilayer dynamic response when needed. Here we extend this hypothesis on early life protomembrane models, using linear and branched alkanes as apolar stabilizing molecules of prebiotic relevance. The structural ordering and chain dynamics of these systems have been investigated as a function of temperature and pressure. We found that both types of alkanes studied, even the simplest linear ones, impact highly the multilamellar vesicle ordering and chain dynamics. Our data show that alkane-enriched membranes have a lower multilamellar vesicle swelling induced by the temperature increase and are significantly less affected by pressure variation as compared to alkane-free samples, suggesting a possible survival strategy for the first living forms.

[1] Univ. Grenoble Alpes, CNRS, LIPhy, Grenoble, France. [2] Institut Laue - Langevin, Grenoble, France. [3] Univ Lyon, INSA Lyon, CNRS UMR5240, Villeurbanne, France. ✉email: jpeters@ill.fr

Over the last decades there has been a growing interest in the field of the origin of life[1–4]. A number of strategies were employed to explore its key aspects, e.g., the proto-cellular compartmentalisation[5,6] or the first genetic code self-replication[7–10], sometimes resulting in contradictory conclusions. The compartmentalisation of cells, in particular, has been the focus of a large number of studies[11–16], because of the essentiality of the cellular boundary to maintain the order in living matter. These studies set the basis of the so-called "lipid world"[5,6,17], in which the formation of lipid material and the self-assembly into vesicles are considered as key phenomena that led to the appearance of life. Simple short-chain molecules with amphiphilic behaviour, e.g., fatty acids and fatty alcohols, are considered the most probable candidates as protomembrane building blocks. The rationale for this lies in the anticipated Fisher–Tropsch-driven prebiotic chemistry which likely formed such molecules[18,19], while the synthesis of phospholipid-like amphiphiles would have required a much more complex chemical pathway[20].

In terms of chemical and physical environment, there is a general consensus that life on Earth required important sources of energy and thus potentially originated under extreme conditions: some of the most accepted scenarios are the oceanic hydrothermal vents[21,22] and the terrestrial hot springs[23,24]. Both alternatives include very high temperatures (up to 100 °C) and, for deep-sea hydrothermal vents, also high hydrostatic pressures (HHP) (up to 800 bar). It is therefore crucial to include these environmental constraints when studying possible protomembrane architectures.

The effects of high pressure on the proto-cell biochemistry have been studied extensively[25]. Several recent reviews have collected detailed information on the response of lipid assemblies to HHP (bilayer thickness increase, changes in curvature, phase transitions, interdigitation)[26,27].

The role of HHP in modifying membrane characteristics, and the possible adaptive strategies to counteract it, have been particularly investigated in the field of extremophiles[28–30]. Piezophiles, i.e. organisms which optimal growth occurs under HHP conditions, have shown the capability to tune their membrane composition in response to pressure and temperature changes of the environment[28], a process called homeoviscous adaptation. Cario et al.[28] also observed that such environmental stimuli affect the amount of non-polar isoprenoid lipids (lycopene derivatives) synthesised by the extremophiles, suggesting a structural role of such molecules in the membrane structure. Similar apolar molecules (squalane) have been proven to promote a lipid phase separation[31] in archaeal model bilayers as well as to trigger non-lamellar phase formation at high temperature and high pressure[32]. These studies show evidences of the impact of non-polar molecules on the membrane's physico-chemical characteristics and response to extreme conditions.

However, most previous studies have been focussing on HHP effects on phospholipid or archaeal lipid membrane structure and dynamics, while little is known about the more prebiotically relevant (single-chain amphiphile based) membrane counterparts. Recently, Kapoor et al.[33] have performed pressure–temperature studies on vesicles prepared from a mixture of decanoic (capric) acid and decanol (1:1 and 2:1 molar ratio), which have much shorter chains of 10 carbon atoms length. They found that both pressure and temperature can be used to modulate the fluidity and conformational order of such protomembranes, and proved the existence of stable vesicles up to 75 °C (at 1 bar) and 2500 bar (at 25 °C).

In the present project, we performed a structural and dynamical study of multilamellar protomembrane vesicles as a function of both temperature and pressure independently, in the ranges $20 < T < 85$ °C and $1 < p < 1000$ bar. The maximum values of both variables are the conditions expected in the proximity of the hot vents. The assemblies used were decanoic acid:decanol mixtures (1:1 mol/mol), similar to the ones studied by Kapoor et al.[33], hereafter called C10 mix, which appear to be the most promising in terms of vesicle stability[34], in the presence of the apolar molecule eicosane, the linear 20-Carbon alkane (2 mol% of C10 mix), or squalane, similar length branched 30-Carbon alkane following the hypotheses of Cario et al.[28]. The differences in the membrane physico-chemical response have been measured and compared in order to gather new evidences on the effect of alkane insertion as a suitable adaptive response to extreme environmental conditions (Fig. 1).

We found that the presence of the alkanes in the membrane has a highly significant effect on the equilibrium inter-membrane spacing of the multilamellar vesicles (MLVs), a sign of its likely role in dampening membrane fluctuations at all temperatures. Squalane showed the most pronounced influence on the MLV

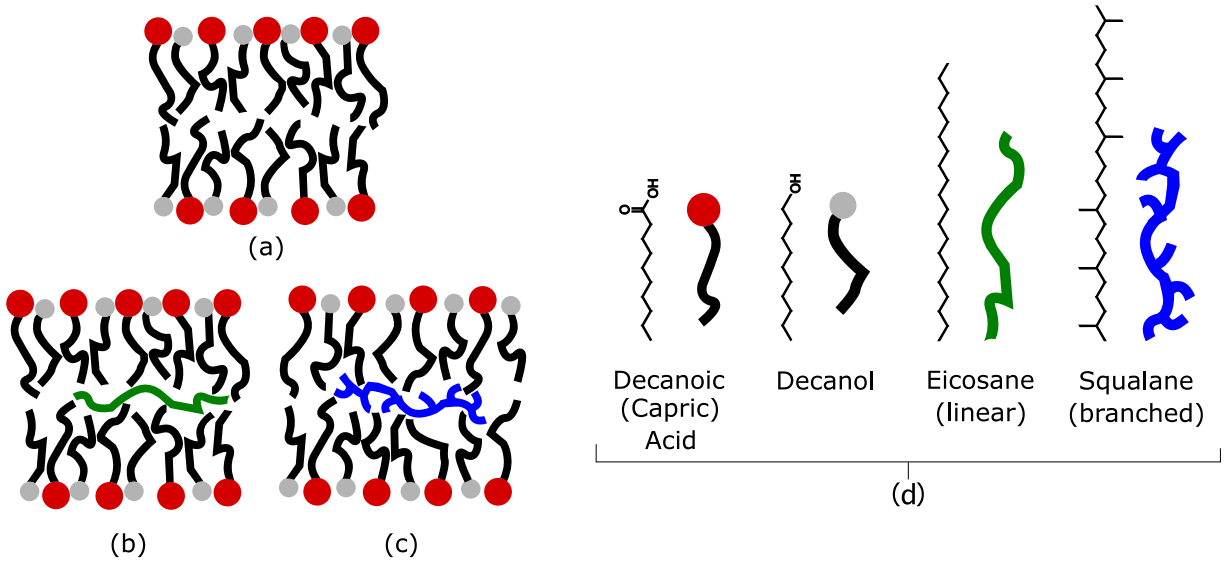

Fig. 1 Protomembrane models. Sketch of the three protomembrane models investigated in this study. **a** C10 mix; **b** C10 mix + 2% eicosane; and **c** C10 mix + 2% squalane. **d** Molecular structure and name of each compound used.

COMMUNICATIONS CHEMISTRY | https://doi.org/10.1038/s42004-021-00467-5 ARTICLE

membrane arrangement. We observed a clear effect of both temperature and pressure in modulating the equilibrium MLV structure in the C10 mix sample, while both alkanes make the membrane less sensitive to pressure. Furthermore, the results of the dynamical study are in line with what we found for the structure modifications of the C10 mix with and without the eicosane. The average hydrogen dynamics of the membrane tails is significantly affected by temperature and pressure only when the alkane (eicosane) is not included in the sample. Upon alkane insertion, the mean hydrogen dynamics is lowered at all p–T investigated, and it does not vary significantly even at the maximum measured values of $T = 85$ °C and $p = 800$ bar.

Our results show that apolar molecules, even simple prebiotically relevant linear alkanes as eicosane, have a clear impact in modifying membrane characteristics and response to the environment. These findings shed light on a possible strategy of survival that could have helped the first living forms to cope with harsh environmental conditions while lacking the modern complex molecular tools, unavailable at the origin of life.

Results and discussion

Effects on membrane structuring. We first studied the dependence of the MLV repeat distance (d-spacing) as a function of temperature and pressure in order to obtain information on the structural equilibrium rearrangements that are induced by the environment. Figure 2 shows an example of small-angle X-ray scattering (SAXS) curves obtained for the sample C10 mix + 2% squalane at ambient pressure (1 bar) at different temperatures. At the lowest temperature $T = 5$ °C, two features are visible: a sharp peak centred at $q \simeq 0.17$ Å^{-1} (corresponding to a d-spacing of ≈37 Å) and a broader, swollen correlation peak centred at $q \simeq 0.09$ Å^{-1} (corresponding to a d-spacing of ≈70 Å). Details about the pressure dependence of the two coexisting phases at $T = 5$ °C can be found in the Supplementary Information (Supplementary Note 1 and Supplementary Figs. 1–4).

We note that very similar correlations were observed in our previous work on C10 mix MLVs (there in absence of alkanes) measured with small-angle neutron scattering (SANS) ($d \approx 37$ and 94 Å, respectively)[34], and where imputed to the existence of a swollen and a collapsed lamellar phases. The latter has been interpreted as coming from a flocculated fraction of the sample which melts above the decanoic acid Krafft temperature (observed at $T \approx 10$ °C)[34]. The Krafft temperature denotes the temperature below which the surfactant solubility (in this case, the decanoic acid) is lower than the critical micelle concentration, so that no micelles or vesicles can form anymore and flocculation occurs. Therefore, at $T = 5$ °C we are in the presence of a two-phase system: one is the MLV phase, with weakly interacting bilayers that leads to the broad correlation observed at lower q (swollen phase); the other one, which can be thought as made of microscopically phase separated aggregates, that gives a sharp correlation in the scattering curve at higher q (collapsed phase).

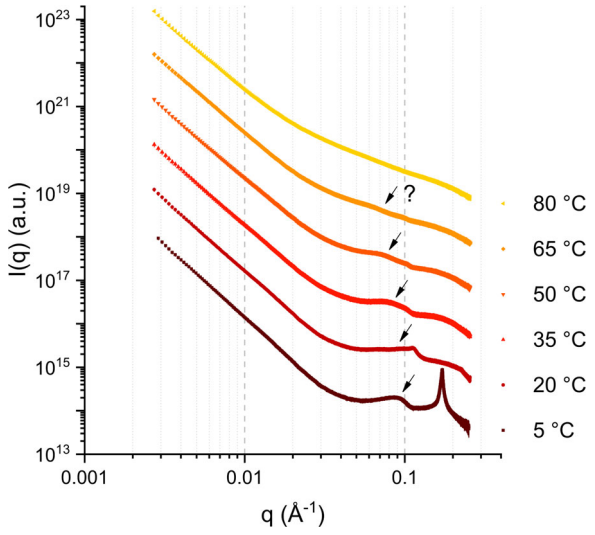

Fig. 2 Example of SAXS curves. SAXS curves obtained for the sample C10 mix + 2% squalane at $p = 1$ bar. The errors are calculated by propagating the errors of the 30 averaged frames (which come from Poisson distribution). Most of the error bars are smaller than the symbol size. All curves were vertically shifted for clarity.

The curve at $T = 20$ °C (Fig. 2) captures an intermediate state where the melting of the collapsed phase is almost completed. At $T = 35$ °C, one main correlation is observed at $q \simeq 0.08$ Å^{-1} (the second order can be detected at $q \simeq 0.16$ Å^{-1} although weak). At $T = 50$ °C, the correlation is further shifted to lower q and broadened, hardly detectable by visual inspection. At $T = 65$ °C one can only guess the position from the trend at low temperature, and finally at $T = 80$ °C the correlation is completely lost. This behaviour, with the position of the correlation shifting to lower q until disappearing, is expected for MLVs that undergo swelling upon temperature increasing, until unbinding[35,36]. In our analysis, we calculated the d-spacing of the three samples at $T \leq 50$ °C only.

The data from the C10 mix sample at $T = 20$ °C and $p = 10$ bar show a swollen, broad phase centred at $q \simeq 0.05$ Å^{-1} (d-spacing ≈ 122 Å) together with a small, thin correlation at $q \simeq 0.08$ Å^{-1} (d-spacing ≈ 75 Å) (Supplementary Fig. 4). The details and the interpretation of such coexistence, observed at all temperatures for this sample, can be found in the Supplementary Information (Supplementary Note 1). In the following, we focussed our investigation on the correlations related to the most swollen phases, characteristics of the fluid and weekly interacting membranes.

All curves for each p–T point were fitted in order to find the average d-spacings, as discussed in the "Methods" section. The results are plotted in Fig. 3 for the three samples measured. The sample containing squalane at 20 °C is missing, because the still ongoing melting of the collapsed phase did not allow a reliable fit of the swollen phase correlation (as it can be inferred from Fig. 2).

A number of insights can be drawn from these results. First, there is a clear effect of the alkane presence in the equilibrium MLV d-spacing as a function of temperature. Both alkanes lower the d-spacing significantly, with the squalane leading to the most prominent shift. Second, there is also a clear effect of pressure on the C10 mix sample in lowering the d-spacing. This is likely to be a sign of the membrane fluid–gel transition, which has been observed to occur at 10 °C at ambient pressure[33,34]. Here the transition seems to happen from $p \simeq 300$ bar at $T = 20$ °C in agreement with Fourier-transform infrared (FTIR) measurements (Supplementary Note 3 and Supplementary Fig. 6). Assuming the linearity of the fluid–gel phase transition with p–T variation, this leads to a shift of ≈3 °C/100 bar. This value is similar with what has been observed with phospholipid membranes (≈2 °C/100 bar)[37]. Following this relationship, the phase transition of the C10 mix at $T = 35$ °C is expected at $p \approx$ 800 bar, although our data do not allow to conclude unambiguously. An analogous pressure effect is much less evident on the C10 mix with eicosane (only a possible shift might occur at $p \simeq$ 800 bar at $T = 20$ °C) and squalane, where the d-spacing is instead increasing slightly with pressure. Indeed, the synergistic effect of pressure and temperature can lead to both kinds of variations in d-spacing in relation with phase transitions, as previously shown for the phospholipid DMPC[38].

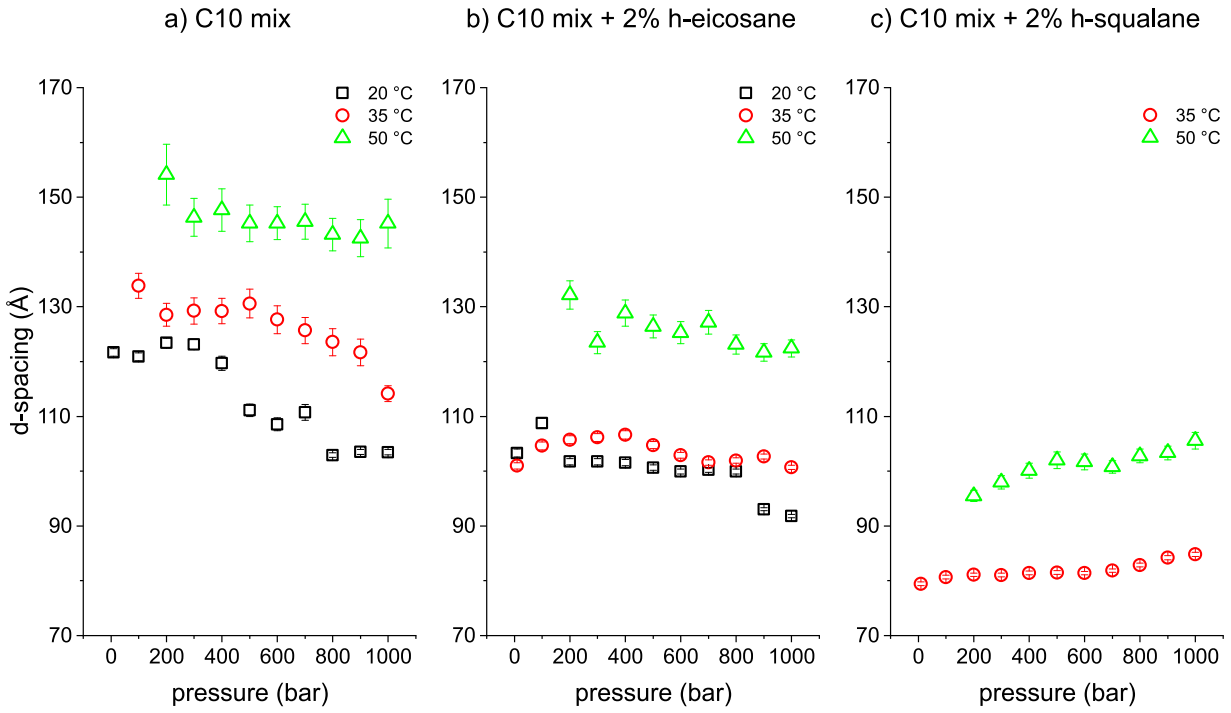

Fig. 3 *d*-spacing vs *p*–*T*. MLV *d*-spacing of the three measured samples at all *T*–*p* points where a lamellar correlation was fitted. **a** C10 mix; **b** C10 mix + 2% h-eicosane; and **c** C10 mix + 2% h-squalane. The errors are calculated by propagation of the fit parameter errors, as detailed in the main text.

Effects on membrane dynamics. The difference between samples missing or containing the alkanes was further investigated by studying the mean hydrogen dynamics of the amphiphile chains forming the membranes. The decanoic acid and decanol hydrophilic groups (R-COOH and R-OH, respectively), being partially ionised at the buffered pH conditions, will contribute with very few hydrogens and therefore we can neglect their contribution.

Elastic incoherent neutron scattering (EINS) experiments were performed on C10 mix with and without perdeuterated eicosane, as a function of temperature and pressure. The use of perdeuterated eicosane allowed ensuring that most of the incoherent scattering signal was coming from the amphiphiles in the membrane, the main object of our study.

The calculated mean square displacement (MSD) values (see the "Methods" section) are plotted in Fig. 4 as a function of the temperature and at the different pressure points. All MSD present very high values what is typical for lipidic motions[39].

The data show clear differences between the MSD of C10 mix with and without eicosane at almost all pressure and temperature values applied. The two samples start from similar MSD values at 25 °C and all pressure points. At the higher temperatures, eicosane keeps the hydrogen MSD to a lower value close to the one at $T = 25$ °C: this can be interpreted as the membrane maintaining a higher rigidity compared to the pure C10 mix one. Conversely, the C10 mix lacking the eicosane shows a more pronounced increase in dynamics upon temperature increase, with an effect that is inversely proportional to the applied pressure.

These results are in line with what has been shown in our SAXS data on C10 mix and C10 mix + 2% eicosane samples (Fig. 3). In fact, at high *d*-spacing, the dominating contribution responsible for the water layer thickness is mostly given by the membrane thermal fluctuations, while all short-range interactions are negligible at such membrane separations. A stiffer membrane, maintaining a lower MSD value as observed for the sample containing eicosane in Fig. 4, will therefore lead to a shrunken MLV and a smaller d-spacing (which is what is observed, see Fig. 3a, b).

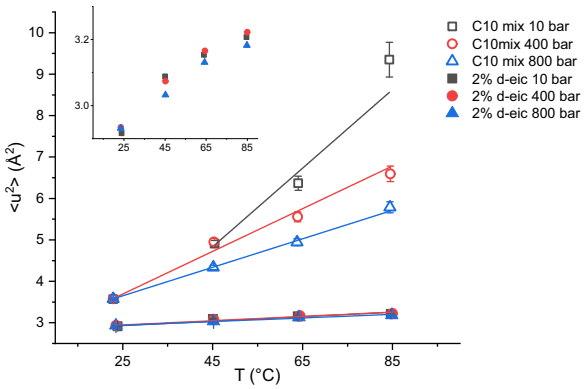

Fig. 4 Atomic mean square displacements. MSD for the two samples studied: C10 mix (empty symbols) and C10 mix with d-eicosane (full symbols). All lines are linear fits to the data. Note the clear dependence on temperature and pressure for the sample missing the eicosane, while all MSD values vary little at all *T*–*p* when the eicosane is added. The errors are calculated by propagation from I_{sum}, as detailed in the main text. Inset: vertical zoom of the C10 mix + 2% d-eicosane data.

Additional insights can be obtained by performing a simple linear fit to the MSD vs T data (solid lines shown in Fig. 4), in order to obtain qualitative information about the pseudo-force constant characteristic of the particular sample and pressure employed, in a similar fashion as described by Zaccai[40] for protein dynamics. In this representation, the slope of the line, namely $d\langle u^2\rangle/dT$, gives an estimation for the pseudo-force constant to be compared among the different samples and pressure points. Note that, as the data of C10 mix at $p = 10$ bar show an important but not linear increase in the dynamics, we performed a linear fit

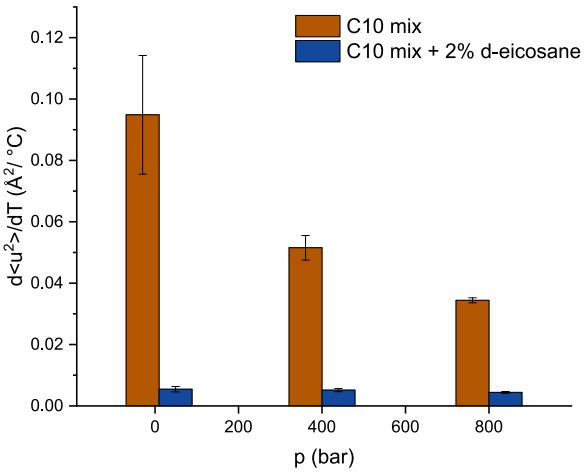

Fig. 5 Pseudo-force constants. Histogram comparing the derivative of the MSD data vs temperature assuming a simple linear model. Note that the value of C10 mix at $p = 10$ bar is a likely underestimation. Each value is shown with its error from the linear fit.

without including the $T = 25$ °C. Even with this strategy, the strong increase in the dynamics at $T = 85$ °C is higher than what is expected for a linear behaviour; therefore, the corresponding pseudo-force constant value must be considered as an underestimation. All the slopes are compared and depicted in Fig. 5.

This representation allows for a clear differentiation between the two systems: without eicosane, the du^2/dT is significantly affected by the applied pressure. Instead, the addition of the alkane causes the membrane to become almost pressure insensitive. This is in full agreement with what has been found from the structural study by SAXS on the sample with and without the eicosane (Fig. 3a, b). Note that the derivative du^2/dT is positive also on the eicosane including sample, which means that the temperature still causes an increase in the MSD in this sample, although of much lower extent as compared to the C10 mix (Fig. 5).

Taken together, these results show that the insertion of alkanes inside model protomembranes, composed of short-chain amphiphiles, has an important impact on the membrane structuring and dynamics. In particular, both alkanes investigated in the structural study (eicosane and squalane) lower the equilibrium d-spacing of the MLVs and cancel the effects that are due to the increase of hydrostatic pressure. Squalane leads to the biggest effect on the structural MLV characterisation, which could explain the findings of branched alkanes being used by modern Archaea[28] as one of the adaptive strategies when facing high-pressure environments. Moreover, the dynamical study proved that the eicosane decreases significantly the effects of HHP and high temperature on the motions of the acyl chains in the membrane.

The observed phenomenon, mediated by a small proportion of alkane molecules, could help explaining how the first living forms have survived the harsh thermodynamic constraints imposed when considering one of the most currently accepted scenarios for the origin of life (i.e. deep-sea hydrothermal vents). Such strategy, for pressure enduring and desensitisation, could also be used to readily explain how those systems could have afterwards migrated from high-pressure environments towards ambient pressure ones, leading to the biosphere as we know it nowadays.

Methods

Sample preparation. Sodium decanoate, 1-decanol, eicosane (hydrogenated and perdeuterated), squalane, bicine buffer and D_2O were purchased from Sigma Aldrich (Merck). All products were used as received from the manufacturer, with no further purification. The chemical and isotopic purity (CP–IP) of the used compounds are the following:

sodium decanoate: ≥98% CP;
1-decanol: ≥98% CP;
h-eicosane: 99% CP;
d-eicosane: 98% CP; 98% IP;
h-squalane: 96% CP;
d-squalane: 98% CP; 98% IP;
bicine: ≥99% CP.

The samples were prepared by first mixing the decanoic acid and the decanol (plus the eicosane/squalane, when needed) in bulk at the proper amount to obtain a 1:1 decanoic acid–decanol final molar ratio (plus 2% molar of the corresponding alkane). Samples were then dissolved in a $CHCl_3$ (Merck) solution to ensure complete mixing, followed by drying under a flux of nitrogen until no evaporation was observed. All samples were placed in a desiccator and left under vacuum overnight. The samples, checked gravimetrically at each step of the preparation, showed a loss of ≈5% that was imputed to a partial evaporation of the decanol[34].

The bicine buffer was prepared at a concentration of 0.2 M in H_2O for standard experiments, and in D_2O for the neutron scattering experiments. The D_2O buffer allowed to minimise the background due to the hydrogen incoherent neutron scattering. In all cases, the buffer was filtered with a 0.2-µm millipore membrane before use and titrated to pH/pD 8.5 with aliquots of NaOH/NaOD. When adjusting the pD of the D_2O solutions to 8.5, we used the formula $pD = pH^* + 0.4$ (ref. [41]), where pH* is the value measured by an H_2O-calibrated pH meter.

Previous work on decanoic acid:decanol systems[33] has shown that, unlike the vesicles made by decanoic acid that are heavily dependent on the solution pH, the ones consisting of the decanoic acid:decanol 1:1 mixture (which we named C10 mix) are stable in a wide pH range (pH 6–12). Furthermore, the temperature-dependent change in the pK_a of bicine buffer is rather low ($dpK_a/dT = -0.018$)[42]. We have chosen pH (or pD) 8.5 so that the minor changes in the buffer pK_a and solution pH given by the temperature increase do not affect the vesicle stability.

The dried organic solutions were suspended in the corresponding buffer for the neutron and X-ray experiments and vigorously vortexed for ≈1 min, leading to final milky solutions. The sample concentration for the X-ray scattering experiments was set to 350 mM, already employed in a previous work[34] on C10 mix MLVs. For neutron scattering experiments, the concentration used was 100 mg/ml corresponding to ≈570 mM in order to obtain a sufficient signal-to-noise ratio. For the complementary neutron scattering experiments, the samples were prepared at 80 mM concentration. The three model membranes measured were:

1. C10 mix
2. C10 mix + 2% (h/d) eicosane
3. C10 mix + 2% (h/d) squalane.

All samples were measured once at each p–T point.

Small-angle neutron scattering. SANS experiments were carried out at the ILL (Grenoble, France) using the D33 instrument[43]. Two detector distances (2 and 10 m) and an incoming beam of $\lambda = 5$ Å were used, corresponding to a range of momentum transfers $0.004 < q < 0.5$ Å^{-1}. The sample suspensions, of 200 µL each, were loaded in 1 mm quartz cells (Hellma, Germany) on a sample holder with thermal regulation. All data were corrected for the scattering of the sample container and the instrumental background. H_2O was measured for detector efficiency calculation and scaling to absolute units (cm^{-1}). A flat background was subtracted to account for the q-independent incoherent neutron scattering signal.

Small-angle X-ray scattering. SAXS experiments were performed on I22 at the Diamond Light Source (Didcot, UK)[44].

An automated high-pressure cell, adapted for SAXS experiments and available as sample environment on the I22 beamline, was used[45]. The samples were loaded into capillaries in 50 µl aliquots and sealed using a glued rubber cap. An empty capillary measurement was performed for background estimation and subtraction. For each acquisition, 30 frames of 2 s were collected and averaged afterwards to avoid saturation of the PILATUS SAXS detector. Every sample was measured at $5 < T < 80$ °C (with steps of 15 °C) and $1 < p < 1000$ bar (with steps of 100 bar), for a total of 66 p–T points. The scans were performed as isotherms, setting the desired temperature, waiting 600 s for sample equilibration and measuring the first pressure point. The sample was then brought to the successive pressure step, and a 5 s equilibration time was set before the new acquisition. The same was repeated for all p–T points.

The I22 beamline at Diamond Light Source (Didcot, UK) is equipped with a fast shutter that is used to make sure that the samples are only illuminated during the short counting times and not during T–p changes and equilibration time. The 17 keV X-rays used for the high-pressure experiments on I22 helps reduce the radiation damage to biological samples[45]. If radiation damage occurred to the samples, this would have resulted in a decrease of the SAXS intensity vs time since the T–p scans were performed on the same sample for a given composition. No decrease in intensity was observed.

The resulting images were radially averaged, leading to a series of one-dimensional intensity $I(q)$ vs q curves, where q is the module of the momentum

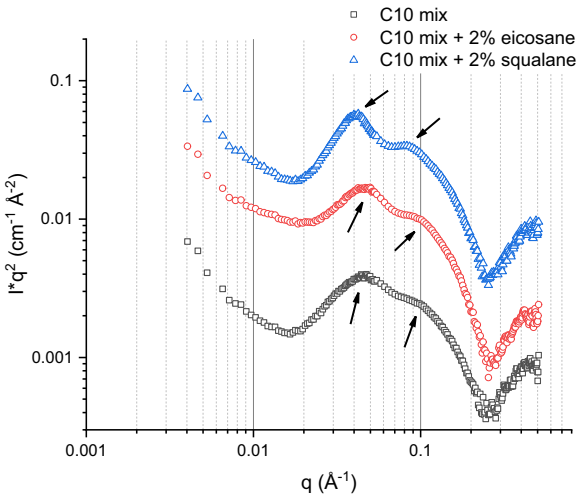

Fig. 6 Sample lamellarity at ambient temperature. SANS curves obtained for the three samples at 80 mM concentration and $T = 21$ °C. The arrows indicate the position of the first two orders of the MLV correlation for the three samples. The curves of eicosane- and squalane-enriched samples were shifted vertically for clarity.

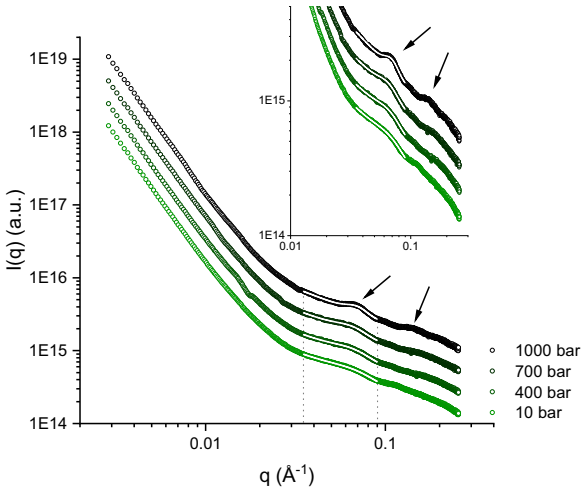

Fig. 7 Fitting the SAXS data. Example of SAXS data fitting using Gaussian functions with a q^{-c} background. The curves show the SAXS signal from the sample C10 mix + 2% eicosane, $T = 20$ °C and $p = 10$, 400, 700, 1000 bar respectively. Arrows show the two first correlation orders, proving the membrane lamellar ordering (together with the data shown in Fig. 6). The white lines are fits to the data. Inset: zoom in the mid-wide q-range. All related fitting parameters, errors and resulting χ^2 can be found in the Supplementary Information (Supplementary Table 1, see also Supplementary Note 2 and Supplementary Fig. 5).

transfer vector and is linked to the scattering angle by $q = 4\pi\sin\theta/\lambda$ (θ is the scattering angle and λ the incident wavelength). The intensity $I(q)$ consists of two terms:

$$I(q) = \left|F(q)^2 * S(q)\right| = |P(q) * S(q)| \quad (1)$$

where $P(q) = F(q)^2$ is the particle (in our case, the vesicle) form factor and $S(q)$ here is the inter-membrane structure factor which is of particular interest in this study. It contains the information about the interaction and the ordering of the membranes within the MLVs. By localising the q positions (which are a feature in the reciprocal space) of the first correlation maxima, and converting them to the real space membrane periodicity via the relation $d_{spacing} = 2\pi/q$, one obtains the mean membrane d-spacing. This quantity is the average value of the membrane repeat distance within MLVs, i.e., sum of the mean bilayer thickness and the mean buffer layer thickness between two adjacent membranes. We verified that the observed correlation is due to a lamellar phase of MLVs from the position of the second-order correlation peak with respect to the first order: $q_{2nd} = 2 \times q_{1st}$ at ambient pressure (Fig. 6) as well as at high pressure (Fig. 7).

Because of the weak $S(q)$ observed and as the main focus was the MLV d-spacing in this study, we did not perform a full fitting of the entire SAXS curves. Instead, we exploited the possibility for the vesicle form factor $P(q)$ to be approximated by a power law decay in the q-range where the first MLV correlation maxima are observed[34,46]. Therefore, the location of each correlation maximum was extracted by fitting Gaussian functions in the range of interest, with a background of the form q^{-k} (with k left as a free parameter for each specific temperature and sample, shared for all pressure points) to eliminate the contribution from the $P(q)$. Such q^{-k} trend is observed as a linear background in log–log plots. The parameters corresponding to the centre of the Gaussian functions where converted into d-spacing values (via $d_{spacing} = 2\pi/q$), as well as the associated errors (through error propagation). Figure 7 shows an example of fits performed.

Elastic incoherent neutron scattering. The incoherent neutron scattering experiments were performed on the backscattering spectrometer IN13 at the Institut Laue-Langevin (ILL Grenoble, France)[47]. Using backscattering geometry, one can access a very high energy resolution ($\Delta E \approx 8$ μeV) which translates into an observable timescale of motions of ≈0.1 ns. In such experiments, the signal obtained is dominated by the incoherent scattering coming from the hydrogen nuclei. In the case of the samples studied here, it means that the signal arises mostly from the acyl chains in the membrane, because the solvent used (and also the alkane molecules) were perdeuterated. This allowed exploiting the large difference in the scattering cross section of the two hydrogen isotopes to only highlight the acyl chain dynamics. The output of such an experiment is a series of curves $I_{inc}(q, E)$ vs q, where the rate of intensity decay gives quantitative information on atomic MSDs at every T–p point investigated.

The HHP equipment for biological samples in solution was developed in collaboration with the Sample Environment group (*SANE*) of the ILL. It consists of a pressure controller, which communicates with the instrument control software *NOMAD*, a high-pressure stick[48] and an HHP cell[49]. The pressure is transmitted from the controller to the sample through a capillary using liquid Fluorinert™[50], which has a pour point of 178 K. As the stick is inserted in the cryostat to regulate temperature, one has to avoid that liquid freezes; therefore, it must be heated by a wire and isolated thermally from its environment by a secondary vacuum. The HHP cell, made of the high-tensile aluminium alloy 7075-T6, is cylindrical with an external diameter of 10 mm and an internal diameter of 6 mm. It withstands pressures up to 1 kbar. The sample solution was separated from Fluorinert™ by a separator on the top of the cell.

Given the spectrometer resolution, the signal is generated by specific molecular motions within the corresponding timescale: methyl rotation, amphiphile rotation along its main axis and in-plane diffusion within the membrane[51]. Every sample was measured at four temperatures (25, 45, 65 and 85 °C) and three pressure values (10, 400 and 800 bar), for a total of 12 p–T points. For every measurement, 2 ml of sample were loaded in the HHP cell. The empty cell and a Vanadium rod measurement were performed in order to subtract the background and to normalise the data to the signal of a totally elastic incoherent scatterer.

Each I_{inc} vs q curve obtained per p–T point was analysed using a model-free approach described in ref. [52]. In the limits of the Gaussian approximation (GA)[53], which assumes harmonic motions of the atoms around their equilibrium positions and thus a linear behaviour of $\log(I_{inc})$ vs q^2, one can write the sum of the intensity curves over q, namely $I_{sum}(T) = \sum_{q_{min}}^{q_{max}} I_{inc}(q, T)$, as follows:

$$I^2_{sum}(T) \propto \frac{1}{\langle u^2 \rangle} \text{Å}^2 \quad (2)$$

with $\langle u^2 \rangle$ the hydrogen MSD and Å the angstrom unit. This gives a direct way of measuring the MSD and the corresponding error by simple error propagation from I_{sum} and allows to profit from a better statistics. The errors on I_{sum} are only dependent on the Poisson distribution of the scattered neutrons. The MSD, a measure of the mean hydrogen dynamics, can therefore be compared between the different samples.

The data range to be considered, when working in the GA, should satisfy the validity condition $\langle u^2 \rangle q^2 \leq 1$ (ref. [54]). In our case, from the reasonable assumption that all our samples consist mainly of spherically shaped objects (the MLVs), one can consider a range slightly beyond the validity condition[54]. Thus, the final range was defined by finding the maximum q for which the curve of highest dynamic (C10 mix $T = 85$ °C, $p = 1$ bar) shows a linear trend in the $\log(I_{inc}(q))$ vs q^2 representation. Some examples of I_{inc} curves and the corresponding range of validity of the GA are shown in Fig. 8.

A normalisation factor, common to all p–T points and samples measured, was applied on the MSD values to obtain results quantitatively comparable with the ones found from the standard GA fits (via the formula $I_{inc}(q) \cong I_0 \exp[-\langle u^2 \rangle q^2/3]$[53]). The latter fits lead to absolute $\langle u^2 \rangle$ values (and thus can be used for normalisation) but they are highly affected by the fitting errors, justifying our use of the alternative fit- and model-free method.

In principle, additional information could be inferred by extending the analysis to the high q-range, using a more complex model[55] or by considering two dynamic populations (low-q region–high-q region) instead of a single one[52]. Nevertheless, we focussed only on the largest amplitude motions (encoded in the lowest q-range)

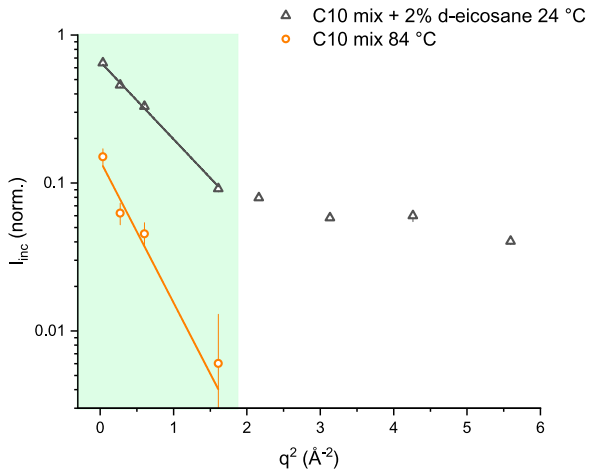

Fig. 8 Elastic intensity decay and GA validity range. Example of intensity curves obtained from the EINS experiment and range of validity of the GA (shown as a linear behaviour in this representation). The data shown are the ones of C10 mix and C10 mix + 2% eicosane at $p = 10$ bar and $T = 84$ and 24 °C, respectively. The light green region highlights the q^2 data range used for the analysis. The $q^2 > 2$ Å^{-2} data for the C10 mix at $T = 84$ °C approach zero and are not visible in the log(I_{inc}) representation. The errors are obtained from Poisson distribution.

because this is the region specifically related to the chain motions[56] and given the very high dynamics of the C10 mix sample which causes a drop of I_{inc} towards zero for $q^2 > 1.6$ Å^{-2} (also visible from Fig. 8).

Data availability

The SANS data that support the findings of this study are available with the identifier Doi: 10.5291/ILL-DATA.9-13-905. The SAXS data are available from the corresponding author upon reasonable request. The EINS data are available with the identifier Doi: 10.5291/ILL-DATA.9-13-828. The FTIR data (Supplementary Fig. 6) are available from the corresponding author upon reasonable request.

Received: 12 November 2020; Accepted: 14 January 2021;
Published online: 26 February 2021

References

1. Miller, S. L. & Urey, H. C. Organic compound synthesis on the primitive Earth. *Science* **130**, 245–251 (1959).
2. Orgel, L. E. The origin of life—a review of facts and speculations. *Trends Biochem. Sci.* **23**, 491–495 (1998).
3. Sutherland, J. D. The origin of life—out of the blue. *Angew. Chem. Int. Ed.* **55**, 104–121 (2016).
4. Saladino, R., Crestini, C., Costanzo, G., Negri, R. & Di Mauro, E. A possible prebiotic synthesis of purine, adenine, cytosine, and 4 (3H)-pyrimidinone from formamide: implications for the origin of life. *Bioorg. Med. Chem.* **9**, 1249–1253 (2001).
5. Segré, D., Ben-Eli, D., Deamer, D. W. & Lancet, D. The lipid world. *Orig. Life Evol. Biosph.* **31**, 119–145 (2001).
6. Paleos, C. M. A decisive step toward the origin of life. *Trends Biochem. Sci.* **40**, 487–488 (2015).
7. Gilbert, W. Origin of life: the RNA world. *Nature* **319**, 618 (1986).
8. Joyce, G. F. RNA evolution and the origins of life. *Nature* **338**, 217–224 (1989).
9. Leslie, E. & Prebiotic, O. Chemistry and the origin of the RNA world. *Crit. Rev. Biochem. Mol. Biol.* **39**, 99–123 (2004).
10. Patel, B. H., Percivalle, C., Ritson, D. J., Duffy, C. D. & Sutherland, J. D. Common origins of RNA, protein and lipid precursors in a cyanosulfidic protometabolism. *Nat. Chem.* **7**, 301–307 (2015).
11. Hargreaves, W. R. & Deamer, D. W. Liposomes from ionic, single-chain amphiphiles. *Biochemistry* **17**, 3759–3768 (1978).
12. Hanczyc, M. M., Fujikawa, S. M. & Szostak, J. W. Experimental models of primitive cellular compartments: encapsulation, growth, and division. *Science* **302**, 618–622 (2003).
13. Chen, I. A. & Szostak, J. W. A kinetic study of the growth of fatty acid vesicles. *Biophys. J.* **87**, 988–998 (2004).
14. Cape, J. L., Monnard, P.-A. & Boncella, J. M. Prebiotically relevant mixed fatty acid vesicles support anionic solute encapsulation and photochemically catalyzed trans-membrane charge transport. *Chem. Sci.* **2**, 661–671 (2011).
15. Maurer, S. E. et al. Vesicle self-assembly of monoalkyl amphiphiles under the effects of high ionic strength, extreme pH, and high temperature environments. *Langmuir* **34**, 15560–15568 (2018).
16. Deamer, D. The role of lipid membranes in life's origin. *Life* **7**, 5 (2017).
17. Szostak, J. W., Bartel, D. P. & Luisi, P. L. Synthesizing life. *Nature* **409**, 387–390 (2001).
18. McCollom, T. M., Ritter, G. & Simoneit, B. R. T. Lipid synthesis under hydrothermal conditions by Fischer-Tropsch-type reactions. *Orig. Life Evol. Biosph.* **29**, 153–166 (1999).
19. Monnard, P.-A. & Deamer, D. W. Preparation of vesicles from nonphospholipid amphiphiles. *Methods in enzymology*, **372**, 133–151 (2003).
20. Fiore, M. & Strazewski, P. Prebiotic lipidic amphiphiles and condensing agents on the early Earth. *Life (Basel)* **6**, 17 (2016).
21. Miller, S. L. & Bada, J. L. Submarine hot springs and the origin of life. *Nature* **334**, 609–611 (1988).
22. Martin, W., Baross, J., Kelley, D. & Russell, M. J. Hydrothermal vents and the origin of life. *Nat. Rev. Microbiol.* **6**, 805–814 (2008).
23. Damer, B. & Deamer, D. The hot spring hypothesis for an origin of life. *Astrobiology* **20**, 429–452 (2019).
24. Ross, D. & Deamer, D. Prebiotic oligomer assembly: what was the energy source? *Astrobiology* **19**, 517–521 (2019).
25. Daniel, I., Oger, P. & Winter, R. Origins of life and biochemistry under high-pressure conditions. *Chem. Soc. Rev.* **35**, 858–875 (2006).
26. Brooks, N. J., Ces, O., Templer, R. H. & Seddon, J. M. Pressure effects on lipid membrane structure and dynamics. *Chem. Phys. Lipids* **164**, 89–98 (2011).
27. Winter, R. Synchrotron X-ray and neutron small-angle scattering of lyotropic lipid mesophases, model biomembranes and proteins in solution at high pressure. *Biochim. Biophys. Acta* **1595**, 160–184 (2002).
28. Cario, A., Grossi, V., Schaeffer, P. & Oger, P. M. Membrane homeoviscous adaptation in the piezo-hyperthermophilic archaeon *Thermococcus barophilus*. *Front. Microbiol.* **6**, 1152 (2015).
29. Oger, P. M. & Cario, A. Adaptation of the membrane in Archaea. *Biophys. Chem.* **183**, 42–56 (2013).
30. Salvador-Castell, M., Tourte, M. & Oger, P. M. In search for the membrane regulators of Archaea. *Int. J. Mol. Sci.* **20**, 4434 (2019).
31. Salvador-Castell, M., Demé, B., Oger, P. & Peters, J. Lipid phase separation induced by the apolar polyisoprenoid squalane demonstrates its role in membrane domain formation in archaeal membranes. *Langmuir* **36**, 7375–7382 (2020).
32. Salvador-Castell, M., Brooks, N. J., Peters, J. & Oger, P. Induction of non-lamellar phases in archaeal lipids at high temperature and high hydrostatic pressure by apolar polyisoprenoids. *Biochim. Biophys. Acta* **1862**, 183130 (2020).
33. Kapoor, S. et al. Prebiotic cell membranes that survive extreme environmental pressure conditions. *Angew. Chem.* **126**, 8537–8541 (2014).
34. Misuraca, L. et al. High-temperature behavior of early life membrane models. *Langmuir* **36**, 13516–13526 (2020).
35. Demé, B., Dubois, M., Gulik-Krzywicki, T. & Zemb, T. Giant collective fluctuations of charged membranes at the lamellar-to-vesicle unbinding transition. 1. Characterization of a new lipid morphology by SANS, SAXS, and electron microscopy. *Langmuir* **18**, 997–1004 (2002).
36. Mutz, M. & Helfrich, W. Unbinding transition of a biological model membrane. *Phys. Rev. Lett.* **62**, 2881 (1989).
37. Winter, R. & Jeworrek, C. Effect of pressure on membranes. *Soft Matter* **5**, 3157–3173 (2009).
38. Trapp, M. et al. High hydrostatic pressure effects investigated by neutron scattering on lipid multilamellar vesicles. *Phys. Chem. Chem. Phys.* **15**, 20951–20956 (2013).
39. Peters, J., Giudici-Orticoni, M. T., Zaccai, G. & Guiral, M. Dynamics measured by neutron scattering correlates with the organization of bioenergetics complexes in natural membranes from hyperthermophile and mesophile bacteria. *Eur. Phys. J. E* **36**, 78 (2013).
40. Zaccai, G. How Soft is a protein? A protein dynamics force constant measured by neutron scattering. *Science* **288**, 1604 LP–1601607 (2000).
41. Krężel, A. & Bal, W. A formula for correlating pKa values determined in D_2O and H_2O. *J. Inorg. Biochem.* **98**, 161–166 (2004).
42. Good, N. E. et al. Hydrogen ion buffers for biological research. *Biochemistry* **5**, 467–477 (1966).
43. Dewhurst, C. D. et al. The small-angle neutron scattering instrument D33 at the Institut Laue–Langevin. *J. Appl. Crystallogr.* **49**, 1–14 (2016).
44. Smith, A. J. et al. I22: SAXS/WAXS beamline at Diamond Light Source—an overview of 10 years operation. Preprint at https://arxiv.org/abs/1903.05405 (2019).

45. Brooks, N. J. et al. Automated high pressure cell for pressure jump x-ray diffraction. *Rev. Sci. Instrum.* **81**, 64103 (2010).
46. Guinier, A. & Fournet, G. Small-angle scattering of X-rays Small angle scattering of X-rays. John Wiley and Son, New York (1955).
47. Francesca, N. et al. IN13 backscattering spectrometer at ILL: looking for motions in biological macromolecules and organisms. *Neutron N.* **19**, 14–18 (2008).
48. Lelièvre-Berna, E. et al. 700 MPa sample stick for studying liquid samples or solid-gas reactions down to 1.8 K and up to 550 K. *J. Neutron Res.* **19**, 77–84 (2017).
49. Peters, J. et al. High hydrostatic pressure equipment for neutron scattering studies of samples in solutions. *High. Press. Res.* **32**, 97–102 (2012).
50. Sidorov, V. A. & Sadykov, R. A. Hydrostatic limits of Fluorinert liquids used for neutron and transport studies at high pressure. *J. Phys. Condens. Matter* **17**, S3005 (2005).
51. Pfeiffer, W., Henkel, T., Sackmann, E., Knoll, W. & Richter, D. Local dynamics of lipid bilayers studied by incoherent quasi-elastic neutron scattering. *Europhys. Lett.* **8**, 201 (1989).
52. Zeller, D., Telling, M. T. F., Zamponi, M., Garcia Sakai, V. & Peters, J. Analysis of elastic incoherent neutron scattering data beyond the Gaussian approximation. *J. Chem. Phys.* **149**, 234908 (2018).
53. Rahman, A., Singwi, K. S. & Sjölander, A. Theory of slow neutron scattering by liquids. *I. Phys. Rev.* **126**, 986 (1962).
54. Tehei, M., Daniel, R. & Zaccai, G. Fundamental and biotechnological applications of neutron scattering measurements for macromolecular dynamics. *Eur. Biophys. J.* **35**, 551–558 (2006).
55. Peters, J. & Kneller, G. R. Motional heterogeneity in human acetylcholinesterase revealed by a non-Gaussian model for elastic incoherent neutron scattering. *J. Chem. Phys.* **139**, 10B620_1 (2013).
56. Knoll, W. et al. Structural and dynamical properties of reconstituted myelin sheaths in the presence of myelin proteins MBP and P2 studied by neutron scattering. *Soft Matter* **10**, 519–529 (2014).

Acknowledgements

This work was supported by the French National Research Agency programme ANR 17-CE11-0012–01 to P.O. and J.P. J.P. was funded by Campus France, programme Hubert Cuprien, with the German-French bilateral research cooperation programme "Procope" 2018–2019 (Contract NR 39974VD). L.M. was supported by a scholarship from the Institut Laue-Langevin (ILL) PhD program. The authors thank ILL for neutron beam-time on IN13. The work was carried out with the support of Diamond Light Source (Didcot, UK), instrument I22 (proposal SM23722). We acknowledge Olga Shebanova for her support during the experiment on I22. The ILL Partnership for Soft Condensed Matter (PSCM) is acknowledged for the access to the lab infrastructures. This work benefited from SasView software, originally developed by the DANSE project under NSF award DMR-0520547 [http://www.sasview.org/]. We are grateful to Josephine LoRicco for her support during the experiments. We gratefully acknowledge Antonio Calio for his help during the EINS data re-analysis. We thank Roland Winter for his help with the FTIR measurements.

Author contributions

This study is part of the Ph.D. project of L.M., carried out under the joint supervision of B.D., P.O. and J.P. L.M. conceived and designed the experiments, analysed the data and wrote the paper. L.M., B.D. and P.O. performed the SAXS experiments. L.M., P.O. and J.P. performed the EINS experiment. L.M., B.D. and J.P. performed the SANS experiment. B.D., P.O. and J.P. jointly supervised the data analysis and contributed to the paper redaction.

Competing interests

The authors declare no competing interests.

Additional information

Supplementary information The online version contains supplementary material available at https://doi.org/10.1038/s42004-021-00467-5.

Correspondence and requests for materials should be addressed to J.P.

Reprints and permission information is available at http://www.nature.com/reprints

Publisher's note Springer Nature remains neutral with regard to jurisdictional claims in published maps and institutional affiliations.

Open Access This article is licensed under a Creative Commons Attribution 4.0 International License, which permits use, sharing, adaptation, distribution and reproduction in any medium or format, as long as you give appropriate credit to the original author(s) and the source, provide a link to the Creative Commons license, and indicate if changes were made. The images or other third party material in this article are included in the article's Creative Commons license, unless indicated otherwise in a credit line to the material. If material is not included in the article's Creative Commons license and your intended use is not permitted by statutory regulation or exceeds the permitted use, you will need to obtain permission directly from the copyright holder. To view a copy of this license, visit http://creativecommons.org/licenses/by/4.0/.

© The Author(s) 2021

Alkanes increase the stability of early life membrane models under extreme pressure and temperature conditions

Loreto Misuraca[1,2], Bruno Demé[2], Philippe Oger[3], Judith Peters[1,2]*

[1] Univ. Grenoble Alpes, CNRS, LIPhy, 38000 Grenoble, France
[2] Institut Laue - Langevin, F-38042 Grenoble Cedex 9, France
[3] Univ Lyon, INSA Lyon, CNRS UMR5240, Villeurbanne, France
*corresponding author: jpeters@ill.fr

Supplementary Information

Supplementary Note 1: SAXS measurements at T = 5 °C

Supplementary Figures 1, 2, 3 show the SAXS curves collected at T = 5 °C in the pressure range 1 ≤ p ≤ 1000 bar. A number of features are present and tell about the effect of pressure on the investigated system at low temperature. The C10 mix sample (Supplementary Figure 1 (a)) shows the presence of a very small correlation at q ≃ 0.08 Å^{-1} (d-spacing ≈ 78.5 Å). The presence of a second order at q ≃ 0.16 Å^{-1} = 2 × 0.08 Å^{-1} proves that this is a lamellar phase. By comparing the curves at p = 1 bar and T = 5 – 20 °C (Supplementary Figure 1 (b)), one can see that a coexisting swollen phase 0.05 – 0.06 Å^{-1} (d-spacing ≈ 105 – 125 Å) is probably present also at the lowest temperature, although it is too weak to be resolved.

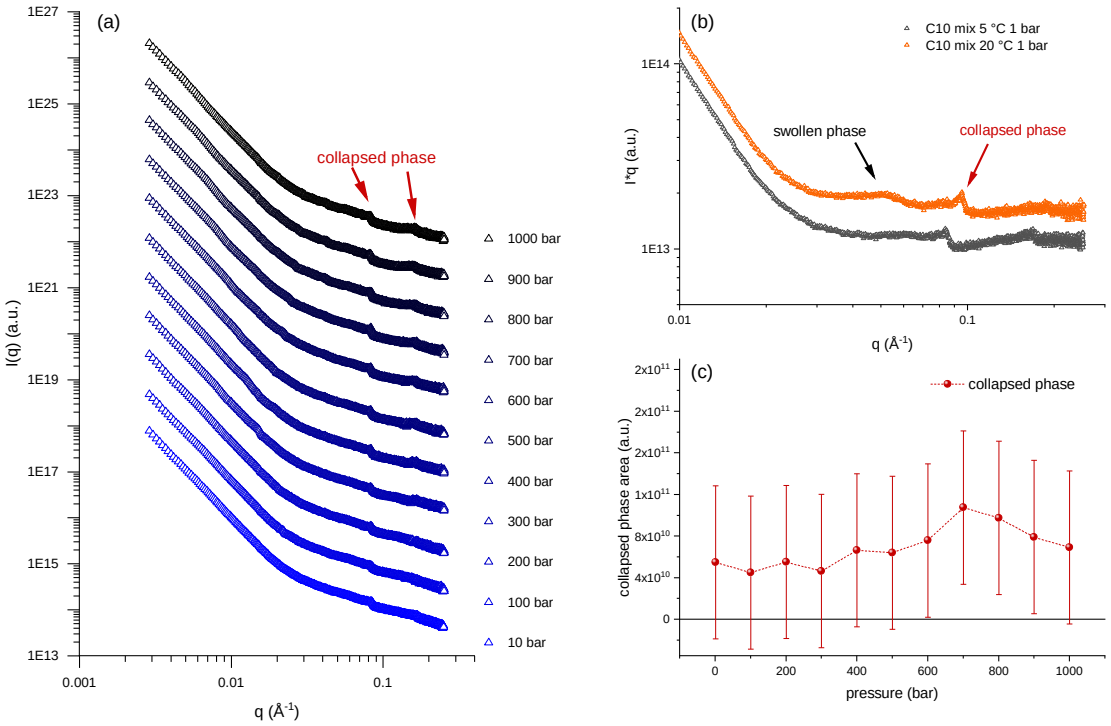

Supplementary Figure 1. C10 mix at 5 °C. a) SAXS data of sample C10 mix, T = 5 °C, at all measured pressure points. b) Comparison of C10 mix curves at T = 5 and 20 °C respectively, in a I*q representation that flattens the curve decay in the surrounding of the membrane correlations. c) Trend with pressure of the peak integrated intensity corresponding to the collapsed phase.

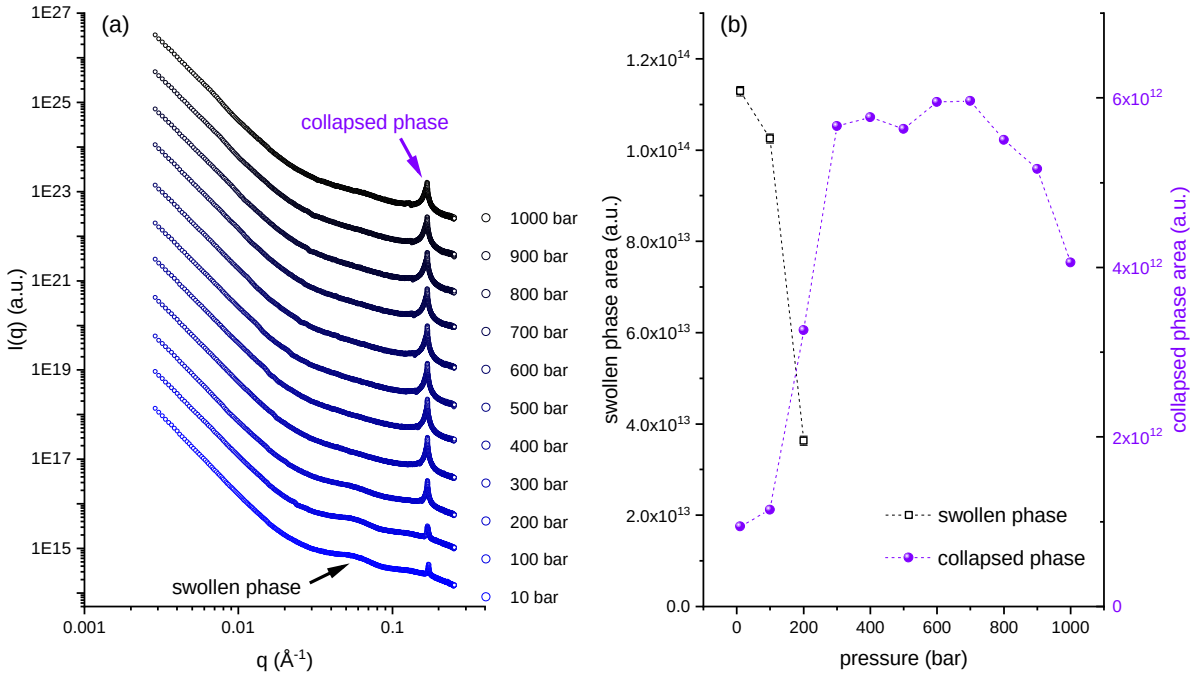

Supplementary Figure 2. C10 mix + 2% eicosane at 5 °C. a) SAXS data of sample C10 mix + 2% eicosane, T = 5 °C, at all measured pressure points. b) Trend with pressure of the peak integrated intensity corresponding to the swollen and the collapsed phase respectively.

The intensity of the peak at q ≃ 0.08 seems to be kept constant at varying pressure, although the very low intensity leaves a high relative uncertainty to its value (Supplementary Figure 1 (c)).

The situation is significantly different for the two other samples containing the alkanes, namely the eicosane and the squalane (Supplementary Figures 2 (a) and 3 (a)). Here, the T = 5 °C curves at p = 10 bar show a well resolved coexistence between the broad swollen phases (centred at q ≃ 0.056 - 0.088 $Å^{-1}$ → d-spacing ≃ 112 – 71 Å, respectively) and well-defined sharp peaks (q ≃ 0.17 $Å^{-1}$ → d-spacing ≃ 37 Å in both cases) which indicates collapsed phases. Upon pressure increasing, both samples show a decrease of the swollen phase signal, accompanied by an increase of the collapsed phase intensity (Supplementary Figures 2 (b) and 3 (b)). The observed phenomenon implies, from one hand, that the collapsed phase detected on the C10 mix sample is likely of a different nature than the one found on the alkane-including samples (a deduction that is also validated by comparing the d-spacings). The fact that the peak of the collapsed phase is observed at a constant q-value allows us to link qualitatively the intensity of the correlation with the volume fraction of sample in that phase. Since the decrease of the swollen phase and the increase of the collapsed one happen simultaneously on increasing pressure, it can be interpreted as a transfer from one phase to the other. This interpretation is in line with what is expected from a typical effect of pressure increase that would favour states that occupy the least volume.

Interestingly, the collapsed phases of C10 mix + 2% eicosane and squalane disappear completely at the higher temperatures (T ≥ 20 °C, as shown in the main text and Supplementary Figure 4). We interpret these phases as related to a fraction of flocculated sample, in view of what was found in our previous work[1].

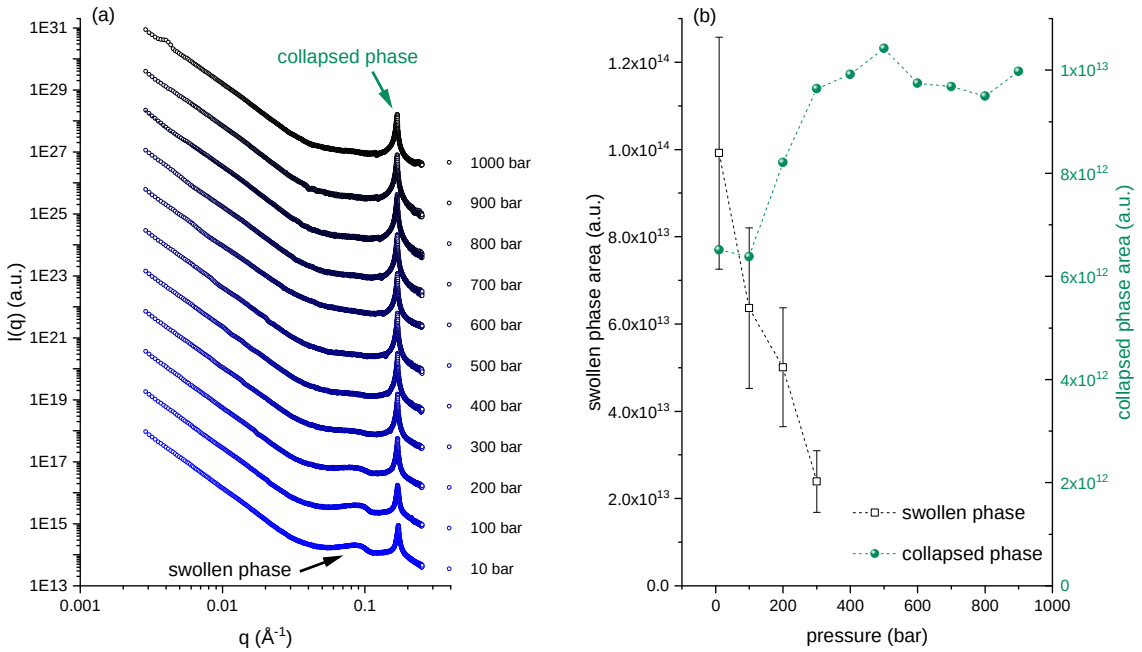

Supplementary Figure 3. C10 mix + 2% squalane at 5 °C. a) SAXS data of sample C10 mix + 2% squalane, T = 5 °C, at all measured pressure points. b) Trend with pressure of the peak integrated intensity corresponding to the swollen and the collapsed phase respectively.

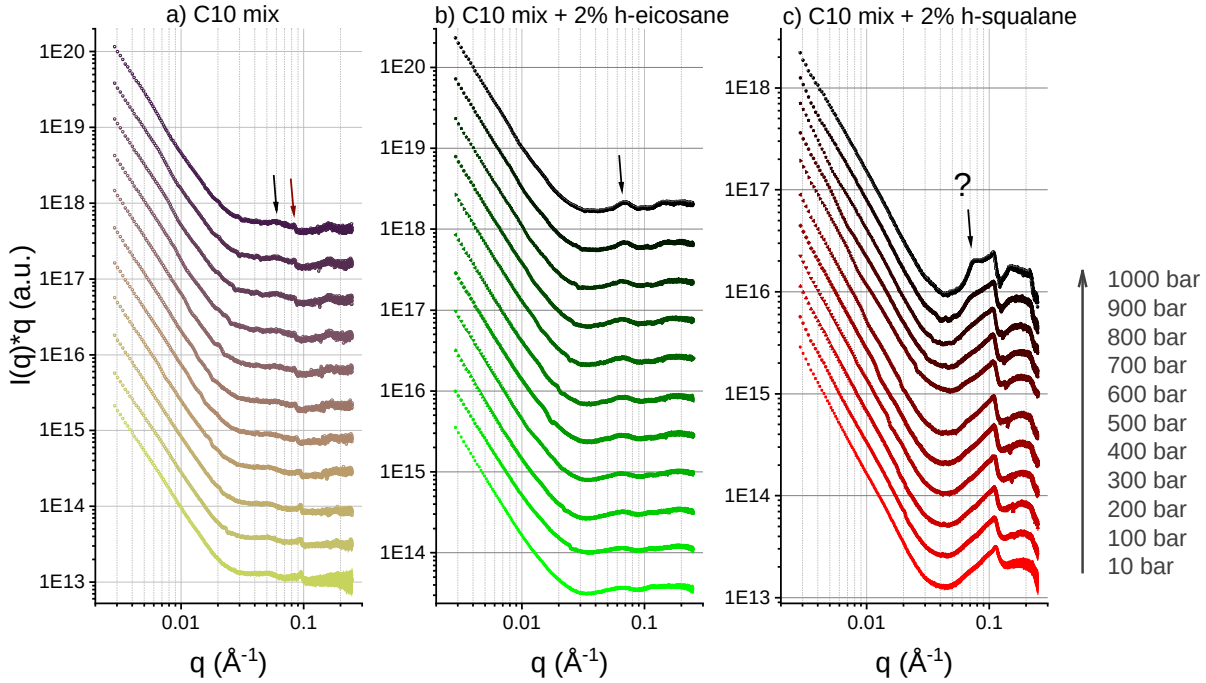

Supplementary Figure 4. SAXS curves obtained for the 3 samples at T = 20°C, in the I*q representation. a) C10 mix; b) C10 mix + 2% h-eicosane; c) C10 mix + 2% h-squalane. Curves have been shifted vertically for clarity. The black arrows point to the 1st order of correlation of the MLVs. Brown arrow indicates the small additional peak on the C10 mix assigned to a different arrangement of the MLV phase. The data of panel (c) were not used in the analysis (as specified in the main text), because a single MLV phase could not be identified (correlation highlighted with an arrow and a question mark).

Supplementary Note 2: SAXS data fitting for T ≥ 20 °C

Supplementary Figure 5 shows the obtained values of the correlation FWHM of the swollen phase investigated in the main text, as function of pressure and at the different temperatures (the peak centers, translated in d-spacing values, are the ones shown in Figure 5 of the main text). The C10 mix (Supplementary Figure 5 (a)) shows a significant increase of the FWHM at T = 20 °C at the intermediate pressure points, which can be an additional sign of phase coexistence in that range. Notably, the C10 mix + squalane sample (Supplementary Figure 5 (c)) shows a counterintuitive FWHM trend between the two measured temperatures: higher temperature should produce more disordered membrane arrangement and therefore lead to a higher correlation FWHM. A reason for this is probably that there is still phase coexistence at T = 35 °C, what is easily visible at the lower temperature T = 20 °C (Figure 4 in the main text). Instead, at T = 35 °C the correlations are probably too close to be resolved, yet slightly shifted leading to an observed higher FWHM.

Supplementary Table 1 lists all fitting parameters for the sample C10 mix + 2% h-eicosane at T = 20 °C (some of the fitting curves are the ones shown in Figure 2 of the main text), as an example of the fits performed. The slope of the power law decay (k) and the peak area (A), were fitted as shared parameters after having verified that the corresponding values were constant upon pressure increasing.

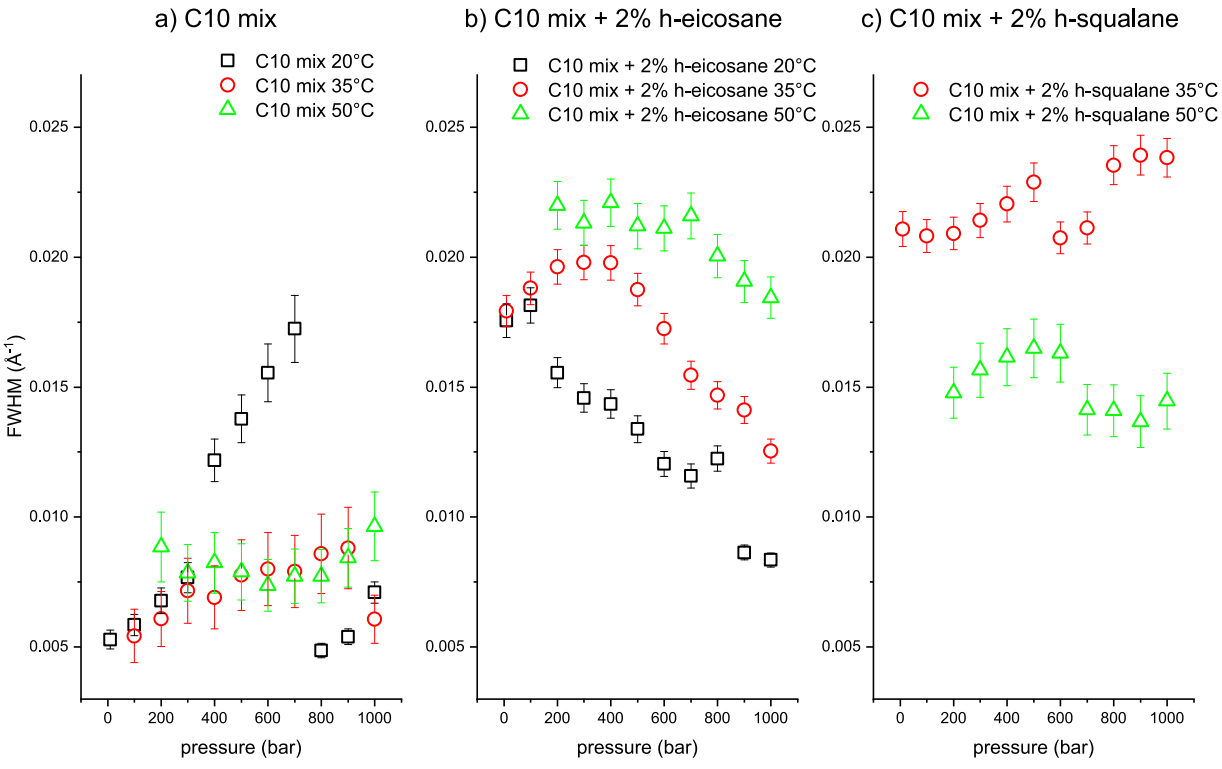

Supplementary Figure 5. MLV peak FWHM of the three measured samples at all the T-p points where the correlation was fitted. a) C10 mix; b) C10 mix + 2% h-eicosane; c) C10 mix + 2% h-squalane.

Supplementary Table 1. Fitting parameters of the SAXS curves for the sample C10 mix + eicosane T = 20 °C.
* shared parameters.

Equation	$m\,q^{-k} + A\,e^{\frac{(q-q_c)^2}{2w^2}}$		
Reduced χ^2*	0.1592		
k*	0.935 ± 0.004		
A*	(83.3 ± 1.3) × 10^{12}		
pressure (bar)	**q_c (Å^{-1})**	**w (Å^{-1})**	**m (× 10^{13})**
1	0.0608 ± 0.0004	0.0176 ± 0.0006	3.77 ± 0.05
100	0.0578 ± 0.0005	0.0181 ± 0.0006	3.91 ± 0.05
200	0.0618 ± 0.0004	0.0156 ±0.0006	3.62 ± 0.05
300	0.0618 ± 0.0003	0.0146 ± 0.0006	3.65 ± 0.05
400	0.0619 ± 0.0003	0.0143 ± 0.0005	3.56 ± 0.05
500	0.0624 ± 0.0003	0.0134 ±0.0005	3.47 ± 0.05
600	0.0629 ± 0.0003	0.0121 ± 0.0005	3.58 ±0.05
700	0.0630 ± 0.0003	0.0116 ±0.0005	3.59 ± 0.05
800	0.0629 ± 0.0003	0.0123 ± 0.0005	3.50 ± 0.05
900	0.0675 ± 0.0002	0.0086 ± 0.0003	3.50 ± 0.05
1000	0.0684 ± 0.0002	0.0084 ± 0.0003	3.55 ± 0.05

Supplementary Note 3: FTIR measurements at ambient temperature

Supplementary Figure 6 shows FTIR measurements acquired for a C10 mix sample at 80 mM concentration and extruded with a 100 nm polycarbonate membrane (Avanti Polar Lipid, Alabaster, AL) to give unilamellar vesicles (ULV), as function of hydrostatic pressure. The pressure was controlled by adding small amounts of BaSO4 as pressure probe[2]. Observing the changes in the position of the chain CH_2 symmetric stretching frequency as function of pressure we observe a phase transition starting at 200 > p > 400 bar. Although the high pressure uncertainty does not allow to obtain a precise value of the phase transition temperature, the results are in agreement with what is found on C10 mix at T = 20 °C with SAXS (Figure 5 in the main text). The values of ν_{symm} we obtained (Supplementary Figure 6 (b)) are in perfect agreement with the gel-fluid phase transition observed for the same system at ambient pressure and T ≃ 10 °C by Kapoor et al.[3].

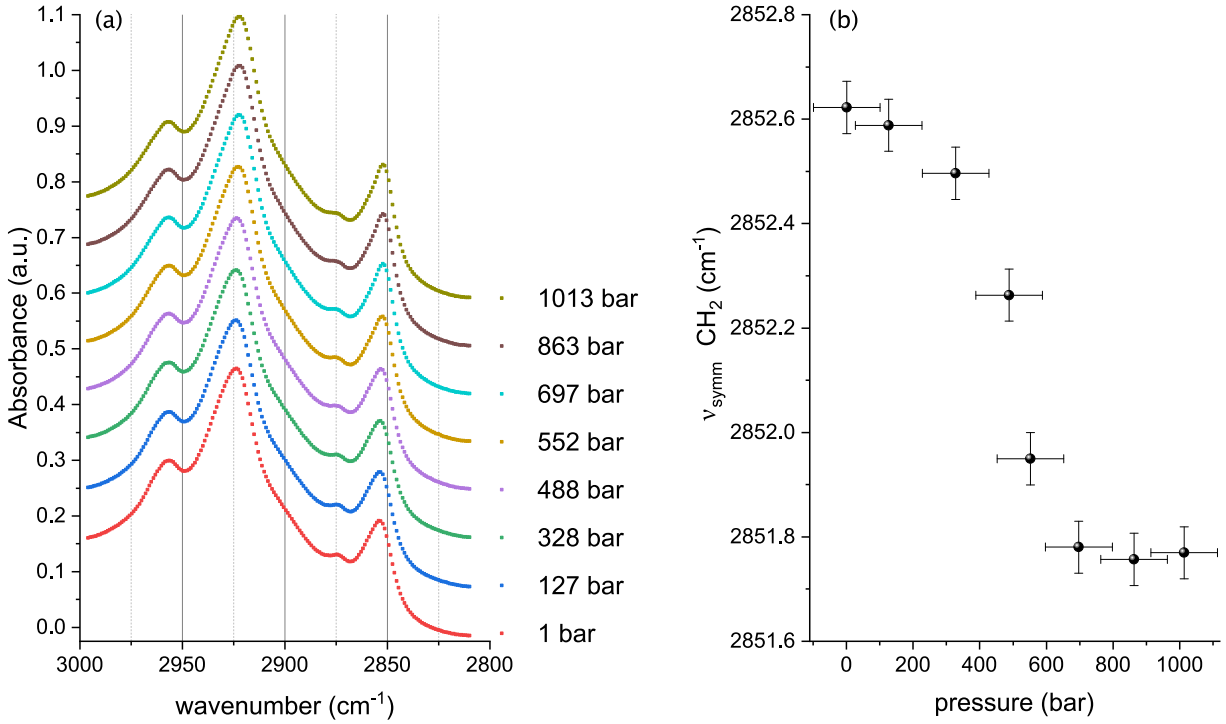

Supplementary Figure 6. Pressure-induced fluid-gel transition of C10 mix membrane at ambient temperature. a) FTIR spectra acquired for C10 mix 80 mM at T = 20 °C and 1 > p > 1013 bar, showing the peaks corresponding to the CH_2 and CH_3 symmetric and asymmetric stretching frequencies. b) Plot of the CH_2 symmetric stretching frequency as function of pressure.

Supplementary References

1. Misuraca, L. *et al.* High-Temperature Behavior of Early Life Membrane Models. *Langmuir* **36**, 13516–13526 (2020).

2. Wong, P. T. T. & Moffat, D. J. A new internal pressure calibrant for high-pressure infrared spectroscopy of aqueous systems. *Appl. Spectrosc.* **43**, 1279–1281 (1989).

3. Kapoor, S. *et al.* Prebiotic cell membranes that survive extreme environmental pressure conditions. *Angew. Chemie* **126**, 8537–8541 (2014).

3.2.1.2 *Notes: Article 2 results in the Thesis context*

The combination of results presented in the Article 1 and Article 2 allows for an interesting observation regarding the use of complementary, and in some cases alternative techniques. In fact, the result of small angle scattering experiments is visible for two very similar samples at equal concentration measured by SANS (right panel of Figure 6, Article 1) and SAXS (Figure 2, Article 2). This remains true for the same sample measured with SAXS as with SANS, namely the C10 mix at 350 mM (the SAXS curves of C10 mix at T $= 20\,^{\circ}$C are shown in the Supplementary Figure 4 of Article 2).

This comparison shows that SANS was much more effective in detecting the membrane correlations for the particular single chain amphiphile systems under study in this project, because of the very low scattering contrast between the amphiphilic headgroups (carboxylic acids or alcohol groups) and H_2O when using SAXS. Conversely, the use of D_2O in the SANS experiments increased substantially the contrast with the membranes, thus allowing an easier detection of the correlations. However, the SAXS measurements were the only structural study with both temperature and pressure that could be done successfully. A proposal for a SANS experiment on D33 using a pressure cell, available from the sample environment at ILL, was accepted with two days of allocated beamtime (10.5291/ILL-DATA.9-13-869). None of the samples could be measured because of leakage on the pressure cell (Figure 14). The reason for the leakage (as also suggested by the colour of the leaked material from the cell) has been later imputed to the reaction of bicine buffer with the copper of the pressure cell (*112*, *113*).

Figure 14: The high pressure cell used for SANS, zoomed at the saffire windows where the beam is transmitted. The picture shows the leakage of material from the windows.

3.2.2 Article 3: Alkanes act as membrane regulators of the response of early membranes to extreme temperatures

3.2.2.1 *Foreword*

As visible from the results presented in Article 1, the vesicles formed by C10 mix did not show any sign of micellar presence. Moreover, an onset temperature (T $\approx$ 60 °C) was found where the C10 mix vesicles undergo conformational changes.

The 3rd Article of this thesis was devoted to study: 1) what kind of conformational change is occurring to the ULV or, more precisely, what the product of such change is; 2) what happens when the vesicles are enriched with the alkane molecules. The use of SANS allowed to observe the vesicle fusion into lipid droplets as result of the temperature increase. The alkanes have the effect of shifting the conformational change to higher temperatures, therefore allowing a fraction of lamellar structures (vesicles) to still be present while the sample not containing alkanes had completed the transition of all vesicle material into droplets. All data show also effects at the lower temperatures, where the membranes appear to be softened when the alkanes are inserted.

For this study, I designed all the experiments and wrote the proposals for neutron beamtime on D33 (SANS) and IN15 (NSE). I prepared the samples for the SANS, NSE and FTIR experiments. I supervised the measurements and data analysis of the DLS experiments, which were performed by my M.Sc. trainee Antonio Caliò. I performed the experiments on IN15 and part of the experiments on D33. I made the FTIR measurements during a secondment at the T.U. Dortmund (Dortmund, DE). I analyzed the data obtained by SANS, NSE and FTIR and wrote the paper.

The paper has been submitted to *Soft Matter (RSC)*.

Alkanes act as membrane regulators of the response of early membranes to extreme temperatures

Loreto Misuraca[a,b], Antonino Caliò[c], Josephine LoRicco[c], Ingo Hoffmann[b], Roland Winter[d], Bruno Demé[b], Judith Peters[a,b], Philippe Oger[c]

[a] Univ. Grenoble Alpes, CNRS, LIPhy, 38000 Grenoble, France
[b] Institut Laue Langevin, F-38042 Grenoble Cedex 9, France
[c] INSA Lyon, Université de Lyon, CNRS, UMR5240, Villeurbanne, France
[d] Fakultät für Chemie und Chemische Biologie, Physikalische Chemie, Technische Universität Dortmund, 44227 Dortmund, Germany

Abstract

One of the first steps necessary for the origin of life is the formation of a membrane, a physical boundary that allows retention of useful molecules in concentrated solutions. The proto-membrane was likely formed by self-assembly of simple, readily available molecules such as short-chain fatty acids and alcohols, questioning the membrane stability in the harsh environmental conditions of the early Earth. We explored a new strategy to overcome the thermal stability issues of protomembranes by inclusion of apolar molecules (alkanes). We found that, in absence of alkane, protomembranes transition into lipid droplets when temperature increases, while alkane-enriched ones persist for longer times. Thus, protomembranes containing alkanes are more stable at high temperatures. This opens new perspectives to modulate the protomembrane behavior through incorporation of different types of suitable apolar molecules, increasing our understanding of the evolution of life's first membranes.

Introduction

The origin and evolution of living forms on Earth occurred approximately between 4.4 (evidence of liquid water and an atmosphere[1]) and 3.5 (earliest dated microfossils[2]) billion years ago. The early Earth would be far from resembling our planet as we know it today, with an early atmosphere resembling that of Venus[3] and a much higher geothermal heat flow[4]. The Earth Archaean crust would have been comprised of a multitude of ubiquitously distributed hydrothermal systems[5,6] (vents[7] or fields[8]). Hydrothermal vents and fields are among the most commonly accepted environments within which life could have originated, because the thermal and chemical gradients could have provided a source of energy long before the proto-living systems could have been able to harvest it themselves.

Both hydrothermal systems share high temperature as a common feature (T= 85 - 110 °C at the terrestrial surface[9], 50 – 350 °C in the proximity of the vents[10]). Deep-sea hydrothermal vents are also a system subject to high hydrostatic pressure (up to p = 1000 bar) and although hydrostatic pressure is known to produce effects opposing those of high temperature, (e.g. on Multi-Lamellar Vesicle (MLV) structure and dynamics[11–15]), this would only partially counter-balance the temperatures reached at the vents. The high temperatures may actually have been key for specific reactions necessary for the emergence of life[16,17], in particular for the synthesis of membrane forming molecules such as Single Chain Amphiphiles (SCAs) through Fischer-Tropsch Type (FTT) reactions[18,19]. It is worth noting that, along with SCAs such as short-chain

fatty acids and alcohols, other products of FTT reactions are n-alkane and n-alkene species[18,19].

Because of the simple reaction pathways required to synthesize SCAs in a prebiotic environment (as opposed to more complex phospholipids[20]), vesicles made by short, single chain carboxylic acids and n-alkanols are the most extensively studied systems for protocell membranes[21,22]. Previous studies have shown that short-chain fatty acids are able to self-assemble into membrane compartments[23] when specific requirements of solution pH and concentration are met[24]. In particular, fatty acid vesicles form at concentrations above a Critical Vesicle Concentration (CVC) and at pH close to the fatty acid dissociation constant (pK_a), both quantities being functions of the fatty acid chain length[24]. Mixing the fatty acid with same chain fatty alcohol has the effect of significantly decreasing the CVC[24] and broadening the pH range of vesicle existence[13]. Furthermore, our previous study[25] demonstrated that, while a pure fatty acid sample above the CVC always shows a coexistence between vesicles and micelles, a mixture of the same fatty acid with the corresponding alcohol gives only vesicle structures at ambient temperature, further demonstrating the strong stabilizing impact that the alcohol has on the membrane. Moreover, mixtures of decanoic acid, decanol and geraniol (an isoprenoid alcohol) were found to improve the vesicle resistance towards ionic solutes relevant to oceanic hydrothermal environments[26].

While the high temperature conditions close to the hydrothermal systems are seen as favorable in order to catalyze the synthesis of the building blocks necessary for life (including SCAs), these same conditions also pose a critical concern in the definition of SCA vesicles as plausible protomembrane candidates. It is unclear how the self-assembled compartments (vesicles) would have been able to maintain their structure and functionality at high temperature. The increase in thermal energy has been shown to cause the dissolution of pure fatty acid vesicles into micelles[25]; in case of the fatty acid : alcohol mixtures, it inhibits the membrane capability to retain oligonucleotides [16] and triggers a conformational transition in the vesicles[25].

High temperature is also a challenging parameter for more complex, modern lipid membranes[27]. We can discover suitable strategies to overcome the issue, by studying extant hyperthermophilic organisms. For instance, in the Archaea domain some strategies for temperature adaptation include: use of branched phytanyl chains (instead of linear chains); ether bonding of the chains with the glycerol (instead of ester bonding)[28]; use of bipolar tetraether lipids which form monolayers[29] or small fractions of apolar isoprenoid hydrocarbons[30–32]. Nevertheless, most of the strategies used by the modern extremophiles requires the use of complex molecules which were certainly not available in the prebiotic environment, with the notable exception of small fractions of apolar (linear) alkanes, which can be synthesized with the same FTT reactions as described before.

The possibility that apolar hydrocarbon molecules enter lipid bilayers and by doing so modify the membrane characteristics and properties, has received attention in past studies, some of them in close relation to the origin of life field. Deamer and coworkers[33,34] proved that polycyclic aromatic hydrocarbons can be inserted in membranes made of decanoic acid and hypothesized their role as pigment systems for a primitive form of photosynthesis. Such a possibility was further confirmed by Cape et al.[35]. Salvador and coworkers[31,32] found that squalane (C30 isoprenoid) can enter an archaea-like lipid membrane by positioning itself in the bilayer mid-plane and can induce non-lamellar phases as a function of temperature and hydrostatic pressure by modifying the membrane curvature. McIntosh et al.[36] showed that C6 – C16 linear alkanes can be inserted into phospholipid DMPC and DPPC bilayers and modify the membrane phase transition temperatures.

The aim of our work is to show that it is possible to incorporate linear (eicosane, C20) or isoprenoid (squalane, C30) alkanes inside model proto-cell membranes composed of SCAs (decanoic acid – decanol mixture, hereafter referred to as C10 mix) and that this incorporation has a significant effect on the protomembrane properties and stability. In particular, linear alkanes are prebiotically plausible components that could have easily mixed with the SCAs leading to alkane-enriched compartments.

In a recent study, we have shown that the alkanes have a significant effect in decreasing the membrane sensitivity (in structure and dynamics) towards hydrostatic pressure variations at some specific temperatures[37]. Here, we show that both linear and isoprenoid alkanes have clear effects in the thermal stability of the model protomembrane. The onset of vesicle size increase from T = 60 °C, previously observed on C10 mix vesicles[25], is found to shift towards higher temperatures when the alkanes are inserted in the membrane. Moreover, the effect of such a high temperature transition was investigated, showing that the effect of the alkanes is to maintain the lamellar structuring of the membrane at a higher temperature before phase separation of the SCAs into lipid droplets occurs. A significant effect on the membrane bending rigidity was found at all temperatures investigated, suggesting the possibility that the alkanes can be used to tune the physical properties of the protomembrane. Finally, the alkanes are found to increase the membrane chain disorder for T ≤ 60 °C.

All these results demonstrate that apolar hydrocarbons, in particular prebiotically available linear alkanes, could have constituted a suitable strategy for the protomembranes to survive the high temperature conditions imposed by the hydrothermal environments. The possibility that such systems (SCAs - alkanes) can acquire a higher thermal stability has significant consequences on our understanding of the possible mechanisms that could eventually have produced a stable living proto-organism.

Results

1. Effect of temperature on conformational changes

We first studied and compared our three model systems (C10 mix, C10 mix + eicosane and C10 mix + squalane) by following the dependence of the vesicle mean size with temperature. This was done by performing dynamic light scattering (DLS) measurements to exploit the vesicle Brownian diffusion as a means to probe their average size. The samples were extruded with a 100 nm pore membrane, in order to start with well monodispersed suspensions. Figure 1 shows the obtained results. The vesicle hydrodynamic radius (R_h) was determined from the diffusion coefficient extracted from the DLS autocorrelation functions as described in the “Materials and Methods” section. The change in R_h is shown as a function of temperature. At elevated temperatures there is a steep increase in the R_h with temperature corresponding to a conformational transition to larger macrostructures which was observed and described previously[25]. A clear difference between the sample lacking any alkane, as compared to all the others, is observed. In particular, the alkanes are found to shift the conformational transition of the C10 mix to a higher temperature (55-60 °C for the C10 mix, 65-70 °C for the others). Furthermore, the alkanes modify the rate of vesicle size increase at low temperature (20 °C < T < 50 °C), leading to a steeper R_h increase in that range. Interestingly, the retardation effect of linear (eicosane) and branched (squalane) alkanes at either 0.5% or 2% are the same within the precision of the technique employed.

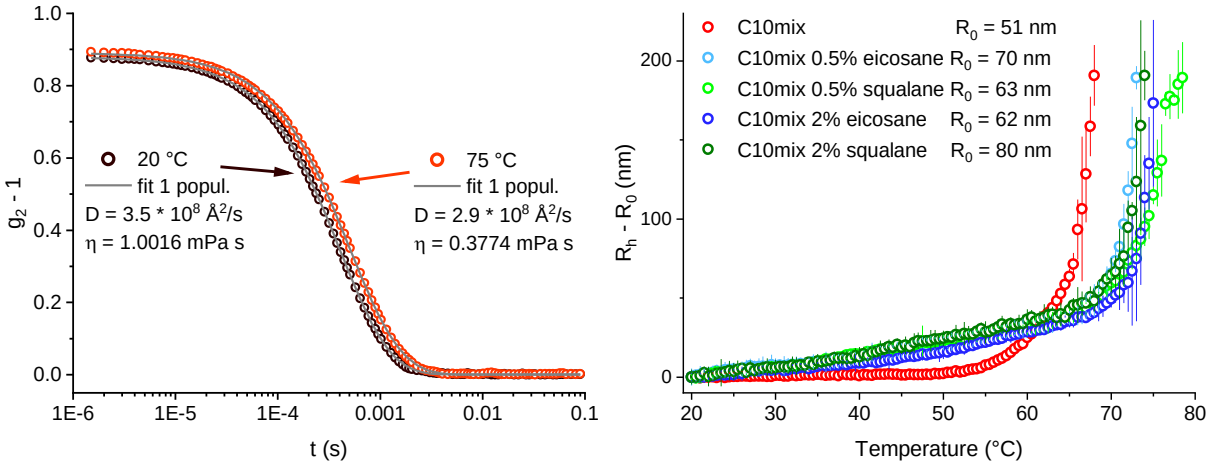

Figure 1. Left: Example of autocorrelation functions, for the sample C10 mix at T = 20 and 75 °C respectively, with the corresponding diffusion coefficients D found from the fits. Viscosity data are taken from[38]. Right: R_h - R_0 (R_0: radius at T = 20 °C) as a function of T for all measured samples. C10 mix data are from[25]. Values are displayed up to $R_h - R_0 \approx 200$ nm, above which the polydispersity was likely too high to give reliable quantitative estimations.

These results give a clear first indication that both types of alkane increase the vesicle thermal stability.

2. Amphiphile partitioning

In order to analyze in more detail the nature of the macro-structures formed by the SCAs at every temperature, small-angle neutron scattering (SANS) experiments were performed.

SANS allows discrimination between different types of macrostructures thanks to its wide q-range. The quantity *q*, known as scattering vector, can be thought as the equivalent in the reciprocal (Fourier) space of the distance variable (*d*) in the real space. Thus, a wide q-range translates into a wide range of length-scales, which can be probed with SANS by analyzing the *q* dependence of the scattering intensity. This allows us to distinguish, for instance, between dense spheres, cylinders, hollow spheres, etc. Moreover, quantitative information about the average sizes, polydispersity, shell thickness of the hollow spheres and membrane correlations (if present) can also be obtained.

In Figure 2, the collected SANS curves are shown together with the best fits obtained. From a first inspection of the curves, it is possible to see some distinct features:

- The curves at lower temperatures reach a plateau value in the lowest q-range. This denotes the so-called *Guinier regime*[39]. Its occurrence indicates the presence of a monodisperse population of spherical objects, a result of the extrusion process. The low-q data can therefore be used to calculate the average object size. In our case, these values are calculated directly by fitting the curves with models contained in the software SASview (http://www.sasview.org/) that cover the full q range explored.
- Mostly at the lowest temperature, but also partially at the higher ones, the region $0.05 < q < 0.15$ Å^{-1} follows a q^{-2} decay. This trend is compatible with lamellar form factors (vesicles), where the thickness of the membrane is measurable through the position of the minimum occurring at slightly higher q values (in our data, visible at $0.2 < q < 0.3$ Å^{-1}; the resulting membrane thickness values can be found in the Supp. Info.).

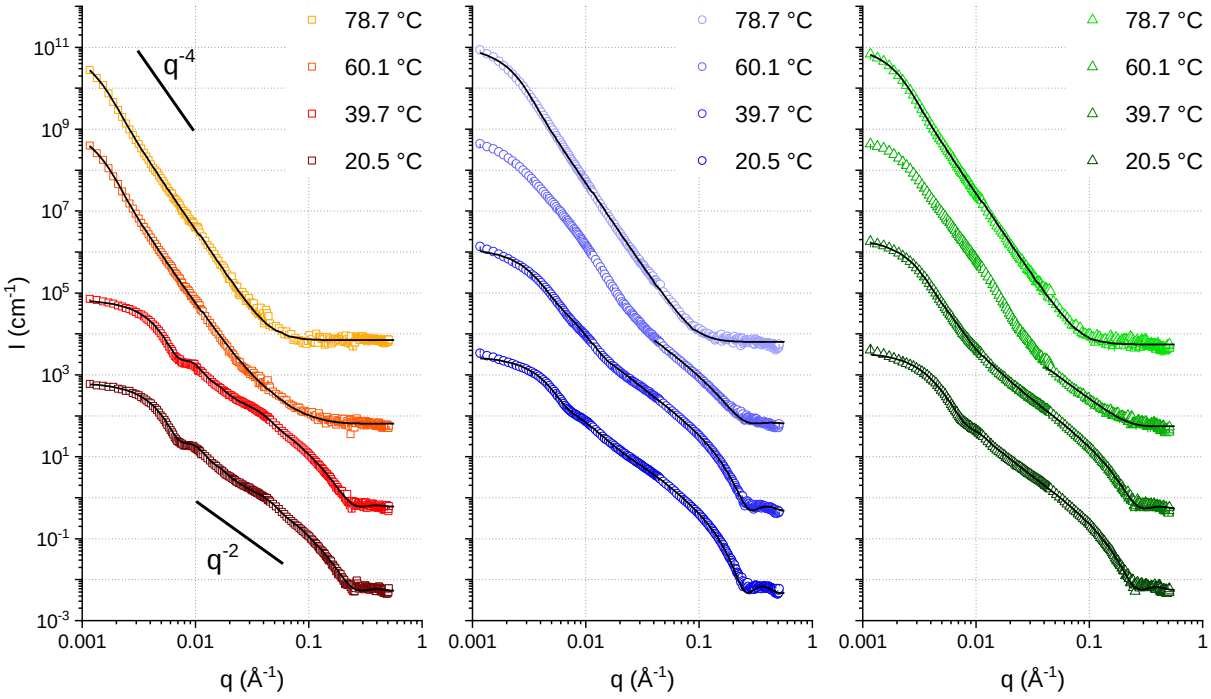

Figure 2. SANS curves of extruded samples at the temperatures investigated. Left: C10 mix sample. Middle: C10 mix + 2% h-eicosane sample. Right: C10 mix + 2% h-squalane sample. The black lines are the best fits to the data. The curves are vertically shifted for clarity.

- The high temperature data clearly show the predominance of a significantly steeper decay, with a q^{-4} power law. This decay, also known as *Porod law*[40], originates from well-defined, smooth interfaces, and is the signature of large aggregates modeled here with a spherical shape. Some of the intermediate temperatures exhibit a coexistence of q^{-4} decay in the lowest q region together with a q^{-2} decay in the intermediate-higher q region.

The coexistence of two distinct assemblies (bilayers and droplets, respectively) can be judged qualitatively (by visual inspection of the curves) as well as quantitatively (by fitting the SANS data). In particular, because of the faster decay of the droplet signal (q^{-4}), the lamellar form factor is dominating in the region at $q > 0.04$ Å^{-1}: this allows for a straightforward discrimination of the fraction of sample that self-assembles into bilayer structures, by proper scaling the q^{-2} in the middle-high q region (Table 1). Figure 3 shows the fraction of lipid forming bilayers as a function of temperature increase.

The most important difference is observed in the data acquired at T = 60 °C. At this temperature, the C10 mix sample shows a very small fraction of lamellar assemblies, while most of the sample appears to have formed large dense spheres (droplets) because of the temperature increase. Instead, samples containing intercalated alkanes retain a larger fraction of lamellar structures at this temperature. Note that at this temperature the SANS curves of the samples containing eicosane and squalane (Figure 2) are found in an intermediate state where it was not possible to fit the fraction of droplets at low q with a single dense sphere form factor. For this reason, the fitting at T = 60 °C for these two samples was performed only in the q range where the lamellar form factor predominates ($q > 0.04$ Å^{-1}), to estimate the corresponding fraction.

Table 1. Main parameters for the fits of the curves at T = 20 and 60 °C. The values for the fractions (lamellar and sphere) are normalized to the lipid volume fraction. ULV: Unilamellar Vesicle; BLV: Bilamellar Vesicle. * Since the Guinier regime is not fully reached at low q for the dense sphere form factors, the radius values found from these fits are not reliable and should be considered as minimum values instead. The full list of fitting parameters can be found in the Supp. Info.

sample	**C10 mix**		**C10 mix + 2% h-eicosane**		**C10 mix + 2% h-squalane**	
temperature (°C)	20.5	60.11	20.5	60.11	20.5	60.11
model	lamellar (ULV + BLV)	sphere + lamellar	lamellar (ULV + BLV)	lamellar	sphere + lamellar (ULV)	lamellar
q range (Å^{-1})	all	all	all	0.04 - 0.566	all	0.04 - 0.566
*lamellar fraction (*10^{-3})*	239 ± 0.8	7.4 ± 0.2	869 ± 1	186 ± 0.6	478.3 ± 0.6	50 ± 2
vesicle radius (Å)	412 ± 2 (ULV) 154 ± 6 (BLV)	---	389 ± 3 (ULV) 157 ± 3 (BLV)	---	397 ± 3	---
*sphere fraction (*10^{-3})*	---	85.0 ± 0.2	---	---	458.3 ± 0.2	---
sphere radius (Å)	---	768 *	---	---	516 *	---

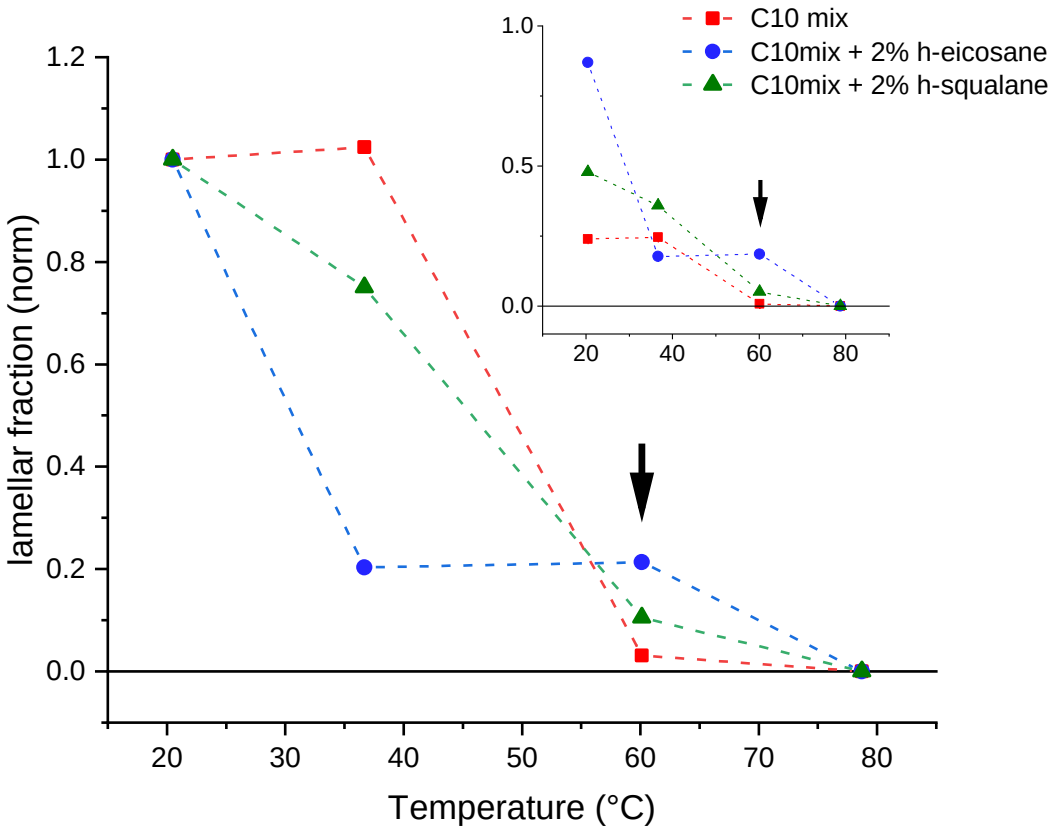

Figure 3. Fraction of the lamellar form factors obtained from fits to every sample and temperature point studied, normalized to the initial value at T = 20 °C. The inset shows the data normalized to the sample volume fraction. Arrows point on the T = 60 °C data, were a significant higher fraction of lamellar phase is observed on the alkane containing samples.

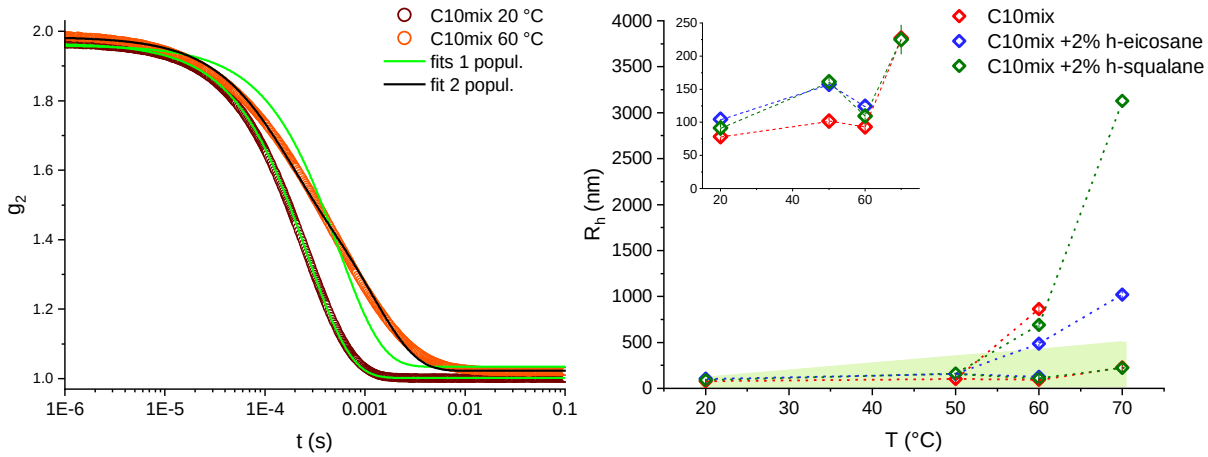

Figure 4. Left panel: Example of autocorrelation curves collected for the C10 mix sample using the *in-situ* DLS at T = 20 and 60 °C, respectively. Green lines show fits using a simple exponential decay function; the black curve is a fit of the T = 60 °C data with a sum of two exponential functions. Right panel: resulting R_h values; outside the green region, the factor $\exp(-Dq^2\tau) \geq 0.95$ ($D \lesssim 10^{-1}$ Å^2/ns) and the diffusive contributions will be neglected (see "Materials and Methods"). Note that the limit in R_h changes with T because it scales with the solvent viscosity. Inset: vertical zoom for $R_h \leq 250$ nm.

As Figure 3 shows, the loss of the lamellar phase fraction from its initial value at T = 20 °C, in favor of dense spheres, is more pronounced in samples containing the alkanes at T = 40 °C, while the situation is reversed at the higher temperature T = 60 °C. Finally, all samples have completed the transition towards the dense sphere assemblies at the highest measured temperature T = 80 °C.

These results demonstrate the membrane stabilizing role of both kind of alkanes, up to at least T = 60 °C. Moreover, they show that the result of the high temperature conformational transition on ULV systems is the formation of a lipid droplet phase.

3. Membrane bending rigidity

As the above experiments have demonstrated, the presence of alkanes in the membrane has a significant impact in modifying the phase boundaries and structural properties of the protomembranes. In order to gain further insight into these effects, we looked at the consequences of temperature on membrane dynamics using neutron spin echo (NSE) spectroscopy performed on extruded vesicles at temperatures in the range 20 < T < 70 °C.

NSE spectroscopy is a technique that allows study of dynamic modes with very long timescales (up to 1ms), for example the collective motions that lead to membrane undulations[41–43]. These fluctuations are a function of the bending rigidity of the membranes, and therefore can be followed by NSE using the formalism described in the "Materials and Methods" section.

A prior analysis was performed on the data acquired by *in-situ* DLS during the NSE measurements. As opposed to the DLS experiments performed offline the neutron beam (data in Figure 1), in this case the autocorrelation functions are averaged over the duration of the NSE scan (≈ 4 h per T step), therefore generally different results and some cases of coexistence between different size populations are to be expected.

In Figure 4, examples of autocorrelation functions at different temperatures are shown, as well as the R_h calculated for each population, temperature and sample probed. Two populations are needed to fit the data at the two highest temperatures measured, T = 60 and 70 °C, with the only exception of the C10 mix + 2% eicosane at T = 70 °C. These results are in line with

what we found by SANS, namely that the SCAs tend to self-assemble into both vesicle and dense sphere structures when reaching high temperatures. Also from the SANS data (Table 1), one can see that the droplets have a much larger average size with respect to the initial size constrained by the extrusion. Therefore, it is likely that the smaller R_h values observed using the *in-situ* DLS (Figure 4) are related to the vesicle assemblies, while the higher R_h values correspond to the lipid droplets instead.

Because of the size distribution of the droplets and from the theoretical definition of the intermediate scattering function (shown in Figure 5 left), NSE data give us selective information on the membrane phase and are not affected by the lipid droplet presence (details are found in the "Materials and Methods" section).

The results in Figure 5 (right panel) allow for a number of interpretations. First, there is a clear temperature effect on lowering the membrane rigidity, as expected. In line with the aforementioned experiments, the data show marked differences between the samples lacking or containing alkanes in the membrane. In particular, the rigidity is lowered by the addition of the alkanes at lower temperatures, while the trend is inverted at 60 and 70 °C with a small alkane-mediated membrane stiffening. Eicosane and squalane give comparable results with each other. The difference at high temperature between the C10 mix and the samples with the alkanes is significant in terms of the data and the associated errors. However (assuming a correct scaling of the bending rigidity, see "Materials and Methods") the difference observed at high temperature is a small fraction of 1 k_BT, questioning the actual physical significance of such difference.

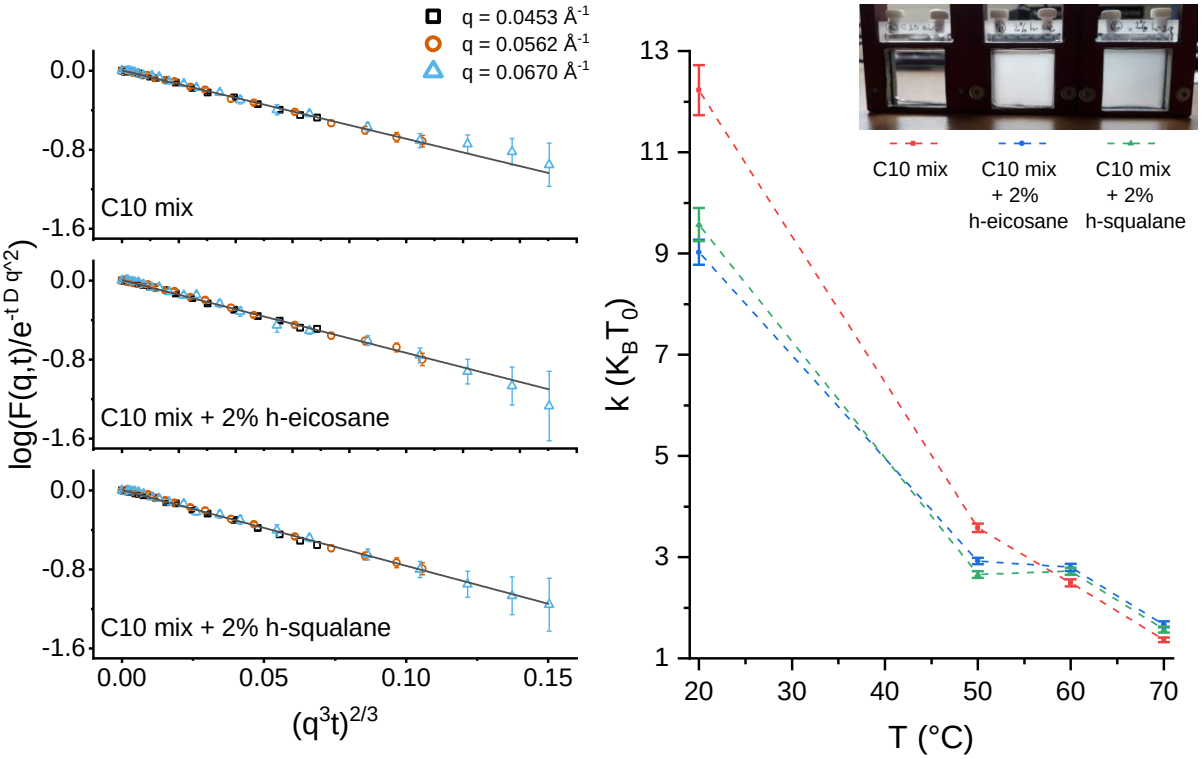

Figure 5. Left: NSE data at T = 70 °C plotted in the representation log[F(q, t)/ exp(-Dq²t)] vs $(q^3t)^{2/3}$. This highlights the stretched exponential decay predicted by the Zilman-Granek theory[41] and additionally shows that a more complex model taking into account the lipid droplet signal is unnecessary (details in the "Materials and Methods" section). Right: plot of the bending rigidity estimates as a function of the temperature. Inset shows the sample appearance after the NSE thermal scans.

A striking difference between the samples with or without alkanes was found by visual inspection of the suspensions after the temperature ramp (inset of Figure 5). The samples, which are indistinguishable with each other when prepared, showed at the end of the scan a very marked difference: the C10 mix lost its turbid appearance, and instead an interface was visible denoting a macroscopic phase separation; the samples with alkanes, on the other hand, were single phased and maintained the turbidity which is typical of samples containing vesicles.

The results show that the alkanes affect significantly the protomembrane bending rigidity: at low temperature, the rigidity is lowered by the alkanes, while the difference is negated (and instead the rigidity is slightly higher) at high temperature.

4. Time evolution of chain conformation and dynamics

As discussed, the NSE data show a significant impact of the alkane molecules in modifying the collective dynamics of the amphiphiles constituting the model membranes, encoded in the effective bending rigidity parameter. It is now useful to investigate whether this impact is also visible at a much smaller length scale, i.e. in the vibrational dynamics of each SCA induced by thermal energy. For that, FTIR spectra were acquired on samples with 1% perdeuterated alkanes in order to focus on a specific vibrational mode of the decanoic acid and decanol acyl chains (in our case, the symmetric stretching of CH_2 groups was chosen) at the same temperature points that were considered in the NSE experiment.

The wavenumber of this band is conformation-sensitive and thus responds, for example, to temperature-induced changes of the trans/gauche ratio in acyl chains. In fact, the position of the symmetric CH_2 stretching vibration is a measure of the number of gauche conformers in the acyl chains. When all methylene groups are in the trans conformation (e.g. in the ordered gel phase of the di-C16 DPPC bilayer), the band is observed around 2849 cm^{-1}. Addition of gauche conformers, accompanied by increased vibrational dynamics, results in a shift to higher frequency. At the main transition from the gel to the fluid-like (liquid-crystalline) phase, which results in melting of the acyl chains, the band shifts by 2-3 cm^{-1}, reaching about 2852 cm^{-1} in the all-fluid phase of the pure lipid bilayer DPPC[44].

Profiting from the much higher speed of acquisition with FTIR spectroscopy, the spectra were acquired continuously every 15 minutes, with jumps in temperature following the same timescale as in the NSE experiments. Figure 6 shows the position of the CH_2 symmetric stretching peak as a function of experimental time, for selected steps in temperature.

The first indication of the data is that the symmetric stretching frequency ν_{symm} quickly stabilizes to a specific value for all temperatures, even at the highest one of 70 °C. This confirms the equilibrium values found by NSE, regardless of the longer acquisition time per temperature point. Most of the spectra at 20 °C are best fit by a sum of two contributions, one at $\nu_{symm} \simeq$ 2852.5 cm^{-1} and the other at $\nu_{symm} \simeq$ 2861 cm^{-1}, the latter not seen in the Figure (see Supp. Info). In a few cases for the C10 mix sample, a single contribution at $\nu_{symm} \simeq$ 2853.5 cm^{-1} was sufficient to describe the data. A coexistence of peaks is likely to be a sign of phase coexistence, such as a gel-to-fluid phase transition region, known to occur in the C10 mix at T $\simeq$ 10 °C[13,25].

The vibrational dynamics of the pure C10 mix appears to be slightly lower than in the other samples at T = 50 and 60 °C, while an inversion occurs at 70 °C. Generally, an increase of ν_{symm} indicates increased conformational dynamics and lipid chain disorder. Interestingly, a marked decrease of the CH_2 symmetric stretching frequency is observed at 70 °C, which

appears to constitute a conformational and dynamic signature of the structural transition identified by the scattering data discussed above (Figure 1 and former study[25]).

The fast cooling down of the alkane containing samples back to 20 °C shows the dynamic reversibility of the latter transition: a first increase towards the value characteristic of 50-60 °C, followed by a decrease until the same initial value of $\nu \simeq 2852.5$ cm^{-1} at 20 °C is reached. The peak coexistence at 20 °C is also fully recovered (Supp. Info).

The data show that the membranes that incorporate the alkanes have a slightly higher lipid chain disorder at $T \leq 60$ °C. The dynamics observed at T = 60 °C, dominated by the lipid droplet phase, shows that the alkanes may increase the lipid packing inside the droplets.

Discussion

Our data show that the alkane incorporation significantly impacts the structure, topology and the dynamics of model protomembrane vesicles in response to temperature variations, in the range $20 < T < 80$ °C. The linear (eicosane) and branched (squalane) alkanes studied in this work gave very similar results in all the experiments performed.

The main effects of the alkanes on the vesicle behavior can be summarized as follows:

- Vesicle size vs T: incorporation of alkanes leads to a larger size increase at low T, up to $T \approx 55$-60 °C. Beyond that temperature range, a morphological and dynamical transition occurs for the C10 mix[25], which is shifted to higher temperatures when the alkanes are added ($T \approx 65$-70 °C).

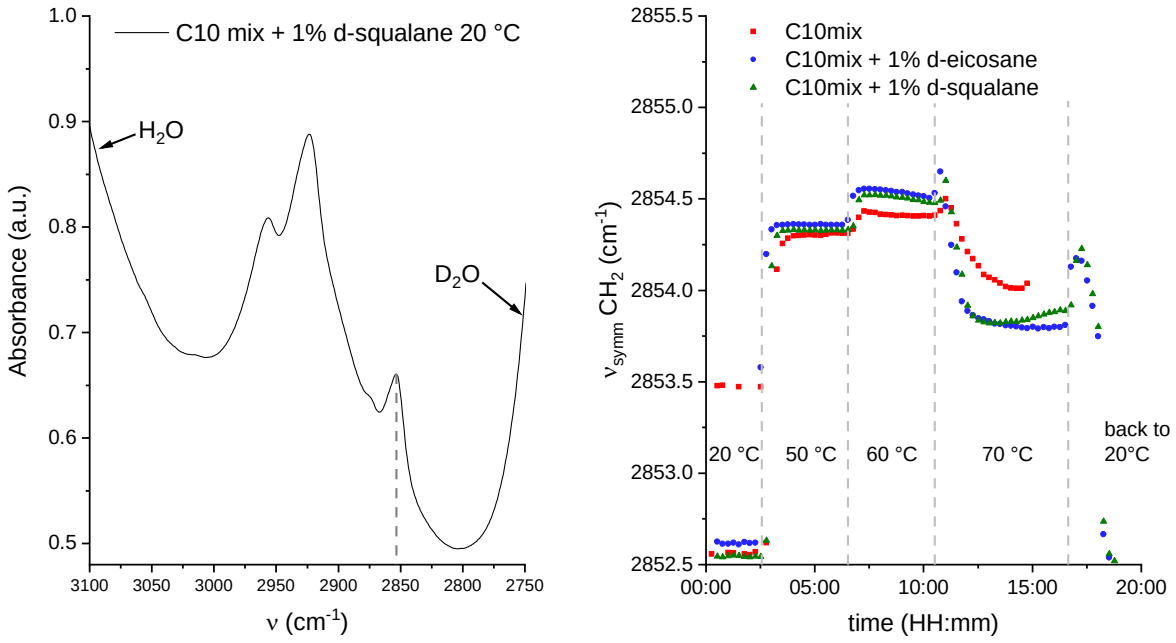

Figure 6. Left: example of a FTIR spectrum for the C10 mix + 5% h-squalane at T = 20 °C, in the range of interest where the symmetric and asymmetric stretching vibrations of CH_2 and CH_3 are found. The dashed line indicates the position of the CH_2 symmetric stretching mode at $\nu_{symm} \approx 2852$ cm^{-1}. Right: ν_{symm} as function of the time, following various temperature-jumps for all the samples.

- Amphiphile partitioning: high temperature causes a splitting in the lipid self-assembly into two kinds of macrostructures: lamellar (bilayer vesicles) and dense spheres (lipid droplets). Alkanes affect the sample partitioning by allowing more of the lamellar fraction to persist at T = 60 °C.
- Membrane bending rigidity: higher bending rigidity is observed in the C10 mix membrane at low temperatures (T = 20 and 50 °C); whereas, the samples with eicosane and squalane have slightly higher rigidities at the higher temperatures (T = 60 and 70 °C).
- Vibrational dynamics: alkanes maintain slightly higher CH_2 dynamics at T ≤ 60 °C, indicated by a small increase of ν_{symm}, while the symmetric stretching frequency is significantly lowered at T = 70 °C, which must be due to structural/morphological transition to a more densely packed state with less conformational and dynamical disorder. The transition back to T = 20 °C is fully reversible for the samples containing alkanes.

The samples were proven to be dynamically stable at all temperatures studied for several hours, hence excluding any possible distortion in the data due to non-equilibrium behavior.

All the observed effects imply that the inclusion of alkanes, even of the simple and prebiotically relevant type (e.g. eicosane), may constitute an effective physical advantage for simple prebiotic model membrane structures to sustain high temperatures. By shifting the temperature of the C10 mix conformational phase transition (Figure 1), the alkanes stabilize the vesicles over a wider temperature range and thus mitigate vesicle fusion and phase separation with coexisting lipid droplets.

Surprisingly, the alkanes seem to have overall opposite effects in the lower temperature range: faster radius increase (Figure 1), lower membrane rigidity (Figure 5), in some cases slightly higher CH_2 dynamics (at T = 50 and 60 °C, Figure 6). The reason for this might have to do with the fluidity of the alkane molecules themselves that depends on the temperature: in fact, the eicosane has a bulk melting point at 37 °C[45], while the squalane (liquid at ambient temperature) has a viscosity that lowers quickly with the temperature[46] (Supp. Info). Therefore, the stabilizing influence of the alkanes on the C10 mix may require these molecules to be in a low-viscosity/fluid state, allowing more efficient mixing (increase of mixing entropy) with the components of the C10 mix that can be provided by the high temperatures.

In the study of membrane stability at high temperature, an essential underlying variable is the length of time for which every thermal stress is applied. This is clearly shown, for instance, by the need for two populations of scatterers to fit the DLS autocorrelation function when the counting time lasted for several hours (as in the NSE experiments, Figure 4). Conversely, a continuous increase in temperature with fast DLS measurements required only a single population even at the highest measured temperatures (Figure 1). This factor needs to be taken into account particularly in cases where the used experimental techniques required long counting times, namely the SANS and NSE measurements. Nevertheless, the validity of all effects we observed at high temperatures is justified by the order at which the samples were measured, as specified in the “Materials and Methods” section. The C10 mix sample was the one that equilibrated for the shortest time before measurement at each temperature, and yet it showed significant variations compared to the other alkane-enriched samples. This ensures that the C10 mix vesicles are indeed less thermally stable than the alkane containing counterparts, and that the observed effects are not a consequence of equilibration time differences between the samples.

The striking difference in the appearance of the samples after the temperature scan in the NSE experiments (inset of Figure 5) indicates that the transition from the lipid droplet state back to

the vesicle state at room temperature occurs quickly for the samples with alkanes, while the C10 mix sample might have phase separated irreversibly in absence of re-mixing or it occurs at a much slower rate.

The phase change towards lipid droplets can also explain the unexpected decrease in the CH_2 symmetric stretching frequency observed at T = 70 °C in the FTIR data (Figure 6). As opposed to NSE, the FTIR data do not disentangle the signal coming from the membrane forming SCAs with the ones condensated into lipid droplets. The amphiphiles within the droplets are probably slightly more densely packed than in the vesicular structures at 50 and 60 °C, leading to a decrease of the number gauche conformers and a minor decrease in chain disorder, with a concomitant decrease of ν_{symm}, but not reaching ν_{symm}-values typical for the gel-like ordered phases seen at low temperatures. Upon addition of eicosane and squalane, this effect is more pronounced, which might be due to a more efficient lipid packing of the droplets of this multicomponent mixture.

The results imply that the inclusion of alkane molecules inside model protocell membranes tunes both structural and dynamical properties (physical and chemical) of the vesicles. In particular, the linear and branched alkanes (eicosane and squalane) have the effect of stabilizing the membranes rendering them more temperature stable, up to at least T = 60 °C and for several hours.

The conformational change at T ≈ 55 - 60 °C resulting from vesicle fusion of the C10 mix is shifted to T ≈ 65 - 70 °C when the alkanes are added. The lamellar (membrane) phase is protected by the alkane presence which allows this phase to remain present at T = 60 °C while the control sample phase separates into lipid droplets. The bending rigidity of the protomembranes is significantly modified by the alkane incorporation: at lower temperatures, the alkane high viscosity interferes with the packing of the SCAs in the bilayer, leading to softer membranes. At higher temperature (T ≥ 60 °C) the SCAs and the alkanes are more efficiently mixed in the hydrocarbon region of the bilayer, canceling the observed difference at low temperature and even making the alkane-containing membranes slightly stiffer. The data showing the mean CH_2 vibrational dynamics also support this idea, pointing to an increase in chain disorder of the samples with alkanes for T ≤ 60 °C.

Therefore, our study suggests that different kinds of alkanes, including types readily available in an early Earth environment, can be incorporated into protomembranes made of short SCAs. At low temperature (T ≤ 50 - 60 °C), the membranes containing alkanes have higher lipid chain disorder and consequently a lower bending rigidity, and perhaps this is also what drives the faster increase in size seen by DLS (Figure 1). Conversely, at higher temperature (T ≥ 50 - 60 °C) the alkanes are better mixed with the membrane chains which, in turn, achieve similar (slightly higher) bending rigidity as the alkane-lacking membranes. The alkane incorporation stabilizes the bilayer at high temperature so that the lipid lamellar phase is partially maintained up to at least T = 60 °C.

We have shown that not only complex hydrocarbons such as polycyclic aromatic hydrocarbons[33–35] or long-chain isoprenoids[30,32], but even much simpler linear alkanes could have been successfully inserted into prebiotic membranes. The inclusion might have served as a successful strategy (through combinatorial chemistry selection) which could have allowed the protomembranes to cope with harsh thermal conditions surrounding hydrothermal systems.

What if one adaptation strategy of modern extremophiles to high temperature, i.e. the quantity modulation of apolar lipids in the membrane, is an evolutionary remnant of the first successful living forms?

Acknowledgements

This work was funded by the French National Research Agency programme ANR 17-CE11-0012-01 to PO and JP. LM is supported by a scholarship from the Institut Laue - Langevin (ILL) PhD program. The authors thank ILL for neutron beamtime on D33 (DOI: 10.5291/ILL-DATA.9-13-905) and IN15 (DOI: 10.5291/ILL-DATA.INTER-464). The ILL Partnership for Soft Condensed Matter (PSCM) is acknowledged for the access to the lab infrastructures and the DLS platform. This work benefited from SasView software, originally developed by the DANSE project under NSF award DMR-0520547 [http://www.sasview.org/]. R.W. acknowledges funding from the Cluster of Excellence RESOLV (Deutsche Forschungsgemeinschaft (DFG, German Research Foundation) under Germany's Excellence Strategy, EXC-2033, Project number 39067787) and from the DFG Research Unit FOR 1979. R. W. and J. P. acknowledge also financial support from the German Academic Exchange Service (DAAD) (travel grant PROCOPE 57386797).

References

[1] S. A. Wilde, J. W. Valley, W. H. Peck, C. M. Graham, *Nature* **2001**, *409*, 175–178.

[2] J. W. Schopf, *Science (80-.).* **1993**, *260*, 640–646.

[3] P. A. Sossi, A. D. Burnham, J. Badro, A. Lanzirotti, M. Newville, H. S. C. O'Neill, *Sci. Adv.* **2020**, *6*, eabd1387.

[4] G. F. Davies, in *Top. Conf. Orig. Earth*, **1988**, p. 15.

[5] J. I. Lunine, *Philos. Trans. R. Soc. B Biol. Sci.* **2006**, *361*, 1721–1731.

[6] J. F. Kasting, M. T. Howard, *Philos. Trans. R. Soc. B Biol. Sci.* **2006**, *361*, 1733–1742.

[7] W. Martin, J. Baross, D. Kelley, M. J. Russell, *Nat. Rev. Microbiol.* **2008**, *6*, 805–814.

[8] B. Damer, D. Deamer, *Astrobiology* **2019**, *20*, 429–452.

[9] J. F. Kasting, T. P. Ackerman, *Science (80-.).* **1986**, *234*, 1383–1385.

[10] I. Daniel, P. Oger, R. Winter, *Chem. Soc. Rev.* **2006**, *35*, 858–875.

[11] R. Winter, *Biochim. Biophys. Acta (BBA)-Protein Struct. Mol. Enzymol.* **2002**, *1595*, 160–184.

[12] R. Winter, C. Jeworrek, *Soft Matter* **2009**, *5*, 3157–3173.

[13] S. Kapoor, M. Berghaus, S. Suladze, D. Prumbaum, S. Grobelny, P. Degen, S. Raunser, R. Winter, *Angew. Chemie* **2014**, *126*, 8537–8541.

[14] M. Trapp, J. Marion, M. Tehei, B. Demé, T. Gutberlet, J. Peters, *Phys. Chem. Chem. Phys.* **2013**, *15*, 20951–20956.

[15] J. Peters, J. Marion, F. J. Becher, M. Trapp, T. Gutberlet, D. J. Bicout, T. Heimburg, *Sci. Rep.* **2017**, *7*, 1–15.

[16] S. S. Mansy, J. W. Szostak, *Proc. Natl. Acad. Sci.* **2008**, *105*, 13351–13355.

[17] T. Oberholzer, M. Albrizio, P. L. Luisi, *Chem. Biol.* **1995**, *2*, 677–682.

[18] T. M. McCollom, G. Ritter, B. R. T. Simoneit, *Orig. Life Evol. Biosph.* **1999**, *29*, 153–166.

[19] B. R. T. Simoneit, *Adv. Sp. Res.* **2004**, *33*, 88–94.

[20] M. Fiore, P. Strazewski, *Life (Basel, Switzerland)* **2016**, *6*, 17.

[21] N. Kundu, D. Mondal, N. Sarkar, *Biophys. Rev.* **2020**, 1–15.

[22] S. Sarkar, S. Das, S. Dagar, M. P. Joshi, C. V Mungi, A. A. Sawant, G. M. Patki, S. Rajamani, *J. Membr. Biol.* **2020**, 1–20.

[23] W. R. Hargreaves, D. W. Deamer, *Biochemistry* **1978**, *17*, 3759–3768.

[24] C. L. Apel, D. W. Deamer, M. N. Mautner, *Biochim. Biophys. Acta (BBA)-Biomembranes* **2002**, *1559*, 1–9.

[25] L. Misuraca, A. Caliò, I. Grillo, A. Grélard, P. Marie Oger, J. Peters, B. Demé, *Langmuir* **2020**, *36*, 13516–13526.

[26] S. F. Jordan, E. Nee, N. Lane, *Interface Focus* **2019**, *9*, 20190067.

[27] J. R. Hazel, *Annu. Rev. Physiol.* **1995**, *57*, 19–42.

[28] J. C. Mathai, G. D. Sprott, M. L. Zeidel, *J. Biol. Chem.* **2001**, *276*, 27266–27271.

[29] M. De Rosa, A. Gambacorta, *Prog. Lipid Res.* **1988**, *27*, 153–175.

[30] A. Cario, V. Grossi, P. Schaeffer, P. M. Oger, *Front. Microbiol.* **2015**, *6*, 1152.

[31] M. Salvador-Castell, B. Demé, P. Oger, J. Peters, *Langmuir* **2020**, *36*, 7375–7382.

[32] M. Salvador-Castell, N. J. Brooks, J. Peters, P. Oger, *Biochim. Biophys. Acta (BBA)-Biomembranes* **2020**, *1862*, 183130.

[33] D. W. Deamer, *Adv. Sp. Res.* **1992**, *12*, 183–189.

[34] J. Groen, D. W. Deamer, A. Kros, P. Ehrenfreund, *Orig. Life Evol. Biosph.* **2012**, *42*, 295–306.

[35] J. L. Cape, P.-A. Monnard, J. M. Boncella, *Chem. Sci.* **2011**, *2*, 661–671.

[36] T. J. McIntosh, S. A. Simon, R. C. MacDonald, *Biochim. Biophys. Acta (BBA)-Biomembranes* **1980**, *597*, 445–463.

[37] L. Misuraca, B. Demé, P. M. Oger, J. Peters, *Commun. Chem. under peer-review* **2020**.

[38] **N.d.**

[39] A. Guinier, G. Fournet, K. L. Yudowitch, **1955**.

[40] G. Porod, O. Glatter, O. Kratky, *by O. Glatter O. Kratk. Acad. Press. London* **1982**, 17.

[41] A. G. Zilman, R. Granek, *Phys. Rev. Lett.* **1996**, *77*, 4788.

[42] U. Seifert, S. A. Langer, *EPL (Europhysics Lett.* **1993**, *23*, 71.

[43] W. Rawicz, K. C. Olbrich, T. McIntosh, D. Needham, E. Evans, *Biophys. J.* **2000**, *79*, 328–339.

[44] O. Reis, R. Winter, T. W. Zerda, *Biochim. Biophys. Acta (BBA)-Biomembranes* **1996**, *1279*, 5–16.

[45] S. Srinivasan, M. S. Diallo, S. K. Saha, O. A. Abass, A. Sharma, G. Balasubramanian, *Int. J. Heat Mass Transf.* **2017**, *114*, 318–323.

[46] K. A. G. Schmidt, D. Pagnutti, M. D. Curran, A. Singh, J. P. M. Trusler, G. C. Maitland, M. McBride-Wright, *J. Chem. Eng. Data* **2015**, *60*, 137–150.

[47] B. J. Frisken, *Appl. Opt.* **2001**, *40*, 4087–4091.

[48] C. D. Dewhurst, I. Grillo, D. Honecker, M. Bonnaud, M. Jacques, C. Amrouni, A. Perillo-Marcone, G. Manzin, R. Cubitt, *J. Appl. Crystallogr.* **2016**, *49*, 1–14.

[49] B. Farago, P. Falus, I. Hoffmann, M. Gradzielski, F. Thomas, C. Gomez, *Neutron News* **2015**, *26*, 15–17.

[50] I. Hoffmann, *Colloid Polym. Sci.* **2014**, *292*, 2053–2069.

[51] S. Gupta, J. U. De Mel, G. J. Schneider, *Curr. Opin. Colloid Interface Sci.* **2019**, *42*, 121–136.

Alkanes act as membrane regulators of the response of early membranes to extreme temperatures

Loreto Misuraca[a,b], Antonino Caliò[c], Josephine LoRicco[c], Ingo Hoffmann[b], Roland Winter[d], Bruno Demé[b], Judith Peters[a,b], Philippe Oger[c]

[a] Univ. Grenoble Alpes, CNRS, LIPhy, 38000 Grenoble, France
[b] Institut Laue Langevin, F-38042 Grenoble Cedex 9, France
[c] INSA Lyon, Université de Lyon, CNRS, UMR5240, Villeurbanne, France
[d] Fakultät für Chemie und Chemische Biologie, Physikalische Chemie, Technische Universität Dortmund, 44227 Dortmund, Germany

Supplementary Information

Materials and Methods

Sample preparation

The samples were prepared following the protocol described in[1]. Sodium decanoate, 1-decanol, eicosane, squalane, bicine buffer and D_2O were purchased from Sigma Aldrich-Merck (Darmstadt, DE). 1:1 mixtures of sodium decanoate and decanol were dissolved in a chloroform:methanol 1:1 mixture, together with the appropriate amount of alkanes when used. After solubilization, samples were dried with a nitrogen flush and left overnight in a desiccator with vacuum pumping. Samples were checked gravimetrically through every step to ensure the complete evaporation of the chloroform/methanol mixture.

The buffers were prepared by dissolving 0.2 M of bicine salt in H_2O (for DLS experiments) or D_2O (for FTIR, SANS, NSE experiments) and titrated to pH 8.5 (pD 8.5 for the deuterated solution). All buffers were filtered through a 0.2 µm Millipore membrane before use.

The dried decanoic acid:decanol (and eventually the alkane) films were suspended in buffer to obtain an 80 mM concentration for each sample and vortexed at maximum speed for ≈ 2 min, until all samples showed no aggregates and the suspensions appeared milky (characteristics of large vesicle formation).

Afterwards, the samples were extruded using the mini-extruder provided from Avanti Polar Lipids (Alabaster, AL), using a 100 nm pore size polycarbonate membrane. The extrusions, 11 passes per sample, were performed with the heating block in thermal equilibrium at 40 °C and less than 24 h before every experiment.

Dynamic Light Scattering (DLS)

The DLS experiments were performed on a Zetasizer Nano ZS90 (Malvern Panalytical Ltd, UK) available at the Institut Laue - Langevin (ILL) Grenoble, with an incoming laser light of λ = 633nm (He-Ne). The samples, extruded to minimize polydispersity and multilamellarity, were loaded into 200 µl quartz cells. The data, acquired at 90° fixed angle as a function of temperature, were collected continuously and then grouped by 3 runs of 30 s, to allow for error estimations.

The resulting DLS autocorrelation functions $g_2(t)$ were analyzed following a method developed and described in[2] in order to extract the Brownian diffusion coefficients D. The model function has the form:

$$g_2(t) - 1 = B + \beta \exp(-2Dq^2t)(1 - \mu_2/2)^2 \quad (1)$$

with $Dq^2 = \Gamma$ (decay rate) the first moment, μ_2 (related to the polydispersity) the second moment, B and β background and scaling factor, respectively.

Then, from each diffusion coefficient D one can estimate the corresponding hydrodynamic radius R_h using the Stokes-Einstein equation:

$$D = k_BT / (6\pi R_h \eta) \quad (2)$$

where k_B is the Boltzmann constant, T the temperature, η the solvent viscosity (assumed as the one of H_2O).

Small-Angle Neutron Scattering (SANS)

SANS experiments were carried out at the ILL (Grenoble, France) using the D33 instrument[3]. Three configurations combining incident wavelengths λ (5 Å and 14 Å) and detector distances (2, 10 and 12m) were used, corresponding to a range of momentum transfers $0.001 < q < 0.5$ $Å^{-1}$.

The measurements were performed using a themostated sample changer allowing a temperature range of 20 to 80 °C. The scans proceeded in the following order: 1) C10 mix; 2) C10 mix + 2% h-eicosane; 3) C10 mix + 2% h-squalane. The samples were kept for a total of ≈ 2 h at each temperature point.

For each SANS curve, analyzed using the SASView software, different model form factors (and when necessary a combination of them) were employed, depending on the need. The full formulas for the theoretical form factors, all available from SASView, can be found in the Supp. Info. In particular, the normalization of the SANS data to absolute scale allowed to quantify and follow the fraction of lipid self-assembled into bilayers at every measured temperature and for every sample, as well as the fraction of sample aggregating into lipid droplets.

Neutron Spin Echo (NSE) spectroscopy

NSE spectroscopy measurements were performed on the instrument IN15[4] at ILL (Grenoble, France). The samples, extruded and placed into 1 mm thick Hellma cells, were measured in the 5° angle configuration, leading to an observable q range of $0.04 < q < 0.07$ $Å^{-1}$. Each sample was measured at the temperatures T = 20, 50, 60, 70 °C. An *in-situ* DLS available on IN15 allowed tracking of the light scattering intensity traces and the vesicle diffusion coefficient of all samples during the measurements. The samples were placed into an automatic sample changer regulated with a thermal bath, therefore they were brought and kept to each temperature point for the same amount of time (≈ 4 h per temperature). The measurements followed the order: 1) C10 mix; 2) C10 mix + 2% h-eicosane; 3) C10 mix + 2% h-squalane.

The data obtained from NSE were analyzed in the framework of the Zilman-Granek theory[5] to model the membrane fluctuations. Each intermediate scattering curve F(q, t) was fit with a function of the form:

$$F(q, t) = \exp(-2Dq^2t)*\exp(-(\Gamma_{ZG}q^3t)^{2/3}) \quad (3)$$

The first term models the entire vesicles' Brownian diffusion with diffusion coefficient D. This parameter is obtained from the *in-situ* DLS data and it is then used as a fixed parameter during the NSE fits. The second term corresponds to the membrane relaxation: it is modeled as a stretched exponential with decay rate Γ_{ZG}. The latter has the following expression[5]:

$$\Gamma_{ZG} = 0.025\gamma\sqrt{\frac{k_BT}{\check{\kappa}}}\frac{k_BT}{\eta} \quad (4)$$

with $\check{\kappa}$ the effective bending/compression modulus, k_B the Boltzmann constant, η the D_2O viscosity, $\gamma \approx 1$ for $\check{\kappa} \gg k_BT$. From $\check{\kappa}$, one can find the actual membrane bending rigidity estimates, using a correction from Seifert and Langer[6] to account for density fluctuations in the membrane[7]:

$$\check{\kappa} = \kappa\left(1 + 24\frac{2d_{mono}^2}{d_{bilayer}^2}\right) \quad (5)$$

with κ the bending rigidity, $d_{bilayer}$ the bilayer thickness, d_{mono} the height of the monolayer neutral surface[8]. The quantity d_{mono} is generally unknown, although it ranges in $d_{bilayer}/4 \leq d_{mono} \leq d_{bilayer}/2$. This quantity has the practical consequence of rescaling $\check{\kappa}$, in order to obtain the bending rigidity constant κ. In the following, we will consider for d_{mono} the hydrocarbon chain length found from previous NMR experiments on the C10 mix membrane ($L_{chain} \cong 8.3$ Å[1]). This is equivalent to modifying Equation 4 by substituting $\check{\kappa} \rightarrow \kappa$ and the prefactor $0.025 \rightarrow 0.0082$, a value that is similar to the most accepted value for phospholipid-based vesicles (0.0069[9]):

$$\Gamma_{ZG} = 0.0082\gamma\sqrt{\frac{k_BT}{\kappa}}\frac{k_BT}{\eta} \quad (6)$$

To analyze the NSE data, some considerations can be made based on knowledge of the instrument time (/energy) window. From Equation 3, one can see that the term related to the Brownian diffusion, namely $\exp(-Dq^2\tau)$, tends to a constant for small enough values of the diffusion coefficient D: $\exp(-Dq^2\tau) \approx 1$ when $D \approx 0$. Therefore, we will neglect the contribution of the Brownian diffusion coming from the largest assemblies as detected from the *in-situ* DLS, and consider only the structures that give the lowest R_h at temperatures where the coexistence is observed, T = 60 and 70 °C (Figure 4). In practice, this means that the diffusion of the large lipid droplets has negligible effect on the NSE data analysis, while the diffusion of the vesicles is taken into account and disentangled from the membrane relaxation signal. This strategy is also supported by what we observed by SANS, where the region $q > 0.04$ Å^{-1} is clearly dominated by the membrane contribution (as a reminder, the NSE measurements were performed in the range $0.04 < q < 0.07$ Å^{-1}).

Concerning the possible contribution of the large lipid droplets in the NSE F(q,t), one can assume it as an elastic constant, which would lead to a modification of Equation 3 as follows:

$$F(q, t) = I_{vesicles} * \exp(-Dq^2t)*\exp(-(\Gamma_{ZG}q^3t)^{2/3}) + I_{droplets} \quad (7)$$

with I_x the intensity ratio of population x in the NSE q-range. However, by plotting the curves in a $\log[F(q, t)/ \exp(-Dq^2t)]$ vs $(q^3t)^{2/3}$ representation, we can show (Figure 5) that all data at T = 70 °C fall extremely well onto a linear master curve (having a slope $m = -\Gamma_{ZG}^{2/3}$). This ensured that all contributions from the lipid droplets could be neglected in the analysis and that the model function of Equation 3 was sufficient to fit the data.

Fourier Transform InfraRed (FTIR) spectroscopy

The FTIR spectra were acquired on a Vertex70 FTIR spectrometer (Bruker, Germany) with 1 cm^{-1} resolution. The temperature steps, as well as the time at which the samples were kept at each temperature, were set to match the NSE experiment on IN15 (≈ 4 h per temperature). Samples were followed by acquiring FTIR spectra every 15 minutes. Every spectrum was automatically averaged among 256 collections by the instrument software.

The data were analyzed following a specific frequency peak at $\nu_{symm} \approx 2850\ cm^{-1}$. This peak, corresponding to the CH_2 symmetric stretching frequency, was chosen for its well resolved position in the FTIR wavelength range. The position of the peak was evaluated by fit with one (or two, when coexistence was observed) Gaussian function in the vicinity of the peak. The temperature and time dependence of the peak provides information about the lipid tail's conformation and vibrational dynamics.

SANS data analysis

Form factor models for SANS data analysis:

The following models (and combinations of them, when needed) were used to fit the SANS data:

1. Unilamellar vesicle[10]

$$P(q) = scale\frac{\Phi}{V_{shell}}\left[\frac{3V_{core}(\rho_{solvent}-\rho_{shell})j_1(qR_{core})}{qR_{core}} + \frac{3V_{tot}(\rho_{shell}-\rho_{solvent})j_1(qR_{tot})}{qR_{tot}}\right]^2 + C \qquad (5)$$

with Φ the shell volume fraction, V the volumes of the core of shell (V_{core}) or the overall vesicle (V_{tot}), R the radii of the core (R_{core}) or the entire vesicle (R_{tot}), ρ the neutron scattering length densities of solvent ($\rho_{solvent}$) and shell (ρ_{shell}), $j_1(x) = (sinx - cosx)/x^2$ the spherical Bessel function and C the flat background level.

The fitting parameters are therefore the following:

- Φ: determined from the sample preparation and always fixed;

- scale: as the curves are in absolute scale, if all samples having volume fraction Φ contribute to the vesicle form factor, then scale = 1;

- background;

- $\rho_{solvent}$: calculated from $\rho = \frac{\sum_{i=1}^{N} b_i}{V}$ and using tabulated values for the neutron coherent scattering lengths b_i of the atoms in the solvent (buffer and D_2O), always fixed for the fittings;

- ρ_{shell}: same as for $\rho_{solvent}$, calculated from the sample molecules and always fixed;

- R_{core};

- bilayer thickness = $R_{tot} - R_{core}$;

- radius polydispersity, assuming a Lognormal distribution;

- thickness polydispersity, assuming a Gaussian distribution.

2. Multilayer vesicle (used for bilamellar vesicle populations)

$$P(q) = scale\frac{\Phi(\rho_{shell}-\rho_{solvent})}{V_{shell}}\sum_{i=1}^{N}\left[\frac{3V(r_i)\sin(qr_i)-qr_i\cos(qr_i)}{(qr_i)^3}-\frac{3V(R_i)\sin(qR_i)-qR_i\cos(qR_i)}{(qR_i)^3}\right]^2+C \quad (6)$$

with r_i the solvent radius before shell I, R_i the shell radius for shell i. The fitting parameters are analogous as in the unilamellar vesicle model, except that it is normalised for the vesicle volume fraction (core + shell) and for the additional parameters:
- solvent thickness = r_i - R_{i-1};
- N: number of shells, fixed to 2 for the bilamellar vesicles.

3. Lamellar[11] (this model was used when the information about the vesicle size could not be obtained)

$$P(q) = 4\pi\frac{scale}{q^4\delta}\Delta\rho^2(1-\cos q\delta)+C$$

where $\Delta\rho^2$ is the scattering length density difference, and δ the layer thickness. This model can be thought of as the limiting form of a *unilamellar vesicle* model with infinitely large radius.

4. Sphere [10] (lipid droplet population)

$$P(q) = \frac{scale}{V}\left[\frac{3V(\rho_{solvent}-\rho_{sphere})(sin(qr)-qrcos(qr))}{(qr)^3}\right]^2+C \quad (7)$$

used to model spheres with uniform neutron scattering length density ρ_{sphere}, radius r and volume V. Free fitting parameters:
- scale: sphere (droplet) volume fraction;
- r: sphere radius.
- radius polydispersity, assuming a Lognormal distribution;

Table S1 (at the end of this text) shows the parameters that have been used for the SANS fit. In every case, the following additional parameters were considered as constant and fixed:

1. Sample neutron scattering length density (NSLD): -0.04 * 10^{-6} $Å^{-2}$
2. Solvent NSLD: 6.24 * 10^{-6} $Å^{-2}$
3. Sample volume fraction: 0.0127

The NSLD values were calculated from the compound chemical formula and the density using SASView (http://www.sasview.org/).

Neutron Spin Echo: *in-situ* DLS

Figure S1 shows the intensity traces acquired during the *in-situ* DLS measurements on IN15. The data give additional evidence about fusion phenomena occurring at high temperature that cause a significant decrease in the amount of scatterers in solution (to which the intensity is partially linked). We made sure that the intensity of the C10 mix sample, although reduced at T = 70 °C, was still significantly higher than the dark counts.

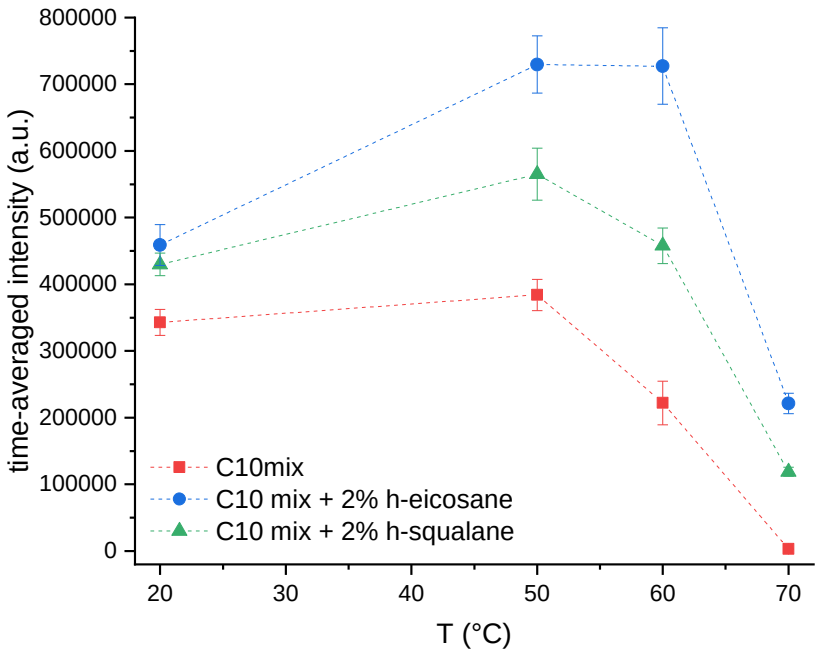

Figure S1. *In-situ* DLS Intensity traces averaged over the full measuring time at each specific temperature for the three measured samples.

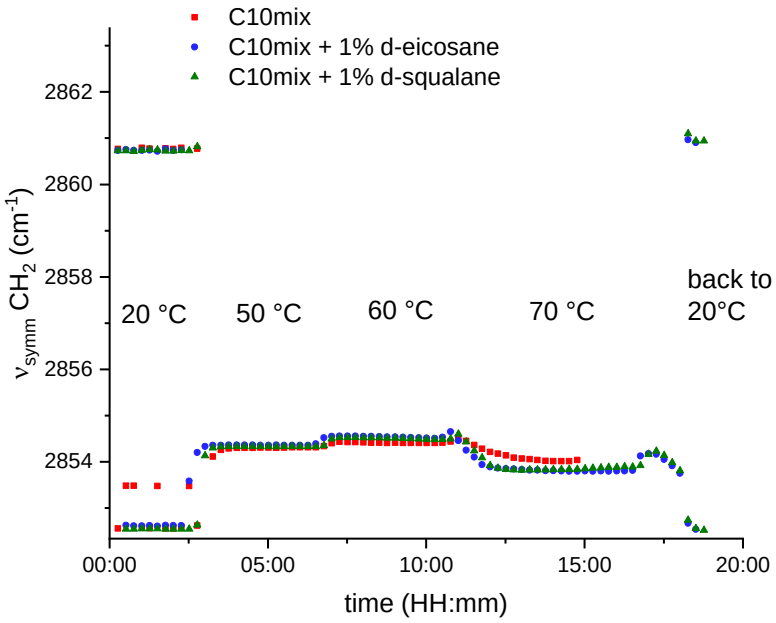

Figure S2. Frequency ν_{symm} as function of the time, following various temperature-jumps for all the samples (similar to Figure 6 in the main text, but here showing the position of the coexisting peak at $\nu_{symm} \approx 2861$ cm^{-1}).

FTIR data analysis

Figure S2 shows the same data presented in Figure 6 (right) in the main text, but on a wider v range to show the peak coexistence (and the position of the second peak at $\nu_{symm} \approx 2861$ cm^{-1}) observed at T = 20 °C at the beginning and the end of the scan.

Alkane viscosity

Figure S3 plots values of the dynamic viscosity of eicosane and squalane as function of temperature, taken from the literature[12,13]. The difference in the vesicle behavior in the low and the high temperature ranges may be linked to the fluidity of the incorporated alkane molecules.

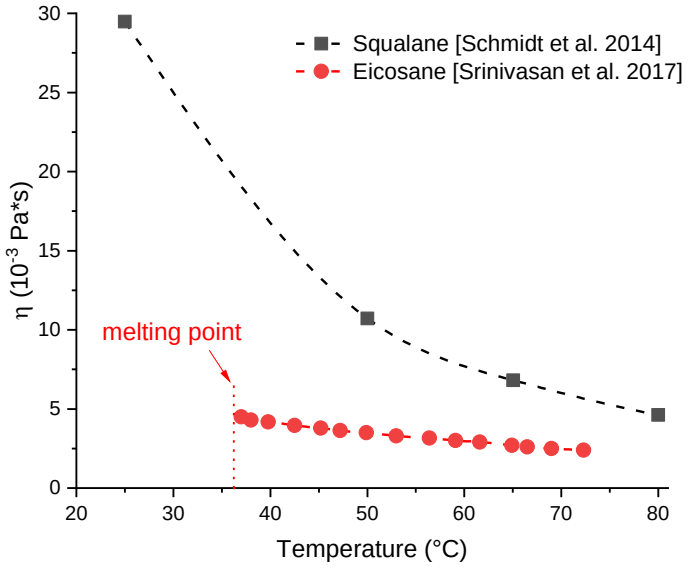

Figure S3. Dynamic viscosity of eicosane and squalane as function of temperature. Data taken from[12,13].

Table 1S. Full list of SANS fit parameters. The values for the fractions (lamellar and sphere) are normalized to the lipid volume fraction. ULV: Unilamellar Vesicle; BLV: Bilamellar Vesicle; PD: polidispersity index. * Since the Guinier regime is not fully reached at low q for the dense sphere form factors, the radius values found from the fits are not reliable and should be considered as minimum values instead.

References

[1] L. Misuraca, A. Caliò, I. Grillo, A. Grélard, P. Marie Oger, J. Peters, B. Demé, *Langmuir* **2020**, *36*, 13516–13526.
[2] B. J. Frisken, *Appl. Opt.* **2001**, *40*, 4087–4091.
[3] C. D. Dewhurst, I. Grillo, D. Honecker, M. Bonnaud, M. Jacques, C. Amrouni, A. Perillo-Marcone, G. Manzin, R. Cubitt, *J. Appl. Crystallogr.* **2016**, *49*, 1–14.
[4] B. Farago, P. Falus, I. Hoffmann, M. Gradzielski, F. Thomas, C. Gomez, *Neutron News* **2015**, *26*, 15–17.
[5] A. G. Zilman, R. Granek, *Phys. Rev. Lett.* **1996**, *77*, 4788.
[6] U. Seifert, S. A. Langer, *EPL (Europhysics Lett.* **1993**, *23*, 71.
[7] W. Rawicz, K. C. Olbrich, T. McIntosh, D. Needham, E. Evans, *Biophys. J.* **2000**, *79*, 328–339.
[8] I. Hoffmann, *Colloid Polym. Sci.* **2014**, *292*, 2053–2069.
[9] S. Gupta, J. U. De Mel, G. J. Schneider, *Curr. Opin. Colloid Interface Sci.* **2019**, *42*, 121–136.
[10] A. Guinier, G. Fournet, K. L. Yudowitch, **1955**.
[11] F. Nallet, R. Laversanne, D. Roux, *J. Phys. II* **1993**, *3*, 487–502.
[12] K. A. G. Schmidt, D. Pagnutti, M. D. Curran, A. Singh, J. P. M. Trusler, G. C. Maitland, M. McBride-Wright, *J. Chem. Eng. Data* **2015**, *60*, 137–150.
[13] S. Srinivasan, M. S. Diallo, S. K. Saha, O. A. Abass, A. Sharma, G. Balasubramanian, *Int. J. Heat Mass Transf.* **2017**, *114*, 318–323.

sample	**C10 mix**				**C10 mix + 2% h-eicosane**				**C10 mix + 2% h-squalane**			
temperature (°C)	20.5	39.69	60.11	78.73	20.5	39.69	60.11	78.73	20.5	39.69	60.11	78.73
fitting model	lamellar (ULV + BLV)	lamellar (ULV + BLV)	sphere + lamellar	sphere	lamellar (ULV + BLV)	sphere + lamellar (ULV)	lamellar	sphere	sphere + lamellar (ULV)	sphere + lamellar (ULV)	lamellar	sphere
q range (Å-1)	all	all	all	all	all	all	0.04 - 0.566	all	all	all	0.04 - 0.566	all
chi^2/(Npts)	6.1	4.9	3.55	2	23	46.4	4.8	83.1	17.9	22.1	2.8	8.6
*lamellar fraction *10^{-3}*	239 ± 0.8	245.2 ± 0.9	7.4 ± 0.2	---	869 ± 1	176.8 ± 0.2	186 ± 0.6	---	478.3 ± 0.6	358.9 ± 0.7	50 ± 2	---
vesicle radius (Å)	412 ± 2 (ULV); 154 ± 6 (BLV)	433 ± 2 (ULV); 164 ± 6 (BLV)	---	---	389 ± 3 (ULV); 157 ± 3 (BLV)	119 ± 1	---	---	397 ± 3	175 ± 2	---	---
membrane thickness (Å)	21.8 ± 0.1	21.8 ± 0.1	20 (fixed)	---	23.6 ± 0.1	21.5 ± 0.1	20.1 ± 0.1	---	22.2 ± 0.1	20.5 ± 0.1	16 ± 1	---
solvent thickness (for BLV) (Å)	115.8 ± 0.5	130.3 ± 0.6	---	---	69.8 ± 0.6	---	---	---	---	---	---	---
*sphere fraction *10^{-3}*	---	---	85.0 ± 0.2	58.8 ± 0.2	---	154.3 ± 0.2	---	424.8 ± 0.3	458.3 ± 0.2	156.1 ± 0.2	---	278.1 ± 0.2
sphere radius (Å)	---	---	768 *	430 *	---	281 *	---	420 *	516 *	439 *	---	425 *
vesicle radius PD	0.19 (ULV); 0.54 (BLV)	0.18 (ULV); 0.48 (BLV)	---	---	0.30 (ULV); 0.67 (BLV)	0.62	---	---	0.45	0.59	---	---
sphere radius PD	---	---	1	1	---	1	---	1	0.13	0.7	---	1
solvent thickness PD (for BLV)	0.22	0.24	---	---	1	---	---	---	---	---	---	---

3.2.2.2 *Notes: Article 3 results in the Thesis context*

One of the main results found and presented in the Article 3 is that the conformational change, observed as an onset of the macromolecular structure (initially vesicle) size increase with temperature observed by DLS, is due to a phase change of the vesicles into dense lipid droplets. At first sight, these results may seem to be contradicting what has been found and discussed in Article 1. There, the data from C10 mix indicated that the totality of the sample was in a lamellar structure even at the highest measured temperature of T = 78.2 °C (Figure 9 of Article 1).

The apparent controversy is solved when considering the difference in the sample states for the two cases. The SANS data in Article 1 refer to a C10 mix sample in form of MLVs (not extruded) at 350 mM concentration, while all samples presented in the Article 3 are in ULV state (extruded through 100 nm pore membranes) at 80 mM.

In order to define the source of the observed difference in the samples behavior, whether it was due to the lamellarity or the concentration difference (or both), an additional set of measurement was performed on D33 on a copy of the C10 mix sample at 80 mM that did not undergo extrusion. Figure 15 shows the resulting curves after the temperature scan, compared to the scan made on the extruded sample.

The data are shown in the Iq^2 representation and have not been shifted vertically, therefore: a) the lamellar phase, which follows a q^{-2} decay, is seen as a constant line with zero slope in this representation; b) the intensity value in the range where the lamellar form factor dominates (0.03 Å < q < 0.1 Å) can be used to compare qualitatively the amount of lamellar fraction.

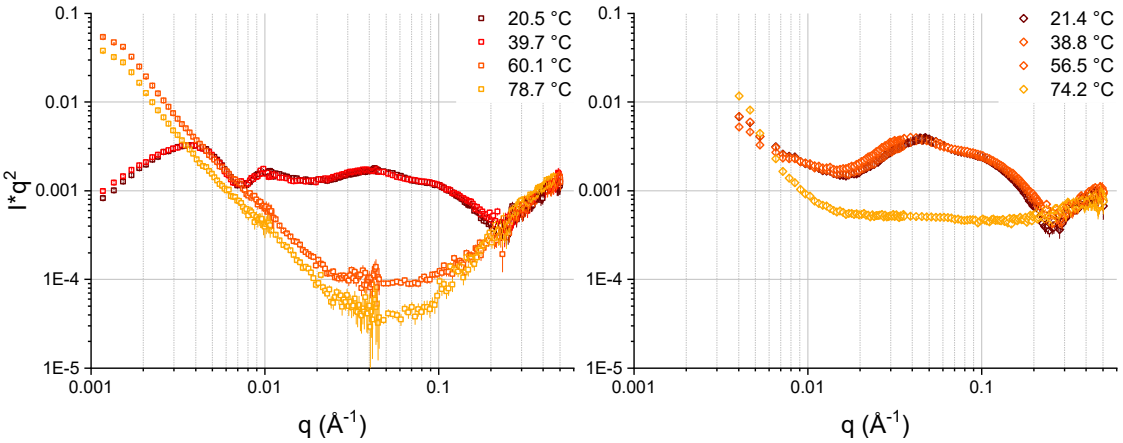

Figure 15: Comparison of SANS curves at four temperatures in the range 20 °C < T < 80 °C, between extruded and non extruded C10 mix 80 mM samples. The curves are shown in the Iq^2 representation, to highlight the presence (and amount) of lamellar phase in the sample. Left: extruded sample (same data shown in the left panel of Figure 2 of Article 3, but in the Iq^2 representation and without vertical shift of the curves). Right: non extruded sample.

The extruded sample (left panel) shows the presence of lamellar phase at ambient temperature ($T = 20\,^{\circ}C$). The curve deviates slightly from the q^{-2} decay because of an additional fraction of bilamellar vesicles (that indeed is needed to fit the curve, as detailed in Article 3). The curve at $T = 40\,^{\circ}C$ is almost completely superimposed to the one at $T = 20\,^{\circ}C$, meaning that the sample did not undergo significant changes. At $T = 60\,^{\circ}C$ the lamellar fraction has almost completely disappeared as the curve follows mostly a q^{-4} decay (characteristic of dense spheres), and at the highest temperature the SANS can be fitted by a dense sphere form factor exclusively.

Conversely, the non extruded sample (right panel) shows the presence of a high amount of sample in the lamellar phase at the first three temperatures with small variations. Here, the deviations from the q^{-2} decay are due to the presence of membrane correlations, as expected for non extruded samples. Even at the highest measured temperature of $T = 74.2\,^{\circ}C$, although the membrane correlation has disappeared and the intensity in the $0.03\,Å < q < 0.1\,Å$ region is lowered, the curve still follows a well defined q^{-2} decay.

This suggests that there is still a significant amount of sample that is assembled into lamellae at the highest temperature, a clear difference with respect to the sample that has been extruded prior to the temperature scan.

The additional result presented here clearly shows that the extrusion has more profound implications on the sample state and response to the environment (in this case, the thermal stress). The molecular rearrangement triggered by the temperature, while still happening on the MLV systems (as proven by the ssNMR data, Figure 5 of Article 1) seems to have different effects, perhaps related to the significant variance in size between ULVs and MLVs or to a further protection offered by the many MLV shells to each other against phase separation.

A systematic study on the impact of membrane lamellarity in the vesicle thermal response should be pursued in future work.

3.2.3 Article 4: Alkane localisation inside a compliant protomembrane model at atomic scale

3.2.3.1 *Foreword*

The presence of the alkane molecules in a model protomembrane composed by single, short chain amphiphiles has been found to bring a series of interesting consequences in the membrane properties and behaviour upon temperature and hydrostatic pressure increase (as shown from the results in the Articles 2 and 3). What is still left to the investigation is how the alkanes position themselves inside the protomembranes, in order to give the many observed effects in the membrane properties.

Initially, the answer to this question was foreseen by the use of SAND and the preparation of sample copies containing either the hydrogenated or the perdeuterated form of the alkanes under study.

However, the preparation of oriented multilamellar stacks on solid substrate (silicon wafer) that is a pre-requisite to successfully perform the *Fourier analysis* with SAND data, revealed to be challenging. The usual approach of solubilizing the lipids in organic solution and spreading them on the flat substrate to dry (commonly used with phospholipids) did not work with decanoic acid nor with C10 mix. In the first case, the obtained sample led to weakly-oriented diffraction patterns (powder diffraction) that were not swelling upon humidity increase (Figure 16 left panel).

Instead, with the C10 mix the film is impossible to create, because the mixture stays liquid at ambient temperature, thus the organic solvent evaporates leaving a liquid droplet on top of the wafer (sample de-wetting). Different organic solvents and ratios were tested (some examples: pure chloroform, chloroform:methanol 2:1 - 1:1 - 1:2, isopropanol, isopropanol:pentane 1:1) but none of them prevented the sample from de-wetting.

The only strategy that allowed to create films was through deposition of vesicles suspended in bicine buffer, left to dry on the flat surface. Nevertheless, this last technique did not lead to any Bragg peak observation for the C10 mix sample (meaning that the sample did not show any membrane ordering); a structuring was observed for samples made purely by decanoic acid vesicles, but only two subsequent orders of diffraction were observed (meaning that a very weak membrane ordering was achieved, Figure 16 right panel). This precluded any further investigation on such samples, because a minimum of 4 Bragg peaks are needed to perform the *Fourier analysis*.

There are many possible reasons for the observed infeasibility in creating ordered membrane stacks with the short, single chain amphiphiles. The first, and

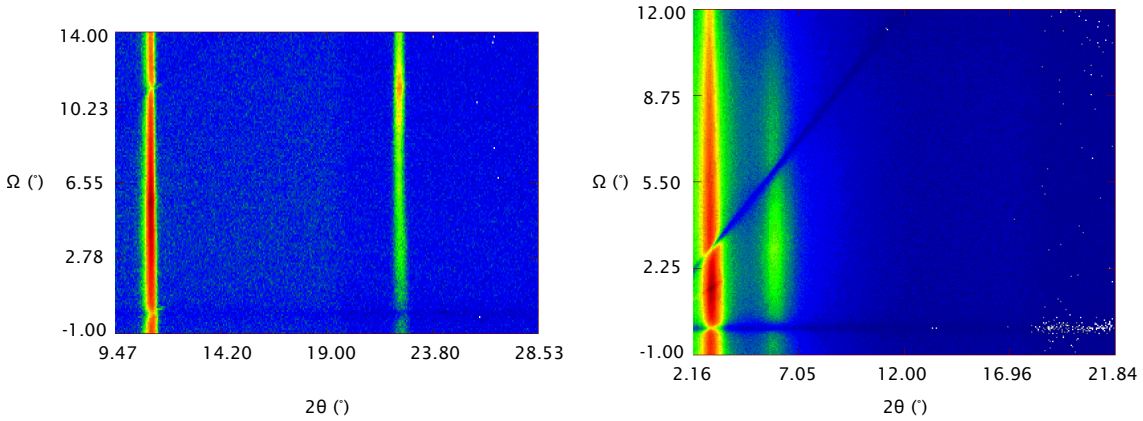

Figure 16: Comparison of reciprocal space maps obtained with SAND. Left: decanoic acid sample prepared from organic solution (chloroform:methanol 1:9), equilibrated at 100% relative humidity of D_2O 100%. The very low $d-spacing \approx 21$ Å, approximately equivalent to double the size of one decanoic acid molecule, implies that there is little to no water present between the layers. Right: decanoic acid sample prepared from vesicle deposition (decanoic acid:bicine 1:1 molar ratio), equilibrated at 95% relative humidity of D_2O 70%. The $d-spacing \approx 86$ Å implies that this sample contains hydrated multilayers, although the only two peaks visible indicate a weak vertical ordering. Note the large difference in 2ϑ scale between the two maps. Full details about the use of D_2O contrasts and relative humidity are found in the Article 4 of this thesis.

maybe the principal reason, is the fact that the headgroup of these molecules is weakly hydrophilic, thus it does not bind efficiently with the surface of the silicon wafer (which is hydrophilic).

An additional test was made by coating the surface of the silicon wafers with Octadecyltrichlorosilane (OTS). OTS is an amphiphilic molecule with a long hydrophobic chain (C18) and a polar headgroup ($SiCl_3$). The coating results in a OTS monolayer on top of the silicon surface, with the acyl chains pointing towards the interface with the air. This now-hydrophobic surface should allow, in principle, the membrane stack formation starting from the hydrophobic chains of the samples. However, the OTS coating did not prevent the samples from de-wetting.

The second, and third reasons to explain the technical difficulties have to do with the very short chain length and the fact that these systems are single-chain amphiphiles. These features probably prevent the formation of an ordered array in the vertical direction of the wafer, and the molecules tend to arrange at random directions instead.

In order to perform the alkane localization, in view of the above mentioned technical issues, an alternative sample was used. This sample was a multilamellar stack of DCPC, a phosphatidylcholine with the same chain length as the decanoic acid and the decanol. From one hand, the more hydrophilic PC headgroup could allow a successful preparation of multilamellar membrane stacks. On the other

hand, the use of the same chain length as the single chain amphiphiles could help linking the alkane positioning into both kind of samples. The details of this work can be found in the following Article 4.

In this work, I wrote the proposals for neutron beamtime, prepared the samples, performed the experiments on D16 (SAND), analyzed the data and wrote the paper.

The paper is in submission to *Biochimica et Biophysica Acta - Biomembranes (Elsevier)*.

Alkane localisation inside a compliant protomembrane model at atomic scale

Loreto Misuraca[a,b], Josephine LoRicco[c], Philippe Oger[c], Judith Peters[a,b], Bruno Demé[b]

[a] Univ. Grenoble Alpes, CNRS, LIPhy, 38000 Grenoble, France
[b] Institut Laue - Langevin, F-38042 Grenoble Cedex 9, France
[c] INSA Lyon, Université de Lyon, CNRS, UMR5240, Villeurbanne, France

Abstract

Model biomembranes composed by short chain lipids are of great interest to study the origin of cellular life. This is because Fischer-Tropsch type reactions, occurring in the early Earth environment, likely favored formation of short lipid chains (C < 12). Recent studies have shown that inclusion of small quantities of apolar hydrocarbons in model proto-membrane forming mixtures has a significant impact on the membrane stability towards high temperature and high pressure conditions. Here, we performed an in-depth structural investigation, using neutron diffraction, of a short chain phospholipid membrane including (or not) linear or branched hydrocarbons. Both water contrast variation, using H_2O and D_2O pure or mixed, as well as membrane swelling through humidity scans were used to determine the corresponding membrane neutron scattering length density profiles. We found that the alkanes eicosane and squalane are incorporated in the midplane of the membrane hydrophobic core. The data show a preferential positioning of these alkanes, sitting perpendicular to the phospholipid tails and therefore causing a slight increase of the membrane thickness. The alkanes may also play a role in reducing membrane swelling upon hydration.

Introduction

The cell membrane is among the most fascinating macromolecular structures that make up all living systems. It is a biological two-dimensional matrix that separates and protects the interior of the cell from its environment. The basic unit of cell membranes (which generally consist of lipids, proteins and carbohydrates) is a bilayer of polar lipids (phospholipids, glycolipids) whose polar head-groups point outwards (the membrane surface), while the hydrophobic acyl chains constitute the membrane core. Biomembranes promote the compartmentalization of living systems, which is an essential property for the definition of life. In fact, the formation of early membranes is believed to have played a key role in the first steps toward the origin of life on our planet[1–5].

Due to the importance of membranes in the origin and definition of life, several membrane structural studies have been performed in order to obtain quantitative information on molecular organization, phase changes and separations, incorporation and effects of host molecules and macromolecules etc. Such structural characterization is generally complicated by the fact that the biologically relevant phases are not crystalline, therefore there is no three-dimensional repeat unit that can be resolved through usual crystallographic methods. Instead, lipids typically arrange into liquid-crystalline phases, e.g. gel (L_β, P_β) or fluid (L_α) lamellar phases which possess intrinsic static and/or dynamic lateral disorder. X-ray and neutron diffraction techniques have been important tools in this respect, because they allow one-dimensional information of the membrane ordering along the bilayer plane normal to be obtained, despite the lateral disorder of the L_α, L_β and fluid phases.

From seminal studies performed back in the 1970s[6–9], a new methodology was developed to extract the neutron and x-ray scattering length density (SLD) profiles of membranes at near-atomic resolution from so-called membrane diffraction data of oriented solid-supported membrane stacks. The analysis of the SLD profiles gives information on the average positioning and dimensions of each membrane constituent[10]: hydrocarbon chains, headgroup components (e.g. the phosphate and the choline groups)[11,12], water and additional incorporated host molecules when present (e.g. cholesterol)[7,8].

With this quantitative information at hand, one can investigate the location of intercalants within the membrane and correlate it with the observed consequences on the membrane structure, as well as its properties and functioning. This was done, for example, by using n-alkanes of varying chain length to investigate the mechanisms of anaesthesia[13,14]. These studies proved that a significant amount of n-alkanes (e.g. hexane[15]) entered the bilayer core, although the resolution was not sufficient to determine whether there was a preferential positioning (i.e. sitting parallel or perpendicular to the lipid acyl chains). Another study[16] was performed using high amount of C6 – C16 n-alkanes (0.3 – 0.9 alkane:lipid ratio) on egg PC membranes, finding that smaller n-alkane chain lengths contributed to an increase in bilayer thickness. More recently, the exact positioning of small amounts of squalane (branched C30 alkane) was determined in model membranes made of DOPC:DOPG[17] and an archaea-mimicking mixture DOPhPC:DOPhPE[18]. In both cases, squalane was found to enter the lipid membrane and to position in the mid-plane of the bilayers perpendicularly to the lipid tails. Moreover, the two studies highlighted the possibilities for such incorporated molecules to act as proton permeability barrier[17] and to trigger domain phase formation[18].

In analogy with previous findings, our group has studied the incorporation of n-alkanes in early life membrane models composed of short single chain amphiphiles (SCAs) with C10 tail length [Misuraca et al., accepted to Comm.Chem.]. The reason for this lies in the likely presence of a broad size distribution of n-alkanes (especially linear ones) along with SCAs in the early Earth environment, as both species are readily formed via Fischer-Tropsch type reactions[19,20]. If a structural role could be identified for such apolar molecules into the prebiotic membranes, this would help explain how SCA membranes could have withstood the harsh environmental conditions of the early planet. In our recent study [Misuraca et al., accepted to Comm.Chem.] we found that the alkanes squalane and eicosane (C20 linear) decrease the temperature induced membrane swelling of multilamellar vesicles (MLVs) and decrease the membrane sensitivity towards high hydrostatic pressure. These results show that incorporation of n-alkanes can indeed confer a higher membrane stability towards high temperature and pressure and therefore could have played a major role in the formation of the first forms of life.

It is now important to determine the actual positioning of such molecules inside short-chain membranes. First, the existence of a preferential direction of the n-alkanes inside the membrane could help gain insight into the mechanisms by which the bilayers acquire a higher thermo- and piezo-stability. Second, it might explain the need for more or less intercalant in order to obtain significant effects in the membrane (for instance, an orientation of the alkanes perpendicular to the acyl chains might correlate with very small amounts needed in the membrane). Third, the positioning may (or may not) affect membrane structural features, e.g. the bilayer thickness, possibly offering a way to obtain a thicker membrane even in conditions where only short chain lipids are available.

Previous structural studies of model membranes have focused on lipids having chain length of 12 carbons or longer[11,12,21]. Here, we perform our investigation using the C10 PC lipid 1,2-didecanoyl-*sn*-glycero-3-phophocholine (hereafter DCPC, Figure 1a) as phospholipid C10 analogue of the previously studies SCA membranes[22] [Misuraca et al., accepted to

Comm.Chem.]. This allows to profit from the optimized procedures for successfully producing PC lipid membrane stacks onto silicon substrates[11], which are needed for obtaining structural information by neutron diffraction. We combined two approaches to neutron diffraction studies, contrast variation and membrane swelling (see Materials and Methods section), to fully characterize DCPC bilayers in the absence or presence of small amounts of three alkanes eicosane (Figure 1b), squalane (Figure 1c) and triacontane (C30 linear, Figure 1d).

We found that the alkanes eicosane and squalane enter the membrane hydrophobic core and lead to an increase of the bilayer thickness compared to the alkane-lacking sample. Conversely, the triacontane does not lead to an increase in membrane thickness, hence questioning its incorporation into the membrane and suggesting a role of the n-alkane length for a successful inclusion in the bilayer. Moreover, a small variation in the decay length of the osmotic pressure vs. distance curves suggests a possible role of the eicosane and squalane in decreasing slightly the membrane swelling limit at maximum hydration.

Materials and method

1. Sample preparation

DCPC was purchased from Avanti Polar Lipids (Alabaster, USA). Hydrogenated and perdeuterated eicosane, squalane and triacontane were purchased from Sigma Aldrich (Merck). All products were used as received from the manufacturer, without further purification. 5 mg of DCPC or DCPC with 4% molar of the corresponding hydrogenated or deuterated alkane (eicosane, squalane or triacontane) were dissolved in chloroform:methanol (2:1), spread on a silicon wafer (Silicon Materials Inc.; Pittsburg, USA) using the “rock and roll” method[23] and dried overnight under vacuum. Next, the samples were placed in sealed Falcon tubes containing 100 µL of H_2O at 40 °C for 24 hours for annealing. Finally, samples were stored at ambient temperature before the experiments.

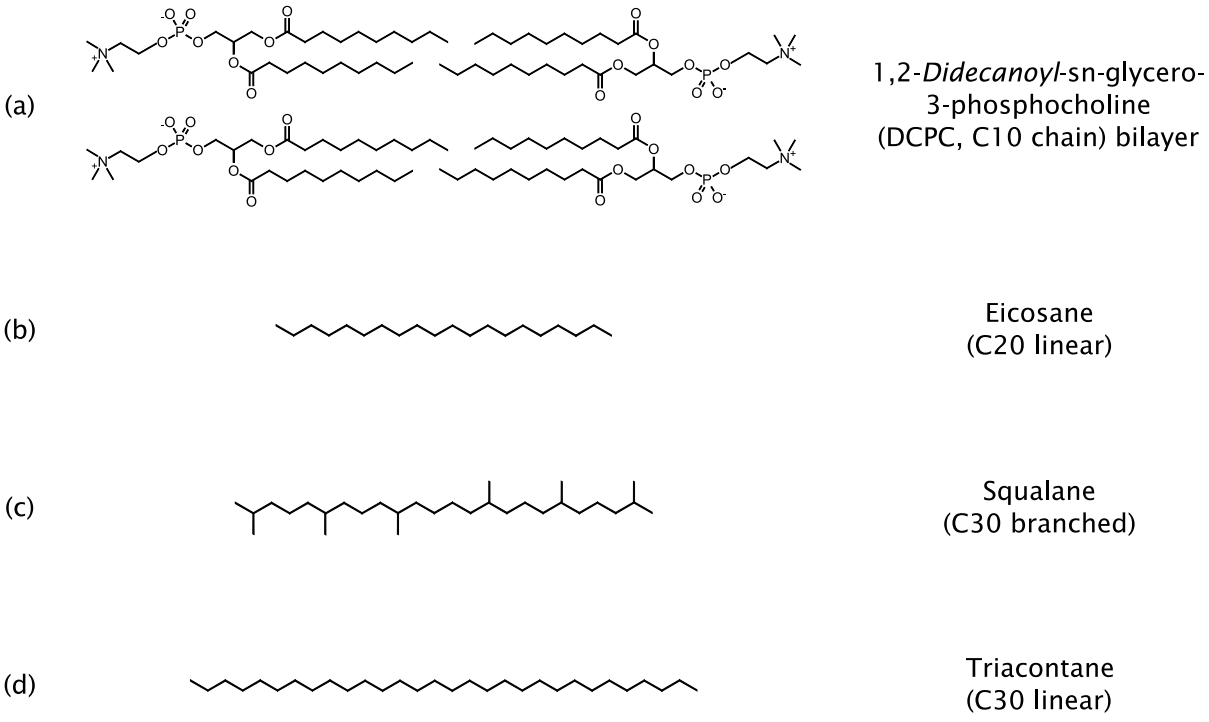

Figure 1. Chemical structure of the compounds used in this work. (a): bilayer of DCPC lipids; (b): eicosane; (c): squalane; (d): triacontane.

2. Neutron Diffraction experiment

Neutron diffraction experiments were performed on the D16 cold neutron diffractometer[24] at the Institut Laue-Langevin (ILL, Grenoble, France). The incident wavelength was 4.465 Å. The position sensitive 2D-detector MILAND (320 x 320 mm^2 with 1 x 1 mm pixel resolution) was set to a sample-to-detector distance of 0.950 mm. Diffraction data (sample rocking scans or Ω-scans) were collected in reflection geometry by scanning the sample angle with respect to the incident beam (Ω) using 0.05° increments at two detector positions, $\Gamma = 12°$ ($-1 < \Omega < 12°$) and $\Gamma = 28°$ ($8 < \Omega < 18°$) in order to collect the maximum number of orders of diffraction (Figure 2). Γ denotes the angle of the detector center with respect to the incident beam. This choice of angular ranges leads to a continuous q-range of 0.06 $Å^{-1}$ - 0.86 $Å^{-1}$, where q is the neutron scattering vector. Diffraction experiments were performed using the BerILL[25] chamber allowing for precise control of the humidity and the temperature. The temperature at the sample position, regulated by a thermal bath, was kept at the constant value of T = 25 °C. The relative humidity (RH) was precisely regulated by the temperature difference between the sample and the water reservoir using a dedicated Lakeshore 336 controller and high-precision temperature sensors[25].

The DCPC samples, pure or containing 4% of either hydrogenated or deuterated alkanes, were measured following two different procedures. In the first (*contrast variation experiments*), samples were incubated at a constant RH of 97% for 2 hours before starting each scan. Each of them were incubated three times inside the humidity chamber at different D_2O contrasts, with the reservoir filled with 20 ml of different mixtures of D_2O/H_2O (8%, 70% or 100%). The different contrasts were used to extract the phase of each Bragg reflection required to determine the membrane neutron scattering length density (NSLD) profile[7].
In the second experimental procedure (*swelling experiments*), the D_2O/H_2O solvent contrast was set to a zero NSLD obtained using the 8% D_2O mixture. Here, the RH was varied from 30% up to ≈ 100% in order to scan the sample lamellar spacing and Bragg reflection intensities as a function of humidity from a dehydrated state up to full hydration. Sample equilibration was gradually increased from 1 hour (used for the lowest humidity steps) up to 2.5 hours for the sample equilibrated at 99.5% RH. For the last measurement aimed at reaching full hydration, samples were equilibrated for 24 hours.

An example of reciprocal space map obtained by merging two Ω-scans is shown in Figure 2. The obtained 2D map corresponds to the reciprocal space map in angular coordinates (Ω vs 2θ)[26]. The first visible feature is the occurrence of a series of reflections located at the same periodicity (q_z) on top of the line $\Omega = (2\theta)/2$ that corresponds to the specular condition. The periodicity identified by the reflections results from the lamellar ordering of the multilayer, with a repeat distance given by one bilayer plus one water layer. Each reflection does not have the shape of a peak in the vertical (Ω) direction, as would be expected from a diffracting crystal. Instead, there are elongated features (called *Bragg sheets*) which are a sign of the disorder (static or dynamic) in the membrane plane ($q_{//}$) and can be considered as a signature of a liquid crystal. Two minima lines are defined from the 2D map, one that is located at constant $\Omega = 0$ and the other tracing the line $\Omega = 2\theta$. These minima corresponds to the so-called *sample horizons*, and occur at the angles where the scattered beam is attenuated by crossing longitudinally the silicon substrate.

3. Data reduction

Data reduction was performed using the ILL software LAMP[27]. Pixel efficiency as well as solid angle corrections were performed using a detector calibration obtained from the flat incoherent scattering signal of a water measurement. The background was obtained by collecting an empty humidity chamber scan and was subtracted from each measurement. The background-subtracted data were then exported for further analysis using Origin Pro (Version 2019, OriginLab Corporation, Northampton, MA, USA).

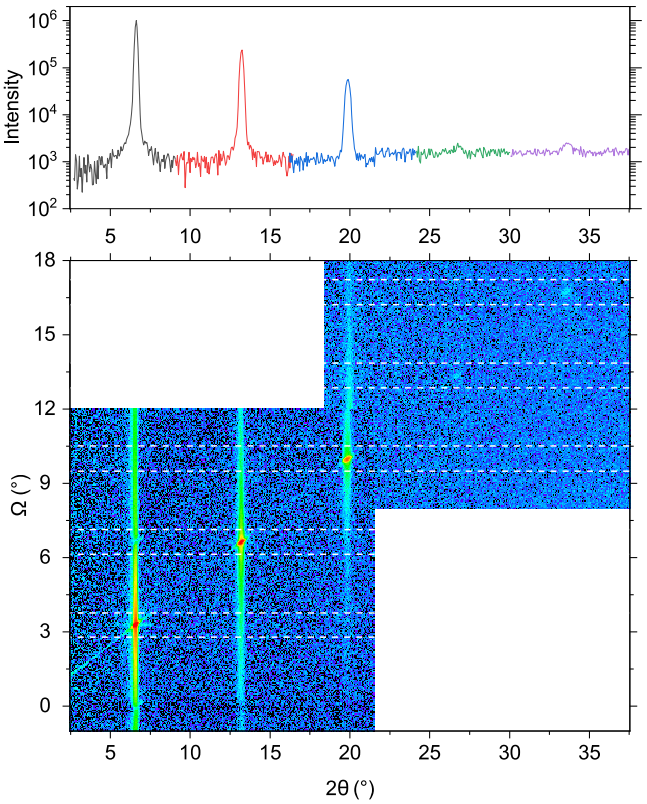

Figure 2. Example of reciprocal space map (Ω vs 2θ). The data shown here are from DCPC at 8% D_2O contrast and 30% relative humidity. Horizontal white dashed lines show the limits of integration for each diffraction order, while the top plot shows the result of the integrations truncated in the selected Ω and 2θ regions of interest for the peak fitting.

The data were reduced to 1D intensities vs 2θ plots by integrating for each peak a slice of Ω = 1° width around the peak center (see Figure 2).

The integrated intensities of the Bragg peaks were analyzed by fits with Gaussian functions, as done previously[28]. The angle (θ) of a Bragg peak is related to the scattering vector (q) by:

$$q = \frac{4\pi sin(\theta)}{\lambda} \quad (1)$$

where λ is the wavelength of the incident neutron beam. The periodicity (d-spacing) was derived as done previously[29,30]. For each sample and experimental condition, a weighted linear fit was performed on a plot of peak positions (in q) as function of the diffraction order (h) (known as *Bragg plot*), the slope (s) of which was used to determine the d-spacing via the equation:

$$d = \frac{2\pi}{s}. \quad (2)$$

The errors on the d-spacings were obtained by propagating the error of the peak position fitting and used in the weighted linear fit to the peak positions vs. Bragg order *h*.

The next step in the data analysis is to convert reciprocal space data into real space 1D structures. For that, the calculated area of each peak was employed to construct neutron scattering length density (NSLD) profiles from the sum of the neutron scattering lengths per unit volume[31]. The way the membrane stack NSLD profiles can be constructed comes from the definition of the scattering intensity I(q) as:

$$I(q) = P(q) * S(q) \quad (3)$$

where P(q), the form factor, contains the information about the repeated unit structure (in our case, one bilayer and one water layer) while S(q), the structure factor, is related to the interactions between adjacent membranes that leads to the Bragg reflections. Therefore, the S(q) features (the Bragg peaks) are modulated by the underlying form factor, and this property can be used to sample the form factor dependence with q at discrete positions exploiting the intensity modulation of all Bragg reflections that are observed in a sample scan[6–8]. The Fourier transform of P(q) in real space provides the NSLD profiles.

In practice, since one only has access to a finite number of q positions through the Bragg reflections, approximated NSLD profiles are calculated from the discrete set of Fourier coefficients F_h (also referred as "structure factors" in the text) using the following equation[6,7,9]:

$$\rho(z) = \sum_{h=1}^{h_{max}} |F_h| v_h cos\left(\frac{2\pi h}{d} z\right) \quad (4)$$

where d is the lamellar periodicity of the bilayer stack in the vertical z direction, $|F_h| = \pm\sqrt{I_h h}$ where I_h is the integrated intensity of the hth order Bragg peak and v_h is the phase of the structure factor terms that are in general complex quantities. However, in the case of centrosymmetric structures such as bilayers, $v_h = \pm 1$ and the phase assignment simplifies into the assignment of a + or - sign for each F_h term[7].

Finally, from the data acquired by scanning the RH (swelling experiments), the osmotic pressure (Π)[32,33] could be calculated from the relative humidity using the following equation:

$$\Pi = \frac{-k_B T}{v_w^0} ln(RH) \quad (5)$$

where RH is defined as P/P$_0$ (e.g. 0.5 for 50% RH), k_B is Boltzmann's constant, T is the temperature in Kelvin, and $v_w^0$is the molecular volume of water[29].

4. <u>Scattering Length Density profile determination</u>

In order to gather insights about the membrane structural changes, the first step was to extract the corresponding NSLD profiles of each sample. This was done by exploiting the modulation in the intensity of each membrane Structure Factor term $F_h(q)$ as detailed in the "Data reduction" section. The main challenge relies in the assignment of the phase which, in the case of centrosymmetric structures such as membrane stacks, simplifies into the assignment of a positive or negative sign to each term. In this work, we combined three strategies to obtain an unambiguous phase assignment:

1. Contrast variation: the use of different D_2O / H_2O isotopic composition allows to vary the water NSLD that is the contrast between bilayers and water layers. By using the fact that the NSLD of water increases linearly with the D_2O percentage, one can detect the occurrence of phase changes.

2. Swelling: when the RH of the environment increases, the membrane stack undergoes swelling, as a result of the its hydration and increase of the water layer thickness. Assuming that the bilayer structure does not change when the water layer increases, one can perform Relative Humidity (RH) scans and use the displacement in q of the Bragg reflections to sample the P(q) in a finite set of q positions[7]. With this technique, one obtains information on the possible sign swapping whenever the tracing of the P(q) vs q highlights the presence of a relative minimum.

3. Physical considerations from the observed NSLD profiles: as highlighted in the former points, the contrast variation and swelling techniques both allow detection of phase changes, but not the absolute phases. However, the features of the NSLD profiles can be qualitatively judged from our knowledge of the system. For instance, the acyl chains placed in the middle of the bilayer should give a broad minimum in the profile because of the high density of low scattering length hydrogen atoms. Conversely, the phosphate groups of the phosphatidylcholines (the DCPC headgroups) give local maxima that will be highly visible at the lowest D_2O contrast used of 8%. In addition, different D_2O contrasts at a constant RH do not change the shape of the NSLD in the hydrocarbon region. Similar considerations were also made when applying scaling and offset factors to the NSLD profiles to allow for comparisons between different samples: there, the NSLD profiles of the different samples were matched with each other in the solvent region, for the measurements performed at the same D_2O / H_2O contrast.

Results

Figure 3 shows the resulting contrast variation plots for the DCPC samples with and without hydrogenated and perdeuterated eicosane or squalane molecules. All numerical values of the structure factor terms and the measured d-spacing can be found in Table 1.

The choice of the sign for the 1st reflection order, the term which is a function of the overall periodicity of the repeat unit (the d-spacing), is assigned as negative in order to obtain a local minimum of the NSLD profiles at the z = 0 position (Figure 4). This translates into the choice of setting the centre of the bilayer repeated unit at the 0 axis position. All other phases were assigned by making sure that, in the following order:

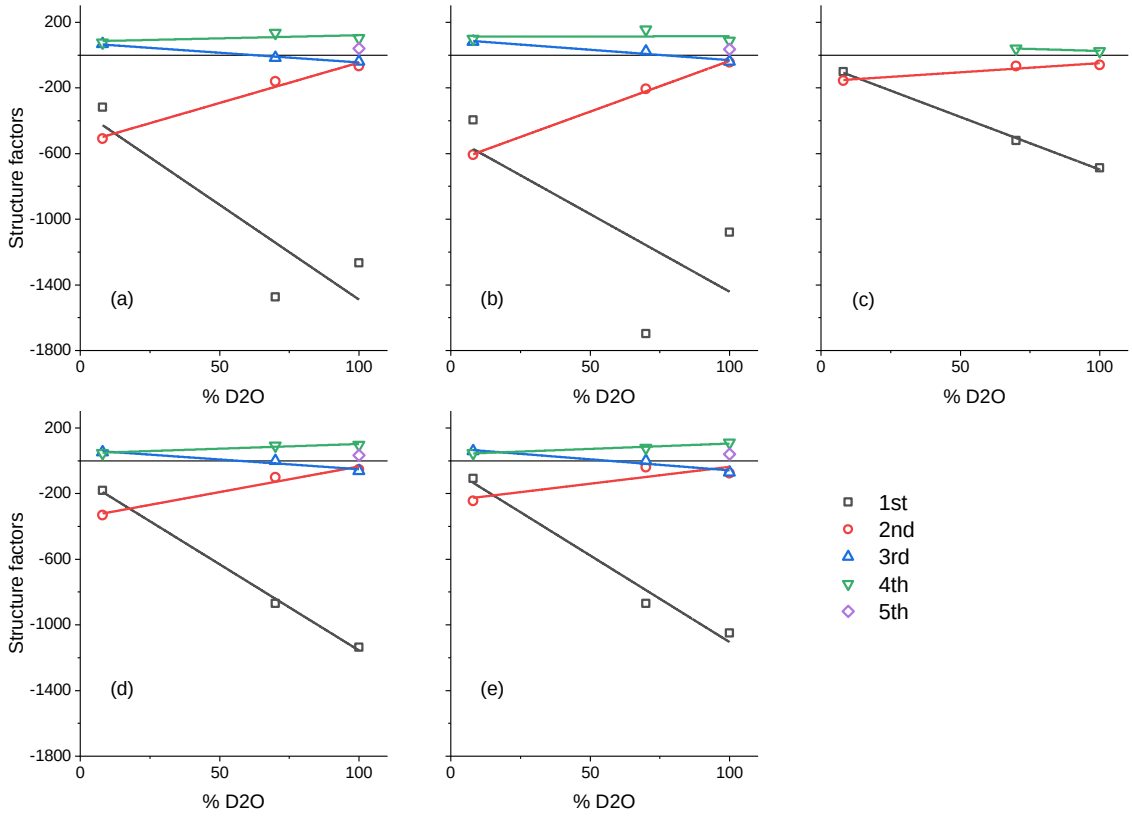

Figure 3. Contrast variation plots for the DCPC samples missing or containing alkanes. (a) DCPC + 4% h-eicosane. (b) DCPC + 4% h-squalane. (c) DCPC. (d) DCPC + 4% d-eicosane. (e) DCPC + 4% d-squalane.

Table 1. Structure factor terms F_h for the samples measured at three D_2O/H_2O contrasts and corresponding d-spacing. * Value calculated from the only 2 reflections observed.

Sample (all at 97% RH)	% D2O	Reflection order					d-spacing (Å)
		F_1	F_2	F_3	F_4	F_5	
DCPC	8	-102.2	-156.6	---	---	---	42.4*
	70	-521.3	-66.6	---	40.1	---	43.2 ± 0.2
	100	-686.8	-59.6	---	25.2	---	41.9 ± 0.1
DCPC + 4% h-eicosane	8	-318.8	-509.1	67	77.2	---	41.9 ± 0.1
	70	-1474.3	-160.3	-17.4	136.2	---	45.5 ± 0.2
	100	-1267.1	-67.3	-39.4	103.5	39.3	42.7 ± 0.1
DCPC + 4% d-eicosane	8	-180.5	-330.6	52.3	47.3	---	41.9 ± 0.1
	70	-870.3	-100.8	0	91.8	---	45.0 ± 0.3
	100	-1136.4	-53.2	-62.3	97.8	34.3	41.9 ± 0.2
DCPC + 4% h-squalane	8	-396	-608.2	81	98.5	---	42.0 ± 0.1
	70	-1696.3	-206.8	21.9	155.8	---	43.1 ± 0.2
	100	-1079	-44.4	-40.6	86.9	34.4	42.5 ± 0.1
DCPC + 4% d-squalane	8	-107.5	-245.6	59.2	47.3	---	42.1 ± 0.1
	70	-869.7	-38.8	0	78.3	---	46.0 ± 0.1
	100	-1050.3	-77.3	-70.6	109.7	40.2	42.5 ± 0.2

1) the linearity in the contrast variation plots was maintained (Figure 3);

2) combining the shape observation of the NSLD profiles at all 3 contrasts;

3) applying the phase change when needed (in our case, for the 3rd Bragg reflection order around 70% D_2O/H_2O percentage, visible in Figure 3).

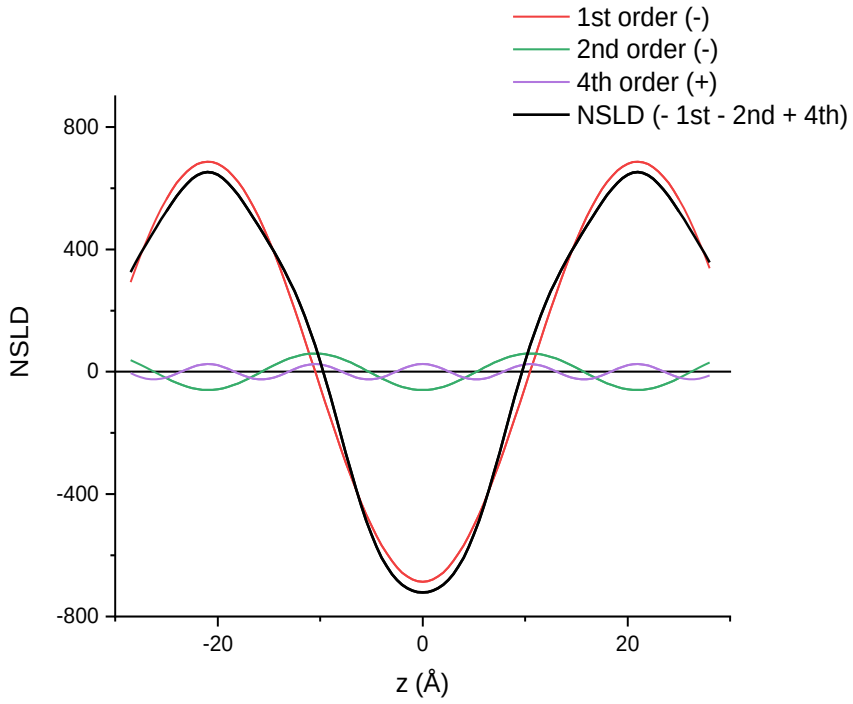

Figure 4. Plot of individual terms that contribute to the NSLD profile of the DCPC sample at 100% D_2O contrast, with the phases assigned as shown in panel (c) of Figure 3.

An imperfect linear trend is observed for the 1st order of reflection of the samples DCPC + 4% h-eicosane and DCPC + 4% h-squalane (panels (a) and (b) in Figure 3). This has been imputed to the very strong scattering signal, occurring already at 70% D_2O/H_2O contrast, which caused possible extinction effects on the first order reflection at 100% D_2O/H_2O (an effect previously observed[8]). Nevertheless, this does not affect the phase assignment.

In addition to phase information obtained using the contrast variation measurements, fully hydrogenated samples (DCPC, DCPC + 4% h-eicosane, DCPC + 4% h-squalane and DCPC + 4% h-triacontane) were measured at different RH in order to trace the q dependence of the membrane form factor P(q) and to possibly detect phase changes at the different hydration levels.

The resulting structure factor terms, after phase assignment, are plotted in Figure 5. Two main results are visible from the figure:

i. In all samples, the 4th order reflection undergoes a phase change at the two lowest RH values (50% and 30%);
ii. The two terms at the highest q position of each reflection (corresponding to the lowest measured RH values of 50% and 30%) are slightly off the main trend of the other data. This could be the sign that, at such low values of humidity, the bilayer structure changed significantly so that the underlying assumption of the swelling experiments (i.e. that the peaks shift upon water layer thickening while the bilayer form factor is constant) is no longer valid.

Nevertheless, the changes are low enough to assume that the considerations about the phases (negative or positive) are still valid. Only the phase of the 4th and 5th order of the 50% and 30% RH values could be questioned, in which case a further validation was performed by inspecting the shape of the corresponding NSLD profiles in the two cases.

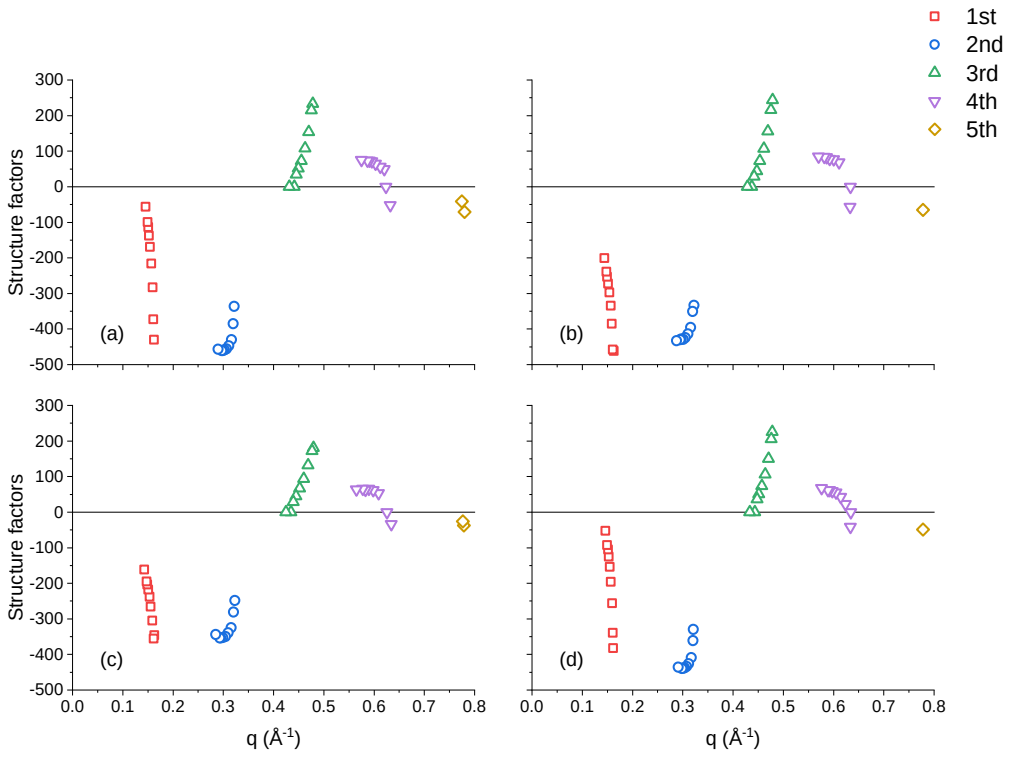

Figure 5. Structure factor terms as function of q obtained through RH scans, with relative phase assigned: (a) DCPC; (b) DCPC + 4% h-eicosane; (c) DCPC + 4% h-squalane; (d) DCPC + 4% h-triacontane.

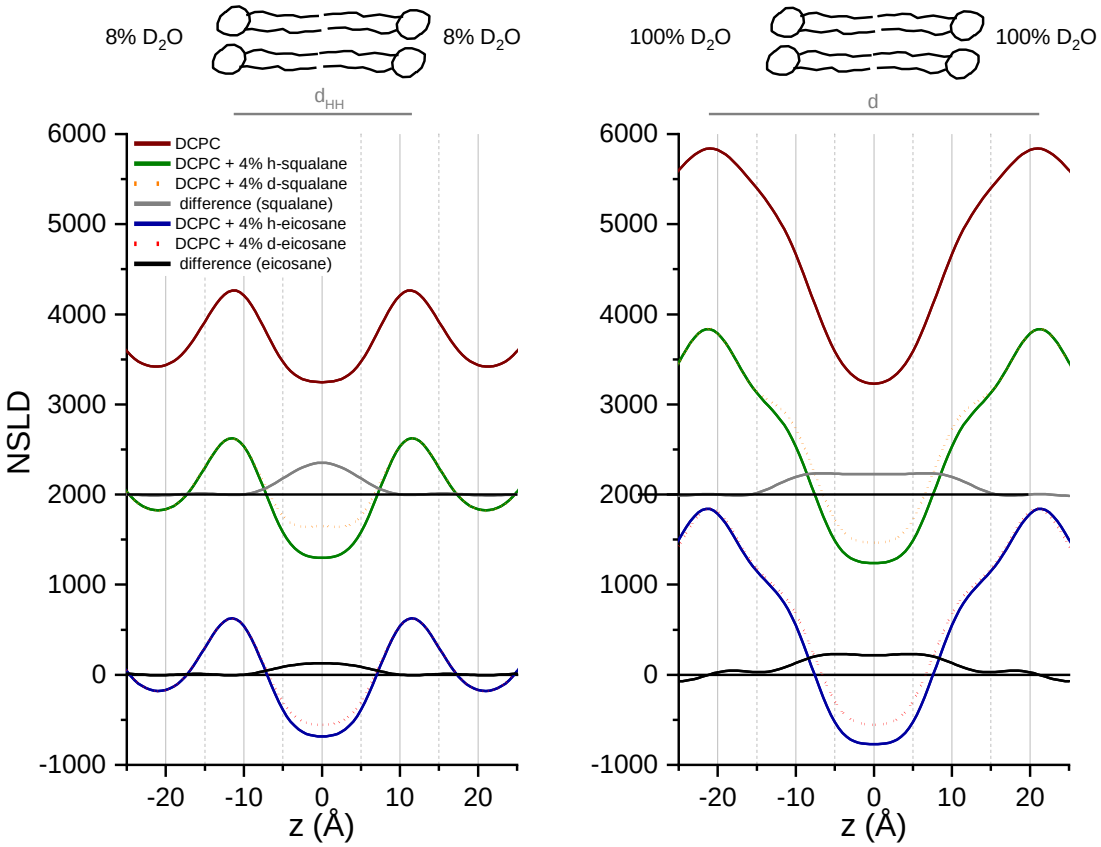

Figure 6. NSLD profiles of samples measured at 97% RH during contrast variation experiments. Left: 8% D_2O/H_2O contrast; right: 100% contrast. The y-axis refers to the eicosane containing samples, while the other NSLD profiles were shifted for clarity. Top image shows a sketch of the two bilayers mapped by the NSLD profiles in the z range shown and the quantities d_{HH} and d identified by the position of the maxima in the two cases.

Alkane localization

With all information about phases and phase changes at hand, the membrane NSLD profiles could be drawn by summing the contributions of each reflection order (all having the form of cosine functions, with an example depicted in Figure 4 and as detailed in the “Materials and Method” section) with the proper amplitude and phase. Figure 6 shows the NSLD profiles of the samples measured during the contrast variation experiments, at 8% and 100% D_2O/H_2O contrasts respectively. The 8% contrast allows easy definition of the position of the headgroup centres, as local maxima located at $z \approx \pm 11.5$ Å from the bilayer core.

On the other hand, in the 100% contrast the higher NSLD of D_2O gives local maxima in the middle of the water region at $z \approx \pm 21.3$ Å from the bilayer mid-point.

By superposing the NSLD profiles in the water regions for the samples containing the hydrogenated and deuterated form of the same alkane (h- and d-eicosane; h- and d-squalane), one can calculate the difference profiles and get information about the average alkane location inside the membrane. As shown in Figure 6, both alkanes are found to be incorporated and sit inside the bilayer in the hydrocarbon region, although a more precise localization (e.g. whether the molecules are placed perpendicularly or parallel to the acyl chains of the bilayer) is not possible. This is potentially due to two reasons:

1. The limited resolution of the NSLD profiles (here drawn using up to 5 Bragg reflections, the only ones experimentally visible);

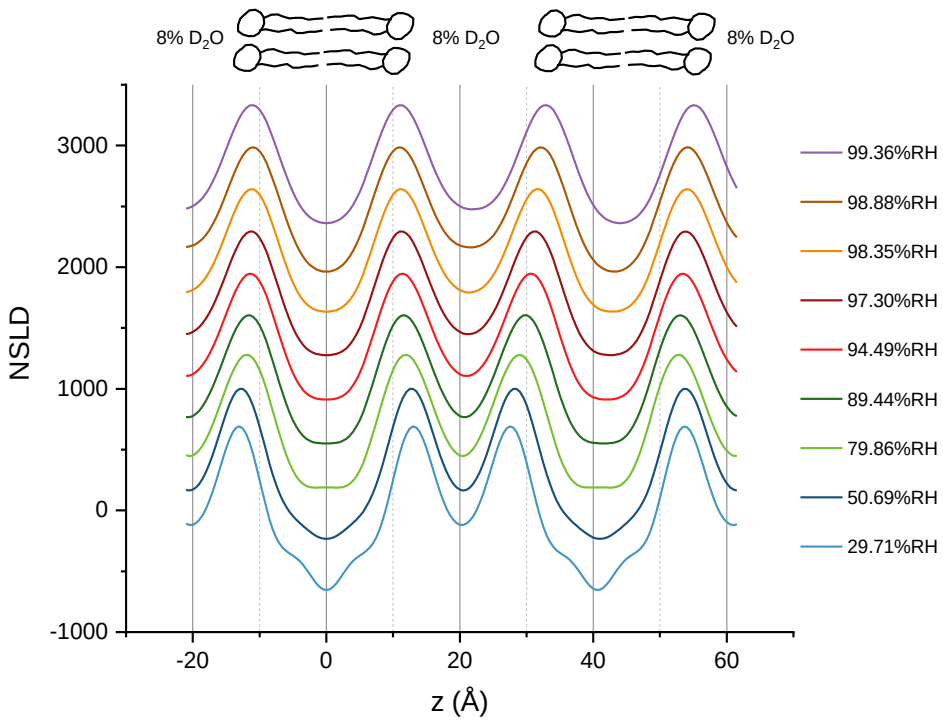

Figure 7. NSLD profiles of a DCPC sample during swelling experiments. Top image shows a sketch of the two bilayers mapped by the NSLD profiles in the z range shown. D_2O contrast was 8%.

2. Intrinsic disorder in the samples at the used alkane/lipid ratio of 4% (e.g. if portions of the alkanes position differently).

Membrane swelling

In addition to screening the phase behaviour of the membrane form factor as a function of humidity, swelling experiments (at 8% D_2O contrast, to easily locate the lipid headgroup position) provided further information on the membrane characteristics and properties. The samples measured here were a) DCPC; b) DCPC + 4% h-eicosane; c) DCPC + 4% h-squalane; d) DCPC + 4% h-triacontane. Figure 7 shows an example of the NSLD profiles obtained at each measured RH for the DCPC sample. Some qualitative features are visible from the plot:

- The lowest humidity values of 30% and 50% show a more pronounced minimum in the centre of the bilayer. This can be attributed to the presence of a higher density of hydrogen atoms at the terminal methyl group position, a feature that disappears at higher humidity values presumably because of an increase in membrane static and/or dynamic disorder.
- The repeat distance (d-spacing) increases with increasing RH, as expected because of the water layer thickening between the bilayers.
- The bilayer thickness decreases with increasing RH, shown in the plot as a shift of the headgroup maxima.

The last two features can be used for quantitative comparison between the different samples investigated. Figure 8 shows the bilayer thickness changes as function of humidity for all samples. We use here the same nomenclature applied in former diffraction studies carried out on DLPC and DMPC samples[11]. As a first definition of bilayer thickness, we define d_{HH} as the distance between the two maxima in the NSLD profiles at 8% D_2O contrast, that correspond to the distance between the phosphate groups of the PC.

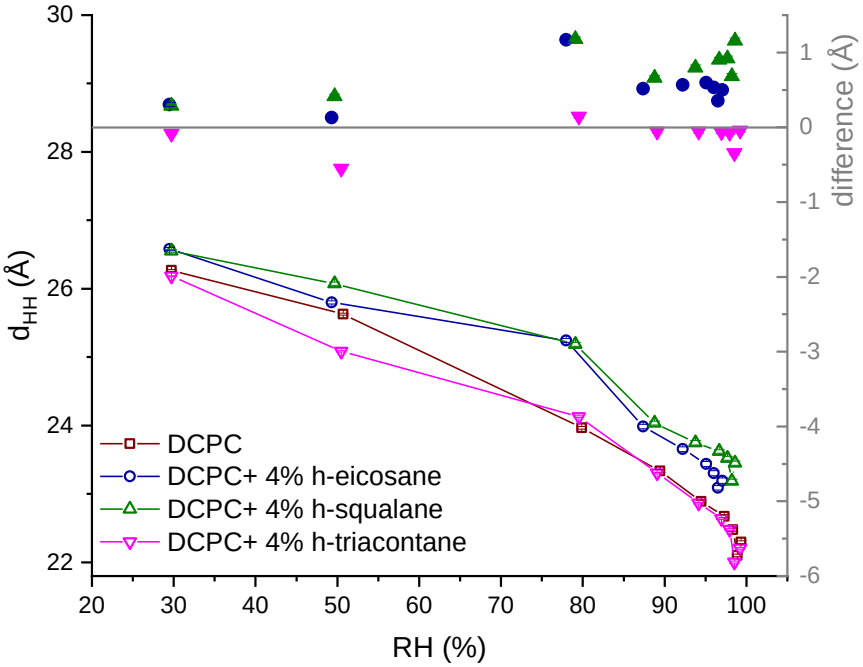

Figure 8. Bilayer thickness d_{HH} as a function of humidity for all measured samples (left scale), and corresponding calculated differences with respect to the DCPC sample (right scale). Lines are guide to the eyes only.

As shown in the graph, d_{HH} decreases for all samples when humidity increases. Interestingly, the membrane thickness of the samples containing eicosane and squalane appears to be offset by a value of approximately [0.5 – 1] Å, while this is not observed for the sample containing triacontane. The lipid molecular volume (V) being constant, the decrease in bilayer thickness (d_{HH} = 2l where l is the lipid length), is consistent with an increase of the area per headgroup (A) upon increase hydration, according to:

$$A = \frac{V}{l}.$$

From the previous data on DMPC and DLPC[11], since the headgroup area should not change between DMPC, DLPC and our DCPC sample, we assume it at the average between the reported values A = 60.6 (DMPC), 63.2 (DLPC) → A ≈ 62 Å^2 [11]. Also, we consider the lipid volume V_L scaling linearly with the chain length (V_L = 1101 and 991 Å^3 for DMPC and DLPC respectively), obtains V_L ≈ 881 Å^3 and a calculated d_{HH} ≈ 20.3 Å for DCPC at full hydration. As our reported value at maximum hydration is d_{HH} ≃ 22 - 23 Å, this result suggests that the DCPC membranes at the highest measured RH were close, but not completely, to full hydration (Figure 8).

The remaining feature of interest, namely the water layer thickness as a function of humidity, is shown in the more widely used pressure – distance curve in Figure 9. In order to estimate the water layer thickness $d_{w'}$, we used existing data in the literature on PC lipids to estimate the thickness of the headgroup[11]. This leads to the following formula for our calculation of $d_{w'}$:

$$d_{w'} = d - d_{b'} = d - d_{HH} - 8.1 \text{ Å}. \quad (6)$$

where $d_{b'}$ is the bilayer thickness calculated from the interfaces water-headgroup.

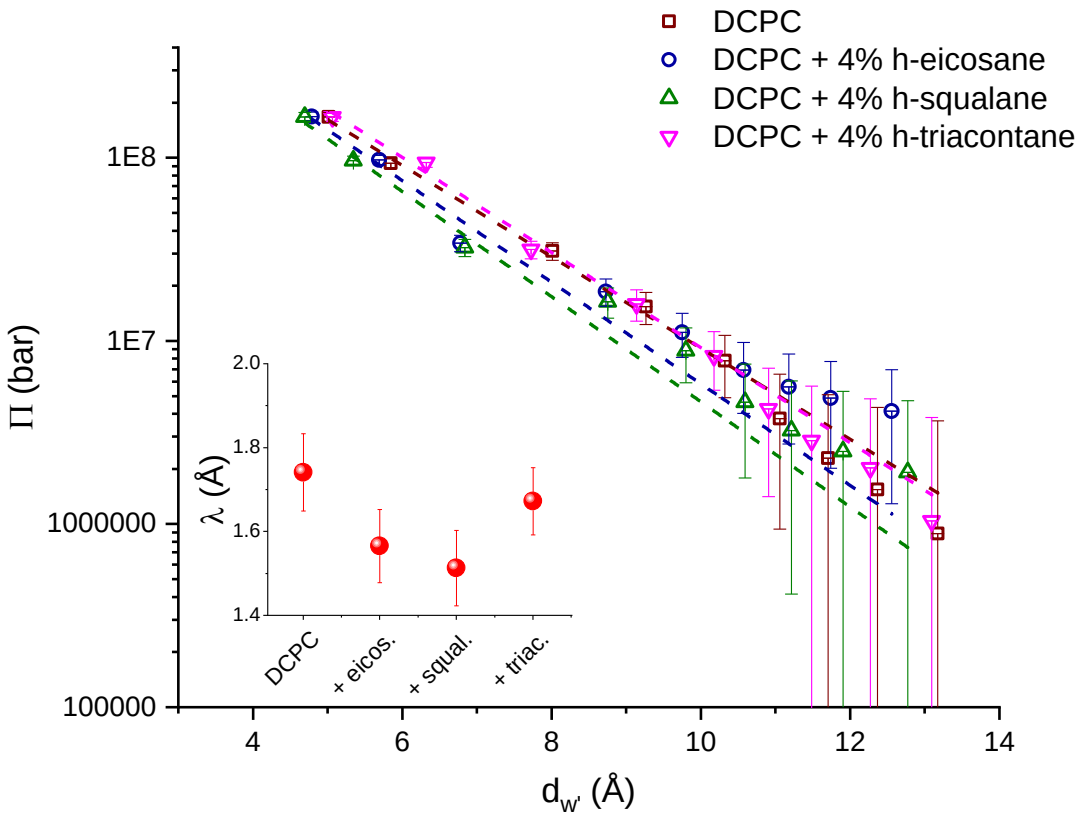

Figure 9. Pressure-distance curves: osmotic pressure Π as function of the water layer thickness $d_{w'}$ calculated for all samples. Inset: decay lengths found from exponential fits for the four samples.

The data show very small qualitative differences probably due to the humidity range explored, still far away from the expected values for maximum swelling (the water layer thickness at full swelling for PC lipids is known to be at $d_{w'} \approx 20\text{-}22$ Å[11] and the bilayer thickness did not shrink to the expected minimum value, as previously reported). Exponential fits of Π as a function of $d_{w'}$ yield an estimation of the decay length λ (inset of Figure 9). Although the differences are too small to conclude unambiguously in the humidity range explored, the samples containing eicosane and squalane show slightly lower decay lengths which could imply a lower swelling limit for these two samples. The obtained λ values are slightly lower than the value reported in the literature for DLPC membranes (λ = 2.7 Å)[29].

Discussion

Our results allow us to gain numerous insights regarding the structure of a short chain membrane model, with and without insertion of additional apolar molecules (linear and branched alkanes).

First, contrast variation measurements clearly show that both the alkanes, eicosane and squalane, are included in the hydrocarbon region of the DCPC bilayer (Figure 5). Although a more precise localization of these molecules is not possible from the contrast variation data (e.g. whether the alkanes sit perpendicular or parallel to the lipid acyl chains), the bilayer thickness values calculated from fitting the maxima of the NSLD profiles at 8% D_2O contrast (Figure 8) show an offset of ≈ 0.5 – 1 Å compared to the alkane-lacking DCPC membrane.

This implies that at least a fraction of the alkanes is sitting perpendicular to the lipid tails, hence causing the observed offset in the bilayer thickness. However, the NSLD profiles of Figure 5 show that this is not the only positioning of the alkanes, because the profile differences would have shown a sharp peak centred at z = 0 Å if that was the case. Instead, the observed broad

profile differences might indicate a dynamic disorder favoured by the highly fluid membrane state, and/or a static one (perhaps because of an excess of alkane molecules that could be accommodated perpendicularly into the membrane, forcing the remaining molecules to orient parallel to the lipid chains).

Interestingly, a slight increase of the bilayer thickness offset with humidity increase (differences in Figure 8) might suggest a small effect of the hydration in increasing the portion of alkane molecules accommodating in the perpendicular mid-plane position.

The thickness offset is not observed on the sample including the triacontane, which suggests size plays a role in the ability of such molecules to be successfully inserted within the bilayer. The long axis length of eicosane (C20) and squalane (C30) being similar (because of the branched structure of the squalane) and of the same order of twice the lipid chain length of DCPC are capable of inserting within the membrane, however the triacontane size could not be accommodated in the hydrocarbon region by intercalating parallel to the lipid chains (see Figure 1). Perhaps due to the need for the membrane to assume a certain undulated in-plane arrangement (governed by the lipid intrinsic geometry and the membrane bending/compression moduli), the arrangement of triacontane perpendicular to the lipid chain is not possible, so that these molecules are excluded from the membrane and are not observed in the calculated NSLD profiles. Such a conclusion remains, however, speculative.

All membrane stacks investigated show a clear effect of the humidity increase in thinning the bilayer up to ≈ 4 Å in the humidity range ≈ 30 - 100%, which is coherent with the increase of the headgroup area observed in PC lipids of longer chain lengths[11]. The extent of such decrease in bilayer size is not affected by the inclusion of alkane molecules. The decay length of the samples containing eicosane and squalane is slightly lower than the pure DCPC sample, implying a possible lower swelling limit induced by the alkane presence. The compatible value of λ between the samples DCPC and DCPC + triacontane gives an additional indication that the latter alkane did not incorporate within the membrane.

To summarize, we have performed an extensive study of DCPC oriented membrane stacks as a function of the relative humidity (RH) and at different D_2O/H_2O contrasts. This allowed us to determine the bilayer NSLD profile and to define unambiguously the phase of each of the structure factor terms F_h.

From that, and by using deuterium labelled alkanes, we found that eicosane and squalane are inserted inside the model membrane in the hydrocarbon region. At least a portion of the alkane molecules inserts perpendicular to the lipid chains, causing a slight increase in the bilayer thickness d_b. The membrane swelling induced by the increase in humidity causes, on one hand, an increase of the intermembrane water thickness (as expected), while on the other hand it leads to a slight decrease in the bilayer thickness, which can be explained by a concomitant size increase of the lipid headgroup upon increasing hydration. The decrease of d_{HH} is not affected by the eicosane or squalane presence inside the membrane.

The sample containing the longer hydrocarbon n-alkane triacontane does not show any increase in the bilayer thickness. This, together with physical considerations about the alkane and lipid molecule sizes, implies that the triacontane molecules do not incorporate inside the membrane, unlike eicosane and squalane. We note that the selective exclusion of triacontane (and inclusion of squalane) molecules was also observed in a former study with different membrane compositions[18]. The slight differences in osmotic pressure decay with water thickness d_w, indicate that the eicosane and squalane may decrease the membrane maximum swelling limit of the membrane.

Therefore, the incorporation of certain alkanes within short chain lipid membranes could have also occurred in an origin of life scenario, where both these alkanes and membrane-forming SCA could have been synthesized abiotically. This membrane enrichment, coupled with the existence of a preferential structural arrangement of the n-alkanes in the hydrophobic core, can effectively increase the membrane thickness and possibly lead to a lower membrane swelling capability. Together with previously observed effects in increasing the membrane thermal and pressure stability [Misuraca et al., accepted to Comm.Chem.], the results suggest a role of the n-alkanes in modifying significantly the membrane structural and functional properties, constituting one of the possible survival strategies against the extreme prebiotic environmental conditions for the first membrane compartments at the origin of life.

Acknowledgements

LM is supported by a scholarship from the Institut Laue - Langevin (ILL) PhD program. The authors thank ILL for neutron beamtime on D16 (DOI: 10.5291/ILL-DATA.9-13-758 and 10.5291/ILL-DATA.9-13-906). The ILL Partnership for Soft Condensed Matter (PSCM) is acknowledged for the access to the lab infrastructures.

References

1. Szostak, J. W., Bartel, D. P. & Luisi, P. L. Synthesizing life. *Nature* **409**, 387–390 (2001).

2. Segré, D., Ben-Eli, D., Deamer, D. W. & Lancet, D. The lipid world. *Orig. Life Evol. Biosph.* **31**, 119–145 (2001).

3. Luisi, P. L., Walde, P. & Oberholzer, T. Lipid vesicles as possible intermediates in the origin of life. *Curr. Opin. Colloid Interface Sci.* **4**, 33–39 (1999).

4. Deamer, D. The role of lipid membranes in life's origin. *Life* **7**, 5 (2017).

5. Fiore, M. & Strazewski, P. Prebiotic Lipidic Amphiphiles and Condensing Agents on the Early Earth. *Life (Basel, Switzerland)* **6**, 17 (2016).

6. Zaccai, G., Blasie, J. K. & Schoenborn, B. P. Neutron diffraction studies on the location of water in lecithin bilayer model membranes. *Proc. Natl. Acad. Sci.* **72**, 376–380 (1975).

7. Worcester, D. L. & Franks, N. P. Structural analysis of hydrated egg lecithin and cholesterol bilayers II. Neutron diffraction. *J. Mol. Biol.* **100**, 359–378 (1976).

8. Franks, N. P. & Lieb, W. R. The structure of lipid bilayers and the effects of general anaesthetics: an x-ray and neutron diffraction study. *J. Mol. Biol.* **133**, 469–500 (1979).

9. Büldt, G., Gally, H. U., Seelig, J. & Zaccai, G. Neutron diffraction studies on phosphatidylcholine model membranes: I. Head group conformation. *J. Mol. Biol.* **134**, 673–691 (1979).

10. Nagle, J. F. & Tristram-Nagle, S. Structure of lipid bilayers. *Biochim. Biophys. Acta (BBA)-Reviews Biomembr.* **1469**, 159–195 (2000).

11. Kučerka, N. *et al.* Structure of fully hydrated fluid phase DMPC and DLPC lipid bilayers using X-ray scattering from oriented multilamellar arrays and from unilamellar vesicles. *Biophys. J.* **88**, 2626–2637 (2005).

12. Kučerka, N., Tristram-Nagle, S. & Nagle, J. F. Structure of fully hydrated fluid phase lipid bilayers with monounsaturated chains. *J. Membr. Biol.* **208**, 193–202 (2006).

13. Haydon, D. A., Hendry, B. M., Levinson, S. R. & Requena, J. Anaesthesia by the n-alkanes. A

comparative study of nerve impulse blockage and the properties of black lipid bilayer membranes. *Biochim. Biophys. Acta (BBA)-Biomembranes* **470**, 17–34 (1977).

14. Haydon, D. A., Hendry, B. M., Levinson, S. R. & Requena, J. The molecular mechanisms of anaesthesia. *Nature* **268**, 356–358 (1977).

15. White, S. H., King, G. I. & Cain, J. E. Location of hexane in lipid bilayers determined by neutron diffraction. *Nature* **290**, 161–163 (1981).

16. McIntosh, T. J., Simon, S. A. & MacDonald, R. C. The organization of n-alkanes in lipid bilayers. *Biochim. Biophys. Acta (BBA)-Biomembranes* **597**, 445–463 (1980).

17. Hauß, T., Dante, S., Dencher, N. A. & Haines, T. H. Squalane is in the midplane of the lipid bilayer: implications for its function as a proton permeability barrier. *Biochim. Biophys. Acta (BBA)-Bioenergetics* **1556**, 149–154 (2002).

18. Salvador-Castell, M., Demé, B., Oger, P. & Peters, J. Lipid phase separation induced by the apolar polyisoprenoid squalane demonstrates its role in membrane domain formation in archaeal membranes. *Langmuir* (2020).

19. McCollom, T. M., Ritter, G. & Simoneit, B. R. T. Lipid synthesis under hydrothermal conditions by Fischer-Tropsch-type reactions. *Orig. Life Evol. Biosph.* **29**, 153–166 (1999).

20. Simoneit, B. R. T. Prebiotic organic synthesis under hydrothermal conditions: an overview. *Adv. Sp. Res.* **33**, 88–94 (2004).

21. Kučerka, N., Nieh, M.-P. & Katsaras, J. Fluid phase lipid areas and bilayer thicknesses of commonly used phosphatidylcholines as a function of temperature. *Biochim. Biophys. Acta (BBA)-Biomembranes* **1808**, 2761–2771 (2011).

22. Misuraca, L. *et al.* High-Temperature Behavior of Early Life Membrane Models. *Langmuir* **36**, 13516–13526 (2020).

23. Tristram-Nagle, S. *et al.* Measurement of chain tilt angle in fully hydrated bilayers of gel phase lecithins. *Biophys. J.* **64**, 1097–1109 (1993).

24. Cristiglio, V., Giroud, B., Didier, L. & Demé, B. D16 is back to business: more neutrons, more space, more fun. *Neutron News* **26**, 22–24 (2015).

25. Gonthier, J. *et al.* BerILL: The ultimate humidity chamber for neutron scattering. *J. Neutron Res.* **21**, 65–76 (2019).

26. Schneck, E. *et al.* Mechanical properties of interacting lipopolysaccharide membranes from bacteria mutants studied by specular and off-specular neutron scattering. *Phys. Rev. E* **80**, 41929 (2009).

27. Richard, D., Ferrand, M. & Kearley, G. J. Analysis and visualisation of neutron-scattering data. *J. Neutron Res.* **4**, 33–39 (1996).

28. Kučerka, N., Nieh, M.-P., Pencer, J., Sachs, J. N. & Katsaras, J. What determines the thickness of a biological membrane. *Gen. Physiol. Biophys* **28**, 117–125 (2009).

29. Kanduč, M. *et al.* Tight cohesion between glycolipid membranes results from balanced water–headgroup interactions. *Nat. Commun.* **8**, 1–9 (2017).

30. Denninger, A. R. *et al.* Neutron scattering from myelin revisited: bilayer asymmetry and water-exchange kinetics. *Acta Crystallogr. Sect. D Biol. Crystallogr.* **70**, 3198–3211 (2014).

31. Marquardt, D., Heberle, F. A., Nickels, J. D., Pabst, G. & Katsaras, J. On scattered waves and

lipid domains: detecting membrane rafts with X-rays and neutrons. *Soft Matter* **11**, 9055–9072 (2015).

32. LeNeveu, D. M., Rand, R. P. & Parsegian, V. A. Measurement of forces between lecithin bilayers. *Nature* **259**, 601–603 (1976).

33. Parsegian, V. A., Fuller, N. & Rand, R. P. Measured work of deformation and repulsion of lecithin bilayers. *Proc. Natl. Acad. Sci.* **76**, 2750–2754 (1979).

4 CONCLUSIONS AND PERSPECTIVES

4.1 A PROMISING NEW PROTOMEMBRANE MODEL

The research presented in this thesis expands our current knowledge and understanding of specific steps in the pathway that, starting from a lifeless assembly of simple prebiotic molecules dipped in a harsh early environment, eventually led to the origin of living forms on our planet (and maybe elsewhere in the universe).

A new protomembrane model, made by simple prebiotically-relevant building blocks readily synthesized via Fischer-Tropsch type reactions (*22*, *61*) and whose presence is ensured by previous findings on meteorites (*27*, *62*), is proposed to account for both the molecular limitations and the need to endure the likely extreme temperature and pressure conditions of the early Earth environment (*35*). The model membrane is a bilayer of single chain amphiphiles, such as decanoic acid and 1-decanol, with additional incorporation of apolar hydrocarbons such as eicosane. The spontaneous assembly of such supramolecular structure is ensured by thermodynamics: on one hand, the apolar molecules tend to be embedded in the amphiphiles' hydrophobic acyl chains; on the other hand, the amphiphilic nature and intrinsic geometry of the used fatty acid and alcohol favours the self-assembly into a bilayer membrane.

The simpler protomembrane model composed by decanoic acid and 1-decanol (C10 mix, lacking the hydrocarbons) has been extensively investigated in former studies (*36*, *39*, *53*, *60*), where features such as lipid concentration, pH stability range and membrane fluidity were first explored. Here, many complementary properties were defined and compared with membranes consisting of decanoic acid only.

First, the system containing the decanol shows the presence of bilayers (vesicles) as the unique molecular assembly at ambient temperature, as opposed to the decanoic acid sample where a coexistence with micelles is always observed. Therefore, not only the decanol leads to a drop of the CVC, but it also causes the complete disappearance of micellar aggregates above the new CVC value. The reason for this effect may be due to a more favourable H-bonding between the decanoic acid and decanol molecules (also discussed by Apel et al. (*60*)), so that the formed pair does not possess anymore the conical geometry that is necessary to form micelles.

Second, the decanol prevents the progressive solubilization of the vesicle material when the temperature increases, what is observed in the pure fatty acid sample instead. This property is probably a consequence of the drop of the CVC value due to the decanol presence. Higher temperatures will favour amphiphile solubilization and thus an increase of the CVC threshold, but the difference between the CVC and the sample concentration of the C10 mix is large enough to prevent any solubilization (what is not the case for the pure decanoic acid sample).

Third, the decanol presence induces a noticeable transition triggered by the high temperature ($T \approx 60\,^{\circ}C$, discussed in Article 1 of this thesis (*110*)). The many implications and consequences of this result are detailed in the next section.

Although of less importance for what concerns the OOL field, the use of decanol in mixture with the decanoic acid confers an additional advantage for the stability of the lamellar phase at low temperature (below $T = 10\,^{\circ}C$). The pure decanoic acid sample undergoes flocculation at low temperature, which results in the disappearance of the MLV correlation (the so-called *swollen phase* described in Article 1). Instead, the C10 mix shows that the MLV phase is still partially present at low temperature, along with a fraction of *collapsed phase*. This happens at the same (or similar) temperature of the lamellar fluid-gel transition, which was observed in a former study (*53*) and also by SAXS studies performed with pressure (Article 2 of this thesis; see also Article 2 Supplementary Information for complementary FTIR measurements).

Enriching the protomembrane with hydrocarbons such as eicosane, squalane and triacontane investigated in this project, brings several modifications to the membrane structure and dynamics in response of temperature and HHP variations. Eicosane and squalane both lower significantly the MLV d-spacing. This suggests a role of the incorporated molecules in dampening the membrane fluctuations, which are the main factor regulating the very large d-spacing values observed in these systems (Article 2). Interestingly, the observed effect does not translate into a significantly lower membrane bending rigidity when the samples are prepared in the ULV state (Article 3). Furthermore, the insertion of eicosane into the MLVs leads to prominent effects on the membrane dynamics probed at molecular level: the hydrogen MSD is lowered at all temperature and hydrostatic pressure values investigated, and the effects of HHP in the dynamics is greatly reduced (or canceled) when the eicosane is added (Article 2).

These observations are promising in that they show that such alkane-enriched protomembranes are in fact not sensitive (in a physico-chemical sense) to the high pressure that would be experienced in the vicinity of the hydrothermal vents where life could have appeared first.

A deep structural characterization of ULVs, prepared with and without eicosane and squalane, shows that the apolar components help maintaining the lamellar

phase up to higher temperatures, by shifting the high temperature transition that has been identified in this work. The membrane bending rigidity is lowered by the presence of eicosane or squalane at ambient temperature, possibly due to increased frustration in the membrane packing. Conversely, because the high temperature ($T = 60 - 70°C$) likely favours a more efficient mixing with the fluid C10 mix acyl chains, the membrane bending rigidity values of C10 mix ULVs with and without the alkanes are similar (Article 3).

Therefore, stable membranes can be formed starting from prebiotically available, single short chain amphiphiles with incorporation of linear or branched apolar molecules placed in the membrane hydrophobic region. Not only these additional components still allow to obtain stable membranes at ambient temperature, but they also increase the thermal stability by dampening the membrane fluctuations, reduce any effect of HHP, and shift the conformational transition of the vesicles at high temperature. The structural role of apolar molecules as adaptive strategy is not an entirely "synthetic" approach, as suggested by recent studies on modern extremophiles (*38*, *114*), hence increasing the plausibility of such model in an OOL scenario.

These findings suggest a possible, novel route to explain how the putative first proto-living forms could have withstood the extreme environmental conditions. Such protomembrane model, along with all the similar ones varying for the presence of one (or more) components, were fully characterized from a physico-chemical point of view with a particular attention to temperature and HHP, paving the way to further studies focussed on the biological functioning of the membrane (e.g. the permeability to solutes, oligonucleotides etc.).

The work of this thesis has been devoted to an analytical study of highly simplified models of protomembranes: this is shown by the exclusive use of C10 chains for the amphiphiles, the choice of only carboxylic acid and alcohol groups as prebiotic "headgroups" and the use of three selected alkane candidates to model the behavior of linear (eicosane, triacontane) and branched (squalane) hydrocarbons. This allowed to clearly identify the effects and consequences of each molecular species (and moiety) to the membrane structure and dynamics.

However, a more representative candidate for a "real world" protomembrane would certainly be a heterogeneous systems, perhaps including many different amphiphile types and chain lengths, as well as a broad distribution of alkanes. From the results obtained in this work, a natural continuation would be a progressive *complexification*, which would permit to explore new features such as the formation of membrane domains, the role of additional "headgroup" moieties (for instance glycerol monoester) and perhaps obtain a better accommodation of the alkanes within the membrane.

Although the primary focus of this work has been to explore possible protomembranes that could form and thrive at the onset of life, the results can as well be exploited in all different contexts where the ordinary phospholipid vesicles (liposomes) are currently employed. As it was shown, single chain amphiphile vesicles can prove stable towards a wide range of conditions, and the differences in the behavior could make them a suitable alternative when needed.

4.2 THE HIGH TEMPERATURE TRANSITION: LIMIT OR RESOURCE

A surprising high temperature transition was identified for the first time in this work, with highly significant effects on all the structural studies that have been performed. The outcome of the transition has proven somewhat elusive and technically difficult to determine unambiguously, but the ensemble of techniques used (together with some indirect hints from the literature) can help in defining a number of characteristics.

First of all, the results detailed in Articles 1 and 3 (and the additional Notes provided in this thesis for Article 3) clearly show that the transition at high temperature leads to different structures when the samples are in the form of ULVs or MLVs. This is an important result that implies more profound effects of the lamellarity state in affecting the membrane stability, even at the high d-spacings observed for the C10 mix systems.

There seem to be two concomitant phenomena occurring at the same (or similar) temperature, in the same fashion of what has been observed at low temperature (fluid-gel transiton together with flocculation). One of them is a vesicle fusion that creates dense structures, presumably oily droplets that phase separate. This phenomenon is observed on ULV samples (Article 3). The other one is also probably coming from vesicle fusion (the only aggregates which are present), but it leads to bigger macromolecular structures that still possess a bilayer. This effect is observed on MLV samples (Article 1). The ssNMR data show that these new structures can be oriented by the magnetic field of the spectrometer. It is unclear, however, if the anisotropic shape of the new assembly is an effect of the high temperature transition itself (and the magnetic field only orients them along a preferential direction) or if the deformation has been induced by the magnetic field (as well as the subsequent orientation), an effect that has been previously observed on other model and natural membranes and that is a function of the vesicle size (*115*, *116*).

It is remarkable that such transition, which seems to be occurring when the amphiphiles possess an excess thermal energy that is not anymore compatible to the small ($< 10^2 nm$) vesicle state, is not observed for the pure decanoic acid sample. However, this could be due to the fact that vesicle solubilization is already occurring for $T > 30\,°C$, therefore very few vesicles are probably still available at $T = 60\,°C$.

One could argue that this transition sets a clear boundary for the vesicle thermal stability (what is certainly true in the case of ULVs). This offers an important perspective for future work in the subject, because it gives a very convenient method for a rapid screening of different sample compositions via ordinary laboratory techniques such as DLS or FTIR. As it was done for the incorporation of eicosane and squalane, a shift of the transition observed by DLS towards higher temperatures will indicate a more thermally stable membrane.

The identification of a high temperature transition that has physical effects on the membrane morphology requires a new critical re-reading of the results which are present in the literature. As discussed in Article 1, it is possible that some of the effects were observed in former data, but either they were imputed uniquely to changes in permeability properties (*36*), either they were considered as an aggregation effect due to the fast cooling down of the samples (*33*). Interestingly, the data from (*33*) (along with additional observations (*117*, *118*)) might indicate that the assemblies formed by bringing the MLVs above the transition temperature $T > 60\,°C$ consist in elongated, filamentous vesicles. Nevertheless, since the data acquired in this work do not allow a conclusive answer to this question for the C10 mix samples (with and without alkanes), such hypothesis remains speculative and needs further experimental proof.

For the case of the ULVs, the fact that the transition leads to dense oil droplets means that at high temperature the H bonds between carboxylic acid (or alcohol) and H_2O are not strong enough to keep all headgroups at the interface with water. Thus, another strategy to counteract the transition (together with the incorporation of alkanes) could be to use a fraction of amphiphiles with a more polar headgroup. One example could be to use the glycerol monoester, for which Mansy et al. (*36*) reported promising results (although these findings only addressed the membrane permeability to oligonucleotides).

Finally, one should not dismiss too quickly the high temperature transition based on the findings on MLVs. Since the lamellar phase was maintained there, it will be interesting to explore in more detail the reason for such difference (for instance, whether it is simply due to differences in size of the starting vesicles). Also, if it can be proven that the outcome of the transition is indeed a series of long, filamentous vesicles, this could be considered as a resource for the single chain amphiphile vesicles rather than a disadvantage. The reversible transition

between small spherical vesicles and elongated ones, formed by fusion, could open new perspectives on the mechanisms of solute mixing and exchange between the initial protocells.

If such hypothesis could be confirmed, it would mean that single chain amphiphile membranes are not just a prebiotic surrogate of the more complex phospholipid membranes, but they would possess additional exclusive properties that would make them more favourable in a context with highly variable temperature. Cryo-TEM is a promising technique for future studies that could help to find a definitive answer in this respect.

4.3 ALKANE POSITIONING INSIDE THE MEMBRANE

One additional question about the new protomembrane model is related to the precise location of the alkanes inside the membrane. This could help gaining insights on how the apolar molecules affect the properties of the bilayer, whether they can cause modifications in the bilayer thickness etc. However, it was not possible to obtain oriented membrane stacks on a solid substrate with the decanoic acid - decanol models, which would have allowed to perform such kind of high-resolution studies with SAND (as discussed in the Foreword of Article 4).

A series of experiments were performed on a double-chain phospholipid analogue of the C10 mix membrane, prepared with DCPC. In that case, it was possible to create oriented multilayers which were used for the diffraction measurements. In DCPC membranes, the eicosane and squalane are found to increase the bilayer thickness, an indication that they are preferentially positioned in the mid-plane of the bilayer, perpendicular to the phospholipid tails (Article 4). This goes in agreement with recent studies performed with squalane on membranes with longer chain lengths and different phospholipid types (*80*, *119*). The findings on DCPC would suggest that the same positioning occurs on the C10 mix membranes.

It is important to note that such implication remains an hypothesis: as it has been shown throughout this work, in many cases the vesicles formed by single chain amphiphiles presented features and behaviour significantly different from the phospholipidic counterparts, therefore the simple analogy with the chain length does not allow any straightforward deduction. However, since previous studies never tested the behavior of phospholipid membranes with chain lengths this short, the results presented in Article 4 confirm that the incorporation of alkanes is still occurring and the preferential positioning is coherent with what was found with longer lipid chain lengths (*119*).

As further perspective, two strategies could be employed in order to find a conclusive answer to alkane positioning inside single chain amphiphile membranes:

- Mixing the decanoic acid and 1-decanol with a fraction of a more polar component (e.g. the decanoic acid glycerol monoester previously mentioned). This is because the insufficient polarity of the used headgroup is one of the main imputed reason for the unsuccessful ordered multilayer formation. It would be crucial to find the most effective organic solvent that permits film deposition of this new mixture and that this film could hydrate and undergo swelling and ordering. The vesicle deposition technique will unlikely lead to a sufficient number of Bragg reflections needed for the Fourier analysis.

- Performing a series of 2D-NMR experiments with isotopic substitution using Magic Angle Spinning (MAS) on vesicles in solution. The use of ^{13}C and ^{2}H labelled decanoic acid and 1-decanol would allow to map all correlations between the amphiphiles' ^{13}C and ^{2}H atoms. From the 2D map, the correlation between the CH_3, the CH_2 close to the methyl, the $CH_{2\beta}$ and the $CH_{2\alpha}$ (the ones which are the closest to the headgroup) can be discriminated. The comparison between the maps obtained for the samples with alkanes and without alkanes, will show displacements in the correlation positions that could tell us which part of the membrane tails are interacting with the alkanes, unveiling their position.

4.4 MEMBRANE DYNAMICS, FLUIDITY AND PERMEABILITY

Further studies on the model protomembrane dynamics have also been performed using different techniques, such as FTIR, EINS (with a different energy resolution from the one whose results are shown in Article 2) and QENS. I have performed all the related experiments and the data analysis of the FTIR data. The analysis of EINS and QENS data was performed by collaborators, and discussion about the various results obtained are currently in progress and are not reported in this thesis.

The outcome from these results is expected to lead to two additional publications: the first, devoted to a multi-scale dynamics characterization of the model protomembranes using FTIR, EINS and QENS (qualitative) data results; the second, about the implementation of a new quantitative theory to model the QENS relaxations that will give detailed information about the motion of all different lipid

portions in the ps-ns range (the model and its first tests with ordinary phospholipids is currently under submission by members of our group).

Measurements focussed to study the membrane fluidity as a function of the temperature have also been performed, using the *Laurdan* fluorophore as a probe to detect changes in the polarity of the fluorophore environment (that can be used to detect phase transitions). The study, carried out by comparing the fluorescence spectra of decanoic acid, C10 mix and DCPC vesicles, will be the object of a separate publication which is under preparation.

The last important investigation that needs to be performed in future work is about the model protomembrane permeability properties. As previously discussed, former studies were performed on the C10 mix system to measure the capability to retain oligonucleotides (*36*).

New measurements need to be done on the systems containing the alkanes, with results to be (re-)interpreted from what has been found on the membrane physico-chemical properties in the present work. Previous studies in our group have shown that the squalane increases water permeability while it decreases proton permeability of archaea-mimicking model membranes (M. Salvador Castell et al., to be submitted), a first indication that the alkane molecules could also affect the biological properties of the protomembranes and may constitute a crucial step towards a better understanding of the origin of life.

5 RÉSUMÉ

INTRODUCTION

La planète Terre a environ 4,5 milliards d'années. Considérant les preuves minéralogiques, qui suggèrent que de l'eau liquide et une atmosphère étaient déjà présentes il y a environ 4,4 milliards d'années (*4*) et les preuves de vie phototrophique (*5*), nous pouvons fixer la fenêtre temporelle la plus sûre pour l'apparition de la vie à [4,4 - 3,5] milliards d'années.

Dans ce travail de thèse, je me suis concentré sur les membranes des premières formes d'entités vivantes qui se sont assemblées à partir d'un ensemble de molécules simples disponibles sur la Terre prébiotique.

La membrane lipidique est une structure formée par des biomolécules hydrophobes ou amphiphiles appelées lipides, qui sont utilisées dans les organismes vivants à de nombreuses fins, comme barrière entre l'intérieure de la cellule et leur environnement, pour le stockage de l'énergie, ou la signalisation. Le caractère amphiphile est celui qui permet l'auto-assemblage en solution des lipides en une variété de structures supra-moléculaires, sous l'effet de l'hydrophobie (*50*). Les structures principales discutées dans ce travail sont les micelles, les vésicules et les gouttelettes. En particulier, les membranes sont les structures qui forment les vésicules et peuvent être utilisées pour imiter les parois des cellules vivantes.

Comme la synthèse prébiotique des molécules amphiphiles privilégie les chaînes les plus courtes (*61*-*63*), ce travail s'est concentré sur les acides gras, les alcools gras et les phospholipides ayant des chaînes saturées de 10 atomes de carbone, parmi les plus courtes capables de s'auto-assembler en bicouches (*34*, *60*). Quatre modèles principaux, tous en étroite relation les uns avec les autres, ont été utilisés et étudiés ici en tant que modèles proto-membranaires :

- Le premier modèle est une membrane constituée d'une bicouche d'acide décanoïque (nom commun : "acide caprique"), qui est l'acide gras linéaire et saturé en C10. Des études à température ambiante ont montré que ce système est stable dans une plage étroite de pH, autour de pH 7.1 (*53*, *60*, *72*).

- Le second modèle est un mélange équimolaire (1 :1) d'acide décanoïque et d'un alcool gras ayant la même longueur de chaîne, le 1-décanol. De nom-

breuses études antérieures ont porté sur des mélanges équimolaires (*53*) ou des rapports différents (par exemple 9 :1 (*60*) ou 2 :1 (*36*)), ce qui en fait l'un des modèles de proto-membrane le plus étudié. Il a été constaté que l'ajout de quantités même faibles d'alcool gras permettait de stabiliser les vésicules même à des valeurs de pH élevées (*39*, *53*, *60*). En outre, la perméabilité de la membrane aux oligonucléotides en fonction de la température (*36*) et la fluidité de la membrane en fonction de la haute pression et de la température (*53*) ont été étudiées pour ce système.

Une étude approfondie et détaillée des propriétés structurelles et dynamiques de ces deux premiers modèles a été réalisée afin d'approfondir les connaissances sur la réponse des deux systèmes aux températures élevées.

- Le troisième modèle est proposé en analogie avec les découvertes récentes dans le domaine des extrêmophiles (*38*, *79*, *120*). Le mélange d'acide décanoïque et de décanol 1 :1 (ci-après "C10 mix") est ici enrichi de petits pourcentages de l'un des alcanes suivants : squalane, un alcane ramifié de 30 atomes de carbone (C30) (*79*, *80*) ; eicosane, un alcane linéaire de 20 atomes de carbone (C20) comme alternative prébiotique plus plausible. Le C10 mix contenant de l'eicosane peut être considéré comme le modèle principal du projet, qui résume les caractéristiques requises de l'abondance moléculaire prébiotique et la nécessité d'une stratégie contre les températures élevées et les hautes pressions hydrostatiques.

La possibilité que ces molécules d'alcane aient pu agir comme stabilisateurs de membrane dans des conditions extrêmes de température et de pression a été étudiée dans des travaux parallèles. Dans le premier, les systèmes de vésicules multilamellaires incluant ou non les alcanes ont été étudiés, à la fois en termes de structure et de dynamique, en fonction de la température et de la pression simultanément. Le second travail est lui axé sur le comportement des vésicules unilamellaires. En particulier, la nature des changements conformationnels observés à $T > 60\,^{\circ}C$ a été explorée et interprétée d'un point de vue structurel et dynamique (molécule unique et collectif).

- Le quatrième modèle est une bicouche constituée d'un phospholipide, la 1,2-didécanoyl-sn-glycéro-3-phospho-choline (ci-après DCPC), phosphatidylcholine constituée d'une tête polaire de type glycéro-phospho-choline et de deux chaînes acyles saturées en C10, avec ajout d'alcanes (soit l'eicosane, le squalane ou le triacontane alcane linéaire en C30). La DCPC a été utilisée comme système proche des autres modelés de protomembrane, pouvant être préparé en empilements multicouches (en raison de sa tête polaire

plus volumineuse et plus hydrophile), possédant deux chaînes linéaires et saturées en C10 identiques à celles des molécules d'acide décanoïque et de décanol.

Ce dernier modèle a été utilisé pour localiser le positionnement des molécules d'alcane, lorsqu'elles sont incluses avec succès dans la membrane, avec une résolution proche du groupement d'atomes (quelques Ångström).

MÉTHODES

La diffusion peut être généralement définie comme le processus par lequel un faisceau incident de particules (photons, neutrons, électrons) change de direction de propagation en raison d'inhomogénéités dans sa cible, l'échantillon. La nouvelle trajectoire et l'énergie du rayonnement diffusé contiennent des informations sur les caractéristiques du milieu diffusant (tailles et formes des particules, corrélations, dynamique des molécules, poids moléculaires, etc.).

Un cas particulier est donné par l'utilisation de neutrons libres comme faisceau incident. Cela constitue le domaine de la diffusion des neutrons, la principale approche expérimentale qui a été utilisée dans ce travail, à la fois pour des recherches structurelles et dynamiques.

Les techniques de diffusion utilisées dans ce travail étaient les suivantes :

1. Diffusion neutronique (diffusion des neutrons aux petits angles, diffraction des neutrons à petits angles, diffusion élastique incohérente des neutrons, spectroscopie d'écho de spin des neutrons) ;

2. Diffusion statique et dynamique de la lumière ;

3. Diffusion des rayons X aux petits angles.

En outre, des techniques supplémentaires ont été utilisées pour compléter les connaissances acquises lors des expériences de diffusion, comme la résonance magnétique nucléaire à l'état solide et la spectroscopie infrarouge à transformée de Fourier.

Selon les besoins, les échantillons ont été préparés sous forme de vésicules unilamellaires, de vésicules multilamellaires ou d'empilements de membranes orientées sur un substrat de silicium plat.

RÉSULTATS

Le rôle de l'alcool gras

Article 1 : Comportement à haute température des modèles de membranes à l'origine de la vie

La première série d'expériences visait à explorer l'effet du mélange de l'alcool gras (décanol) avec un acide gras de même longueur de chaîne (acide décanoïque). Pour cela, un tel mélange a été étudié et comparé à toutes les étapes avec un autre échantillon composé uniquement de l'acide décanoïque.

Résumé de l'article 1 publié dans *Langmuir (ACS)* (*110*) :

Les scénarii sur l'origine de la vie supposent généralement un début de formation cellulaire dans les sources chaudes terrestres ou dans les profondeurs des océans, à proximité des sources chaudes, où l'énergie était disponible pour les réactions non enzymatiques. Les membranes des protocellules devaient donc résister à des conditions extrêmes différentes de ce que l'on trouve aujourd'hui à la surface de la Terre. Nous présentons ici une étude exhaustive de la stabilité à la température jusqu'à 80 °C des vésicules formées par un mélange d'acides gras à chaîne courte et d'alcools, qui sont des candidats plausibles pour des membranes permettant la compartimentation des protocellules. Nous confirmons que la présence d'alcool a un fort impact structurant et stabilisateur des structures lamellaires. De plus, à une température élevée (> 60 °C), on observe une transition conformationnelle des vésicules, qui résulte de la fusion vésiculaire. Parce que les environnements les plus susceptibles d'être à l'origine de la vie impliquent tous des températures élevées, nos résultats impliquent la nécessité de prendre en compte une telle transition et ses effets lors de l'étude du comportement d'un modèle protomembranaire.

Effets et positionnement des alcanes

Article 2 : Les alcanes augmentent la stabilité des modèles de proto-membrane dans des conditions de pression et de température extrêmes

Ayant défini le rôle important et les conséquences de la présence du décanol en mélange avec l'acide décanoïque, les études suivantes ont été consacrées à l'exploration des effets des alcanes dans la membrane modèle. Le premier des trois travaux, qui ont été réalisés sur cet effet, a exploré l'effet combiné de la température et de la pression hydrostatique dans l'arrangement lamellaire et la dynamique de la chaîne amphiphile de systèmes de vésicules multilamellaires.

Résumé de l'article 2, publié dans *Communications Chemistry (Nature)* (*111*) :

La vie terrestre est apparue sur notre planète dans une fenêtre temporelle de [4,4 - 3,5] milliards d'années. Pendant cette période, il est suggéré que les premières formes proto-cellulaires se sont développées dans l'entourage des cheminées hydrothermales des grands fonds marins, structures qui sont encore présentes aujourd'hui le long des fractures de la croûte océanique. Ces environnements sont caractérisés par des températures et des conditions de pression hydrostatiques extrêmes qui interrogent sur la capacité des premiers compartiments membranaires à rester stables dans ces conditions. Des études récentes ont proposé une stratégie adaptative employée par les extrémophiles actuels : l'utilisation de molécules apolaires comme composants structurels de la membrane afin de moduler la réponse dynamique des deux couches lorsque cela est nécessaire. Nous étendons ici cette hypothèse aux modèles de protomembrane des premiers stades de la vie, en utilisant des alcanes linéaires et ramifiés comme molécules stabilisatrices apolaires ayant une pertinence prébiotique. L'ordre structurel et la dynamique des chaînes de ces systèmes ont été étudiés en fonction de la température et de la pression. Nous avons découvert que les deux types d'alcanes étudiés, même les plus simples, ont un impact important sur l'organisation des vésicules multilamellaires et la dynamique des chaînes. Nos données montrent que les membranes enrichies en alcanes présentent un gonflement plus faible des vésicules multilamellaires induit par l'augmentation de la température et sont nettement moins affectées par les variations de pression que les échantillons exempts d'alcanes, ce qui suggère une possible stratégie de survie pour les premières formes vivantes.

Article 3 : Les alcanes agissent comme régulateurs membranaires de la réponse des premières membranes aux températures extrêmes

Comme le montrent les résultats présentés dans l'article 1, les vésicules formées par le C10 mix n'ont montré aucun signe de présence micellaire. De plus, une température d'apparition (T = 60 °C) a été trouvée là où les vésicules de mélange C10 subissent des changements de conformation. Le 3ème article de cette thèse était consacré à étudier : 1) quel type de changement conformationnel a lieu dans les vésicules unilamellaires ou, plus précisément, quel est le produit de ce changement ; 2) ce qu'il se passe lorsque les vésicules sont enrichies avec les molécules d'alcane.

Résumé de l'article soumis à *Soft Matter (RSC)* :

L'une des premières étapes nécessaires à l'origine de la vie est la formation d'une membrane, une frontière qui permet la rétention de molécules utiles dans des solutions concentrées. La protomembrane a probablement été formée par

l'auto-assemblage de molécules simples et facilement disponibles telles que les acides gras à chaîne courte et les alcools, mettant en doute la stabilité de la membrane dans les conditions environnementales des débuts de la Terre. Nous avons exploré une nouvelle stratégie pour surmonter les problèmes de stabilité thermique des protomembranes par inclusion de molécules apolaires (alcanes). Nous avons constaté qu'en l'absence d'alcane, les protomembranes se transforment en gouttelettes de lipides lorsque la température augmente, tandis que celles qui sont enrichies en alcanes persistent plus longtemps. Ainsi, les protomembranes contenant des alcanes sont plus stables à haute température. Cela ouvre de nouvelles perspectives pour moduler le comportement protomembranaire par l'incorporation de différents types de molécules apolaires appropriées, ce qui nous permet de mieux comprendre l'évolution des premières membranes.

Article 4 : Localisation des alcanes à l'intérieur d'un modèle de protomembrane souple à l'échelle atomique

La présence de molécules d'alcane dans un modèle de protomembrane composé d'amphiphiles à chaîne courte unique a une série de conséquences intéressantes sur les propriétés et le comportement de la membrane lors d'une augmentation de la température et de la pression hydrostatique (comme le montrent les résultats des articles 2 et 3).

En raison de difficultés techniques pour obtenir des empilements réguliers de membranes (multicouches) avec des amphiphiles à chaîne unique, la localisation des alcanes a été effectuée sur un échantillon similaire. Cet échantillon était un empilement multilamellaire de DCPC, une phosphatidylcholine ayant la même longueur de chaînes que l'acide décanoïque et le décanol. D'une part, le groupe de tête de PC plus hydrophile pouvait permettre la préparation des membranes sous la forme de multicouches. D'autre part, l'utilisation de la même longueur de chaînes que les amphiphiles à chaîne unique pourrait aider à relier le positionnement des alcanes dans les deux types d'échantillons.

Les résultats sont en cours de soumission dans *Biochimica et Biophysica Acta – Biomembranes (Elsevier)*. Ci-dessous la traduction du résumé :

Les biomembranes modèles composées de lipides à chaîne courte présentent un grand intérêt pour étudier l'origine de la vie cellulaire. En effet, les réactions de type Fischer-Tropsch, qui se produisent dans l'environnement terrestre primitif, ont probablement favorisé la formation de courtes chaînes lipidiques ($n < 12$). Des études récentes ont montré que l'inclusion de petites quantités d'hydrocarbures apolaires dans des proto-membranes modèles ont un impact significatif sur la stabilité de la membrane à haute température et dans des conditions de haute pression. Ici, nous avons effectué une étude structurale approfondie, en utilisant

la diffraction des neutrons, par des multicouches de membrane phospholipidique à chaîne courte, avec ou sans incorporation d'hydrocarbure linéaire ou ramifié. La variation de contraste, en utilisant H_2O et D_2O pour ou mélangés, ainsi que l'analyse du gonflement des membranes sous humidité contrôlée ont été utilisés pour déterminer les profils de densité de longueur de diffusion des neutrons des membranes. Nous avons constaté que les alcanes eicosane et squalane sont incorporés dans le plan médian du noyau hydrophobe de la membrane. Les données montrent un positionnement préférentiel de ces alcanes perpendiculairement aux chaînes aliphatiques de phospholipides et provoquent ainsi une légère augmentation de l'épaisseur de la membrane. Les alcanes peuvent également jouer un rôle dans la réduction du gonflement des membranes lors de l'hydratation.

CONCLUSIONS

Un nouveau modèle de protomembrane, constitué de simples éléments de construction prébiotiques facilement synthétisés par des réactions de type Fischer-Tropsch (*22*, *61*) et dont la présence est assurée par des découvertes antérieures sur les météorites (*27*, *62*), est proposé pour tenir compte à la fois des limitations moléculaires et de la nécessité d'endurer les conditions de température et de pression extrêmes probables de l'environnement terrestre primitif (*35*). La membrane modèle est une bicouche d'amphiphiles à chaîne unique, tels que l'acide décanoïque et le 1-décanol, avec une incorporation supplémentaire d'hydrocarbures apolaires tels que l'eicosane.

Le rôle du 1-décanol et des alcanes a été défini et étudié en détail en fonction des changements de température et de pression. Plusieurs effets de la présence de 1-décanol ont été observés. Premièrement, le système contenant le décanol montre la présence de bicouches (vésicules) comme unique assemblage moléculaire à température ambiante, par opposition à l'échantillon d'acide décanoïque où une coexistence avec des micelles est toujours observée. Deuxièmement, le décanol empêche la solubilisation progressive de la matière des vésicules lorsque la température augmente, ce qui est plutôt observé dans l'échantillon d'acide gras pur. Troisièmement, la présence de décanol induit une transition notable déclenchée par la température élevée ($T \approx 60\,^{\circ}C$, discutée dans l'article 1 de cette thèse (*110*)).

L'enrichissement de la protomembrane avec des hydrocarbures tels que l'eicosane, le squalane et le triacontane étudiés dans ce projet, apporte plusieurs modifications à la structure et à la dynamique de la membrane en réponse aux variations de température et de pression hydrostatique. L'eicosane et le squalane ré-

duisent tous deux de manière significative l'espacement entre les membranes des vésicules multilamellaires. Cela suggère un rôle des molécules incorporées dans l'amortissement des fluctuations de la membrane, qui sont le principal facteur de régulation des très grandes valeurs d'espacement observées dans ces systèmes (article 2). Il est intéressant de noter que l'effet observé ne se traduit pas par une rigidité de courbure de la membrane plus grande lorsque les échantillons sont préparés à l'état unilamellaire (article 3). En outre, l'insertion de l'eicosane dans le vésicules multilamellaires entraîne des effets importants sur la dynamique membranaire sondée au niveau moléculaire : le déplacement quadratique moyen des hydrogènes est abaissé à toutes les valeurs de température et de pression hydrostatique étudiées, et les effets des hautes pressions sur la dynamique sont fortement réduits (ou annulés) en présence d'eicosane (article 2).

Ces observations sont prometteuses dans la mesure où elles montrent que ces protomembranes enrichies en alcanes ne sont en fait pas sensibles (au sens physicochimique) à la haute pression qui serait ressentie à proximité des cheminées hydrothermales où la vie aurait pu apparaître en premier.

Par conséquent, des membranes stables peuvent être formées à partir d'amphiphiles à chaîne courte unique, disponibles prébiotiquement, avec incorporation de molécules apolaires linéaires ou ramifiées placées au centre de la région hydrophobe de la membrane. Non seulement ces composants supplémentaires permettent encore d'obtenir des membranes plus stables à température ambiante, mais ils augmentent également la stabilité thermique en amortissant les fluctuations de la membrane, réduisent tout effet de la pression hydrostatique élevée, et décalent la transition conformationnelle des vésicules à plus haute température.

En ce qui concerne le positionnement précis des alcanes à l'intérieur de la membrane, les expériences réalisées sur le DCPC montrent que l'eicosane et le squalane provoquent une augmentation de l'épaisseur de la bicouche, ce qui indique qu'ils sont préférentiellement positionnés dans le plan médian de la bicouche, perpendiculairement aux chaines aliphatiques des phospholipides (article 4).

Toutes ces études jettent les bases pour de futures recherches plus approfondies sur les propriétés biologiques de la protomembrane modèle (par exemple la fluidité et la perméabilité), qui pourraient aider à obtenir une image complète du processus de compartimentation à l'origine de la vie.

ACKNOWLEDGEMENTS

One could argue that the hardest task of a Ph.D. thesis may be the writing of the acknowledgement section. This Ph.D. came at the end of 3.5 years of work, struggles, travels, countless nice moments shared with many people. In some respect, the kind of work of a Ph.D. student is very peculiar and it often resembles an emotional roller coaster rather than an "ordinary" job. Many close people have helped me on my way to this title, in my working and private environment: here I will mention the ones that helped me at work, I will take care to express my deep gratitude to all the others elsewhere.

First, I want to thank my three supervisors for having accompanied me during this journey. Philippe, with his remarks and continuous criticism pushed me to experiment more, to be more convinced and convincing in my writing. Judith, it was always impressive to see how readily and rapidly she reviewed every single thing for which I needed advises, and because she never forgot how important it is to acknowledge and give support to her students. Bruno, my next-door supervisor which had surely the largest piece of all my discussions about work, fails, dead ends, or conversations about just everything; our being always "on the same wavelength", the fact that I could always count on his availability and constructive feedback anytime was an invaluable help and I felt just blessed for it: Thank you!

Many others from the instruments and labs I used at ILL deserve my special gratitude. The D16 team with Viviana and Olivier and their effective help even in the weirdest hours or conditions. Isabelle, who helped me getting started with SANS and for her full positive attitude towards the very first and not-so-successful tests (ILL misses you!) and Sylvain that often transformed a coffee break into the moment where I learnt how to solve my hardest issues with SANS data. Ingo for his time spent explaining to me the magic of neutron spin echo. IN13 and the high pressure team Yann, Claude and James for their help with the thousand issues experienced with the pressure equipment. The D33 and IN6 teams. All the lab responsibles and technicians, in particular Martina, Leo, Sandrine and also Samantha for having helped me orient myself and be fully effective in the lab.

All the jury members for my Ph.D. dissertation: Prof. Daniela Uhríková, Dr. Jean-Paul Douliez, Prof. Roland Winter, Prof. Giovanna Fragneto, Dr. Juliette Jouhet, Prof. Hans Geiselmann. I contributed actively in the choice of the commission and

I was honoured to have them examining my work. I add to them Dr. Francesca Natali who followed up my progress during the years as a member of the "Comitè de Suivi de Thèse" together with Dr. Jouhet.

Everyone who made it possible for me to perform additional experiments in the external labs in Dortmund, Bordeaux and Didcot, in particular the ones that were not already mentioned here above: Dr. Axelle Grélard, Dr. Erick Dufourc, Dr. Rosario Oliva, the I22 instrument team.

(Soon to be Dr.) Antonio Caliò for having shared with me some of the experimental struggles during his internship and all the others from the LIPhy-M2E team: Josie (and our miserable beamtime dinners!), Aline, Tatsuhito, Dominik.

The entire LSS group, I was proud of being part of it and it was just a pleasure to see how easy was to ask and get any kind of help from each one of you; the entire ILL staff, I feel lucky that I could do my Ph.D. here and I would choose it again and again if I would go back in time!

Last, but definitely not least, all of my fellow students at ILL who have shared with me so much of these Ph.D. years, inside and outside the campus. Every coffee break, every lunch, every beer and every other gathering together made all of this worth each second. It is perhaps my deepest regret that we won't be able anymore to share nice moments as easily as before. Long ago I stopped referring to many of you as my "colleagues", because "friends" is the appropriate word. I hope we will meet again as often as possible in our future and see where life has brought each one of us. Thank you for everything!

Dr. Loreto Misuraca

REFERENCES

1. N. R. Pace, *Cell* **65**, 531–533 (1991).
2. W. K. Hartmann, D. R. Davis, *Icarus* **24**, 504–515 (1975).
3. P. A. Sossi *et al.*, *Science Advances* **6**, eabd1387 (2020).
4. S. A. Wilde, J. W. Valley, W. H. Peck, C. M. Graham, *Nature* **409**, 175–178 (2001).
5. J. W. Schopf, *Science* **260**, 640–646 (1993).
6. S. J. Mojzsis *et al.*, *Nature* **384**, 55–59 (1996).
7. E. A. Bell, P. Boehnke, T. M. Harrison, W. L. Mao, *Proceedings of the National Academy of Sciences* **112**, 14518–14521 (2015).
8. I. Daniel, P. Oger, R. Winter, *Chemical Society Reviews* **35**, 858–875 (2006).
9. L. E. Orgel, *Trends in biochemical sciences* **23**, 491–495 (1998).
10. Y. Kawaguchi *et al.*, *Astrobiology* **16**, 363–376 (2016).
11. A. Yamagishi *et al.*, *Astrobiology* **18**, 1369–1374 (2018).
12. S. L. Miller *et al.*, *Science* **117**, 528–529 (1953).
13. D. Ring, Y. Wolman, N. Friedmann, S. L. Miller, *Proceedings of the National Academy of Sciences* **69**, 765–768 (1972).
14. Y. Wolman, W. J. Haverland, S. L. Miller, *Proceedings of the National Academy of Sciences* **69**, 809–811 (1972).
15. J. Oró, *Biochemical and Biophysical Research Communications* **2**, 407–412 (1960).
16. J. P. Ferris, R. A. Sanchez, L. E. Orgel, *Journal of molecular biology* **33**, 693–704 (1968).
17. J. F. Kasting, *Science* **259**, 920–926 (1993).
18. K. Kvenvolden *et al.*, *Nature* **228**, 923–926 (1970).
19. P. Schmitt-Kopplin *et al.*, *Proceedings of the National Academy of Sciences* **107**, 2763–2768 (2010).
20. D. W. Deamer, *Nature* **317**, 792–794 (1985).
21. W. Martin, J. Baross, D. Kelley, M. J. Russell, *Nature Reviews Microbiology* **6**, 805–814 (2008).

22. T. M. McCollom, G. Ritter, B. R. Simoneit, *Origins of Life and Evolution of the Biosphere* **29**, 153–166 (1999).

23. *Basilicofresco - Derivative work from Image:Murchison meteorite.jpg, CC BY-SA 3.0*, (https://commons.wikimedia.org/w/index.php?curid=4301968).

24. *NOAA, Public Domain*, (https://commons.wikimedia.org/w/index.php?curid=3597762).

25. R. A. Sanchez, J. P. Ferbis, L. E. Orgel, *Journal of Molecular Biology* **30**, 223–253 (1967).

26. W. V. Allen, C. Ponnamperuma, *Biosystems* **1**, 24–28 (1967).

27. J. G. Lawless, G. U. Yuen, *Nature* **282**, 396–398 (1979).

28. M. Maurette, *Origins of Life and Evolution of the Biosphere* **28**, 385–412 (1998).

29. B. Damer, D. Deamer, *Life* **5**, 872–887 (2015).

30. B. Damer, D. Deamer, *Astrobiology* **20**, 429–452 (2020).

31. P.-A. Monnard, C. L. Apel, A. Kanavarioti, D. W. Deamer, *Astrobiology* **2**, 139–152 (2002).

32. S. E. Maurer *et al.*, *Langmuir* **34**, 15560–15568 (2018).

33. S. F. Jordan *et al.*, *Nature Ecology & Evolution* **3**, 1705–1714 (2019).

34. D. Deamer, *Life* **7**, 5 (2017).

35. J. F. Kasting, T. P. Ackerman, *Science* **234**, 1383–1385 (1986).

36. S. S. Mansy, J. W. Szostak, *Proceedings of the National Academy of Sciences* **105**, 13351–13355 (2008).

37. T. Oberholzer, M. Albrizio, P. L. Luisi, *Chemistry & biology* **2**, 677–682 (1995).

38. A. Cario, V. Grossi, P. Schaeffer, P. M. Oger, *Frontiers in microbiology* **6**, 1152 (2015).

39. W. R. Hargreaves, D. W. Deamer, *Biochemistry* **17**, 3759–3768 (1978).

40. R. Winter, C. Jeworrek, *Soft Matter* **5**, 3157–3173 (2009).

41. M. Trapp *et al.*, *Physical Chemistry Chemical Physics* **15**, 20951–20956 (2013).

42. R. Winter, *Biochimica et Biophysica Acta (BBA)-Protein Structure and Molecular Enzymology* **1595**, 160–184 (2002).

43. N. J. Brooks, O. Ces, R. H. Templer, J. M. Seddon, *Chemistry and physics of lipids* **164**, 89–98 (2011).

44. D. Kipping, *Proceedings of the National Academy of Sciences* **117**, 11995–12003 (2020).

45. D. Segré, D. Ben-Eli, D. W. Deamer, D. Lancet, *Origins of Life and Evolution of the Biosphere* **31**, 119–145 (2001).

46. W. Gilbert, *nature* **319**, 618–618 (1986).

47. C. Paleos, *Trends in biochemical sciences* **40**, 487–488 (2015).

48. M. M. Hanczyc, P.-A. Monnard, *Current Opinion in Chemical Biology* **40**, 78–86 (2017).

49. J. Jouhet, *Frontiers in plant science* **4**, 494 (2013).

50. C. Tanford, *The hydrophobic effect: formation of micelles and biological membranes 2d ed* (J. Wiley., 1980).

51. J. Israelachvili, *Faradav Trans. ll* **72**, 1525–1568 (1976).

52. I. A. Chen, K. Salehi-Ashtiani, J. W. Szostak, *Journal of the American Chemical Society* **127**, 13213–13219 (2005).

53. S. Kapoor *et al.*, *Angewandte Chemie* **126**, 8537–8541 (2014).

54. M. Fiore, P. Strazewski, *Life* **6**, 17 (2016).

55. K. Morigaki, P. Walde, *Current Opinion in Colloid & Interface Science* **12**, 75–80 (2007).

56. A.-L. Fameau, T. Zemb, *Advances in colloid and interface science* **207**, 43–64 (2014).

57. P. Walde, T. Namani, K. Morigaki, H. Hauser, *Liposome technology* **1**, 1–19 (2007).

58. D. F. Evans, H. Wennerström, *The colloidal domain: where physics, chemistry, biology, and technology meet* (Wiley-vch New York, 1999).

59. J. Gebicki, M. Hicks, *Nature* **243**, 232–234 (1973).

60. C. L. Apel, D. W. Deamer, M. N. Mautner, *Biochimica et Biophysica Acta (BBA)-Biomembranes* **1559**, 1–9 (2002).

61. B. R. Simoneit, *Advances in Space Research* **33**, 88–94 (2004).

62. G. U. Yuen, K. A. Kvenvolden, *Nature* **246**, 301–303 (1973).

63. I. Budin, N. Prywes, N. Zhang, J. W. Szostak, *Biophysical journal* **107**, 1582–1590 (2014).

64. M. M. Hanczyc, S. M. Fujikawa, J. W. Szostak, *Science* **302**, 618–622 (2003).

65. I. A. Chen, J. W. Szostak, *Biophysical Journal* **87**, 988–998 (2004).

66. I. Budin, A. Debnath, J. W. Szostak, *Journal of the American Chemical Society* **134**, 20812–20819 (2012).

67. P.-A. Monnard, D. W. Deamer, in *Methods in enzymology* (Elsevier, 2003), vol. 372, pp. 133–151.

68. C. E. Cornell *et al.*, *Proceedings of the National Academy of Sciences* **116**, 17239–17244 (2019).

69. S. F. Jordan, E. Nee, N. Lane, *Interface focus* **9**, 20190067 (2019).

70. J. Groen, D. W. Deamer, A. Kros, P. Ehrenfreund, *Origins of Life and Evolution of Biospheres* **42**, 295–306 (2012).

71. D. W. Deamer, *Advances in Space Research* **12**, 183–189 (1992).

72. J. L. Cape, P.-A. Monnard, J. M. Boncella, *Chemical Science* **2**, 661–671 (2011).

73. A. I. Oparin (1953).

74. S. L. Miller, J. W. Schopf, A. Lazcano, *Journal of molecular evolution* **44**, 351–353 (1997).

75. S. Koga, D. S. Williams, A. W. Perriman, S. Mann, *Nature chemistry* **3**, 720–724 (2011).

76. M. M. Hanczyc, T. Toyota, T. Ikegami, N. Packard, T. Sugawara, *Journal of the American Chemical Society* **129**, 9386–9391 (2007).

77. N. Martin *et al.*, *Nature communications* **9**, 1–12 (2018).

78. T. D. Tang *et al.*, *Nature chemistry* **6**, 527 (2014).

79. M. Salvador-Castell, N. J. Brooks, J. Peters, P. Oger, *Biochimica et Biophysica Acta (BBA)-Biomembranes* **1862**, 183130 (2020).

80. M. Salvador-Castell, B. Demé, P. Oger, J. Peters, *Langmuir* **36**, 7375–7382 (2020).

81. M. Bée, *Quasielastic neutron scattering*.

82. G. L. Squires, *Introduction to the theory of thermal neutron scattering* (Courier Corporation, 1996).

83. L. Van Hove, *Physical Review* **95**, 249 (1954).

84. S. W. Lovesey (1984).

85. *Web page of the Institut Laue-Langevin (France)*, (https://www.ill.eu/reactor-and-safety/high-flux-reactor/technical-characteristics/).

86. A. Guinier, G. Fournet, K. L. Yudowitch (1955).

87. *SasView software, originally developed by the DANSE project under NSF award DMR-0520547*, (http://www.sasview.org/).

88. G. Porod, *Kolloid-Zeitschrift* **124**, 83–114 (1951).

89. F. Nallet, R. Laversanne, D. Roux, *Journal de Physique II* **3**, 487–502 (1993).

90. G. Zaccai, J. Blasie, B. Schoenborn, *Proceedings of the National Academy of Sciences* **72**, 376–380 (1975).

91. D. Worcester, N. Franks, *Journal of molecular biology* **100**, 359–378 (1976).

92. N. Franks, W. Lieb, *Journal of molecular biology* **133**, 469–500 (1979).

93. G. Büldt, H. Gally, J. Seelig, G. Zaccai, *Journal of molecular biology* **134**, 673–691 (1979).

94. A. Rahman, K. Singwi, A. Sjölander, *Physical Review* **126**, 986 (1962).

95. M. Tehei, R. Daniel, G. Zaccai, *European Biophysics Journal* **35**, 551–558 (2006).

96. J. Peters, G. R. Kneller, *The Journal of Chemical Physics* **139**, 10B620_1 (2013).

97. D. Zeller, M. Telling, M. Zamponi, V. Garcia Sakai, J. Peters, *The Journal of Chemical Physics* **149**, 234908 (2018).

98. B. J. Berne, R. Pecora, *Dynamic light scattering: with applications to chemistry, biology, and physics* (Courier Corporation, 2000).

99. A. Siegert, *MIT Radiation Lab*, 1943.

100. B. J. Frisken, *Applied optics* **40**, 4087–4091 (2001).

101. F. Mezei, *Zeitschrift für Physik A Hadrons and nuclei* **255**, 146–160 (1972).

102. A. Zilman, R. Granek, *Physical review letters* **77**, 4788 (1996).

103. U. Seifert, S. A. Langer, *EPL (Europhysics letters)* **23**, 71 (1993).

104. W. Rawicz, K. C. Olbrich, T. McIntosh, D. Needham, E. Evans, *Biophysical journal* **79**, 328–339 (2000).

105. I. Hoffmann, *Colloid and Polymer Science* **292**, 2053–2069 (2014).

106. J. H. Davis, *Biochimica et Biophysica Acta (BBA)-Reviews on Biomembranes* **737**, 117–171 (1983).

107. J. Seelig, *Quarterly reviews of biophysics* **10**, 353–418 (1977).

108. R. Bärenwald, A. Achilles, F. Lange, T. M. Ferreira, K. Saalwächter, *Polymers* **8**, 439 (2016).

109. J.-P. Douliez, A. Leonard, E. J. Dufourc, *Biophysical journal* **68**, 1727–1739 (1995).

110. L. Misuraca *et al.*, *Langmuir* **36**, 13516–13526 (2020).

111. L. Misuraca, B. Demé, P. Oger, J. Peters, *Communications Chemistry* **4**, 1–8 (2021).

112. M. Taha, M. M. Khalil, S. A. Mohamed, *Journal of Chemical & Engineering Data* **50**, 882–887 (2005).

113. A. Tesmar *et al.*, *Journal of Thermal Analysis and Calorimetry* **126**, 97–102 (2016).

114. M. Salvador-Castell, M. Tourte, P. M. Oger, *International journal of molecular sciences* **20**, 4434 (2019).

115. T. Pott, E. J. Dufourc, *Biophysical Journal* **68**, 965–977 (1995).

116. R. Dazzoni *et al.*, *Scientific reports* **10**, 1–14 (2020).

117. T. F. Zhu, J. W. Szostak, *Journal of the American Chemical Society* **131**, 5705–5713 (2009).

118. C. Hentrich, J. W. Szostak, *Langmuir* **30**, 14916–14925 (2014).

119. T. Hauß, S. Dante, N. A. Dencher, T. H. Haines, *Biochimica et Biophysica Acta (BBA)-Bioenergetics* **1556**, 149–154 (2002).

120. M. Salvador-Castell *et al.*, *Communications biology* **4**, 1–13 (2021).

Abstract

Life is a stable state of matter away from equilibrium, the appearance of which has always puzzled mankind. It emerged at least once in the Universe, and the fact that we know (and are) the outcome of this successful event, provides us with valuable insights. For instance, for its ubiquity in the current living systems, the existence of a compartment (the cell membrane) must have been one of the crucial aspects also at the early stages of life. All commonly accepted scenarios for the onset of life formation include extreme environments, with very high temperatures of often > 100 °C and, in some cases, high hydrostatic pressure up to 1000 bar. Therefore, it is mandatory to study the impact of such conditions on the proto-cells membranes (protomembranes) characteristics and functionality. This thesis work defines and studies a model of protomembrane made by simple, prebiotically available molecules, which may have offered a defense strategy against the harsh environmental physical conditions of the early Earth. The model is a mixture of short-chain fatty acid and fatty alcohol that includes a linear hydrocarbon as additional, apolar membrane component. The physico-chemical contribution and effect of each and every constituent of this model was investigated. The alcohol addition has a major role on membrane structure and properties, especially at high temperature where it protects the vesicles from dissolving and allows them to fuse into larger macrostructures. Apolar molecules enter the membrane hydrocarbon region, improve significantly its stability at high temperature and make it physically insensitive to the high pressure. All these results make the proposed model a very promising protomembrane candidate, offering a stable compartment and a useful strategy against the environmental conditions imposed at the origin of life.

Resumé

La vie est un état stable de la matière hors équilibre, dont l'origine a toujours intrigué l'humanité. Le fait qu'elle ait émergé au moins une fois dans l'Univers et que nous connaissions (et soyons) le résultat de cet événement, fournit des informations précieuses pour la recherche. Par exemple, à cause de son ubiquité dans tous les systèmes vivants connus, l'existence d'un compartiment (la membrane cellulaire) doit avoir été l'un des aspects essentiels à l'émergence de la vie. La plupart des scénarios communément acceptés pour l'apparition de la vie ont recours à des environnements extrêmes, avec des températures très élevées dépassant souvent 100 °C et, dans certains cas, une pression hydrostatique élevée qui peut atteindre plus de 1000 bar. En conséquence, il est essentiel de prendre en compte l'impact de ces conditions extrêmes sur les caractéristiques et la fonctionnalité des membranes des proto-cellules (protomembranes). Ce travail de thèse définit et étudie un modèle de protomembrane qui est constitué de molécules simples, disponibles prébiotiquement, et qui pourrait offrir une stratégie d'adaptation face aux conditions environnementales extrêmes de la Terre primitive. Ce modèle est un mélange d'acides gras et d'alcools gras à chaînes courtes qui contient un hydrocarbure linéaire apolaire en tant que composant membranaire additionnel. La contribution physico-chimique relative de chaque constituant a été étudiée expérimentalement. L'alcool gras induit un effet remarquable sur la structure et les propriétés de la protomembrane, surtout à haute température où il protège les vésicules de la dissolution et leur permet de se fondre pour donner des macrostructures plus grandes. Les molécules apolaires rentrent dans la région hydrocarbonée de la membrane, améliorent significativement sa stabilité à haute température et la rendent insensible à la pression élevée. Tous ces résultats font du modèle proposé un candidat de protomembrane très prometteur, qui offre un compartiment stable et une stratégie utile face aux conditions extrêmes imposées par l'environnement à l'origine de la vie.